POLITECNICO DI MILANO
DEPARTMENT OF ELECTRONICS, INFORMATION AND BIOENGINEERING
DOCTORAL PROGRAMME IN INFORMATION TECHNOLOGY

FEMTOSCOPE ARRAY FOR CORRELATION AND SPECTROSCOPY (FARCOS): SIMULATION AND CHARACTERIZATION OF THE DETECTION LAYERS

Doctoral Dissertation of:
Pietro ZAMBON

Advisor:
Prof. C. Guazzoni

Coadvisor:
Prof. A. Castoldi

Tutor:
Prof. A. Geraci

The Chair of the Doctoral Program:
Prof. C. Fiorini

2013 – XXVI

Abstract

FARCOS (Femtoscope ARay for COrrelation and Spectroscopy) is a novel detection system featuring high angular and energy resolution able to reconstruct the particles momentum at high precision for different physical cases in heavy-ion collision nuclear physics experiments at intermediate energies. It is based on Double Sided Silicon Strip Detectors (DSSSD) and CsI(Tl) scintillation crystals and its goal is to achieve a full particle identification and correlation by exploiting, together with the standard identification techniques (ΔE-E, ToF), Pulse Shape Analysis techniques both on the CsI(Tl) signals and, more ambitiously, on the DSSSD in order to lower the energy identification threshold. The possibility to use our digital Data Acquisition system for the direct waveforms digitization would be beneficial to this purpose. In order to optimize the DSSSD performances we carefully investigated the fundamental physical parameters such as dark currents, capacitances and related entities as a function of the applied bias and of the frequency. In addition, we performed a detailed amplitude and position detectors response mapping exploiting the monochromatic pulsed ion beams available at the INFN-LaBeC facility (Firenze). Special attention is given to the impact of inter-strip beam incidence on the shape of the induced signals, among the main causes that can greatly spoil the overall identification capabilities. We also present the development and the full qualification of a novel simulation tool for the 3D electron-hole transport computation in 2D semiconductor detectors suitable for high charge injection levels and for highly segmented detectors as a powerful and reliable tool to investigate the signal formation dynamics in the DSSSD at operat-

ing conditions. In this respect we report a batch of dedicated simulations specifically targeted to help clarifying the experimental results obtained with the inter-strip incidence. To improve also our knowledge of the CsI(Tl) crystals scintillation properties, we extracted the time constants and intensities defining the scintillation response by a direct fitting of the digitized waveforms, showing their dependence on the energy, charge and mass – at least in a given range – of the impinging particle. On these basis we probed the merits of novel particle identification matrices. Lastly, we show some preliminary results of the first on-beam test involving full FARCOS telescopes carried out at the INFN-LNS laboratories (Catania) with the main purpose to test the overall system functionality and to probe the light yield non-uniformity of the CsI(Tl) crystals exploiting known reactions. The overall performances, though susceptible of further improvements, are excellent.

This work has been supported by INFN (Istituto Nazionale di Fisica Nucleare) in the framework of the EXOCHIM experiment and by the MIUR (Ministero dell'Università e della Ricerca Scientifica) program PRIN2009, protocol 2009RLCYL8.

Contents

1 Introduction **1**

1.1 Experimental Techniques and Requirements 2
1.1.1 Physics of the Experiments 2
1.1.2 Detection Systems Requirements 5
1.2 Interaction of Charged Particles with Matter 6
1.3 Classical Particles Identification Techniques 8
1.3.1 $\Delta E - E$ 8
1.3.2 Pulse Shape Discrimination in CsI(Tl) 10
1.3.3 Time of Flight 12
1.3.4 Pulse Shape Discrimination in Si 12
1.4 Examples of State of Art 4π Multidetector and Detection Systems for Correlation and Spectroscopy 14
1.4.1 CHIMERA 15
1.4.2 MUST and MUST2 18
1.4.3 HIRA 22
1.5 Novel Tools and Techniques for Particle Identification . . . 27

2 The FARCOS Project **29**

2.1 Introduction 29
2.2 FARCOS Components 30
2.2.1 Detection layers 30
2.2.2 Front-end Electronics for the Silicon Layers 32
2.2.3 Data Acquisition System 35
2.3 Expected Performances of the Silicon Detection Layers . . . 38

3 Characterization of the FARCOS Double Sided Silicon Strip Detectors 41
3.1 Introduction 41
3.2 Capacitance Measurements 42
3.2.1 Experimental Setup 43
3.2.2 The Impedance Measurement Model 46
3.2.3 Results 47
3.3 Energy and Position Response Map with Monochromatic Single Ions 60
3.3.1 The Pulsed Ion Beam-Line DEFEL of the LaBeC Accelerator 61
3.3.2 Experimental Setup 62
3.3.3 Experimental Conditions 65
3.3.4 Energy Calibration and Resolution 67
3.3.5 Position Response Matrix – Inter-Strip Effects 71
3.4 Conclusion 77

4 3D Simulation Code for Charge Transport and Signal Formation in 2D Semiconductor Detectors Suitable for High Charge Injection Levels and High Electrode Segmentation 81
4.1 Introduction 81
4.2 Physical Model and Simulation Method 82
4.2.1 Mobility and Diffusion Models 85
4.3 Code Validation 87
4.3.1 Cloud expansion in free space due to thermal diffusion only 87
4.3.2 Cloud expansion with finite detector thickness due to Coulomb repulsion only 88
4.4 Comparison with an Approximated Analytical Solution . . . 89
4.5 Enhanced Numerical Methods 92
4.5.1 Charge clustering 93
4.5.2 Adaptive carrier position update 93
4.6 Simulations of the Double Sided Silicon Strip Detector of FARCOS 95
4.6.1 Simulation Setup 96
4.6.2 Results of the Simulations 100
4.6.3 Comparison with Experimental Data 110
4.7 Conclusion 117

5 Extrapolation of CsI(Tl) Scintillation Parameters and Novel Particle Identification Techniques 119

5.1 Introduction 119
5.2 Experimental Setup and Modeling 121
5.2.1 The Digital Data Acquisition Chain of the CHIMERA Detector 121
5.2.2 Model of the Preamplifier Output Signal 122
5.3 Four-Vector Extraction and Energy Calibration 124
5.3.1 Adopted Analysis Method for the Four–Vector Extraction 124
5.3.2 Energy Calibration 127
5.4 Four-Vector Dependence on the Energy and on the Particle Type 128
5.5 Reconstruction of Conventional 2D Detection Maps 134
5.6 Search for Novel 2D Detection Maps 135
5.6.1 Approximated Analytical Model for Fast/Slow and Rise–Time Correlation 136
5.6.2 Merits of New Detection Maps at GSI Energies . . . 141
5.7 Conclusion 144

6 First On-Beam Test of a FARCOS telescope **147**
6.1 Introduction 147
6.2 Experimental Conditions 147
6.3 Preliminary Results 148
6.3.1 DSSSD Energy Calibration 149
6.3.2 $\Delta E - E$ Scatter Plots and CsI Energy Spectra 149
6.4 Conclusion 157

7 Conclusion **159**

A Technical Drawings and PCBs Layout **163**

Bibliography **191**

CHAPTER 1

Introduction

The *Equation of State* (EOS) of nuclear matter is of fundamental importance in the study of the properties of stable and unstable (radioactive) nuclei and in the study of the properties of compact astrophysical objects such as neutron stars, core-collapsing supernovae and black-holes formation [1]. In order to put some light on still open questions concerning the EOS, heavy-ion collisions are the only mean available on earth to probe the properties of nuclear matters under extreme condition. During heavy-ion collision at intermediate energies a large variety of particles and fragments are produced in one single experiment. The detection of all reaction products on an event-by-event basis and the measurement of their reciprocal correlation allows quantitative understanding of the reaction dynamics and probing space-time properties of emitting sources. The challenge in the experimental identification is posed by the great variety of emission mechanisms and researchers efforts are concentrated on obtaining a well defined characterization in terms of dynamic and thermal properties of the emitted particles. To find answers to the still open problems such as the space-time dynamics of the produced fragments, their thermal properties (*i.e.* the excitation energy), internal temperature or spin, the density at which nuclear fragmentation occurs and the liquid-gas phase transitions, several experi-

mental techniques have been established as well as corresponding detection systems [2]. This work is devoted to the study and the characterization of a novel detection system called FARCOS (*Femstoscopy ARray for COrrelation and Spectroscopy*), a compact, modular and versatile telescope array made of Double Sided Silicon Strip Detectors and CsI(Tl) scintillators. Its increased energy and spatial resolution, wide solid angle coverage and its unique capability to perform pulse shape identification techniques make it a promising investigation tool for many physical cases even at low energies and at the low intensities available at the new radioactive beam facilities.

The chapter is organized as follows. Section 1.1 gives the experimental techniques used in heavy-ion collision physics at intermediate energies and the general requirements imposed on detection systems. Section 1.2 gives the basics of the interaction of charged particles with matter – *i.e.* heavy-ion collision fragments with detectors – necessary for the correct comprehension of the experimental and theoretical work exposed in the following. Section 1.3 summarizes the standard particle identification techniques made available by a multi-stage detector such as FARCOS – $\Delta E - E$, Pulse Shape Discrimination in CsI(Tl) scintillators, ToF and Pulse Shape Discrimination in Si detectors. Section 1.4 reviews the state of the art of detection system with which FARCOS must compete – HiRA and MUST2 – or work in conjunction with – CHIMERA. Section 1.5 introduces the concept and the potentialities of digital DAQ systems and the importance of having suitable numerical tools for the simulation of the detectors response.

1.1 Experimental Techniques and Requirements

1.1.1 Physics of the Experiments

Heavy ions head-on collisions at Fermi energies – ranging between about 20 MeV/u to 200 MeV/u – exposes the nuclei to a violent collective compression phase where the overlapping nuclear matter is predicted to reach values of density well above the saturation value $\rho_0 = 0.17$ nucleon/fm^3. The following expansion phase brings the density down to significant low values, the so-called freeze-out phase ($\rho \sim 0.3\rho_0$), which turns up in the multi-fragmentation phase where many excited clusters and light particles are ejected from the collision center. Fig. 1.1 shows an artistic representation of the time evolution of a heavy-ion collision, highlighting the different reaction phases.

If on one side there is still not the certainty whether the system achieves

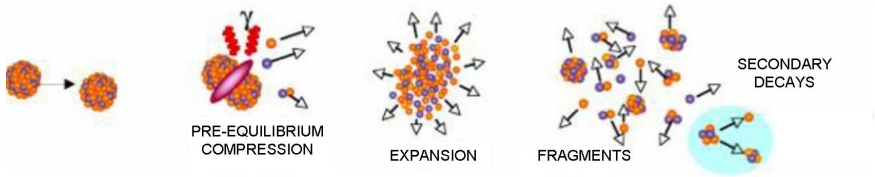

Figure 1.1: *Artistic representation of the time evolution of an heavy-ion collision with highlighted the different reaction phases. To give an idea of the time scale of the process, the freeze-out phase (fragment ejection) occurs some* 10^{-22} *s after the beginning of the collision.*

the full equilibrium in the freeze-out phase, on the other there are clear evidences of the presence of secondary decays from emitted fragments. This complex scenario can be investigated with the powerful techniques of intensity interferometry and correlation functions [3]. Correlation functions at small relative momentum allow measurements of the order of magnitude of 10^{-15} m for spatial dimensions and of $10^{-23} \div 10^{-20}$ s for time intervals [4]. Though this great achievement, one of the fundamental problems is to disentangle the prompt emitting sources from secondary emitting sources which feature time scales order of magnitude greater. The difficulty is even magnified by the extreme sensitivity to the impact parameter such as beam energy, the centrality of the collision (impact parameter), and the mass of the system [3]. Nevertheless a suitable gating of the impact parameters, reaction plane, charged particle multiplicity and other global parameters comes in partial aid to decipher the several emitting source components [2].

Proton-proton correlation function is the most common technique exploited in *Hanbury-Brown-Twiss* (HBT) intensity interferometry studies. It is defined as follow:

$$Y_{12}(\vec{p}_1, \vec{p}_2) = C_{12} \cdot (1 + R_{\vec{P}}(\vec{q}))\, Y_1(\vec{p}_1) Y_2(\vec{p}_2) \tag{1.1}$$

where $Y_{12}(\vec{p}_1, \vec{p}_2)$ is the coincident yield of the two particles detected at the same event, C_{12} is a normalization constant obtained by imposing $R_{\vec{P}}(\vec{q}) = 0$ for very large value of relative momentum $\vec{q}$ of the particles, $Y_1(\vec{p}_1)$ and $Y_2(\vec{p}_2)$ are the yields of the single particles, $\vec{P}$ is the total momentum of the pair and $1 + R_{\vec{P}}(\vec{q})$ is the proton-proton correlation function.

Thanks to the anti-symmetrization of the two-body wave function, the shape of the correlation function can be related to the different emission time delay between the protons. This is formally stated it the *Koonin-Pratt* (KP) equation:

$$1 + R_{\vec{P}}(\vec{q}) = 1 + \int S_{\vec{P}}(\vec{r}) \cdot K(\vec{q}, \vec{r}) \cdot d\vec{r} \tag{1.2}$$

where $1+R_{\vec{P}}(\vec{q})$ is the two-proton correlation function, $S_{\vec{P}}(\vec{r})$ is the two-particle emitting source defined as the probability of emitting two protons with a relative distance $\vec{r}$ measured at the time when the second particle is emitted. $K(\vec{q}, \vec{r})$ is the kernel function and it contains the whole information about the final-state interaction between the two coincident protons, including their quantum statistics. Since the correlation function is measured and the kernel function is well known for protons, solving the KP equation means extracting the source function, which retains the information on the space-time properties of the particle-emitting sources. This can be achieved through different approaches, namely *Model Sources approaches*, *Shape-Analysis approaches* and *Transport Model approaches*. The first assumes a specific function underlying the shape of the correlation function. The second releases such arbitrary assumption and numerically invert the equation. The *Imaging technique* is the most known and used method that belong to this group. The third compares the measured function to numerically computed models and allows probing transport properties such as nucleon-nucleon collision cross-section and the density dependence of the symmetry energy.

As an example, in Fig. 1.2 (a) we show a set of proton-proton correlation functions, each of them corresponding to a different total momentum gating, for the reaction ^{14}N+^{197}Au at 75 MeV per nucleon. The dashed lines are computed assuming Gaussian-shaped source function. Fig. 1.2 (b) shows the corresponding source functions computed with the imaging technique with no *a priori* assumption on the shape [2]. It worths noticing that the order of magnitude of the spatial resolution is the fm.

Since during heavy-ion collisions at intermediate energies a large variety of particles and fragments are produced, it is necessary to extend the application of the correlation function methods to the *Light Charged Particles* (LCP) and *Intermediate Mass Fragment* (IMF) other than protons. The complex scenario that emerges from these studies, consequence of the complex structure of LCPs and IMF, calls for higher-resolution detection systems in order to be properly addressed. Correlation functions with LCPs are at the basis of the emission time and chronology assessment for the particle-emitting sources, the understanding of which would facilitate the comprehension on primary fragments production mechanisms in heavy-ion collisions. IMF-IMF correlation functions are another important subject of study since they allow the extraction of the space-time properties of the

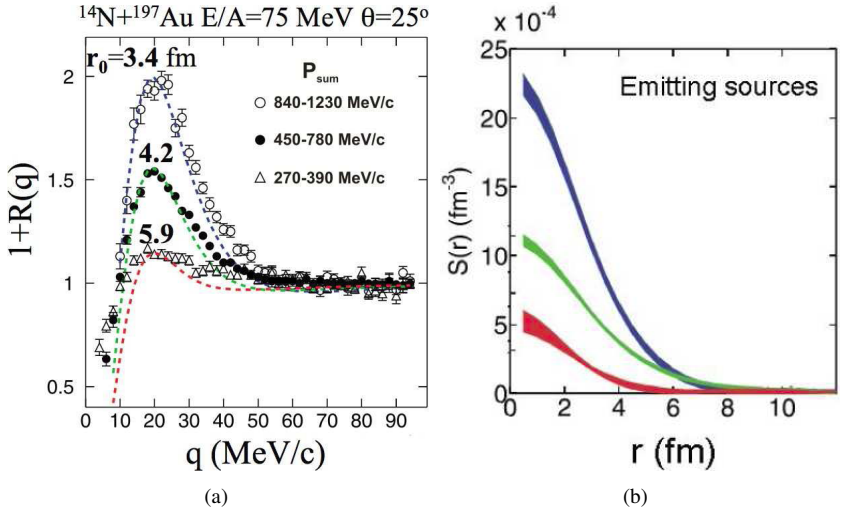

Figure 1.2: *Example of (a) proton-proton correlation function for the reaction $^{14}N+^{197}Au$ at 75 MeV per nucleon. Each curve derive from a different total momentum gating. The dashed lines are computed assuming Gaussian-shaped source function. (b) corresponding source functions computed with the imaging techniques [2].*

nuclear system produced during the reaction at the time of their freeze-out stage. This gives a unique eye on multi-fragmentation phenomena and their possible link to a liquid-gas phase transition in nuclear matter.

Two-nucleon correlation is also a precious tool to investigate the isospin dependence of the nuclear equation of state, which is perhaps the most uncertain property of neutron-rich matter.

The correlation function concept can be extended to a multi-particle scenario to explore the spectroscopic properties of the unbound states produced during the evolution of the nuclear system that follows the collision. This technique, called *Multi-Particle Correlation Spectroscopy* (MPCS), is a powerful tool since it allows disentangling simultaneous decays from sequential decays processes and gives access to the characterization of the short-living exotic nuclei [2] [5].

1.1.2 Detection Systems Requirements

Correlation measurements and the study of direct reactions in inverse kinematics with stable and radioactive ion beams (RIBs) push toward the measurements of the momentum vector and of its correlation that imposes high energy and angular resolution. In addition two- or more-particle correlation measurements require large statistics that can be gained widening the solid

angular coverage. The conflicting quest of performing correlation measurements of LCPs and IMFs or of joint detection of the emitted light particle and the residual heavy fragment arising from the stripping occurred in the incoming RIB in the study of direct reactions in inverse kinematics requires a wide dynamic range of the detector-frontend electronics system. Moreover the low energy foreseen for the RIB at SPES and SPIRAL2 requires low identification thresholds both for LCPs and IMFs, and the study of the correlation of LCPs even at high energies imposes a high stopping power. Last but not least the geometry has to be as simple and versatile as possible to allow modular assembling and easy coupling with other detectors (4π arrays, spectrometers, neutron detectors). The transportability of the system will allow temporary installation in different facilities to profit of the different beams there accelerated [6].

1.2 Interaction of Charged Particles with Matter

In order to better understand the physical constraints at the basis of any detector's design and expected performances, it is essential to have minimum knowledge of the properties of the interaction between the impinging particles/radiation and the detector material. Since we are dealing with detectors for multi-fragmentation experiments in nuclear physics, we concentrate on the behavior of charged particles passing through matter [7].

Charged particles interact with matter primarily through Coulomb force between their positive charge and the negative charge of the orbital electrons within the absorber atoms. Interactions with nuclei are also possible but rather rare and normally their contribution to the response of radiation detector is not significant. As soon as the particle enters the absorber material, it immediately interacts simultaneously with many electrons, experiencing impulses from the attractive Coulomb forces. Depending on the proximity of the encounter, the impulse may be sufficient to rise the electron to a higher-level shell (*excitation*) within the absorber atom or to remove completely the electron from the atom (*ionization*). Since the maximum energy that can be transferred to a single electron is quite small (roughly 1/500 of the particle energy per nucleon), the particle must lose its energy in many interactions resulting in a continuous decrease of the velocity until it is completely stopped. Except at their very end, the tracks tend to be quite straight because the particle is not greatly deflected by any encounter and the interactions occurs in all directions simultaneously. Charged particles are therefore characterized by a penetration *range* typical of the absorber material and beyond which no particle may go. In particularly close en-

counters, an electron may undergo a large impulse that after having left its parent atom, it may still have energy enough to create further ions. In normal condition, this is the main means of energy loss for charged particles. The range of these free electrons is always small compared to the incident particle's one.

In a silicon detector, due to the peculiarity of the electronic band structure, the overall effect of all such processes is to create an electron-hole pair every $\sim$3.6 eV of ionization energy.

The *linear stopping power* or *specific energy loss* S for a charged particle in a given absorber is defined as:

$$S = -\frac{dE}{dx} \tag{1.3}$$

which is nothing but the differential energy loss of the particle divided by the corresponding differential path. The classical expression that describes the specific energy loss is known as *Bethe formula* [8]:

$$-\frac{dE}{dx} = \frac{4\pi q^4 z^2}{m_0 v^2} NB \tag{1.4}$$

and

$$B \equiv Z\left[\ln\left(\frac{2m_0v^2}{I}\right) - \ln\left(1-\frac{v^2}{c^2}\right) - \frac{v^2}{c^2}\right] \tag{1.5}$$

where v and z are the velocity and the charge number of the impinging particle, N and Z are the number density and atomic number of the absorber atom, m_0 is the electron rest mass and q is the elementary charge. The parameter I represents the average excitation and ionization potential of the absorber and it is normally experimentally determined. From these equations we can infer, as a rule of thumb, that the impinging particle loses energy approximately as $1/v^2$, heuristically explained with the consideration that a slower particle passes more time in the proximity of the electrons resulting in a greater energy transfer, and that particle with greater charge have larger specific energy loss. The Bethe formula tends instead to fail at very low particle energies where the positively charged particles tend to pick up electrons from the absorber reducing their charge z. This typically occurs at the end of the absorption track, but for heavy charged fragments the electron pick up begins immediately at the start of the track reducing the specific energy loss in reason of the changed z. This makes the prediction of penetration properties for heavy charged fragments more difficult.

A plot of the specific energy loss along the track of a charged particle such as that shown in Fig. 4.11 is known as the *Bragg curve*. The two curves represents the qualitative behavior of a single particle and of an average over a bunch of identical particles. The difference between the two must be ascribed to the randomness of the ionization process that results in a statistical spread of the energy loss at any given penetration depth. This effect is called *energy straggling*. The energy straggling is also responsible for the range straggling, that is the fluctuation in path length for individual particles of the same initial energy.

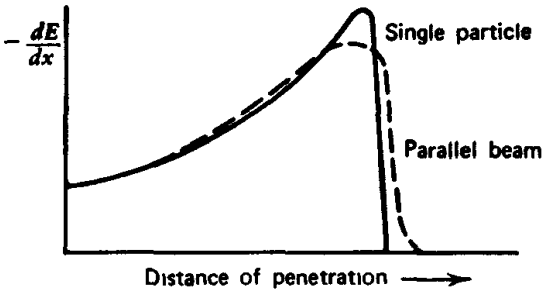

Figure 1.3: *Qualitative example of Bragg curves, being the solid one for a single particle while the dotted one for an average over a bunch of identical particles. [7].*

Fig. 1.4 shows an example of computed ranges is Silicon for several light charged particle, function of the impinging energy.

1.3 Classical Particles Identification Techniques

1.3.1 $\Delta E - E$

Often detection system employed in heavy-ion collision experiments features two or more detection stages. It comes naturally then to explore the mutual dependence of the energy released by the impinging particles in consecutive stages. This is called $\Delta E - E$ technique.

The energy is usually conceived as the amplitude of the signal delivered by the detectors, suitably shaped and sampled by a QDC. In the case of semiconductor detectors (*e.g.* Si) and in our energy range we have a constant proportionality between the energy released by the impinging particle and the amplitude of the integrated signal, regardless of the type of the particle (charge Z and mass A). On the contrary, in the case of scintillators (*e.g.* CsI) the dependence of the signal amplitude is no more linear with respect to the energy and it is also a function of the charge and mass of the particle.

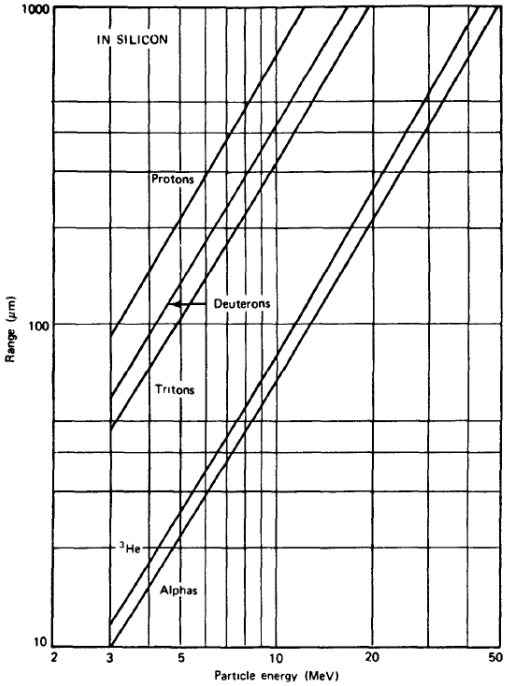

Figure 1.4: *Range-Energy curve computed for different light charged particles in Silicon. [7].*

According to the number of detection stages, several $\Delta E - E$ plots are possible. In the case of a three stage telescope, each with increasing stopping power as in modern solutions included FARCOS, there are basically two possibilities. If the particle is low energetic and stops in the second stage, ΔE is the energy released in the first detector while E is the remaining released in the second detector. If the particle is highly energetic and stops in the third and last stage, a second possibility is to take ΔE as the energy released in the second detector and E as the remaining released in the third detector. For very low energetic particles, *i.e.* that stop in the first detector, it is not possible to perform this technique.

Fig. 1.5 (a) and (b) show examples of $\Delta E - E$ plots taken with the CHIMERA detector for the reaction ^{20}Ne+^{12}C at 21.5 MeV/u and at a polar angle $\theta = 12.3°$, being (b) the zoomed version of (a). ΔE corresponds to the energy released in the first detection stage – silicon *p-i-n* diode – and E to the energy released in the second detection stage – thick CsI(Tl) scintillator. In (a) it is clearly visible the charge identification power for the heavy fragments while in (b) the identification power extends to charge Z

and mass A for light charged particles.

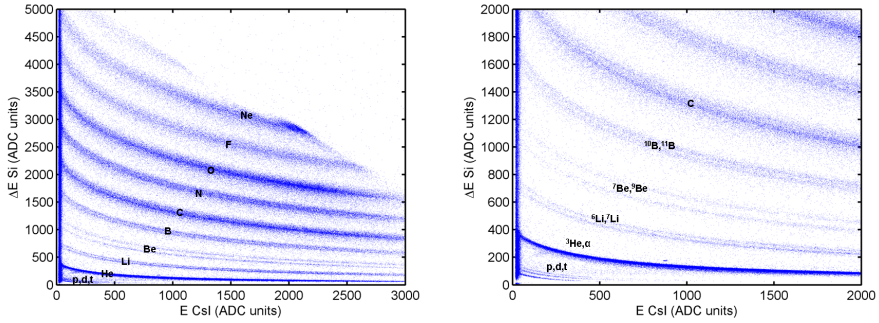

Figure 1.5: *Example of ΔE-E plots taken with the CHIMERA detector for the reaction $^{20}Ne+^{12}C$ at 21.5 MeV/u and at a polar angle $\theta = 12.3°$ and for two different zooming factors. (a) shows the charge identification power for heavy fragments while (b) shows the charge and mass resolution power for light charged particles.*

1.3.2 Pulse Shape Discrimination in CsI(Tl)

The isotopic separation of Light Charged Particle (LCP) is also possible exploiting the dependence of the CsI(Tl) signal on the charge, mass and energy of the impinging particle. How the CsI(Tl) signals depend on the characteristic of the particle is matter of Chapter 5, for now it worths mention that the scintillation light response features a *fast* and a *slow* component, the first of the order of hundreds of ns, the last of the order of μs. Among the several techniques that allows extracting the entities related to the two components, CHIMERA uses the *common gate method*. Fig. 1.6 shows a schematic diagram of the common gate method applied to a waveform. The two waveforms corresponds to the shaped photodiode signal associated to the CsI(Tl) crystal and to the same signal stretched when it reaches the maximum. Using a common gate to integrate the tail of the signal, proportional to the slow component, it is possible to extract the *Slow* parameter, while integrating the stretched signal, proportional to the fast component, it is possible to extract the *Fast* parameter. Fig. 1.7 shows as an example the *Fast-Slow* identification matrix taken with CHIMERA for the reaction ^{124}Sn+^{64}Ni at 35 MeV/u and at a polar angle $\theta = 21.5°$ [9].

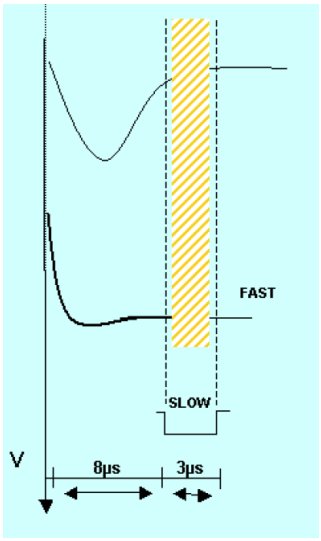

Figure 1.6: *Schematic diagram of the common gate method applied to a waveform coming from the shaping of a photodiode signal associated to the CsI(Tl) crystal [9].*

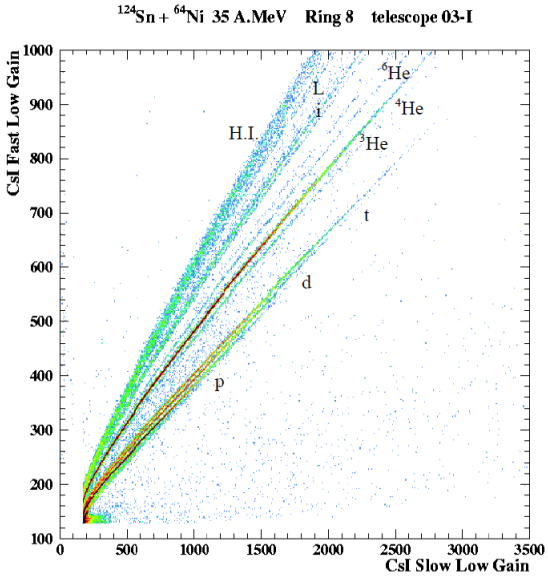

Figure 1.7: *Example of Fast-Slow identification matrix taken with the CHIMERA detector for the reaction $^{124}Sn+^{64}Ni$ at 35 MeV/u and at a polar angle $\theta = 21.5°$ [9].*

1.3.3 Time of Flight

The *Time of Flight* (ToF) technique is a powerful tool to extract the velocity of the fragments produced in the nuclear reaction and is at the basis of mass identification for particles stopping in the first detection stage, and for charge identification when particles punch through the first detector since it is combined with the other identification plots[1]. The ToF measurement is essentially the difference between two timing signals. One refers to the time of the impact on the detector, extracted from the detector signal itself, the other comes from a reference signal usually delivered by accelerators. The relation between fragments mass and the time of flight is the velocity term in the kinetic energy equation, which at non-relativistic energies gives:

$$m = \frac{2E\left(t - t_0\right)^2}{d^2} \tag{1.6}$$

where m is the mass, d the distance of the detector from the target, t is the measured value and t_0 is an offset which depends on the experimental conditions. The determination of t_0 can be not trivial since it depends on the various delaying effects of the cables and on the technique used to extract the arrival time on the detector.

Fig. 1.8 shows an example of ToF identification matrix where the time of flight is plotted with respect to the energy released in the first detector. Data are taken with CHIMERA for the reaction ^{124}Sn+^{64}Ni at 35 MeV/u and at a polar angle $\theta = 10^{\circ}$. On the graph two well distinct regions are visible. The **A** region refers to particles stopping in the detector for which it is valid Eq. 1.6, while **B** region refers to particles punching through the first detector where the amount of energy released depends on the specific energy loss of the particle [9].

1.3.4 Pulse Shape Discrimination in Si

The shape of a signal delivered by a silicon detector depends strongly on the density and on the spatial distribution of the electron-hole charge cloud generated within the volume by the detected ion. On their turn, density and spatial distribution depend on the impinging particle energy, charge and mass. Exploiting these dependencies it is possible to achieve particles charge identification also for ions stopping in the first silicon detection layer thus lowering the detection threshold. A suitable signal parameter can be

[1] This second possibility is performed only in particular cases such as when particles are so energetic that they cannot be stopped even in the second detection stage. Usually, indeed, the identification using the $-E$ is more effective.

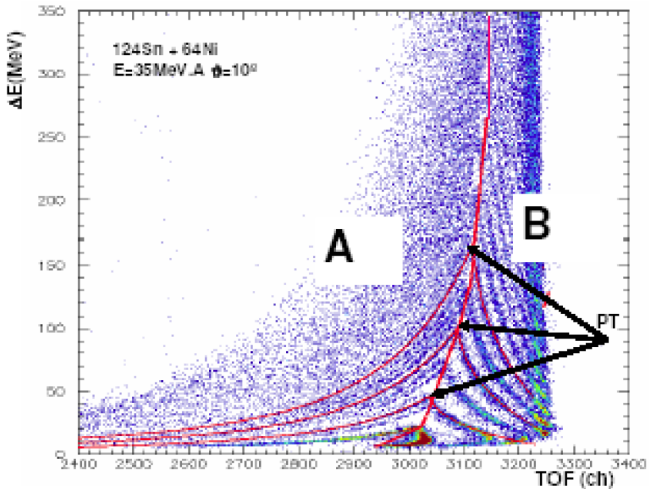

Figure 1.8: *Example of ToF identification matrix taken with the CHIMERA detector for the reaction $^{124}Sn+^{64}Ni$ at 35 MeV/u and at a polar angle $\theta = 10°$ [9]. The region labeled with **A** refers to particles stopping in the detector for which Eq. 1.6 holds, while the region labeled with **B** refers to particles punching through the first detector.*

identified in the rise-time, since it reflects the collection processes of the charge cloud by the electrodes, and it is usually plotted against the signal amplitude that stands for the energy [10] [11] [12]. It has been noticed that the identification performances vary significantly with respect to the detector injection side. Indeed, when the particle is entering from the detector front side (*pn* junction side) and its range is comparable with the thickness of the detector, a clear charge discrimination is obtained, but when on the contrary the particle's range is small in comparison with the detector thickness, the measured rise-time coalesce into a single broad band. The charge separation of this second case can be enhanced by letting the particle enter on the back side of the detector (ohmic junction side). The reason is that the lower electric field in the entrance region leads to longer plasma erosion time, which depend dramatically on the charge density, and to the longer path that holes, slower than electrons and main responsible for the signal formation, must cover. In addition the rising field profile with penetration depth minimize the plasma erosion effect at the Bragg peak near the end of the trace. The charge separation achievable with this technique in combination with the mass discrimination obtainable with a simultaneous time of flight measurement using a pulsed beam allows the complete identification of ions stopped in the first detector [13] [14].

Pulse shape discrimination can be accomplished with both analog data

acquisition systems, with the proper choice of shaping and timing amplifiers and constant fraction discriminators, and digital data acquisition systems. Fig. 1.9 shows an example of energy–rise-time identification matrix in conjunction with the $\Delta E - E$ plot obtained for particles punching through the silicon detector. It refers to the reaction ^{20}Ne+^{12}C at 21 MeV/u taken with the CHIMERA detector at polar angle $\theta = 5.8^{\circ}$ exploiting a digital DAQ system. The rise-time refers to the 10%-90% of the charge preamplifier output and the detector is mounted in front injection [13].

Fig. 1.10 shows for comparison the energy–rise-time identification plot and $\Delta E - E$ plot for the same reaction, at polar angle 11.5° but with the detector mounted in back injection [13].

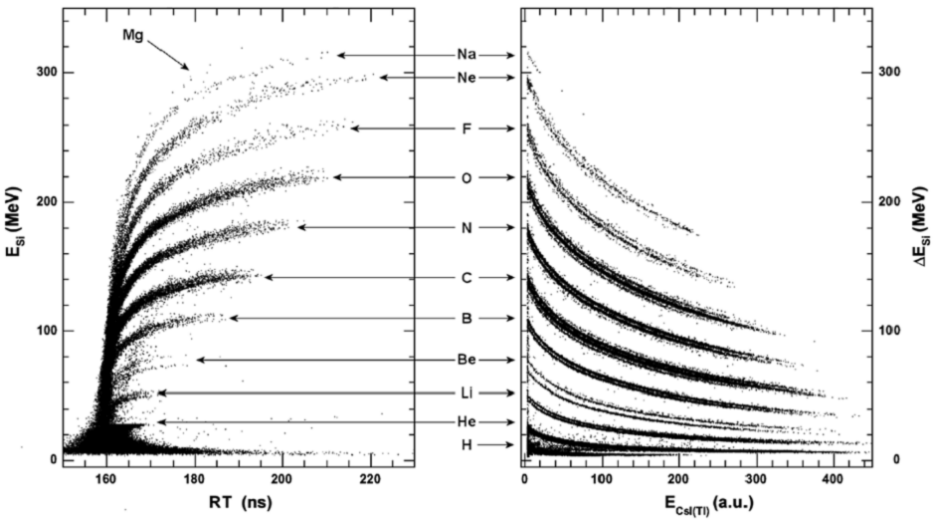

Figure 1.9: *Example of energy–rise-time identification matrix in conjunction with the $\Delta E - E$ plot obtained for particles punching through the silicon detector taken with the CHIMERA detector for the reaction ^{20}Ne+^{12}C at 21 MeV/u and at a polar angle $\theta = 5.8^{\circ}$ and detector mounted in front injection [13].*

1.4 Examples of State of Art 4π Multidetector and Detection Systems for Correlation and Spectroscopy

In recent years, the interest of the nuclear physics community about the still open problems regarding the fundamental properties of nuclear matter enunciated in Section 1.1 pushed toward the establishment of worldwide collaborations aimed to the development and employment of novel detection systems suitable to fulfill all the new pressing requirements in terms

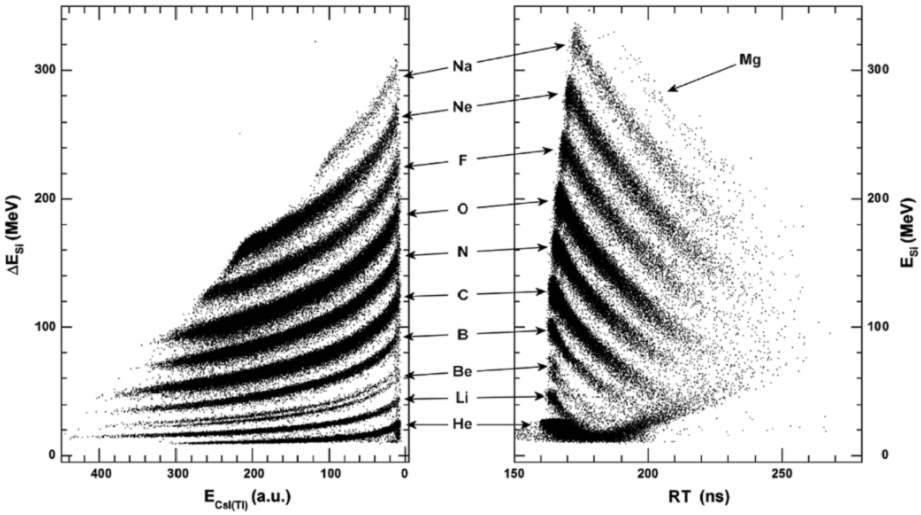

Figure 1.10: *Example of energy–rise-time identification matrix in conjunction with the $\Delta E - E$ plot obtained for particles punching through the silicon detector taken with the CHIMERA detector for the reaction $^{20}Ne+^{12}C$ at 21 MeV/u and at a polar angle $\theta = 5.8^{\circ}$ and detector mounted in back injection [13].*

of performances. Here we present some of the most significant detection systems currently in use with which FARCOS, our new endeavor, must compete – MUST2 and HiRA – or possibly work in conjunction with – CHIMERA.

1.4.1 CHIMERA

In 2003 the *Charge Heavy Ion Mass and Energy Resolving Array* (CHIMERA) detectors array see its dawn in its final 4π configuration at the INFN-Laboratori Nazionali del Sud, Catania [3] [15]. The purpose of CHIMERA detector was to investigate nucleus-nucleus collisions in the Fermi energy domain – also called intermediate energies – from 20 MeV per nucleon to 100 MeV per nucleon. In this energy range, indeed, is noticed a transition between one-body mean-field regime to two-body nucleon-nucleon interaction regime, and one of the distinct characteristics of this regime is the abundant *Intermediate Mass Fragment* (IMF) production. To fully characterize the dynamics of reactions following nuclear collisions and hence to understand some basic properties of the Equation of State (EOS) of the nuclear matter is necessary to detect and identify almost all the byproducts. The design of CHIMERA reflects this needs.

Detection Apparatus

CHIMERA is fundamentally composed by two parts for a total of 1192 detection cells as shown in Fig. 1.11. The forward part is made of 688 detection telescopes arranged in nine rings covering the angular range from 1° to 30°, with full 2π azimuthal symmetry around the beam axis. The distance between the target and the rings goes from 350 cm to 100 cm with increasing angle. The backward part is instead composed by 504 telescopes, arranged in a spherical structure of 40 cm radius around the target. The sphere covers the detection angles from 30° to 176°. Considering the beam entrance and exit holes and the frame of the detectors, the overall detection solid angle is about 94% of 4π.

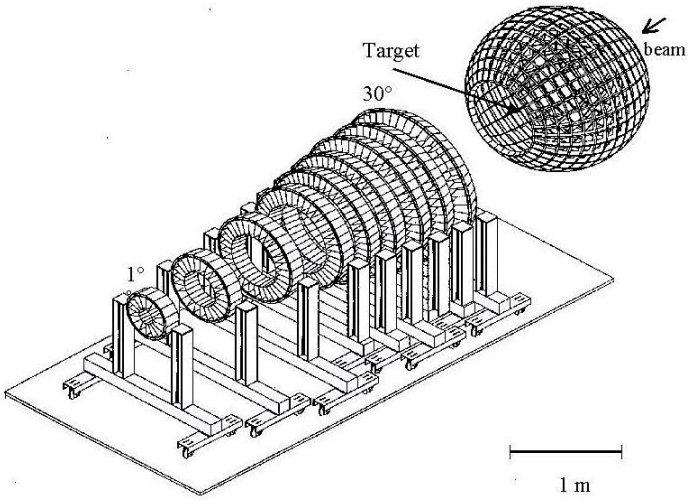

Figure 1.11: *Overview of the whole CHIMERA detection array [15].*

Every telescope is composed by two detection stages. The first is a couple of 300 μm plain silicon detectors (200 μm for the most forward ring). The resistivity of the detectors ranges between 3000 Ωcm and 5000 Ωcm while their capacitance ranges from 500 pF to 2200 pF depending on the area. The second is a CsI(Tl) scintillator with thickness ranging from 3 cm at backward angles to 12 cm at the most forward angles, coupled to a photodiode for the light read-out. All the system operates in vacuum and it is installed in a dedicated chamber.

Read-out Electronics

The almost 6000 channels (4 detectors for each of the 1192 modules) of CHIMERA are read-out by different electronic chains depending on they pertain to the silicon detectors or the CsI detectors [16] [9]. In a first case the current pulse delivered by the diode is integrated by a custom developed SMD preamplifier suitable for timing measurements with high capacitance detectors. The rise time is $\sim$50 ns and the sensitivity varies according to the polar angle – 2 mV/MeV for $1^\circ \leq \theta \leq 30^\circ$ (forward section of CHIMERA), 4.5 mV/MeV for $\theta > 30^\circ$ (backward section of CHIMERA). Each signal delivered by the charge preamplifier is split in two branches, one for the energy measurement which is shaped with a shaping time of 0.7 μs and one for the timing measurement. The power consumption per channel is ~ 250 mW. Both parameters are carefully digitized and sent to the data acquisition system outside the vacuum chamber. In a second case the signals delivered by the photodiodes reading-out the scintillation light are integrated by charge preamplifier with a gain ranging from 50 mV/MeV to 100 mV/MeV and are optimized for the photodiode capacitance. Signals are then fed to external amplifiers – realized in NIM technology – that feature a selectable shaping time in the range 0.5 μs and 3 μs. The amplifiers have two outputs, each of them goes to a different QDC for the extraction of the "fast" and "slow" components in order to perform the pulse shape discrimination. Additional 600 timing channels have been permanently implemented in order to allow pulse shape discrimination techniques also for silicon detectors.

Sometimes, not on a routine basis, a small fraction of the amplified and shaped signals of the silicon detectors and CsI scintillators is also subject to a full digital read-out in order to increase particles identification by means of on-line computations exploiting algorithms hardly realizable with analog techniques. The digitization is accomplished by commercial SADC SIS3301 [17], an eight channel 6U VME digitizer/transient recorder with sampling rate of up to 100 MHz for every single channel and 14 bit resolution. The amplifier preceding the digitizer fulfills the Nyquist requirement and covers at best the input dynamic range of the SADC.

Particle Identification and Performances

CHIMERA is capable of four different particle identification techniques. First, the commonly used $\Delta E - E$ method for charge identification of heavy ions and for isotopic identification of IMF with atomic number Z<10. Second, the Time-of-Flight technique performed with signals coming from the silicon detectors allows the mass identification. ToF is obtained by compar-

ing the timing of the detector signal and the timing of the radio frequency reference signal (RF) of the cyclotron delivering the beam. Third, the Light Charged Particles that lose a negligible energy amount in the silicon detectors but are stopped in the scintillator crystal are identified by applying a pulse shape discrimination method on the signals delivered by the photodiodes, *i.e.* the extraction of the "fast" and "slow" component. Fourth: the recent implementation of a full digital DAQ system and the implementation of 600 new timing channels opened the possibility to perform pulse shape discrimination also on a subset of silicon detectors, where the lowest energetic particles are completely stopped. By measuring the signals risetime versus the energy it is achievable a complete charge identification, thus lowering the global detection threshold [13].

Table 1.1 reports CHIMERA performances in terms of identification capabilities for light particles with Z$\leq$3 while Table 1.2 for fragments with Z>3. The energy detection threshold is estimated to be about 1 MeV/u.

Table 1.1: *Identification for light particles with Z$\leq$ 3 [15]*

Energy (MeV/u)	Technique	Measure
< 6	ToF	M
$6 - 30$	$\Delta E - E$	Z and M
> 20	PSD CsI	Z and M

Table 1.2: *Identification for fragments with Z$>$ 3 [15]*

Energy (MeV/u)	Technique	Measure
$5 - 12$	PSD Si	Z
$< 12 - 15$	ToF	M
$> 12 - 15$	$\Delta E - E$	Z

1.4.2 MUST and MUST2

In 1998 a collaboration of IPN-Orsay, DAPNIA-SPhN Saclay and DPTA-SPN Bruyères le Châtel gave birth to the *Mur à Strips* (MUST) detector [18], a modular array consisting of eight large area silicon strip-Si(Li)-CsI telescopes with associated electronics and data acquisition system dedicated to the study of reactions induced by radioactive beams on light particles in inverse kinematics (p,p'), (d,p), (d,^{3}He), (t,p)... to obtain informations of nuclei far from the stability valley, one of the new frontier of nuclear physics experiments in these years. The means by which MUST was able to reconstruct the characteristics of a reaction was to measure the

energy and angle of recoiling light particles that are spread over a wider angular range with respect to the outgoing heavy nuclei which are very forward focused, being the obtainable spatial resolution not sufficient. Also, the coincidence measurement capability is another key factor to understand the dynamic of reactions. To give an idea of the desired performances, MUST has been designed to cope with a wide energy range for the light charged particles that for proton means 500 keV to 70 MeV, with an energy resolution better than 100 keV and an angular resolution better than 1°.

In 2003 a collaboration including IPN-Orsay, IRFU/SPhN and GANIL advanced to MUST2 [19] [20]. MUST2 is an enhanced version of MUST since it features a larger active area, a greater number of strips, compactness and above all the read-out electronics which is based on an ASIC. The choice of an integrated electronics solution brings the advantages of a physical compactness and of a competitive cost per channel, considering the continously increasing number of channels.

Detection Layers

The MUST2 array consists of six identical telescopes arranged as a truncated pyramid with a base of 13 cm $\times$ 13 cm with a vertex at 15 cm. The desired standard flight distance is 15 cm and the geometry of the telescopes is highly dictated by this choice. With this configuration MUST2 has an angular coverage with efficiencies of approximately 70% up to angles of 45°. Fig. 1.12 shows a technical drawing of the mounted MUST2 array.

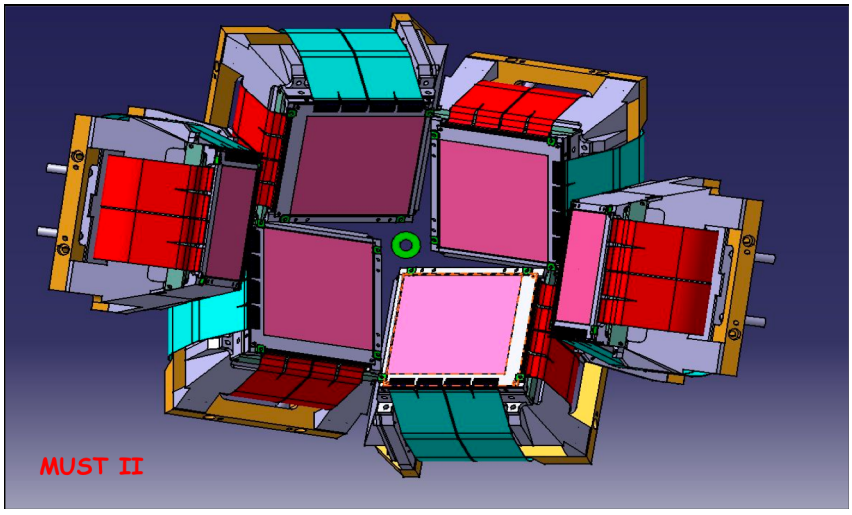

Figure 1.12: *Schematic drawing of the MUST2 6-telescopes array [21].*

Each telescope features three detection stages. The first is a double sided silicon strip detector (DSSSD), with active area 9.8 cm $\times$ 9.8 cm with 128 strips on either sides. The crystal is a $\langle 100 \rangle$ oriented n-type with resistivity $\sim$6 kΩ-cm and 300 μm thick. On both sides, the strip pitch is 0.76 mm and the inter-strip silicon dioxide isolation width is 56 μm. The capacitance of each strip is approximately 65 pF.

The second stage consists of two lithium-drifted silicon detectors of thickness 4.5 mm. Each crystal of about 10 cm $\times$ 5 cm is segmented into 8 pads on the p^+-type side.

4 cm thick CsI scintillators coupled to Hamamatsu 2 cm $\times$ 2 cm photodiodes are provided to stop the more energetic particles. Fig. 1.13 shows an exploded view of a single telescope enlightening the three detection stages.

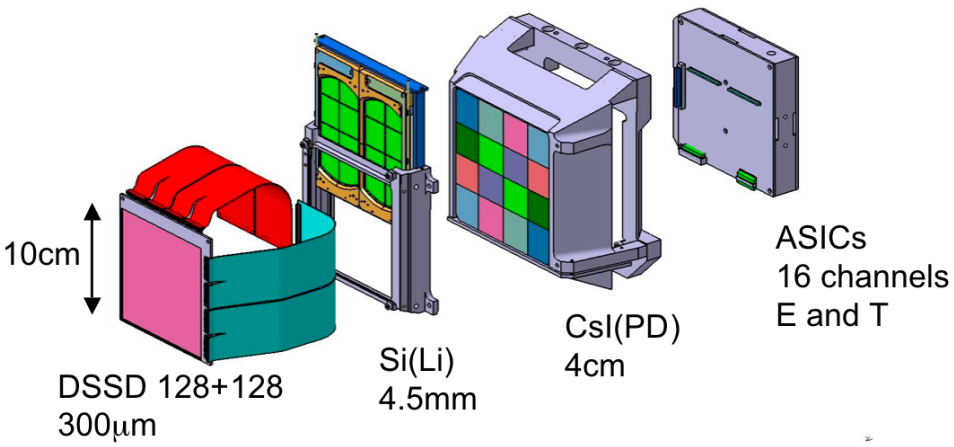

Figure 1.13: *Exploded view of a MUST2 telescope [21].*

Read-out Electronics

The read-out electronics of MUST2 consists of three basic units: MATE, MUFEE and MUVI. *Must ASIC for Time and Energy* (MATE) [22] is a 16 channel ASIC (BICMOS technology A.M.S. 0.8 μm) that process the signals delivered by the DSSSD, Si(Li) and the photodiodes detectors. The Charge Sensitive Amplifier (CSA) at the beginning of the chain consists of a single-ended folded cascode that can deal with bipolar signals and features a 160 mV/MeV, 64 mV/MeV and 700 mV/MeV gain for the DSSSD, Si(Li) and CsI (Si-equivalent) respectively and a rise time of approximately 10 ns. Three types of informations are available. First: the value of the energy losses from particles hitting the telescope. The energy measurement

block is composed by a shaper which is a CR-RC filter with 1 μs peaking time for the DSSSD and 3 μs for Si(Li) and CsI followed by a track&hold that memorizes the maximum amplitude. Second: the value of the Time-of-Flight (ToF) from a leading edge discriminator with adjustable threshold (8 bit DAC) and time-to-amplitude converter (TAC, 300 ns and 600 ns range, $2.28{\cdot}10^{-2}\%$ I.N.L). Third: the value of the DC leakage current for monitoring purposes. The power consumption must be kept low (28 mW/Channel) since the whole electronics works in vacuum.

Must Front End Electronics (MUFEE) is a board that accommodates the MATE ASICs and it is connected to the detectors via 20 cm long Kapton cables. MUFEE has an internal pulse generator to allow the test of the different functions and the calibration of energy and time channels. An external pulse generator input is also available. To ensure a good immunity against electromagnetic disturbances, all control signals are distribute in Low Voltage Differential Signal (LVDS) except the STOP-TDC.

Must in VXI (MUVI) is a unit in VXI-C standard of the acquisition system that assure the slow control and data coding for the telescopes.

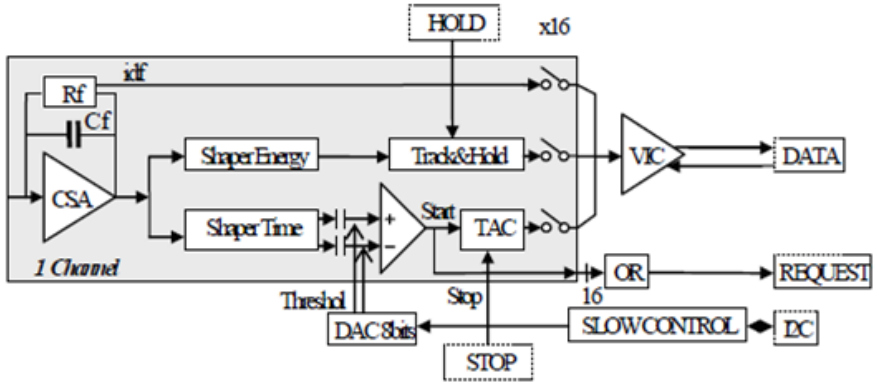

Figure 1.14: *Basic schematic of one channel of the MATE ASIC [22].*

Particle Identification and Performances

The identification of particles produced in the collisions relies on the conventional $\Delta E - E$ and on the Time-of-Flight techniques. Being MUST2 a three stage telescope, various possibilities are foreseen. For low energetic particles, *i.e.* particles stopping in the first 300 μm DSSSD (*e.g.* 6 MeV protons), no $\Delta E - E$ is of course possible, so the identification in mass is performed by measuring the energy deposited in the DSSSD versus the

time of flight of the particle. In this case the use of an external detector such as a beam tracking detector of RF signal from the accelerator is needed to assure a reference time. More energetic particles can be stopped either in the second (Si(Li)) or in the last (CsI) detection layer (*e.g.* 25 MeV and 150 MeV protons) and the $\Delta E - E$ techniques can be now performed. In the first case ΔE represents the energy loss in the DSSSD while E the energy loss in the Si(Li), in the latter case ΔE represents the energy loss in the Si(Li) while E the energy loss in the CsI. All these techniques guarantee a good isotopic discrimination.

Calibrations performed on MUST2 with a mixed nuclei α source (^{239}Pu, ^{241}Am and ^{244}Cm) reveal for the DSSSD an energy resolution of 35 keV FWHM , when the contribution of the 128 horizontal and 128 vertical strip are superposed. The estimated contribution of the front-end electronics to the energy resolution is about 16 keV FWHM. Further, the time resolution for 6 MeV protons is 240 ps FWHM. Resolutions of 120 keV and 330 keV are aimed for Si(Li) and CsI respectively, for 5.48 MeV α-particles.

1.4.3 HIRA

The *High Resolution Array* (HiRA) [23] project was born in 1999 from a National Science Foundation's Major Research Instrumentation initiative joining together Indiana University, Michigan State University and Washington University. HiRA is a large solid-angle array of silicon strip detectors that have been developed for use in a variety of nuclear structure, nuclear astrophysics and nuclear reaction experiments with rare isotope beams. It tries to cope with the weakness of exotic nuclei beams available even at the most advanced facilities by covering a great part, if not all, of the interesting kinematically allowable space. Conceptually, it belong to the same family of devices such as LASSA [24], MUST and MUST2, where several detection layers have been developed to stop and identify the fast beams produced by projectile fragmentation. The design and construction of HiRA is based on the experience of the design, construction and performances of the previous generation detection array LASSA.

Detection Layers

HiRA consists of 20 identical telescopes arranged in a modular and expandable array. Each telescope features an active area of 6.25 cm $\times$ 6.25 cm.

The first detection layer is a thin 65 μm single-sided silicon strip detector (SSSSD) with 32 strips while the second is a thick 1500 μm double-sided

silicon strip detector (DSSSD) with 32 strips on the front side (junction side) and orthogonally 32 strips on the back side (ohmic side). Both the silicon detectors are designed on the standard BB7 technology and manufactured by Micron Semiconductor [25]. They are made of a n-type bulk silicon with p^+ implantation to form the junction near the front. The 32 strips span the 6.25 cm of active area with a pitch of 1.95 mm, but while on the junction side the inter-strip width is 25 μm, on the ohmic side it is 40 μm. In addition, to reduce surface leakage current, on the front side a sequence of 10 guard rings surrounds the active strips taking up 2 mm on all sides. The 10 rings are left floating with respect to the front or back voltage. Typical values of the dark current are about 1 μA for the 65 μm detector, 1-3 μA for the 1500 μm one. The pixelation of the second stage is such that if the detector is 35 cm far from the target, the angular resolution is 0.15°.

The last detection stage is composed by four CsI(Tl) crystal manufactured by Scionix. The trapezoidal shape features an area of 3.5 cm $\times$ 3.5 cm on the front and 3.9 cm $\times$ 3.9 cm in the rear. The total thickness is 4 cm. Behind each crystal there is a 3.9 cm $\times$ 3.9 cm $\times$ 1.3 cm light guide which deliver the scintillation light to 1.8 cm $\times$ 1.8 cm photodiodes.

Fig. 1.15 shows a technical drawing of a single telescope. The color code reveals the functionalities of the various part composing the telescope. From left to right: the red frame is collimator to prevent low energy particles from stopping in the guard ring structure that surrounds the first Si detector; the green frame holds the first Si detector (65 μm SSSSD); the small light green frame that follows is slotted to allow the insertion of α particle sources for calibration purpose; the blue frame holds the second Si detector (1500 μm DSSSD). Dowel pins align this stack of detectors and frames to each other and to the orange frame that follows. Aluminum plates surround this stack, providing additional strength and electronic shielding. The orange frame, below the double-sided detector, also supports four CsI(Tl) green crystals which are mounted in quadrants behind the silicon detectors. These crystals are 4 cm thick and are trapezoidal with front and back surface areas. Glued to the back of each CsI(Tl) crystal is a 1.3 cm thick purple light guide followed by a photodiode (not visible) with active areas of 1.8 cm $\times$ 1.8 cm. Directly behind the photodiodes are the CsI(Tl) photodiode preamplifiers. The back panel of the detector has four slots through which the silicon and CsI(Tl) signal cables pass through.

The photograph in Fig. 1.16 shows a possible configuration for 16 HiRA telescopes arranged for transfer reaction experiments [26].

All the CsI(Tl) scintillators have been proved to guarantee a 1% unifor-

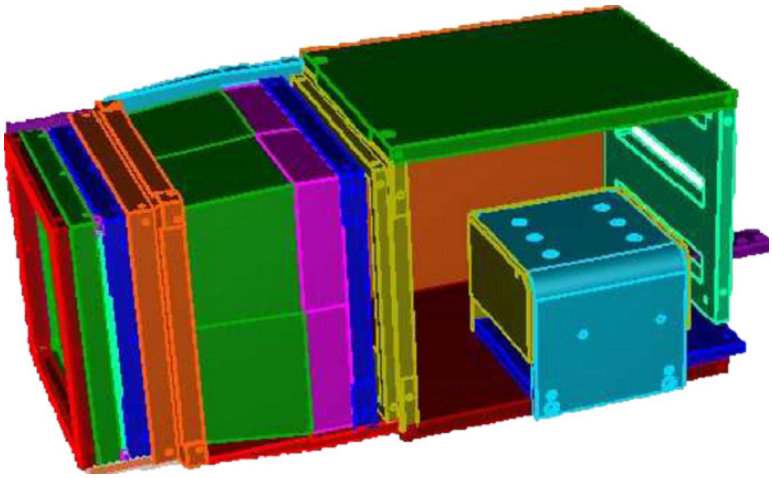

Figure 1.15: *Technical drawing of a single HiRA telescope color-coded (see text for the complete description) [23].*

Figure 1.16: *Photograph of 16 HiRA telescopes configured for transfer reaction experiment [26].*

mity for 5.486 MeV particles from an ^{241}Am source. Smooth variations in the thallium doping concentration lead to light output non-uniformity that can be corrected. There are residuals non-uniformities on the level of 0.3% that can not be eliminated since the reason is unknown.

Read-out Electronics

The versatility of the HiRA detector employment must be reflected in the design of its front-end electronics. Moreover, as the number of channel increases, a standard signal processing become unfeasible. Therefore an Application Specific Integrated Circuit has been developed (AMIS CMOS 0.5 μm technology). The block diagram of an ASIC channel is shown in Fig. 1.17. The first element in the chain is the Charge Sensitive Preamplifier (CSA), implemented in a triple scheme: low-gain, high-gain and complete by pass. The low-gain CSA gives a linear dynamic range up to 500 MeV in silicon, while the high-gain up to 100 MeV. After the CSA or external preamplifiers the signal is split with one signal going into the Nowlin pseudo constant-fraction discriminator (CFD). The discriminator consists of a zero-cross discriminator and a leading edge discriminator. It is the latter which sets the threshold. The other signal is routed to a shaping amplifier, producing an approximately Gaussian shaped signal, with a shaping time of about 1 μs. The signals can be positive or negative. The shaper is a unity gain amplifier so all the chip gain comes from the CSA. The discriminator has a trigger threshold controlled by an internal digital-to-analog converter (DAC), which can be set both positive and negative for either input level for each of the 16 channels individually. The discriminator output has three functions, start a time-to-voltage converter (TVC), update a hit register, which can be used to determine trigger criteria, and initiate a peak search. When a discriminator fires, the shaped signal will go through a peak find circuit and the peak value will be held until it is read out or forced to clear. The TVC, which has two time range settings of about 150 ns and 1 μs, is stopped by an external common stop signal. The peak of the time signal is then stored until it is read or forced clear. One ASIC consists of 16 channels, so several chip-boards were built to accommodate two ASIC each. A final motherboard contains the needed chip-boards, an FPGA to control the chip-boards and other logic functionalities. The ASICs were designed to run in sparse readout, in which a discriminator signal sets a hit register for a specific channel. The hit register bit is then required for readout of that channel to occur. This is highly desirable as otherwise the readout time for an entire tower can be quite long. There are situations where one might want to force-read electronic channels that did not trigger their discriminators. For this reason software was developed to force the discriminators on all channels to trigger, initiating a full read of all detectors connected to the motherboard. Aside from the motherboard, one only needs two VME modules to handle all information with the electronics.

The first is a SIS3301 105MHz sequencing ADC that contains 4 pairs of sampling ADCs. Each motherboard uses one pair from the sampling ADC. The second is a XLM80 universal logic module which handles the control of the readout and the storing of addresses from each motherboard along with the ADC clock.

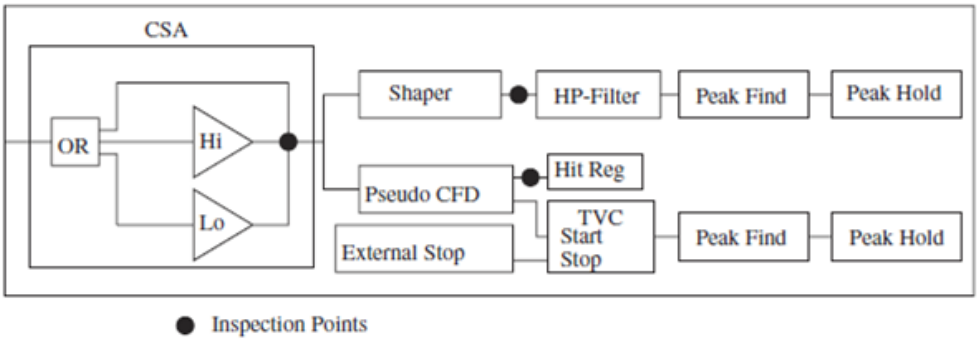

Figure 1.17: *Diagram of one channel of the HiRA ASIC [26].*

Each HiRA CsI(Tl) crystal is read-out by photodiodes directly connected to their preamplifier circuit, mounted on a small board within the telescope frame. The board provides bias, signals and test inputs. The output signals are processed by an external CAMAC Pico System shaper discriminator module and then by CAEN V758 VME peak-sensing ADCs.

Particle Identification and Performances

One of HiRA strong point is, as the other mentioned devices, the study of light particle transfer reaction in inverse kinematics, even though in some cases for a complete kinematic measurement additional spectrometer are needed to detect missing heavy ion residues, as well as additional detection systems of time-of-flight and position-sensitive detectors for beam energy and incoming angle.

HiRA's particle identification relies on the technique of energy loss, $\Delta E - E$ identification. There are two possible types of $\Delta E - E$ plots, depending on the energy of the impinging particle. For high-energy particles that penetrate and stop into the CsI(Tl) scintillator, the second Si microstrip detector is used as ΔE stage while the CsI as E stage. When, on the contrary, the particle energy is not enough to pass through the second Si detector, the ΔE stage is performed by the first Si detector and the E stage by the second itself. With this technique, HiRA is expected to resolve in mass and charge up to oxygen isotopes.

Calibration tests performed on the silicon strip detectors with ^{228}Th eight-energies α source coupled to a conventional front-end electronics have shown the resolution power in the energy range 5-9 MeV which goes from about 31 keV FWHM to about 35 keV FWHM for an average strip of the junction side of the 1500 μm DSSSD.

1.5 Novel Tools and Techniques for Particle Identification

In the framework of a general advance in detection systems design in nuclear physics, we would like to emphasize the potentialities offered by a digital Data Acquisition (DAQ) system, as the one we have developed within the CHIMERA/FARCOS collaboration and carefully described in Chapter 2. Indeed, all the standard particle identification methods relies on the *analog* extraction of the significant desired parameters from the charge sensitive amplification (CSA) chain output. What we want to stress is the fact that *all* the information regarding the interaction between the impinging particle and the detector is reflected in the *shape* of the waveform at the output of the CSA chain. Measurements such as signal amplitude (energy) and timing of the leading edge (for ToF) are the most common ones and their importance is uncontested, but they do not reveal everything. This limit is becoming even more evident in the case of highly-segmented semiconductor detectors such as the silicon strip detectors, where the complexity of some induced signals is detrimental for a correct assessment of the classical aforementioned parameters, or considering the need of lowering the identification threshold – *i.e.* particles stopping in the first silicon detection stage – where at least a second parameter must be extracted in order to obtain charge identification (*e.g.* the rise-time, see [13] for a first experimental attempt with CHIMERA, [14] and [27] for a theoretical analysis and simulations). If we were able to record the *whole* waveforms delivered by the detectors we could access – in line of principle – all the available information retained within them. A fully digital treatment of the signals at the output of the CSA would cope with this request.

We give then a brief list of the main advantages given by the use of a digital DAQ system. First, the use of modern fast computers allows fast on-line and real-time analysis on the digitized data. Second, working with the digitized waveforms allows performing computation with algorithms which are hardly realizable with analog techniques for physical or practical reasons; as an example optimal filters, smart selection or discard of events according to determined criteria. Third, the insensitivity to pick-up noises and disturbances as soon as the waveforms are digitized. Fourth, the possi-

bility to store the digitized waveforms for further off-line analyses and the creation of valuable data-set. The flexibility of the digital way seems even more attractive considering the always increasing number of channels in modern detection systems [28].

In this work we extensively exploited the digital DAQ capabilities in the framework of the characterization of the FARCOS detection layers, see Chapters 3, 5 and 6. The advantages with respect to the traditional analogue DAQ appears evident.

On another hand, the possibilities opened by a digital signal treatment do not prescind from the comprehension of the fundamental mechanisms of signal formation within the detectors. Due to their complexity, simulation tools have thus become a necessary instrument for detector scientists. They offer the possibility to test hypothetical devices even not yet manufactured as well as a unique insight into the device behavior by allowing the observation of entities that cannot be measured on real devices. The goal of any simulation tool is to provide a level of sophistication sufficient to capture the essential physics underlying but at the same time minimizing the computational burden in order to obtain results in a suitable time frame [29].

In nuclear physics, the high degree of segmentation of modern detector arrays and the wide range of charge injection levels pose serious problems to an intuitive interpretation of the results, sometimes so complicated that the real cause can be misunderstood. Coulomb repulsion, for instance, and eventually plasma effects become relevant at high level of charge injection in the computation of the transport properties of the generated carriers and their impact on the shape and duration of the induced signals as well as on spatial and time resolution must be taken into account. Moreover, the increased complexity of the induced signals pattern in monolithic multi-channel detectors – *e.g.* due to charge sharing effects, multi-electrode induction, charge trapping, etc. – must be carefully studied to optimize detector parameters and signal processing techniques [30].

To this purpose we tailored a simulation tool able to fulfill these requirements and it is described in full detail in Chapter 4 along with some of the most significant simulation results obtained for the FARCOS silicon detection layers.

CHAPTER 2

The FARCOS Project

2.1 Introduction

The FARCOS project – *Femtoscope ARray for COrrelations and Spectroscopy* – started in 2011 in the framework of the INFN *Exochim* experiment based at INFN-Sezione di Catania (Italy). Like the most recent competitor detection systems MUST2 (1.4.2) and HiRA (1.4.3), it addresses those topics concerning correlation measurements in multi-fragmentation experiments involving stable and radioactive beams to investigate the still open cases in nuclear physics.

FARCOS is conceived as a versatile and modular array of telescopes each composed by three detection stages – two Double Sided Silicon Strip Detectors (DSSSD) and thick CsI(Tl) scintillators. The design specifications try to cope with the most stringent requirements in terms of angular and energy resolution needed to reconstruct the particles momentum with high precision not differently from the competitor detection systems, but its peculiar ambition to combine the high granularity with pulse shape techniques [10] [11] [12] [31] would make it extremely competitive in the international outlook. This indeed would allow – at least in line of principle

NOTE: The content of this chapter is partly based on the paper [6] coauthored by myself.

– the complete identification even of the lowest energetic particles stopping in the first detection stage. A digital DAQ system would be extremely beneficial in this sense.

FARCOS can be used alone but it would also be interesting to couple it with 4π detectors such as CHIMERA (described in Section 1.4.1, pag. 15) or Indra [32] to enrich the physics range with studies of two- and multi-particle correlations in heavy ion collision at Fermi energies in different angular regions depending on the physics case under investigation. Nevertheless, it can be also used as a plug-in for other detectors located at other cyclotrons and accelerators.

The chapter is organized as follows. Section 2.2 illustrates the main components of a FARCOS detection system – detection layers, front-end electronics and digital data acquisition system. Section 2.3 discusses the expected performances of the silicon detectors.

2.2 FARCOS Components

2.2.1 Detection layers

Fig. 2.1 shows an exploded view of a FARCOS telescope and Fig. 2.2 shows the composed telescope from different points of view. Each telescope is composed by three detection layers. Double Sided Silicon Strip Detectors (DSSSD) – 300 and 1500 μm thick, respectively – are used as first and second detection stages respectively and 4 CsI(Tl) scintillators used as third stage.

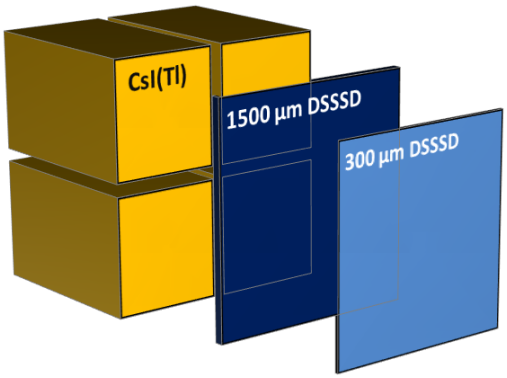

Figure 2.1: *Exploded view of the FARCOS telescope.*

Each Double Sided Silicon Strip Detector, provided by Micron Semiconductor on a standard design (BB7) [25] with a minimum area PCB

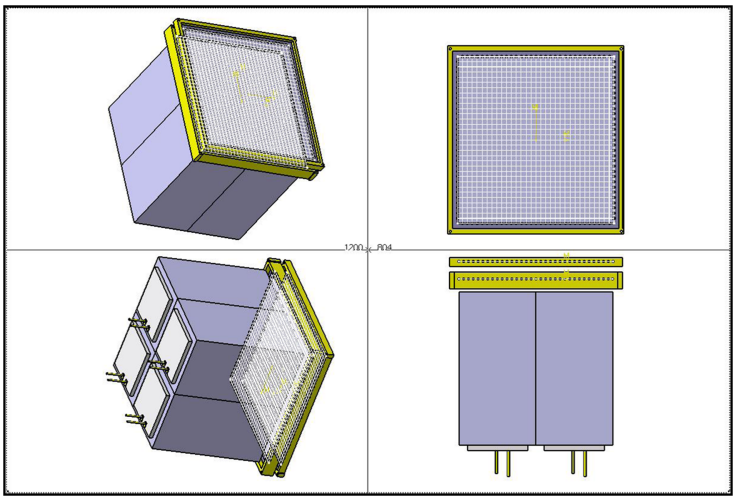

Figure 2.2: *Views from different angles of a full FARCOS telescope. The four gray blocks are the CsI(Tl) scintillator with the reading photodiode on the rear of each of them. The two yellow-framed parts are the DSSSD, the thin one before the thick one.*

frame (4 mm wide), features an active area of 64 mm $\times$ 64 mm. It is divided into 32 horizontal and 32 vertical strips, with which it is possible to generate 1024 individual pixels of 2 mm $\times$ 2 mm. This spatial resolution is enough to guarantee an angular resolution of 0.1° when placed at 1 m from the target. The inter-strip gap is 25 μm on the junction side and 40 μm on the ohmic side, where p-stop implants are provided for strip insulation (15 μm wide). The thickness of the aluminum contacting layer above the strips is 300 nm while the thickness of the inter-stirp insulating silicon dioxide layer is 900 nm. A multi-guard ring structure is provided on the detector periphery of the junction side but it is left floating. Kapton cables (nearly 20 cm-long) are directly wire-bonded to each side of the detector. Fig. 2.3 shows a technical drawing of a DSSSD and its Kapton cables. A part from the thickness of the first silicon detector and the fact that it is double sided, FARCOS silicon detectors are similar to the HiRA's ones.

The 4 highly homogeneous CsI(Tl) crystals acting as third detection stage are provided by Scionix, with Tl concentration of the order of 1200 to 1500 ppm, and are arranged in a window shape configuration. Each crystal is 6 cm thick and wrapped with 0.12 mm-thick white reflector including 50 μm of aluminized Mylar. The entrance window is composed by 2μm-thick aluminized Mylar with a density of 0.29 g/cm^2. The output light is read out by a *Hamamatsu* 18 mm $\times$ 18 mm PIN diode S3204-08, attached to the rear face of each crystal.

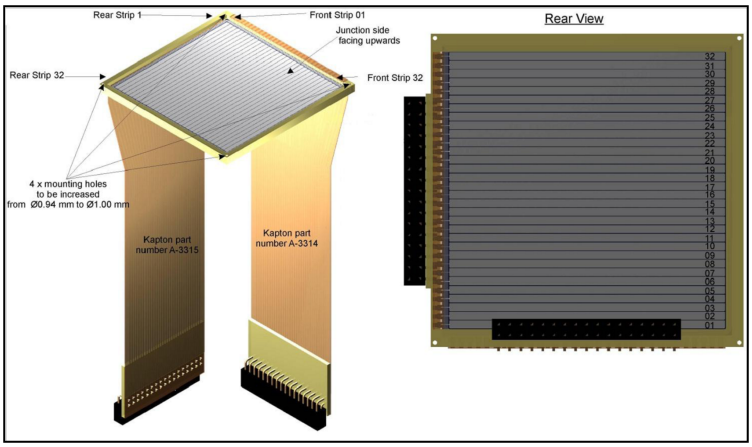

Figure 2.3: *Technical drawing of a Double Sided Silicon Strip Detector together with its Kapton cables [33].*

Depending on the physics cases the experiment is addressed, FARCOS telescopes can be put together in the most suitable configuration. The idea of modularity is well illustrated in Fig. 2.4(a) and (b) that show two examples of possible compositions of the FARCOS telescopes. The first is the typical arrangement which is expected when the decay of fragments produced by projectile excitation and breakup is studied: the array can be centered around the beam axis and it may be inserted in a 4π detector such as CHIMERA in order to improve the event characterization. On the contrary, the second fits well for the study of two-particles correlation in heavy-ion collisions, where a wall of high-resolution telescopes is needed. In any case the geometry of the clusters follows the same radius with respect to the center of the target [4].

2.2.2 Front-end Electronics for the Silicon Layers

The signals coming from the DSSSD are read out by charge preamplifiers (CPAs). Preliminary tests have been performed with the *Mesytec* MPR16 16 channels CPA. However these modules are not suited for the final assembly due to their bulky structure and large power dissipation (68 mW - 100 mW per channel). Therefore custom multi-channel hybrid large bandwidth charge preamplifiers with pseudo-differential output have been developed. The simplified schematics of one channel is shown in Fig. 2.5. The power consumption per channel is about 36 mW with a measured rise time in the range 3-7 ns, for an input capacitance ranging from 0 pF to 100 pF. 32 channels are assembled in a compact module of 8 cm $\times$ 10.5 cm. Modules

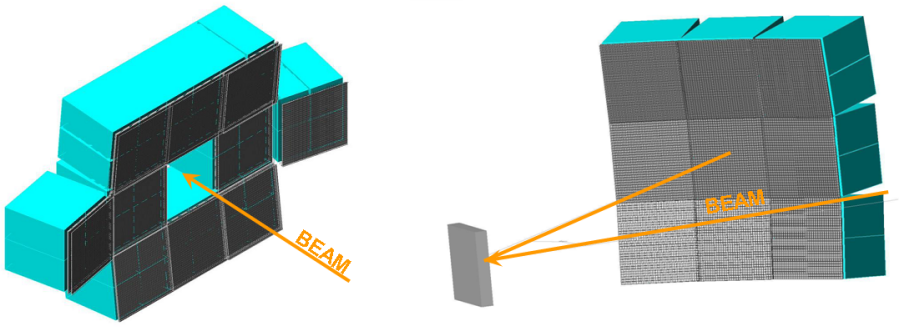

(a) (b)

Figure 2.4: *Examples of possible configurations for FARCOS array used (a) for studies of fragments decay produced by projectile excitation and breakup and (b) for studies of two-particles correlations in heavy ion collision where a complete wall is mandatory [4].*

with different sensitivities (10, 20 and 45 mV/MeV) are available. The expected performance of these preamplifiers, when coupled with the DSSSD, are discussed in Section 2.3.

We have also developed a novel design that accommodates three different remotely user-selectable sensitivities in one single module that provides an increased stability even in presence of external disturbances. The increased stability is accomplished by avoiding the use of CFAs (Current Feedback Aplifiers) in the feedback loop exploiting a classical folded-cascode topology with variable feedback capacitance that provides the sensitivities 45, 22, 15 and 10 mV/MeV. The output is still pseudo-differential. Fig. 2.6 shows the simplified schematics of one channel. The power consumption per channel is about 66 mW and the measured rise time is in the range 10-45 ns for an input capacitance ranging from 0 pF to 100 pF for the highest sensitivity, while is in the range 3-10 ns for an input capacitance ranging from 0 pF to 100 pF for the lowest sensitivity. 32 channels are assembled in a compact module of 8 cm $\times$ 12 cm.

For a third phase of the project – when the number of channels will dramatically increase – a VLSI design is under way in 0.35 μm AMS CMOS technology. To this aim both voltage mode and current mode solutions are under investigation to better trade-off between power consumption and performance.

We modified a previously designed custom anti-aliasing filter and ampli-

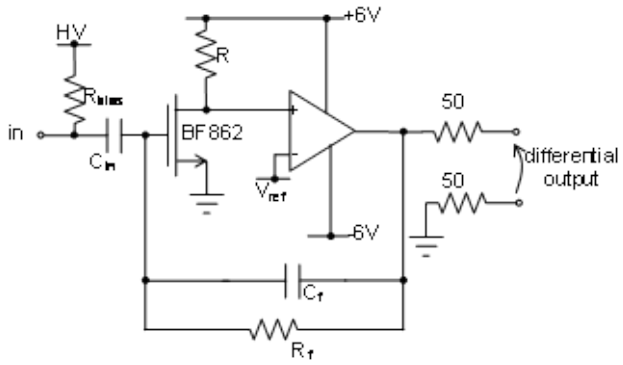

Figure 2.5: *Semplified schematic of one channel of the custom CPAs.*

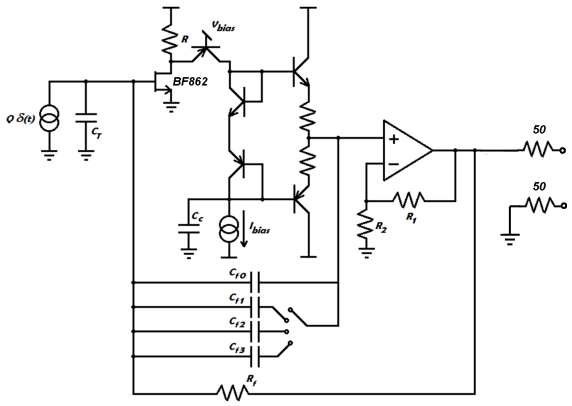

Figure 2.6: *Semplified schematic of one channel of the custom CPAs.*

fier [34], to receive the pseudo-differential signals coming from the preamplifiers. A standard single-unit 16 channel NIM module provides in a single device:

- a second order anti-aliasing filter with two programmable cutting frequencies (8 MHz and 40 MHz);
- a programmable-gain amplifier (gains of $1\times$, $2\times$, $4\times$, $8\times$) to cope with the full dynamic range of the ADC, able to select the polarity of the output signal by means of an inverting or non-inverting circuit;
- a programmable output offset voltage with AC or DC input coupling selection. Two identical outputs are available, one to serve the conventional analog acquisition chain and the other one for the digital DAQ.

All the parameters (gains, AC-DC coupling selection, offset, polarity, anti-aliasing frequencies) are programmable (channel-by-channel) via an RS485 serial interface with an individual address jumper selectable for each module by means of a dedicated selection panel on the host PC. Each module is equipped with a microcontroller to store the programmed parameters into a non-volatile memory and to restore them at power on. In addition the module features a spare output on which it is possible to multiplex one of 16 outputs channels that is automatically asserted when addressed by the programming console. The maximum input dynamics is 4 V. The maximum output dynamics is 8 V with 50 Ω back termination. The overall integral-non-linearity has been measured to be below 0.05% of the whole dynamic range and the input-referred noise is below 60 μV r.m.s. when the 40 MHz cutting frequency is selected and below 40 μV when the 8 MHz cutting frequency is selected.

2.2.3 Data Acquisition System

Two different data acquisition systems are foreseen to readout the telescope signals. A conventional analog data acquisition system borrowed from the CHIMERA 4π multidetector [3] allows, at present, reading – with pulse shape analysis capability – a total of 4 clusters composed by 4×64 channels of the 300 μm-thick DSSSDs, 4×64 channels of the 1500 μm-thick DSSSD, and 4×4 CsI(Tl) crystals for a total of 528 channels.

We developed also a custom digital DAQ Digital acquisition able to fully digitize the waveforms of the 64 channels of one selected DSSSD and of the 4 corresponding CsI(TI) scintillators for on-line monitoring, raw waveforms storage, detailed pulse shape analysis, etc. The key feature for having the two systems running in parallel is the use of the custom AAA modules described in the previous session. Let's shortly review the architecture and structure of the custom digital DAQ, whose simplified schematics is shown in Fig. 2.7.

The signals coming from one of the outputs of the AAA modules are digitized with a set of sampling ADC boards, hosted in a VME crate located in the experimental room. In the work presented in Chapter 6 (pag. 147) and in Section 3.3 (pag. 60), we used 8 *SIS3301* [17] boards for the 64 channels of the DSSSD, and one *SIS3302* [35] board for CsI(TI) scintillators signals (only for Chapter 6) and the external trigger signal from the control electronics. The *SIS3301* and the *SIS3302* boards are 8-channels, 100 MS/s digitizers, with a dynamic range of 5 V and a resolution of 14 bits and 16 bits, respectively.

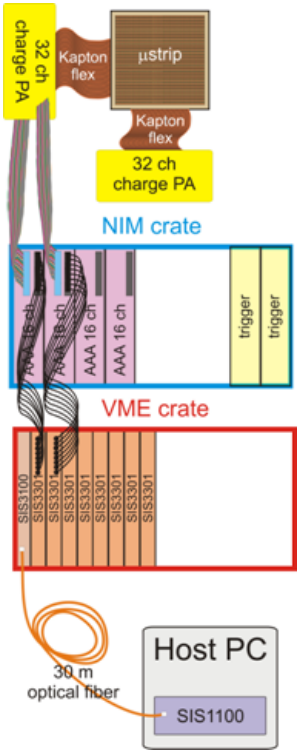

Figure 2.7: *Illustration of the Digital DAQ.*

The VME crate is connected to an host PC located in the acquisition room, with a VME-to-PCI bridge, composed of a *SIS3100* VME board and a *SIS1100* PCI board [36], linked with a 30 m long optical fiber.

The trigger signal is built by exploiting the *auto-trigger* function of the SADC boards. During acquisition, the samples from the SADC are continuously fed to the on-board FPGA, which generates a trigger output signal when the input signal crosses a user-defined threshold. The trigger outputs from all boards are then OR-ed together using a *LeCroy* 429A logic fan-in fan-out NIM module, and the result is fed back to the STOP input of each board. In this way, we can choose the acquisition channels that generate the global trigger signal and individually configure the threshold level, via software with no need to enter the experimental room, normally not accessible during measurements. Also the external trigger (coming from the machine itself or other trigger systems) is sampled as an acquisition channel and can be selected to trigger the digital DAQ acquisition system, instead of exploiting the threshold-crossing event of any channel.

A dedicated acquisition control software is used to manage the acquisi-

tion. It runs on the host PC, under a distribution of Slackware Linux. Fig. 2.8 shows a scheme of principle of the control software. The acquisition control software uploads the configuration parameters on the boards, starts the acquisition and downloads the acquired pulse shapes. The boards operate in *stop mode*: after the acquisition has been started, all channels are continuously sampled until a trigger signal is received, then after further acquiring a predefined number of samples the acquisition stops.

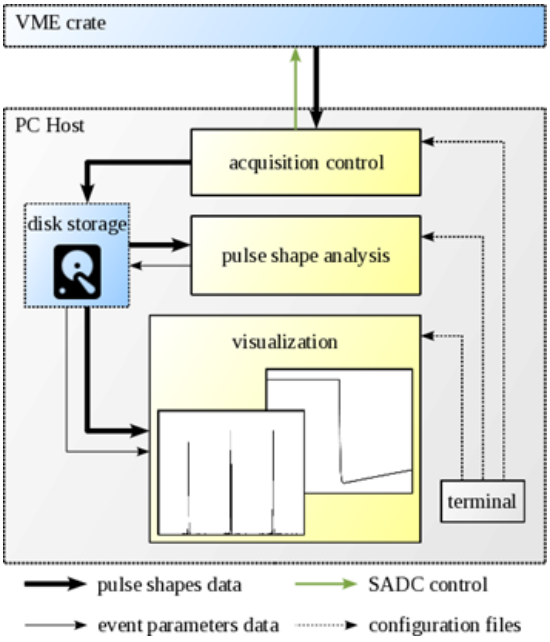

Figure 2.8: *Block diagram of the control software with the indication of the data and control parameters flow between different software components.*

Since each board runs independently, there is no a priori guarantee that every trigger signal is processed by all boards, because different boards can be in different acquisition states at the same time. In principle, each board would be able to collect a sequence of events on its own, but in the case a trigger signal is lost by only a subset of the boards, the correlation of the pulse shapes collected by different boards would be lost. To avoid this, we chose to operate also in *single mode*, where after each trigger event we download the pulse shapes from the boards and restart the acquisition from the host PC. The system is able to operate in this mode up to a trigger frequency of slightly more than 100 Hz and a data bandwidth of about 30 MB/s using all the nine boards. The collected data is stored locally on hard drives.

In order to process and visualize the data, a suite of custom made programs has been developed. An analysis software operates on the raw pulse shapes with various algorithms, in particular a baseline restorer, digital FIR filters and the computation of various event parameters. The analysis software is driven by text configuration files which define the sequence of processing algorithms to be applied on each channel. A visualization software, based on the ROOT library [37], is used to display the pulse waveforms, for diagnostic purposes, and the event parameters computed with the analysis software as histograms or scatter plots. The software includes also routines for the fitting of the spectra, and can be scripted in order to ease the analysis of large number of channels and acquisition runs.

The pulse shape data and event parameters are stored in a custom developed binary file format, which allows the storage of all the data of an acquisition run in a single file, but also extracting data pertaining to a single channel or a given sequence of events - particularly useful when data are collected from a large number of channels, but we focus the analysis only on a subset of them.

All the custom software is based on text configuration files and scripts, and can be controlled from a terminal.

2.3 Expected Performances of the Silicon Detection Layers

The resolution of one channel of the silicon detection layer together with its front-end preamplifier can be expressed in terms of its equivalent noise charge, usually expressed as the sum of three independent contributions:

$$ENC^2 = ENC^2_{series} + ENC^2_{1/f} + ENC^2_{parallel} \tag{2.1}$$

where

$$\begin{aligned} ENC^2_{series} &= A_1 C_D \left(\sqrt{\frac{C_D}{C_G}} + \sqrt{\frac{C_G}{C_D}}\right)^2 \frac{2\alpha k_B T}{\omega_T} \frac{1}{\tau} \\ ENC^2_{1/f} &= A_2 C_D \left(\sqrt{\frac{C_D}{C_G}} + \sqrt{\frac{C_G}{C_D}}\right)^2 \pi A_f C_G \\ ENC^2_{parallel} &= A_3 q I_L \tau \end{aligned} \tag{2.2}$$

The first contribution is mainly due to the channel thermal noise of the input FET. The second one is due to the *1/f* noise associated to its drain current. The third contribution is due to the shot noise of the leakage current of the detector and of the FET as well as to the thermal noise of any resistor

connected to the gate of the input FET (*i.e.* biasing resistor and feedback resistance). The capacitances C_D and C_G are, respectively, the detector-plus-feedback and parasitic capacitances ($C_D = C_{det} + C_f + C_{stray}$) and the gate-to-source capacitance of the transistor. ω_T (rad/s) is the transistor cutoff frequency, defined as $\omega_T = g_m/C_G$. The time constant τ is the peaking time of the output pulse. Coefficients A_1,A_2 and A_3 are constants – of the order of the unity – which depend on the filtering type. In 2.2 some terms depends on the transistor drain current (g_m and A_f) and others on the strip width, once fixed the strip length (I_L, C_{det},). It is therefore interesting to study the dependence of the achievable resolution on these two quantities: the strip width and the first transistor current. In addition since we are operating in vacuum and the power budget is limited, it is interesting to note that if we decrease the strip width – with a positive impact on the detector capacitance –, the number of channels increases and, when the power budget is fixed, the current available to bias the first transistor decreases - thus deteriorating the thermal noise of the first transistor (Philips BF862 in the present case). Fig. 2.9(a) and Fig. 2.9(b) show the achievable energy resolutions, expressed in terms of FWHM, in the case of 300 μm thick and 1500 μm thick DSSSDs, respectively as a function of the first transistor drain current and of the strip width for a fixed peaking time of 200 ns and for signal collected at the junction side strips. The considered leakage current density comes from the experimental measurements and the considered shaping amplifier is a triangular filter with 200 ns shaping time. Better resolutions can be achieved in the case of strips wider than 1 mm with longer shaping times due to the dominance of the white series noise. The dash-dotted lines represent the curves of constant power dissipation, while the gray shadowed area below 1 mA shows the limitation imposed by the BF862 minimum drain current. For a given power dissipation, the desired resolution can't be obtained if the degree of segmentation is too high. The vertical gray dotted line acts as guideline for the resolution achievable with the proposed BB7 DSSSD. Once we consider the signals collected at the ohmic side strips the resolution worsens due to the much lower inter-strip resistance that contributes with its thermal noise.

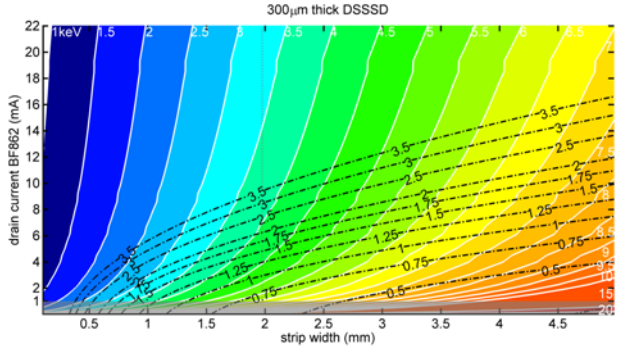

(a)

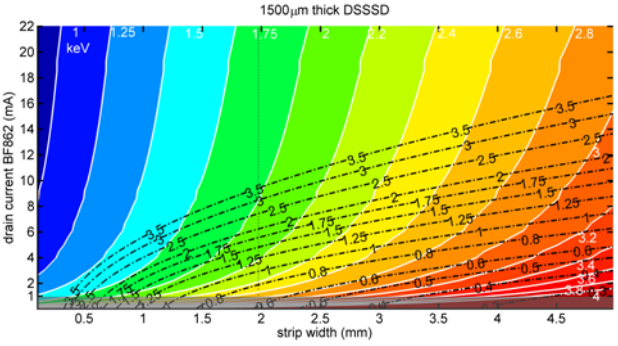

(b)

Figure 2.9: *Energy resolutions, expressed in terms of FWHM, in the case of (a) 300 μm thick and (b) 1500 μm thick DSSSDs, respectively as a function of the first transistor drain current and of the strip width for a fixed peaking time of 200 ns. The dash-dotted lines represent the curves of constant power dissipation, while the gray shadowed area below 1 mA shows the limitation imposed by the BF862 minimum drain current. The vertical gray dotted line acts as guideline for the resolution achievable with the proposed BB7 DSSSD.*

CHAPTER 3

Characterization of the FARCOS Double Sided Silicon Strip Detectors

3.1 Introduction

The Double Sided Silicon Strip Detectors (DSSSD) are the first and second detection stages of a FARCOS telescope and their aim is to act as ΔE stages when the impinging particle has enough energy to pass through toward the CsI(Tl) crystal. When on the contrary the impinging particle is not sufficiently energetic and stops within the first silicon detector they are used to perform pulse shape analysis, made possible by the digital data acquisition system. Their high segmentation guarantees the desired requirements in terms of angular and energy resolution, but it also exposes a series of non-trivial effects due to the channels mutual interaction at a physics level. In order to achieve a complete and correct assessment on the performance of the DSSSD, it is mandatory a full characterization of its properties taking into account also the front-end electronics and the analysis techniques. The chapter is organized as follows. In Section 3.2 we present the Capacitance-Voltage measurements for both detector thicknesses (300 μm and 1500 μm)

NOTE: The content of this chapter is partly based on the papers [38] and [39] coauthored by myself.

separating the two main contributions – bulk capacitance and inter-strip capacitance. We then show in Section 3.3 the main results of the characterization campaign held at the pulsed proton beam-line DEFEL of the LaBeC Accelerator – INFN Firenze – where we probed the energy and position response map for both the detectors in terms of energy calibration, resolution and impact of the inter-strip region on the shape of the signals delivered to the electronics. A brief description of the DEFEL beam-line is also given since it is essentials for the comprehension of the experiment.

3.2 Capacitance Measurements

The fundamental nature of Capacitance-Voltage measurement makes it a unique tool in semiconductor science to investigate material and device parameters. Moreover, the knowledge of the impedance characteristics of a semiconductor detector is of primary importance for engineers who found on it the design of the front-end electronics as well as the estimation of the theoretical detector's performances.

In the framework of the DSSSD characterization, we conducted a detailed CV-measurements campaign in order to assess the electrical properties of individual strips on both the *p*-implanted side (front side) and on the ohmic side (back side). We tested DSSSD with thicknesses d=300 μm and d=1500 μm, with reverse bias voltage sweeping from 0 V up to well above the depletion voltage. We investigated the different components of the total strip capacitance, namely the capacitance toward all the electrodes of the opposite side of the detector that we call *bulk capacitance*, and the capacitance of a strip with respect to the neighbor one that we call *inter-strip capacitance*. Borders effects has also been evaluated. In addition to the voltage dependence of the capacitance values, we also examined the dependence on the frequency of the probing signal over a wide range.

The importance of these measurements is related to the dependence of the equivalent nose charge (ENC), therefore of the achievable resolution performances, on the electrode capacitance, which is also of fundamental importance in the front-end electronics design phase. In addition, other physical parameters extracted from the CV-measurements such as the exact depletion voltage and the bulk effective doping are fundamental for the correct device modeling in the simulation phase. Substantially, the exhaustive knowledge of the basic physical properties of the DSSSDs is preparatory also for a well-aware application of pulse shape analysis techniques.

3.2.1 Experimental Setup

The DSSSD is housed on a dedicated Aluminum holder which is placed inside a vacuum chamber and kept lifted off the bottom by means of spacers. The technical drawing is reported in Fig. A.1 of Appendix A (pag. 163) together with its top and bottom cover, Fig. A.2 and Fig. A.3 respectively, always in Appendix A. We found that the vacuum was necessary to guarantee the stability of the bias condition for the environment humidity plays a detrimental role in the settling times. Our system ensures a vacuum level inside the chamber on the order of 10^{-4} mbar, good enough for the purpose. Ground shielding and a condition of pitch black come for free. Each side of the detector is connected through its Kapton cable to a custom made PCB board specifically designed to deviate every single channel either to the bias source or to the LCR-meter. The layout of the top and bottom layers of the PCB deviation boards are reported in Fig. A.4 and Fig. A.5, respectively, in Appendix A. Fig. 3.1 shows a close up of the DSSSD mounted inside the vacuum chamber and the custom made deviation PCB boards connected to the LCR-meter and the bias source.

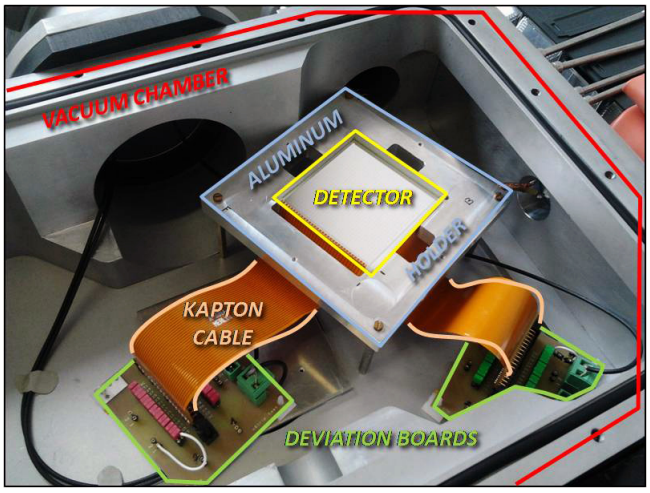

Figure 3.1: *Close up of the DSSSD mounted inside the vacuum chamber and the custom made deviation PCB boards for the CV measurements.*

The reverse bias voltage source is a *Keithley Picoammeter/Voltage Source* model 487 which can operate up to ± 500 V. Its Low and High Voltage terminals are directly connected the strips not subject to measurement. The LCR-meter is instead an Agilent E4980A Precision LCR Meter (20 Hz – 2 MHz). The provided measurement probe box has been replaced with a custom developed enhanced one since the decoupling capacitors for mea-

surements under an external bias could only hold up to $\pm$200 V, which was not enough for our purposes. In our version we plug in the four test cables of the LCR-meter and the Low and High Voltage provided by the bias voltage source and their superposition is provided to the selected DUT-High and DUT-Low strips. The layout of the top and bottom layers of the custom measurement probe PCB boards are reported in Fig. A.6 and Fig. A.7, respectively, in Appendix A (pag. 163). The Low Voltage is typically held to ground and High Voltage provides the bias voltage of the correct polarity. The test signal amplitude is kept constant for all the measurements performed and its value is 20 mV, while its frequency ranges from 200 Hz to 1 MHz. The *open-circuit* and *short-circuit* correction functions of the LCR-meter guarantee a good offset subtraction at every tested frequency, as verified by measuring a standard ceramic capacitance of known value (10 pF).

The configuration for bulk capacitance measurement is quite different from the inter-strip one. The former foresees the connection of the selected strip of the desired detector side to DUT-Low, while the other strips of the same side are independently connected to the Low-Voltage source. The other side is all connected to DUT-High. Although the voltage probe signal is given to the DUT-High, the current response signal is read by DUT-Low so we are actually measuring the capacitance of the selected strip, with the advantage of having the strips aside DUT-Low grounded and not just connected to a voltage source that may introduce abnormal distortions in the CV measurement especially at high frequencies. In a preliminary test, we connected all the strips aside DUT-Low to ground via an ammeter for bias current monitoring purposes, but we found that it would introduce significant distortions in the CV measurement and therefore it has been discarded. Fig. 3.2 shows a sketch of the setup configuration for the bulk capacitance measurements.

The configuration for the inter-strip capacitance, on the contrary, foresees the connection of the two selected strips of the same detector side to DUT-High and DUT-Low respectively, while all the other strips of the same side are connected to Low Voltage (*i.e.* ground). The other detector side is connected directly to High Voltage which provides the bias voltage. In this case High Voltage is not given to the measurement probe box, because DUT-High and DUT-Low must be at the same bias level. Fig. 3.3 show a sketch of the setup configuration for the inter-strip capacitance measurements.

Finally, both the voltage source and the LCR-meter are connected via GPIB or USB to a remote PC where a custom developed software manages

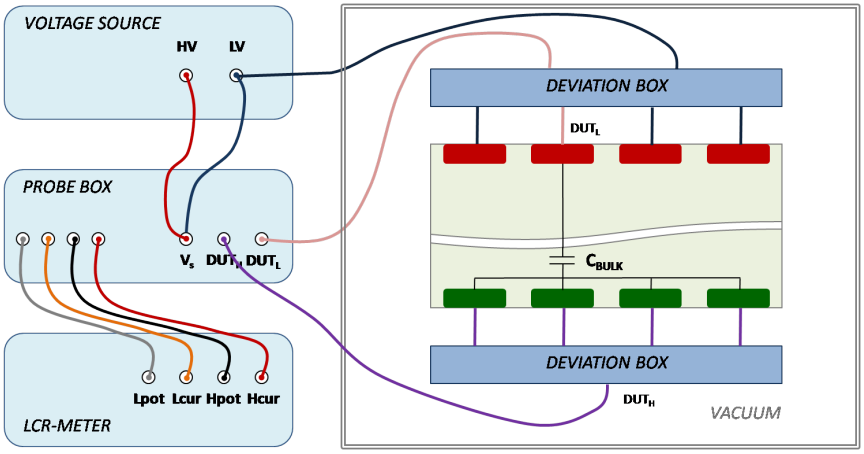

Figure 3.2: *Sketch of the setup configuration for bulk capacitance measurements.*

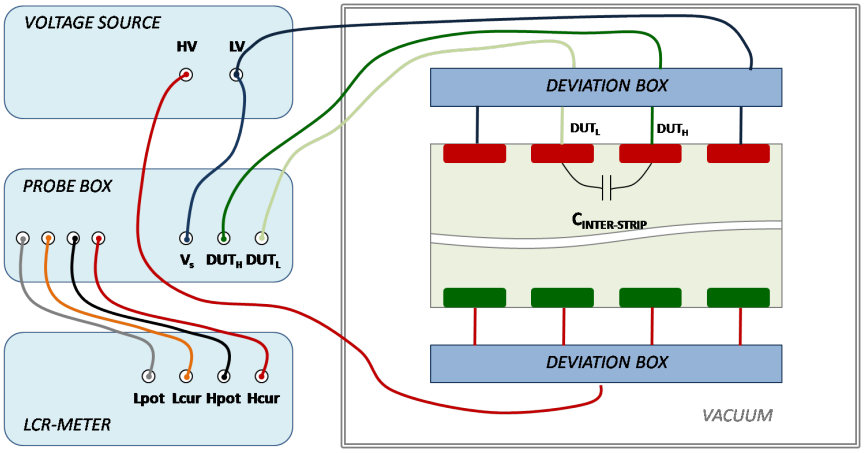

Figure 3.3: *Sketch of the setup configuration for the inter-strip capacitance measurements.*

all the measurement aspects, namely setting the instruments parameters, run two nested cycles of acquisition – the frequency sweep being nested in the voltage sweep –, switching on and off the detector bias, download and save to file all data.

A picture of the whole experimental setup is shown in Fig. 3.4 along with the indications of the main components.

We performed the measurements on the 300 μm DSSSD n. 2824-16 and on the 1500 μm DSSSD n. 2883-12.

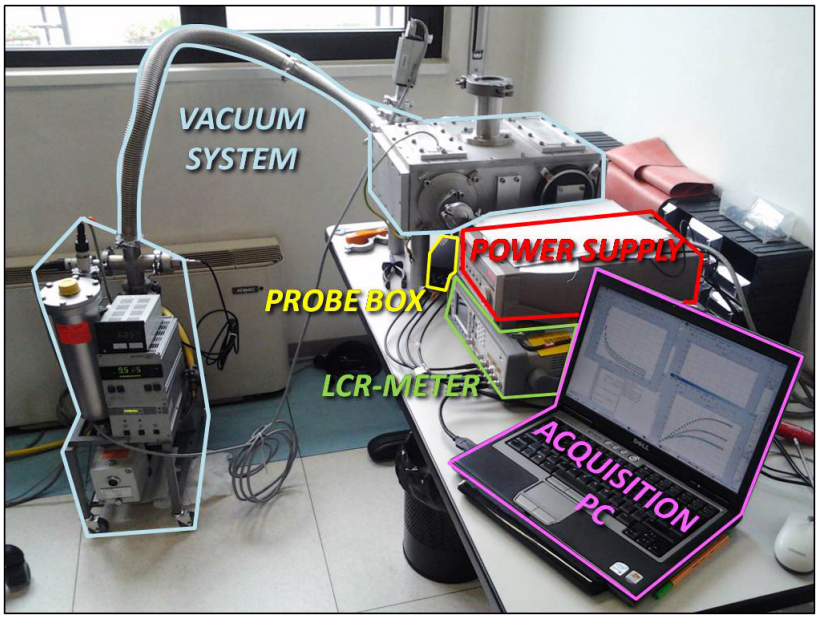

Figure 3.4: *Photograph of the whole experimental setup for the CV measurements.*

3.2.2 The Impedance Measurement Model

In both cases – bulk capacitance measurements and inter-strip capacitance measurements – the electric model set in the LCR-meter is the *parallel* (C_p in parallel with a resistance R_p), since the expected capacitance range is on the order of tens of pF, which leads to a high (reactive) impedance value and hence any series resistance can be neglected. This is true especially when the detector is biased over depletion – *i.e.* bias voltage above the depletion voltage – that is the normal operating condition. The LCR-meter hence returns the value of the measured capacitance and of the *dissipation factor* D, which is defined as:

$$D = \frac{R}{|X|} \tag{3.1}$$

where R is the real part of the measured impedance and $|X|$ is the absolute value of the reactive part of the measured impedance. D is also known as $\tan\delta$, where δ is defined as the angle between the imaginary axis and the impedance vector in the complex plane.

When the detector is reverse biased, the parallel resistance can play an important part and especially in the inter-strip capacitance measurement it must be taken into account in the analysis.

It must be noted that ideally D is always a positive value, since R it is always positive and X is taken with the modulus since it always negative (the phase shift of a capacitance is -90°). Deviations from the ideal are due to a possible lack of accuracy of the LCR-meter or to issues in the detector bias conditions. Lastly, we estimate the *total* strip capacitance as the sum of the bulk capacitance and twice the inter-strip capacitance, with the exception of the border strips which account just for one inter-strip component, but have the capacitance to the guard.

3.2.3 Results

Total Bias Currents

Fig. 3.5 (a) and (b) show the IV characteristics of the 300 μm-thick detector and of the 1500 μm-thick detector, respectively. Each graph combines two measurements made independently. The subset labeled with AIR refers to a preliminary measurement of the total bias current made in air with a simple setup made by a voltage source biasing one side of the detector and an ammeter between the other side and ground and it is shown in red. The subset labeled with VACUUM refers to the current measurement performed in vacuum along with the first attempt of CV measurements, before the ammeter was discarded. The blue curves correspond to the total bias current but the one of the strip n. 11, under CV measurement, while the light blue curve in Fig. 3.5 (a) corresponds to the total bias current but the one of the strip n. 01.

The large difference between the currents measured in air and in vacuum is related to surface effects which increase the generation of electron-hole pairs in the gap between the strips. The boundary conditions imposed by the silicon dioxide layer of the inter-strip gap are indeed deeply sensitive to air humidity.

On the contrary, the small difference between the total current but strip n. 11 and the total current but strip n. 01 for the case of the 300 μm-thick detector is due to the fact that strip n. 01 is much more leaky than the central ones because of border effects.

Bulk Capacitance – 300 μm DSSSD

Fig. 3.6 (a) and (b) show respectively the capacitance versus voltage measurements of the bulk capacitance of front strip n. 10 and the relative dissipation factor. Each curve pertains to a specific frequency of the voltage signal test, which ranges from 200 Hz to 1 MHz as shown in the legend.

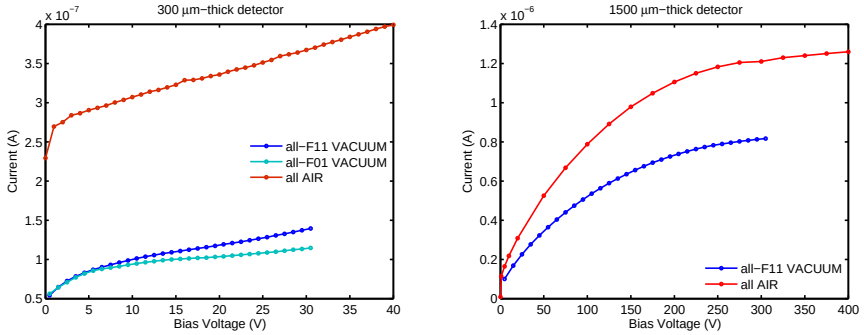

(a) (b)

Figure 3.5: *Current versus voltage characteristics for the 300 µm-thick detector (a) and the 1500 µm-thick detector (b). Red curves refer to measurements performed in air. Blue curves, on the contrary, refers to the total-but strip n. 11 current measured in vacuum along with the CV measurements with the preliminary setup. The light blue curve in (a) corresponds the total but strip n. 01 current measured with the same setup of the blue ones.*

For all the considered frequencies except the highest (1 MHz) we ascertain an almost identical capacitance behavior. Only at high frequency we observe a slight decrease of the capacitance value which could be due to some actual physical effect. Concerning the D value, we observe that it decreases as the bias voltage increases and as the frequency decreases. This can be explained considering that as the bias voltage decreases the series resistance increases, bending the impedance complex vector toward the real axis thus making D bigger. The effect is enhanced by the frequency since the reactive part of the impedance, at the denominator of D, decreases for increasing values of frequency, thus making the ratio more unfavorable. The small anomalous negative value assumed by D at high bias voltage and at the highest frequency could be due to measurement inaccuracies.

Fig. 3.7 (a) and (b) show the capacitance versus voltage measurements of the bulk capacitance of strip n. 13 of the back side and its dissipation factor, respectively. The capacitance does not differ much from the one of front strip n. 10 at all frequencies, except from the one at the highest frequency (1 MHz) at the lowest value of bias voltage. We believe that this phenomenon and the anomalous negative D value showed for low bias voltages and high frequencies are due to the interactions of the strip under test with the neighboring ones. Strips of the back side are indeed ohmically connected until the depletion voltage is reached ($\sim$ 20 V) and a possible unbalance of the bias conditions between the strips can lead to small currents

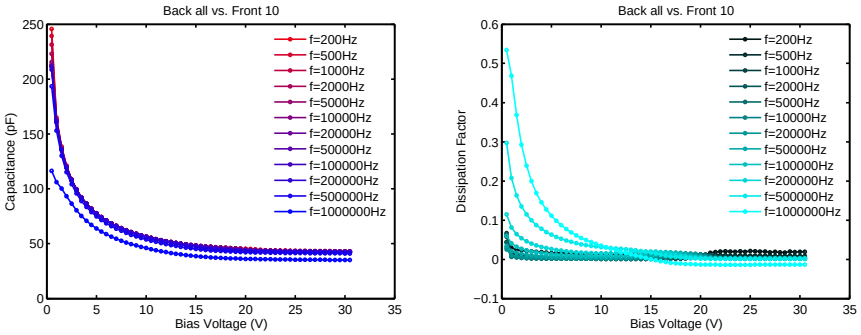

(a) (b)

Figure 3.6: *(a) Capacitance versus voltage measurements for the bulk capacitance of front strip n. 10 of the 300 μm DSSSD, for different values of the voltage test signal frequency. (b) Dissipation Factor versus the bias voltage for all the considered frequencies.*

flowing from one to the neighbor, spoiling the correct assessment of the actual test current signal used for the capacitance measurement. Strips of the front side do not show such behavior since they are "naturally" isolated one another by the *pn*-junctions.

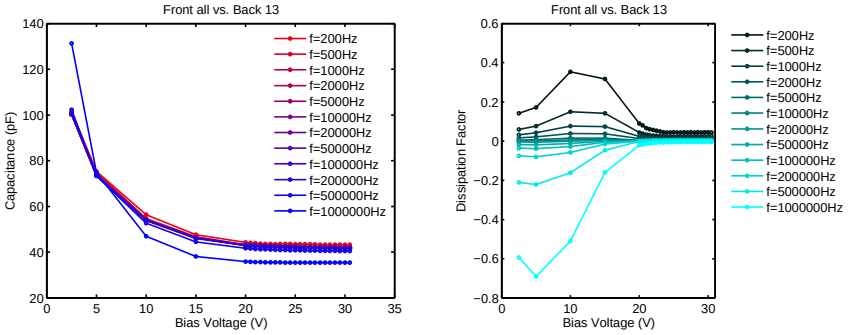

(a) (b)

Figure 3.7: *(a) Capacitance versus voltage measurements for the bulk capacitance of back strip n. 13 of the 300 μm DSSSD, for different values of the voltage test signal frequency. (b) Dissipation factor versus the bias voltage for all the considered frequencies.*

For the sake of completeness we have also computed the accuracy of the measurements due to the intrinsic capability of the Agilent E4980A LCR–meter. The results are shown in Fig. 3.8 (a) and (b) for the capacitance ver-

sus voltage measurement and for the dissipation factor, respectively. Since the accuracy depends in both cases on the capacitance value and on the signal frequency, we plotted bi-dimensional logarithmic color-maps that indicate the accuracy, expressed in percentage of the measured capacitance or in absolute value for D, and superposed the measured capacitance value for the case of front strip n. 10 analyzed before. Each line correspond to a voltage sweep made at constant frequency.

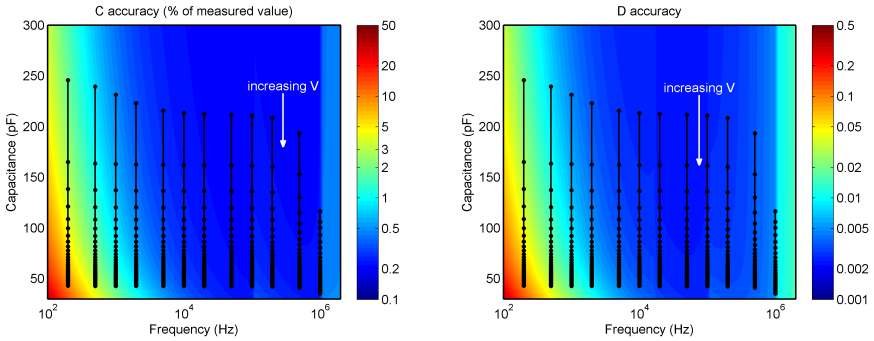

(a) (b)

Figure 3.8: *Measurement accuracy due to the LCR-meter for the Capacitance (a) and the Dissipation Factor (b). Each color-maps represent the accuracy of the measurement expressed in the percentage of the measured capacitance or in absolute value for D, function of the frequency and the capacitance value itself. The superposed lines correspond to the measured capacitance for the case of front strip n. 10, 300 μm thick detector, each line being made at constant frequency and for a voltage sweep.*

From the capacitance-voltage measurements we can also derive the depletion voltage of the detector and the value of the doping of the almost intrinsic (n^-) bulk region. The first has been estimated around 23 V, while the second around 2.36×10^{11} cm^{-3} (resistivity 19 kΩcm). The values of the bulk capacitance arranges, at usual operating voltages, at about 41 pF for either the front and the back strips.

Bulk Capacitance – 1500 μm DSSSD

Fig. 3.9 (a) and (b) show the capacitance versus voltage measurements of the bulk capacitance of front strip n. 10 and the related dissipation factor. For both the measurements, the considerations made for the 300 μm-thick detector analogous case hold.

Fig. 3.10 (a) and (b) report the case of bulk capacitance versus voltage and the corresponding dissipation factor of strip n. 13 of the back side. The values of the capacitance do not differ much from the front side case, except

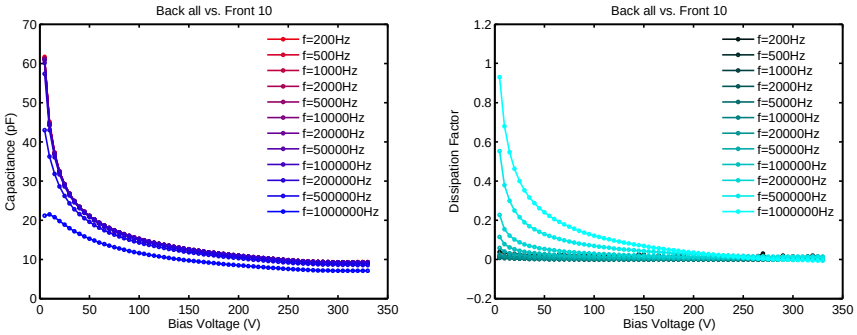

(a) (b)

Figure 3.9: *(a) Capacitance versus voltage measurements for the bulk capacitance of front strip n. 10 of the 1500 μm DSSSD, for different values of the voltage test signal frequency. (b) Dissipation factor versus the bias voltage for all the considered frequencies.*

for the case at highest frequency (1 MHz). This and the anomalous negative D value for voltages below the depletion is, as for the case of the 300 μm-thick detector, to be imputed to the interaction of the strip under test with the neighboring ones in terms of non-negligible unavoidable differential current.

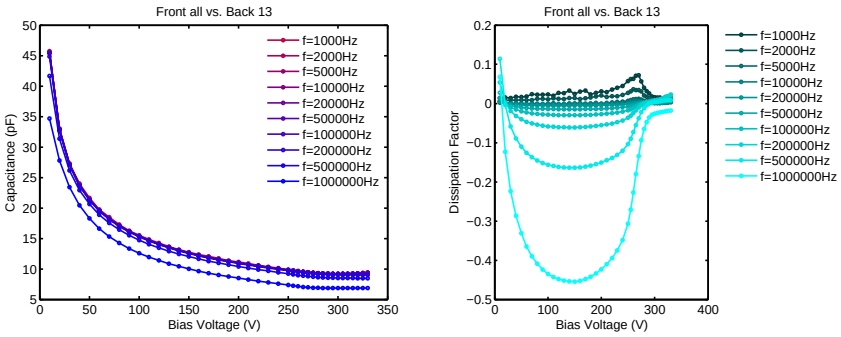

(a) (b)

Figure 3.10: *(a) Capacitance versus voltage measurements for the bulk capacitance of the strip n. 13 of the back side of the 1500 μm DSSSD, for different values of the voltage test signal frequency. (b) Dissipation factor versus the bias voltage for all the considered frequencies.*

Also in this case we computed the accuracy of the measurement due to the intrinsic capability of the LCR-meter. It is shown in Fig. 3.11 (a) for the

capacitance measurement, in (b) for the dissipation factor for the values of front strip n. 10 case. The superposed lines are the measured capacitances for the case of the strip n. 10 of the front side analyzed before. Each line correspond to a voltage sweep made at constant frequency.

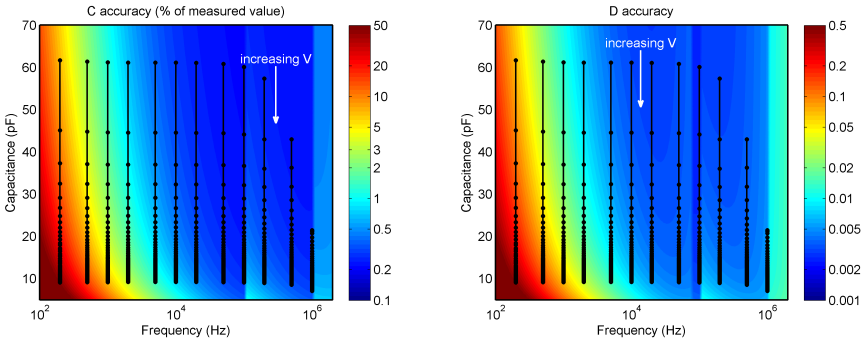

(a) (b)

Figure 3.11: *Measurement accuracy due to the LCR-meter for the capacitance (a) and the dissipation factor (b). Each color-maps represent the accuracy of the measurement expressed in the percentage of the measured capacitance or in absolute value for D, function of the frequency and the capacitance value itself. The superposed lines correspond to the measured capacitance for the case of front strip n. 10, 1500 μm thick detector, each line being made at constant frequency and for a voltage sweep.*

The estimated value of the depletion voltage is, in this case, of 270 V, while for the bulk doping the extracted value is 1.7×10^{11} cm^{-3} (resistivity 26 kΩcm). The values of the bulk capacitance arranges, at usual operating voltages, at about 8.5 pF for either the front and the back strips.

Bulk Capacitance at Border Strips

The former and the latter strip of each side of the detector are special cases due to presence of the border region. Moreover, on the front side, the border is surrounded by a series of guard rings which are left floating and interact in a non-trivial way with the first and last strip even at operating conditions (*i.e.* reverse bias well above the depletion voltage). Fig. 3.12 (a) and (b) show the bulk capacitance of front strip n. 01 and back strip n. 01 of the 300 μm-thick detector, respectively. The effect of the guard rings is clearly visible in the front case where the value of the capacitance shows an even greater dependence on the frequency with respect to the back side case and also from the little but significant increase of the capacitance value at all frequencies. Fig. 3.13 (a) and (b) show the case of front strip n. 01 and back strip n. 01 of the 1500 μm-thick detector. The contribution

of the guard rings is here less evident and due to the increased detector thickness and consequently the reduced relative impact of the strip-guard ring interaction.

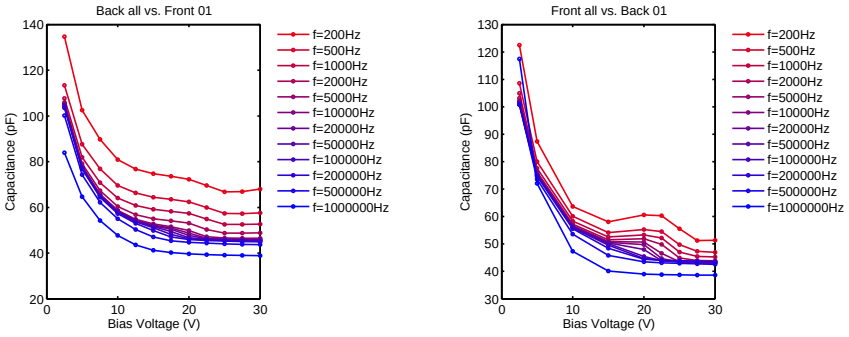

(a) (b)

Figure 3.12: *Bulk capacitance–voltage measurement for n. 01 (a) and back strip n. 01 (b) in the case of 300 μm-thick detector. On the front side case the contribution of the floating guard rings increase the dependence on the frequency and increases the value of the measured capacitance.*

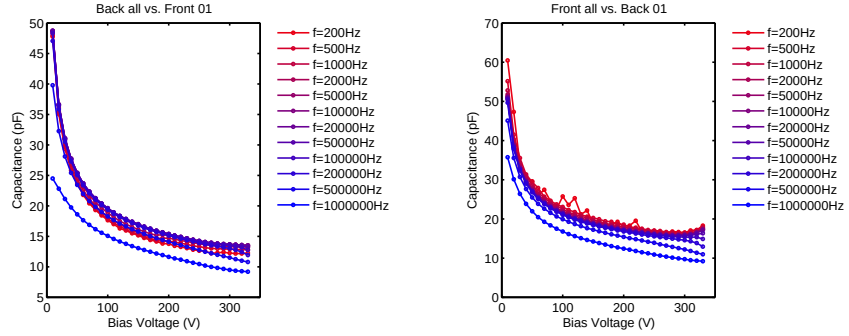

(a) (b)

Figure 3.13: *Bulk capacitance–voltage measurement for front strip n. 01 (a) and back strip n. 01 (b) in the case of 1500 μm-thick detector. Border effects are less evident than the case of 300 μm-thick detector since the increased detector thickness reduces the relative impact of the strip-guard ring interaction.*

Inter-Strip Capacitance – 300 μm DSSSD

Fig. 3.14 (a) and (b) show the measured inter-strip capacitance versus voltage between the strip n. 10 and n. 11 of the front (junction) side and the

corresponding dissipation factor for different frequencies. The value of the capacitance shows a remarkable dependence on the frequency and this is expected since the inter-strip region suffers for surface effects underneath the silicon dioxide layer that are deeply related to the time scale of the test signal. To better grasp the double dependence we plotted the capacitance as a function of the voltage and the frequency in Fig. 3.15.

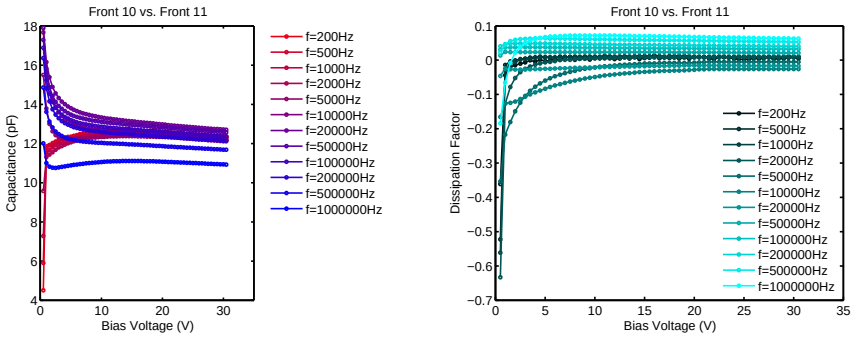

(a) (b)

Figure 3.14: *Inter-strip capacitance-voltage measurement between strip n. 10 and n. 11 of the front side for the 300 μm case (a) and corresponding dissipation factor (b).*

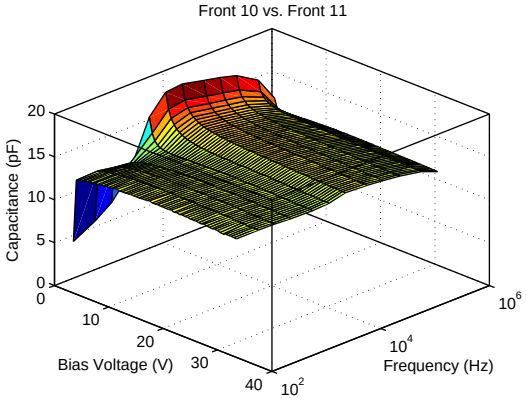

Figure 3.15: *Inter-strip capacitance-voltage measurement between strip n. 10 and n. 11 of the front side for the 300 μm case plotted as a surface to better grasp the frequency dependence.*

Fig. 3.16 reports instead the inter-strip capacitance versus voltage between the strip n. 13 and n. 14 of the back (ohmic) side for different frequencies. The capacitance measured at bias voltages below the depletion

value ($\sim$ 23 V) loses its physical meaning since the two strips are coupled by an impedance which is not purely capacitive, but features also a resistive component due to the ohmic nature of the back contacts. To give a better insight on the coupling impedance we plotted in Fig. 3.17 a polar graph of the total complex impedance measured by the LCR-meter. In the graph, the modulus of the impedance vector is in logarithmic scale. Each curve pertains to a specific frequency and corresponds to a voltage sweep. With increasing voltage, the impedance vector turns from the positive real axis to the negative imaginary axis and when the depletion voltage is reached the impedance arranges firmly as a pure capacitive load. The physical origin of this behavior is that the back n^+ strips are "resistively" connected through the n^- bulk region until the depletion region reaches the back side, which happens at the depletion voltage (the depletion region "comes" from the junction side). Below such voltage, the strips experience a resistive coupling in parallel with a small capacitance which both increases as the bulk region is depleted. For the seek of completeness Fig. 3.18 shows the inter-strip resistance (extracted from the parallel model) R_p between the considered strips. Correctly, the value increases to reach a maximum at the depletion voltage and there is not a significant dependence on the frequency until the full depletion condition is reached, when time-dependent surface effects contribute significantly.

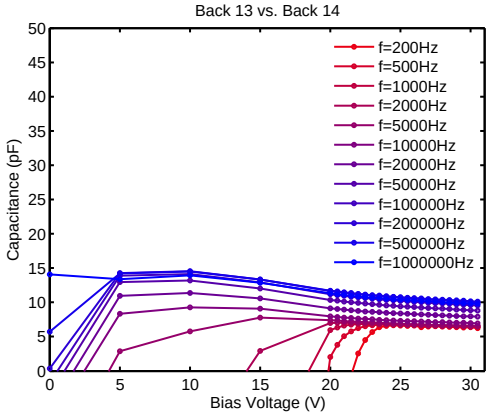

Figure 3.16: *Inter-strip capacitance-voltage measurement between strip n. 13 and n. 14 of the back side for the 300 μm-thick case for all the considered frequencies.*

In Fig. 3.19 we reported the measurement accuracy for both the inter-strip capacitance and dissipation factor measurements for the front side case. It worths noticing that for lowest frequencies both the accuracies on the capacitance and on D are poor and the hence the reported measured

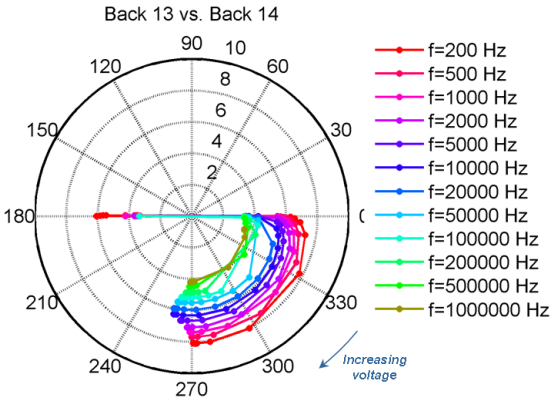

Figure 3.17: *Polar plot of the complex total impedance measured by the LCR-meter between the strip n. 13 and n. 14 of the back side of the 300 μm-thick detector. The modulus of the impedance is in logarithmic scale. Each line pertains to a specific frequency and correspond to a voltage sweep with voltage.*

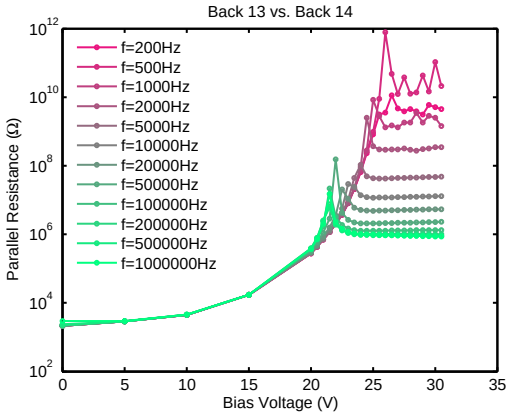

Figure 3.18: *Inter-strip parallel resistance versus voltage between strip n. 13 and n. 14 of the back side for the 300 μm-thick case for all the considered frequencies.*

values should be taken with care.

The value of the inter-strip capacitance at operating voltages can hence be estimated as 11-13 pF for the front side (frequency dependent) and 6-10 pF – even if in this case the dominant component is the resistive coupling – for the back side (increasing with frequency), which is correctly lower for the wider geometrical separation between the strips, which is roughly 25

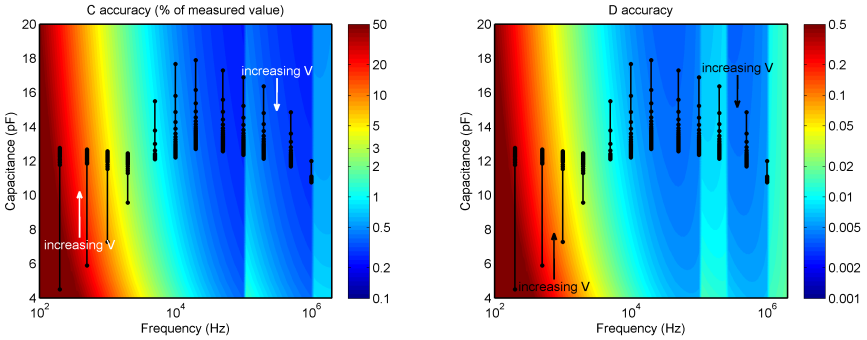

(a) (b)

Figure 3.19: *Measurement accuracy due to the LCR-meter for capacitance (a) and the dissipation factor (b). Each color-maps represent the accuracy of the measurement expressed as the percentage of the measured capacitance or in absolute value for D, function of the frequency and the capacitance value itself. The superposed lines correspond to the measured inter-strip capacitance for the case of front strip n. 10 versus n. 11, 300 μm thick detector, each line being made at constant frequency and for a voltage sweep.*

μm on the front side and roughly 40 μm on the back side.

Inter-Strip Capacitance – 1500 μm DSSSD

Fig. 3.20 (a) and (b) show the measured inter-strip capacitance versus voltage between strips n. 10 and n. 11 of the front (junction) side and the corresponding dissipation factor for different frequencies. The bump in frequency observed for the 300 μm is not present here.

Fig. 3.21 reports instead the inter-strip capacitance versus voltage between the strip n. 13 and n. 14 of the back (ohmic) side for different frequencies. Similarly to the 300 μm-thick detector case, below the depletion voltage the strips coupling is not merely capacitive but also resistive due to the ohmic nature of the back contacts. The overall impedance coupling as measured by the LCR-meter is shown in the polar plot of Fig. 3.22. Each curve pertains to a specific frequency and the modulus of the vectors is in logarithmic scale. With increasing voltage, the complex vector turns from a mainly resistive load to a pure capacitive load. Fig. 3.22 shows the inter-strip resistance R_p extracted using the parallel model. Correctly, all the curves measured at different frequencies coalesce into a single curve until the depletion voltage is reached, meaning that a "physical" resistance is actually present.

In Fig. 3.24 we reported the measurement accuracy for both the inter-

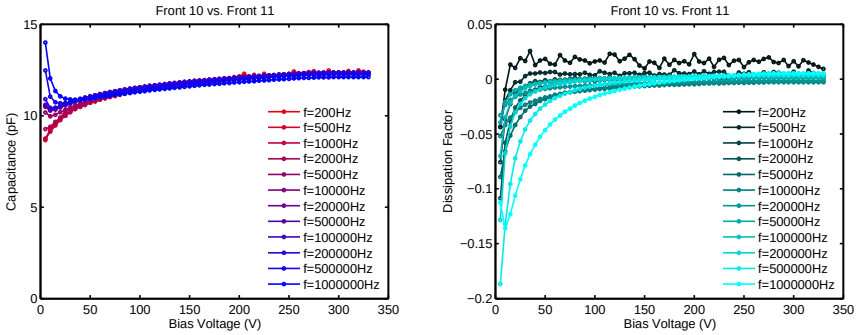

(a) (b)

Figure 3.20: *Inter-strip capacitance–voltage measurement between strip n. 10 and n. 11 of the front side for the 1500 μm case (a) and corresponding dissipation factor (b).*

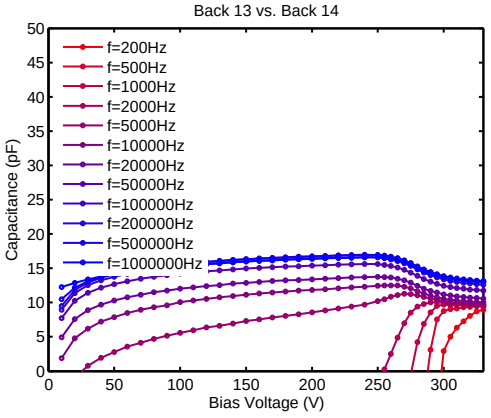

Figure 3.21: *Inter-strip capacitance-voltage measurement between strip n. 13 and n. 14 of the back side for the 1500 μm case.*

strip capacitance and dissipation factor measurement for the front side case. Also in this case it must be noted that for the lowest frequencies, both the accuracies for the capacitance and for D are poor thus affecting the quality of the reported measurements.

The value of the inter-strip capacitance at operating voltages can hence be estimated as 12 pF for the front side and 10-14 pF for the back side (increasing with frequency).

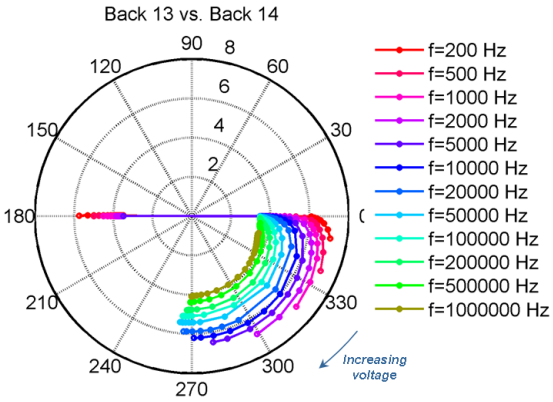

Figure 3.22: *Polar plot of the complex total impedance measured by the LCR-meter between the strip n. 13 and n. 14 of the back side of the 1500 μm-thick detector. The modulus of the impedance is in logarithmic scale. Each line pertains to a specific frequency and correspond to a voltage sweep with voltage.*

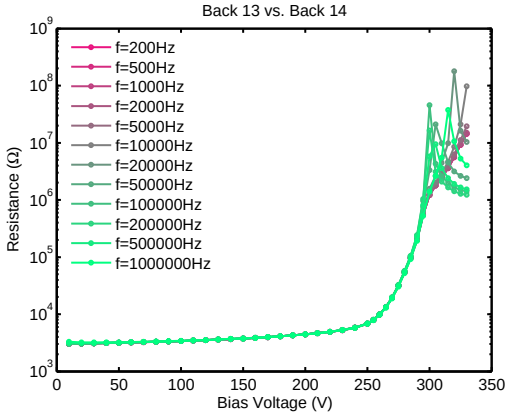

Figure 3.23: *Inter-strip parallel resistance versus voltage between strip n. 13 and n. 14 of the back side for the 1500 μm-thick case for all the considered frequencies.*

Total Capacitances

At usual operating voltages, the *total strip capacitance* is the sum of the bulk capacitance and two times the inter-strip capacitance and this leads, for the 300 μm DSSSD, to the range of values 63-67 pF for a front side strip and 53-61 pF for a back side strip, with the exception of the border strips which on the contrary show the bulk capacitance plus one inter-strip

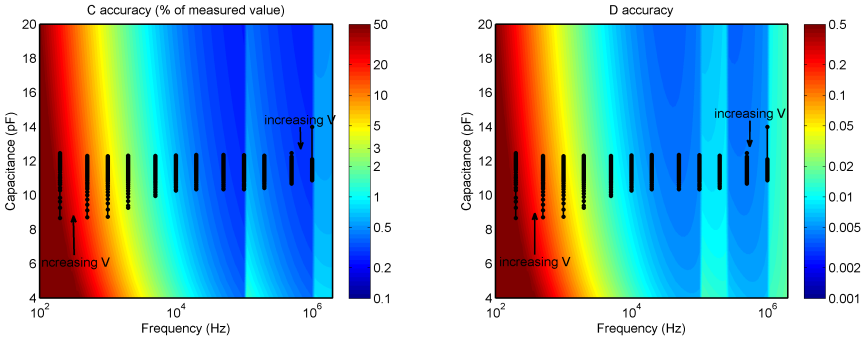

(a) (b)

Figure 3.24: *Measurement accuracy due to the LCR-meter for the capacitance (a) and the dissipation factor (b). Each color-maps represent the accuracy of the measurement expressed as the percentage of the measured capacitance or in absolute value for D, function of the frequency and the capacitance value itself. The superposed lines correspond to the measured inter-strip capacitance for the case of front strip n. 10 versus n. 11, 1500 μm thick detector, each line being made at constant frequency and for a voltage sweep.*

capacitance[1], that is 49-80 pF for a front side strip and 44-61 pF for a back side strip. For the 1500 μm DSSSD, instead, a front strip exhibits 32.5 pF and a back strip 28.5-36.5 pF, while the border strips show 21.5-25 pF on the front side and 23.5-26 pF on the back side. It must be considered that the lower capacitance value for the border strips do not lead necessary to better performances in terms of energy resolution, since their dark current is typically higher with respect to the other strips thus leading to a larger parallel noise which turns out to actually reduce the energy resolution.

3.3 Energy and Position Response Map with Monochromatic Single Ions

In the framework of the characterization of the FARCOS Double Sided Silicon Strip Detectors it is fundamental to assess the dependence of the detector response on the energy and on the position of the impinging particle. In order to measure the response matrix we used a pulsed mono-energetic ion beam. By using a pulsed beam, single mono-energetic ions can be generated which are used to precisely probe the detector-electronic system response with high spatial and temporal resolution. Moreover by tuning the

[1]The interaction of the border strips with the surrounding guard ring (front side) or bulk (back side) is included in their bulk capacitance measurement

proton energy or by increasing the number of protons per bunch it is possible to probe different levels of charge density and/or different ionization profiles across the detector depth.

3.3.1 The Pulsed Ion Beam-Line DEFEL of the LaBeC Accelerator

The pulsed monoenergetic proton beam coming from the DEFEL beamline [40] of the 3MV Tandetron accelerator of the LaBeC (*Laboratorio di Tecniche Nucleari per i Beni Culturali*) [41], located in Sesto Fiorentino (FI), Italy, is an attractive tool to probe the response of the detector-frontend system at different levels of charge injection. Fig. 3.25 shows an aerial view of experimental area, with the Tandetron accelerator in the foreground.

At DEFEL the continuous beam coming from the accelerator is deflected by means of an electrostatic chopper transversally across a slit allowing a bunch of protons (or ions) to proceed downstream through an aperture only during a very short time interval of the order of 1 ns. The key components of the electrostatic chopper are the predeflector and the deflector systems. They both consist in a couple of plates parallel to the beamline whose driving electronics is shown together with schematic drawing of the DEFEL beamline in Fig. 3.26. The working principle of the chopper is the following. During the stationary state, mosfet Q_d is off and so a voltage V_d= 200 V is applied to the upper plate while a steady voltage V_d= 100 V is applied to the lower one: the ions are deflected downward. When a trigger pulse is applied, Q_d is quickly brought to conduction, the voltage on the upper plate drops approximately to ground and the beam moves upward. The beam is allowed to enter the experimental chamber only during the voltage transition. The predeflector always deflect the beam keeping the upper plate at V_p= 800 V and the lower plate at ground. When Q_p is brought to saturation the upper plate is discharged and the beam is allowed to pass. The synchronization signals of the predeflector and deflector voltages is shown in Fig. 3.27.

The adjustment of the size of the aperture with a motorized slit, and of the intensity of the continuous beam, is the key feature to create a pulsed beam with a variable and finely controllable number of particles in each pulse (down to an average value much below 1 particle per trigger and with a position of interaction in a defined area of down to 30 μm $\times$ 30 μm). Proton energies are tunable in the range 1 - 6 MeV. The repetition rate is selectable from a manual single shot up to tens of kHz (limited by power dissipation effects on the drivers). Other ion types can be accelerated: He^{2+} up to 8 MeV, Li^{3+} up to 11 MeV, C^{4+} up to 14 MeV. In this energy inter-

val, the proton range is perfectly matched with the typical wafer thickness, namely proton range in silicon is 16 μm at 1 MeV and raises up to 295 μm at 6 MeV [42]. The proton straggling in silicon ranges from 0.8 μm at 1 MeV to 4 μm at 3 MeV and 12 μm at 6 MeV [43]. The end-station of the beamline is equipped with a large experimental vacuum chamber housing the detector under test mounted on X-Y stages that can be moved orthogonal to the beam axis thus changing the impact point of the ions.

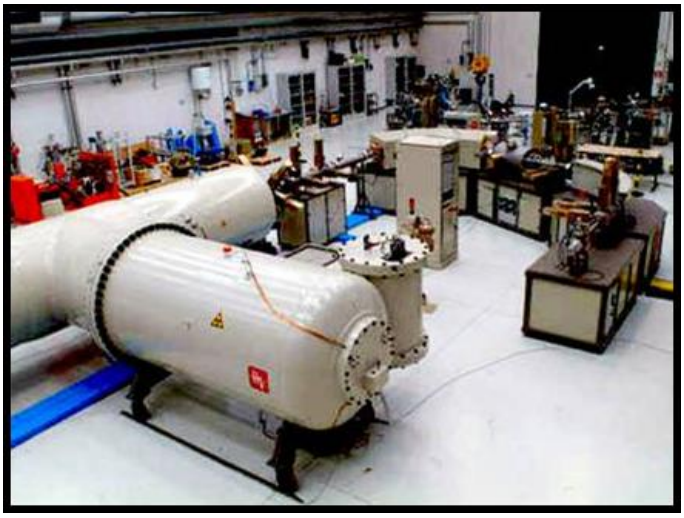

Figure 3.25: *Aerial view of the experimental area inside the LaBeC facility at Sesto Fiorentino (FI), Italy. In the foreground stands out the 3 MV Tandetron accelerator.*

3.3.2 Experimental Setup

Fig. 3.28 shows the scheme of principle of the experimental setup. The detector under test together with the charge preamplifiers (see Subsection 2.2.2 pag. 32) are located inside the experimental chamber. The anti-aliasing amplifiers, the trigger system and the digitizer (see Subsection 2.2.3 pag. 35) are located in the controlled area out of the vacuum chamber. The host PC that supervises the acquisition process is located outside the radiation controlled area and connected to the VME crate through an optical fiber.

Detector Mounting

Fig. 3.29 shows a photograph of the DSSSD experimental setup in the DEFEL vacuum chamber. The detector under test is mounted on the aforementioned *X-Y* stages. The PCB detector frame is housed on a dedicated

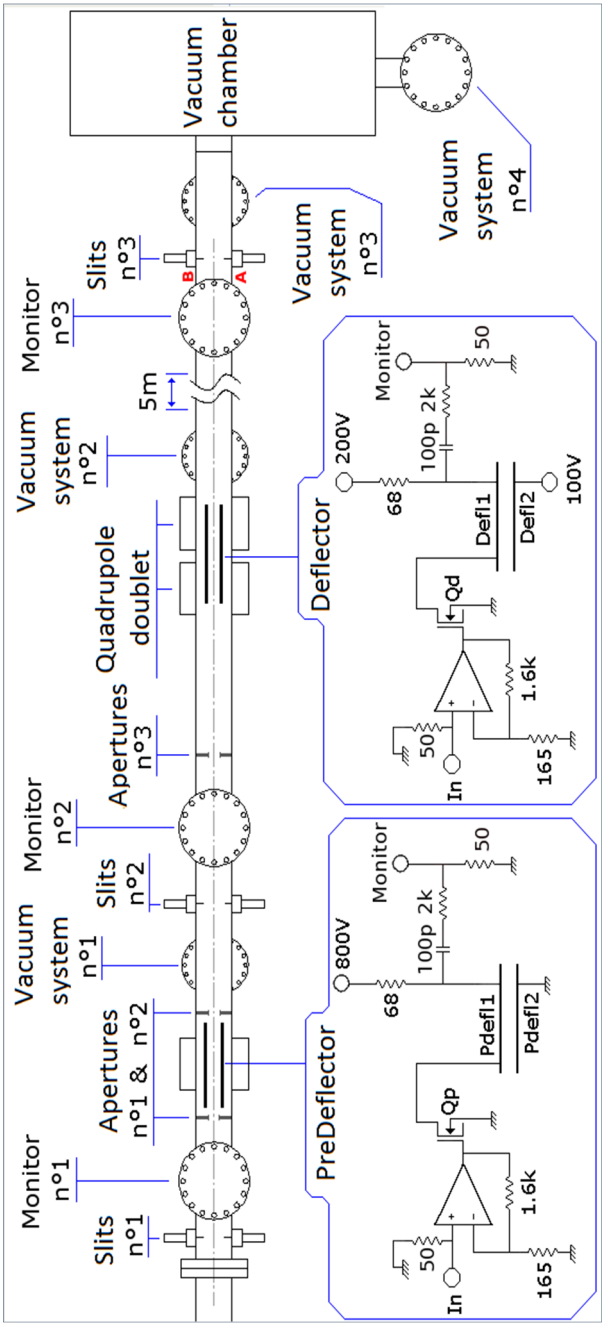

Figure 3.26: *Schematic drawing of the DEFEL line with all of its components highlighted, including the predeflector and deflector drivers [44].*

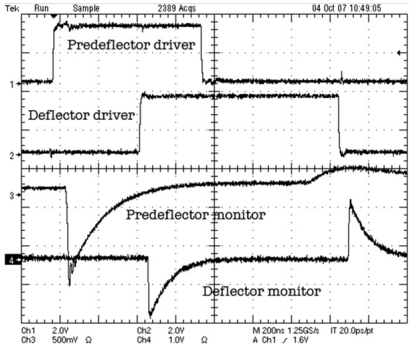

Figure 3.27: *Predeflector-deflector synchronization signals for the creation of bunches of protons from a continuous beam [40].*

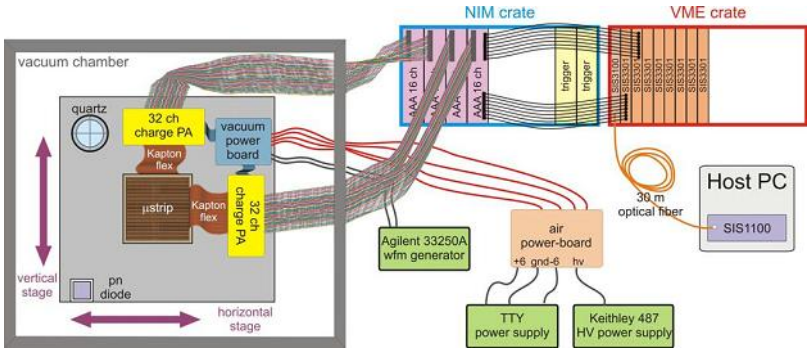

Figure 3.28: *Scheme of principle of the experimental setup at the DEFEl beamline. The host PC is located outside the radiation controlled area.*

Aluminum holder fixed to a metallic mounting frame coupled to the 2D motion stages that can be controlled remotely. The mounting frame houses also a *pn*-diode detector for beam intensity adjustment and a quartz glass for precise positioning and alignment of the proton beam. An optical camera allows alignment of the proton beam to reference markers on the quartz glass and on the detector chip. The mechanical frame, if needed, holds also different versions of charge preamplifiers that are directly connected to the Kapton cable coming from the detector and the so-called vacuum power board, responsible of distributing the needed filtered bias voltages to the preamplifiers and the detector together with the test signal coming from the pulser. The whole system has been designed such as we can easily change the injection side of the detector or even the detector prototype in an effective way. The so-called air power board – located outside the vacuum chamber – provides first order passive filtering of the detector and the

preamplifier bias voltages and also a monitor of the absorbed current.

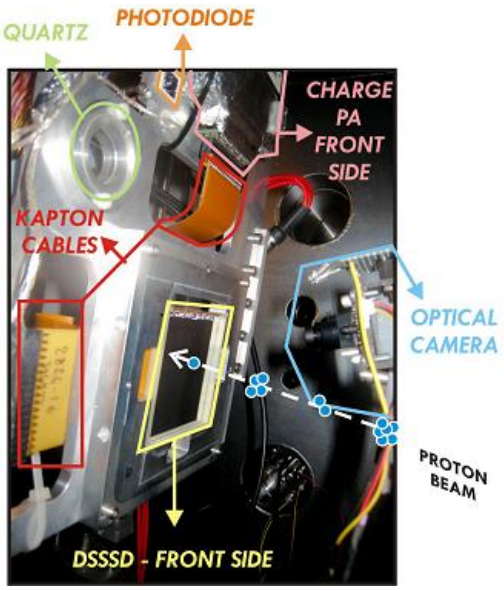

Figure 3.29: *Photograph of the DSSSD mounted on the mechanical frame and housed in the vacuum chamber.*

A photograph of the digital DAQ system equipment and of the power supplies just outside the experimental chamber is shown in Fig. 3.30. The digital DAQ system is the one described in Section 2.2.3.

3.3.3 Experimental Conditions

The data here presented derive from two beamtimes at the DEFEL beamline held in September 2012 and in June-July 2013, for a total of about two weeks and a half. The 300 μm-thick and 1500 μm-thick detector response matrix has been measured both in front injection (ions incident on the junction side) and in back injection (ions incident on the ohmic side). Different beams were accelerated: 1 MeV (16 μm projected range in silicon), 3 MeV (92 μm projected range) and 5 MeV (216 μm projected range) protons and 7.5 MeV Li ions (l5 μm projected range). The importance of having different ion-energy pairs lies in the different ionization profiles and consequently in the different associated charge densities, allowing us to probe the detector response under various charge injection conditions. It must be stressed that, as a consequence, a bunch of three 1 MeV protons – for example – do not give the same detector response of one single 3 MeV proton since the ionization profiles are not the same for the two energies

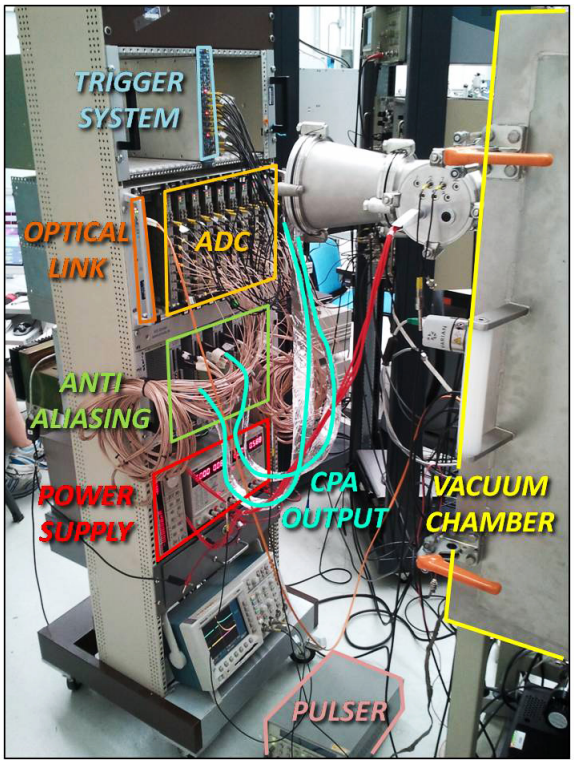

Figure 3.30: *Photograph of the digital DAQ system equipment and of the power supplies just outside the vacuum chamber.*

and though the beam is collimated (50 μm $\times$ 50 μm at best) the three 1 MeV protons would typically impinge on the detector sufficiently far apart to be considered independent one another, not allowing us to "sum" the charge densities. Fig. 3.31 shows the ionization profiles in silicon for the considered ions computed with SRIM2008 [43].

The vacuum level in the experimental chamber is kept well below $1{\cdot}10^{-4}$ mbar during all the measurements. The pulsed beam repetition rate is kept constant for all the measurements and equal to 100 Hz. The slits opening that defines the beam spot size were in the range 50-200 μm $\times$ 50-200 μm according to the type of measurement performed. The DSSSD were biased at 25 V for the 300 μm thick and 300 V for the 1500 μm thick in all the measurements. Over-bias voltages up to 20V for the 300 μm thick and 30 V for the 1500 μm thick have been successfully tested.

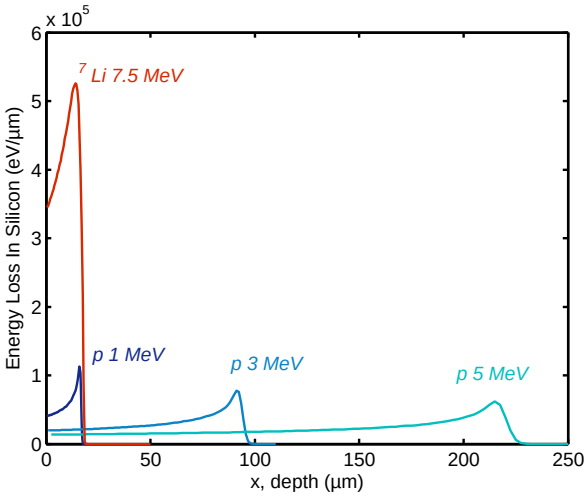

Figure 3.31: *Ionization profile for 1 MeV, 3 MeV and 5MeV protons and 7.5 MeV ^{7}Li ion in silicon, from SRIM2008 [43]. The Bragg peak in silicon is at about 16 μm, 91 μm, 213 μm and 14 μm respectively.*

3.3.4 Energy Calibration and Resolution

We recorded the energy spectra under different conditions of proton and Li ion beam energy. Since the charge collection time of the detector is much longer than the beam pulse duration, each bunch gives rise to a single event of amplitude proportional to the bunch multiplicity. The number of ions in a bunch reflects their statistical distribution in the original beam; as a result, the spectrum envelope is roughly a Poissonian distribution. Fig. 3.32 (a) and (b) show an example of energy spectra collected in the case of 3 MeV proton interaction on one strip of the junction side and one strip of the ohmic side, respectively, for the 300 μm DSSSD coupled with the custom made charge preamplifier. The insets show a detail of the single 3 MeV proton peak together with its Gaussian fitting that allows the estimation of the peak centroid and FWHM. The digitized waveforms were post-processed off-line with a digital triangular filter with 201 taps kernel width.

Taking advantage of the proton bursts technique, it is possible to obtain an accurate energy calibration of each strip and of the corresponding preamplifier in a wide energy range from MeV up to even GeV energies, depending on the intensity of the incident beam.

By least-square Gaussian fitting each peak of the spectra as the one shown in Fig. 3.32 and extracting its centroid it is possible to derive the

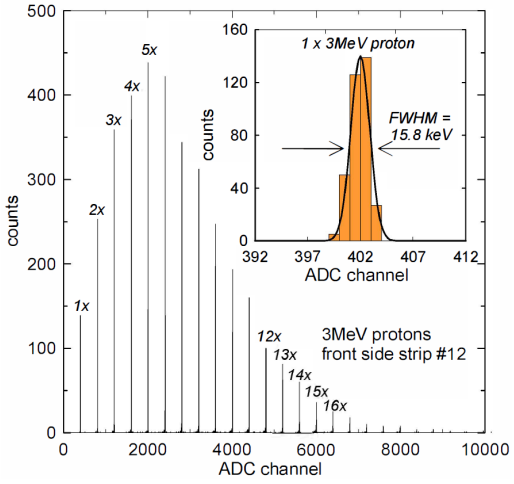

(a)

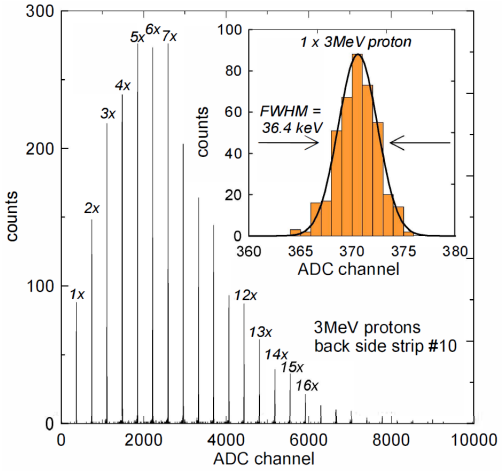

(b)

Figure 3.32: *Energy spectrum collected in the case of 3 MeV proton interaction on one strip of the front side (a) and one strip of the ohmic side (b). Since the number of ions per bunch reflects their original distribution in the beam, the spectra envelope is roughly a Poissonian. The insets show a detail of the single 3 MeV proton peak together with its Gaussian fitting that allows the estimation of the peak centroid and FWHM.*

ADC bins/energy correspondence and hence the calibration curve. Fig. 3.33 (a) shows the calibration made for the front-side strip n. 12 superposing the peaks of the 3 MeV protons plus the 7.5 MeV Li ions acquired with the same configuration (back injection, AAA gain 2x), restricting to

energies below 30 MeV in order to compare the two particle families in the same range. The energy values have been finely corrected for the energy lost in the aluminum layer above the strips which does not contribute to the signal formation (6.6 keV for 3 MeV protons and 120 keV for 7.5 MeV Li ions) and also for the extraction energy of the ions from the source before the accelerating phase. The resulting sensitivity is 39.851 mV/MeV (7.502 keV/LSB).

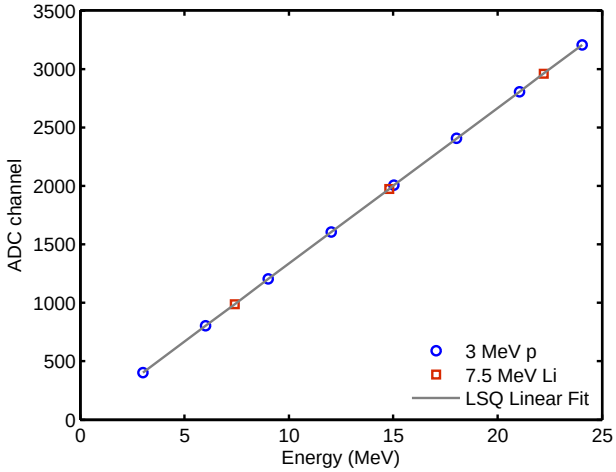

Figure 3.33: *Energy calibration for the front-side strip n. 12 considering the peaks of the 3 MeV protons plus the 7.5 MeV Li ion, acquired in the same configuration (back injection, AAA gain 2x) and with energy corrected as described in the text. The sensitivity resulting from the least-square linear fitting is 39.851 mV/MeV (7.502 keV/LSB).*

Proton bursts can also be used to measure the linearity of the overall system, including Si-detector, preamplifier, anti-aliasing amplifier and digitizer. This kind of qualification of the performance of the silicon detector is extremely useful since it allows obtaining an independent calibration for the on-beam measurements, with a high degree of confidence, due to the intrinsic calibration of the source and to the wide explorable range. Fig. 3.34 shows the integral non-linearity for the same strip seen before. The excellent overall INL r.m.s. value is 0.45 LSB (3.35 keV) which is below the 0.1% over all the considered energy range.

Considering the single-proton peak of each spectrum, as the ones shown in the insets of Fig. 3.32 (a) and (b), it is possible to derive the energy resolution, expressed as the FWHM of the Gaussian shape fitting the peak. Digitized waveforms were post-processed off-line with a digital triangular filter with different kernel lengths. We probed several filter shapes, includ-

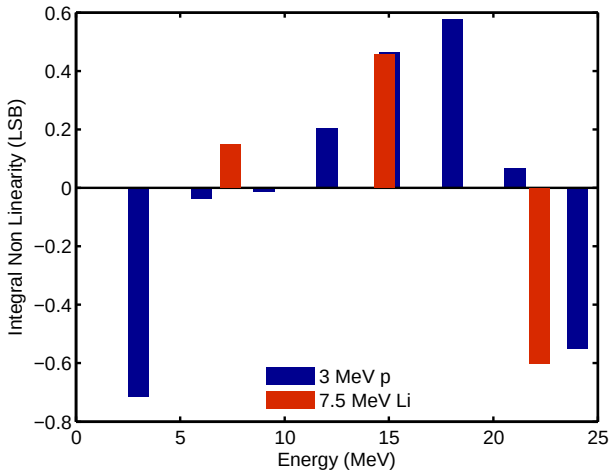

Figure 3.34: *Integral non-linearity for the case of Fig. 3.33. The overall INL r.m.s. value is 0.45 LSB (3.35 keV).*

ing bipolar filters with or without a flat region that in theory would better approximate the "optimum" filter[2], but their performances were worse than the ones of the triangular. A possible reason of this behavior may be that the main source of noise/disturbance is injected in the signal path *after* the charge preamplifiers. As expected the strips of the front side exhibit an energy resolution better than the ones of the ohmic side, due to a larger contribution of the parallel noise, mainly arising from the inter-strip resistance. In addition in this measurement we pay also the price of an unwanted noise pick-up on some of the ohmic side strips. Fig. 3.35 shows the measured energy resolution as a function of the digital triangular filter half-width for a front-side strip (n. 12) representative of the behavior of all the others and of two of the ohmic side strips, one showing the expected good performance (n. 2) and a second one (n. 12) prone to the unwanted pick-ups, always for the case of 3 MeV proton on the 300 μm DSSSD. Even if the measured resolution is already quite good there is room for improvement with respect to the theoretical limits imposed by the electronic noise and the Fano intrinsic resolution.

[2]When referred to the *detector* signal, the filter shape must be integrated since the integration performed by the charge preamplifier must be taken into account

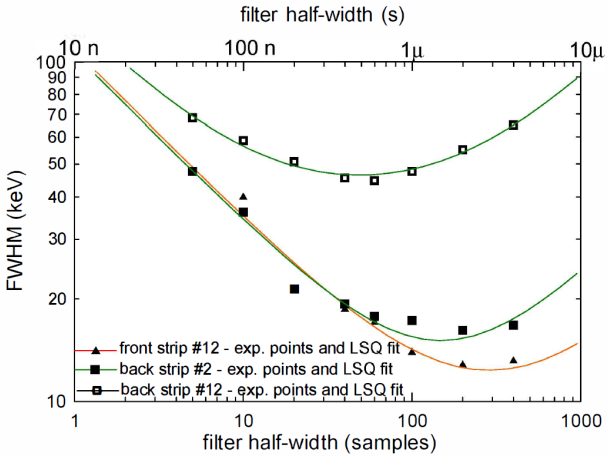

Figure 3.35: *Energy resolution expressed in FWHM of the single 3 MeV proton peak for one strip of the front side and two of the ohmic side, representative of the behavior of all the others, as measured with 3 MeV proton on the 300 μm DSSSD as a function of the digital triangular filter half-width.*

3.3.5 Position Response Matrix – Inter-Strip Effects

Profiting of the high spatial resolution of the proton beam we were able to map the detector response in several significant positions, such as full-strip regions, inter-strip regions and detector-border regions, with the purpose to investigate the shape of the recorded waveforms as a function of the position of interaction. In this Section we restrict the analysis on the inter-strip regions to gain a better insight in the sharing phenomena that could greatly spoil the pulse shape analysis capability of the system.

The chance to access the whole original waveforms made possible thanks to the digital DAQ system, in conjunction with the dedicated numerical simulations exposed in Chapter 4, allowed us also to put some light on the issue of the "opposite" polarity signals arising in the case of inter-strip injection that have been reported in literature at least since the eighties up to more recent years, see [18] in the case of MUST detector but also [45] [46] and [47] for other examples. There is the tendency to refer to the interpretation given by Yorkstone in [48] who ascribes the opposite polarity signals to the charge loss occurring in the voltage pocket under the silicon dioxide layer between the strips, at least for low penetrating α-particles. We have evidences that even though this is a in important point in the analysis of the inter-strip effect, the actual cause of the occurrence of opposite or bipolar signals in one of the two considered strips is an effect of pure electrostatic charge induction. This Section deals with the analysis of the experimental

data only, while the theoretical interpretation and the quantitative comparison with the results of dedicated simulations is deferred to Section 4.6 (pag. 95).

The analysis has been made as follows. We recorded on an event-by-event basis the waveforms pertaining to two neighbor strips of the desired detector side, then we extracted the MAX – maximum value, always positive – and the MIN – minimum value, always negative – from the baseline subtracted and filtered (201 taps triangular filter) waveforms and scatter-plotted the $MAX + MIN$ of one strip versus the $MAX + MIN$ of the neighbor strip. In the following, positive waveforms are considered of the "correct" polarity, so we digitally inverted the back-side strip outputs since their "original" polarity was negative, in order to compare homogeneously strips of both sides (due to the arrangement of the connectors in the flange of the vacuum chamber there was an inversion of the polarity of the preamplifier's output). In addition, since the beam spot (100 μm $\times$ 100 μm) was larger than the inter-strip gap (25 μm junction side, 40 μm ohmic side) and no precise information of the impact point was possible, we sorted all the events in descending order by the $MAX_i - MAX_{i+1}$ values, where i and $i + 1$ stand for the two consecutive strips, assuming a monotonic behavior of the MAX with respect to the impact position. This make possible to plot the MAX and MIN of both the strips in a kind of fine "scan" of the inter-strip gap.

We show selected results for the 3 MeV protons and for the 7.5 MeV Li ions beam impinging on both the 300 μm DSSSD and 1500 μm DSSSD. The choice of these two ions is dictated by their different penetration depth (Bragg peak at 92 μm in silicon for 3 MeV proton, at 15 μm for 7.5 MeV Li ion). We have indeed noticed that this parameter greatly affects the shape of the collected signals[3] making them appropriate examples. Therefore the behavior of the 1 MeV protons is very similar to the 7.5 MeV Li ions while the one of the 5 MeV protons is similar to the 3 MeV protons.

300 μm DSSSD

Fig. 3.36 (a) shows the scatter plot of the $MAX + MIN$ of the front-side neighbor strips n. 10 and n. 11 with 3 MeV protons impinging in the inter-strip gap – front injection. The clusters related to the full collection of the charge generated by the proton as well as their all possible pairs – *i.e.* one proton at each strip in case of two-proton bunches and so on – are clearly visible. All the events between the clusters are due to pure charge

[3]The reason is the peculiar shape of the strips *weighting potentials*, topic that will be dealt in Section 4.6 (pag. 95)

sharing, since their sum is a constant, as showed in Fig. 3.36 (b) where the MAX and MIN parameters of the sorted events pertaining to the one proton subset are plotted. Fig. 3.36 (c) and (d) show the same plots for back-side strips n. 12 and n. 13 with 3 MeV protons impinging in the inter-strip gap – back injection. Even if the beam was slightly shifted toward strip n. 13, though not clearly visible the wider inter-strip gap causes a greater number of events to undergo charge-sharing effects.

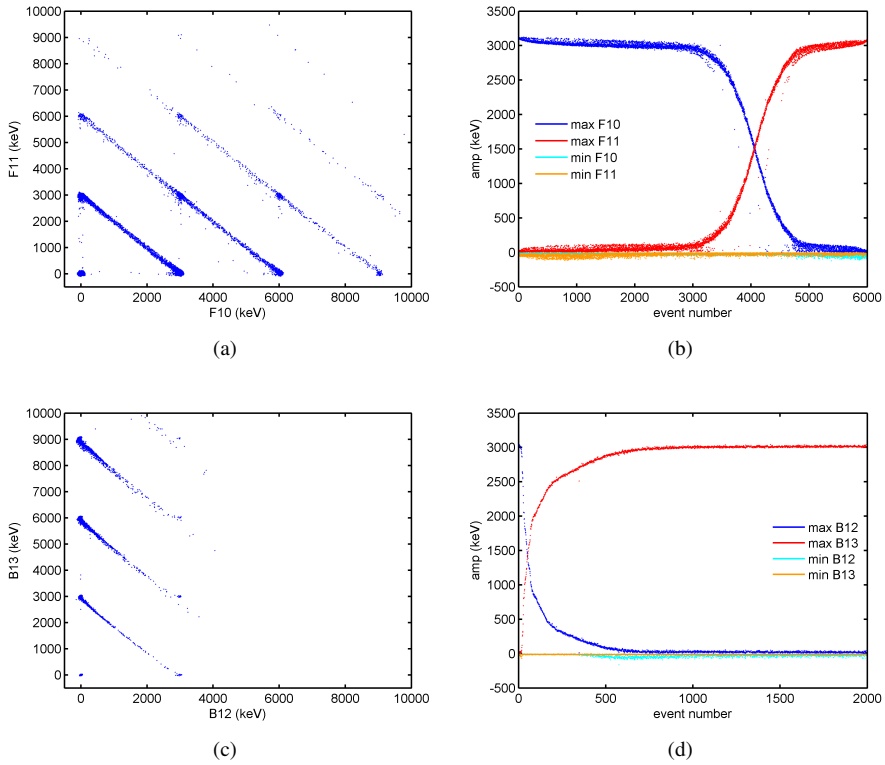

Figure 3.36: *3 MeV protons impinging on the inter-strip region of the 300 μm DSSSD between front-side strips n. 10 and n. 11 – front injection (a) and (b), between back-side strips n. 12 and n. 13 – back injection (c) and (d). On the left column the scatter plots of the $MAX + MIN$ of the two neighbor strips, on the right column the plot of the sorted events parameters pertaining to the one proton subset.*

The results are visibly different in the case of 7.5 MeV Li ion beam. Fig. 3.37 (a) shows the $MAX + MIN$ scatter plot of the front-side strips n. 10 and n. 11 – front injection. Slightly negative values begin to appear. Fig. 3.37 (b) is more clarifying since it disentangle the parameters MAX and MIN for the event pertaining to the one Li ion subset – negative peaks

on one strip appear when the ion is impinging closely to the other strip. Moreover, at the center of the inter-strip region the sum of the two MAX is less than the the full collection, meaning that a substantial fraction of the charge cloud (electrons in this case), which has been generated almost superficially, has been lost in the potential pocket beneath the dioxide layer and do not contribute to the signal formation within our time scale. The situation is magnified in the case of back injection due to the wider inter-strip gap and to the fact that in this case holes, rather than electrons and significantly slower, are responsible for the signal formation process. In Fig. 3.37 (c) the $MAX + MIN$ of back-side strips n. 12 and n. 13 subsets are shifted and bended significantly. Fig. 3.37 (d) shows how the negative peaks arise on one strip when the Li ion impinges right after the mid-point of the gap toward the neighboring strip. This means that there can be not only signals with the opposite polarity but also bipolar. Even in this case the amount of charge lost is significant, due to the loss of holes between the back-side strips.

1500 μm DSSSD

Fig. 3.38 (a) shows the scatter plot of the $MAX + MIN$ of the two neighbor strips of front side strips n. 10 and n. 11 with 3 MeV protons impinging in the inter-strip gap – front injection, while Fig. 3.38 (b) the MAX and MIN parameters of the sorted events pertaining to the one proton subset. The situation is substantially similar to the one reported for the 300 μm DSSSD. The back injection case shown in Fig. 3.38 (c) and (d) for back-side strips n. 13 and n. 14 on the contrary sees the appearance of small negative peaks. This is caused by the fact that in this case the 3 MeV proton absorption depth can be considered almost "superficial" since we are dealing with a thicker detector.

Fig. 3.39 (a) and (b) show the case of front-side strips n. 10 and n. 11 with 7.5 MeV Li ions impinging in the inter-strip gap – front injection, while Fig. 3.39 (c) and (d) show the case of the back-side strips n. 13 and n. 14 – back injection. The situation is similar to the 300 μm DSSSD case, but with even larger negative peaks for the same considerations that with a thicker detector the relative penetration depth of the 7.5 MeV Li ion is even shorter.

The raw waveforms – baseline subtracted – plotted in Fig. 3.40 and Fig. 3.41 pertain respectively to the highlighted zones of Fig. 3.38 (a) – front-side strips with a 3 MeV proton impinging at the inter-strip gap (front injection) – and of Fig. 3.39 (c) – back-side strips with a 7.5 MeV Li ion impinging at the inter-strip gap (back injection)– for a comparison between

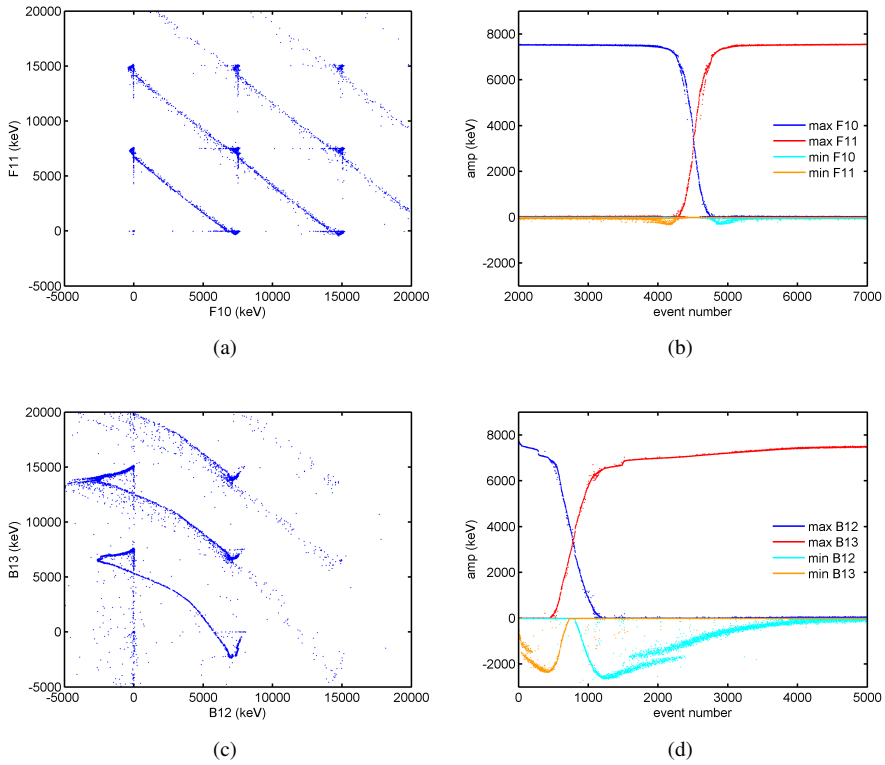

Figure 3.37: *7.5 MeV Li ions impinging on the inter-strip region of the 300 μm DSSSD between front-side strips n. 10 and n. 11 – front injection (a) and (b), between back-side strips n. 12 and n. 13 – back injection (c) and (d). On the left column the scatter plots of the $MAX + MIN$ of the two neighbor strips, on the right column the plot of the sorted events parameters pertaining to the one Li ion subset.*

the case without and with the clearest bipolar and opposite polarity signals. Position α corresponds to a a particle impinging fully on the first strip, δ to a particle impinging at the inter-strip mid-point and β and γ to particles impinging between the first strip and the inter-strip mid-point. Positions beyond the mid-point has been omitted since the situation is symmetrical.

For the 3 MeV protons case we assist to a plain charge-sharing, even if for strip n. 11 at position α and β we see at the beginning of the transient a small negative spike that can be ascribed to a beginning of "opposite polarity signal" phenomenon. Instead, for the 7.5 MeV Li ion case, whose raw waveforms are "originally" negative since they belong to the opposite detector side and are here turned upside down for the sake of clarity, we observe the appearance of huge bipolar and opposite polarity signals for

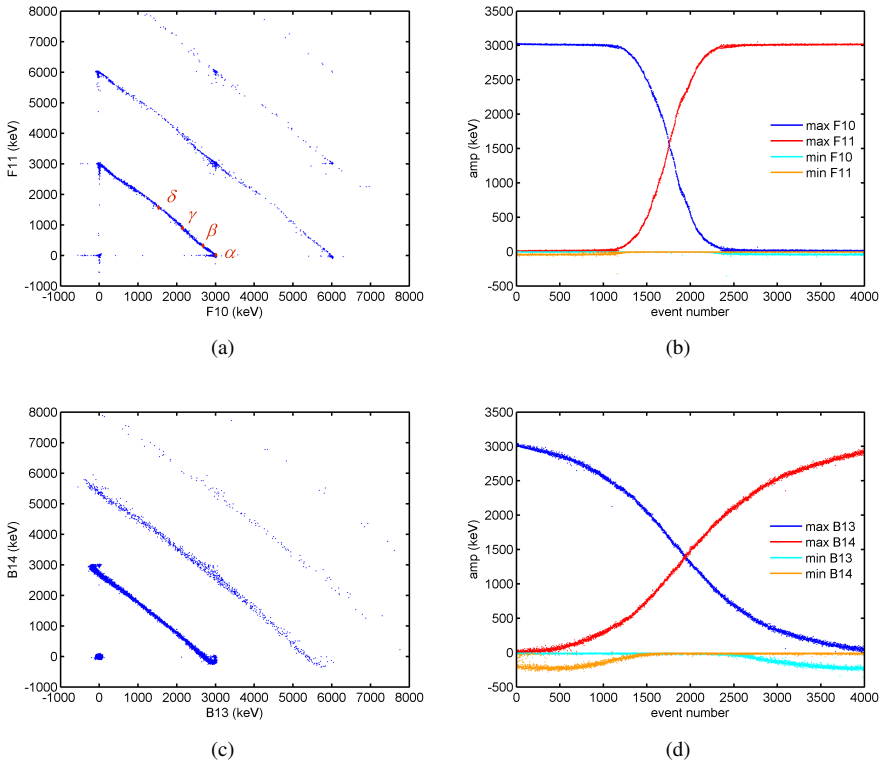

Figure 3.38: *3 MeV protons impinging on the inter-strip region of the 1500 μm DSSSD between front-side strip n. 10 and n. 11 – front injection (a) and (b), between back-side strips n. 13 and n. 14 – back injection (c) and (d). On the left column the scatter plots of the $MAX + MIN$ of the two neighbor strips, on the right column the plot of the sorted events parameters pertaining to the one proton subset.*

the farthest strip. Moving from position α to position γ we assist to pure opposite polarity signals, with at most some charge loss effects when at the end of the transient the value remains slightly above zero, evolving in bipolar signals, meaning that the strip is collecting part of the holes, and becoming at last of the correct polarity when a symmetrical condition is reached with respect to the other strip. Again the sum of the peak values of the two strips at position γ is slightly less than the full collection due to the charge lost below the inter-strip gap potential pocket.

The non-monotonic behavior of the opposite polarity and bipolar waveforms is a clear hint of the presence of pure charge induction effects which are ultimately related to the electrodes *weighting potential*, topic specifically addressed both theoretically and quantitatively in Section 4.6 (pag.

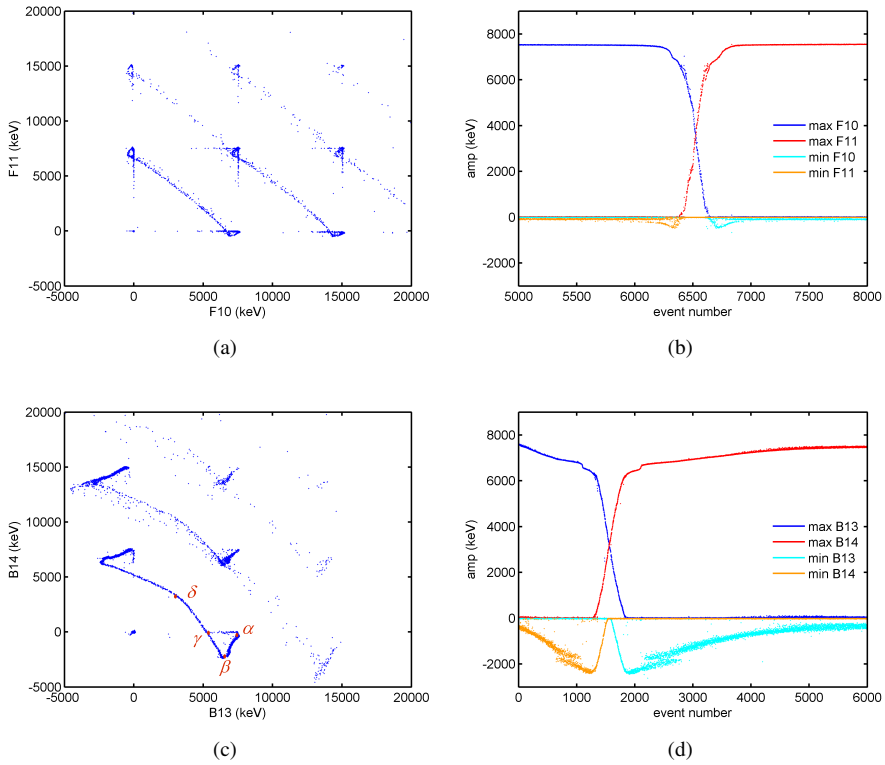

Figure 3.39: *7.5 MeV Li ion impinging on the inter-strip region of the 1500 μm DSSSD between front-side strips n. 10 and n. 11 – front injection (a) and (b), between back-side strips n. 13 and n. 14 – back injection (c) and (d). On the left column the scatter plots of the $MAX + MIN$ of the two neighbor strips, on the right column the plot of the sorted events parameters pertaining to the one Li ion subset.*

95).

3.4 Conclusion

We carried out a detailed characterization of the FARCOS Double Sided Silicon Strip Detectors (thicknesses 300 μm and 1500 μm) in terms of capacitance-voltage measurements investigating the main contributions of the single strip capacitance, namely the bulk capacitance – the capacitance of one strip toward the whole other side – and the inter-strip capacitance – the capacitance between two neighbor strips of the same detector side. The effect of the test signal frequency on the capacitance measurement has also been evaluated as well as the impact of the LCR-meter measurement accu-

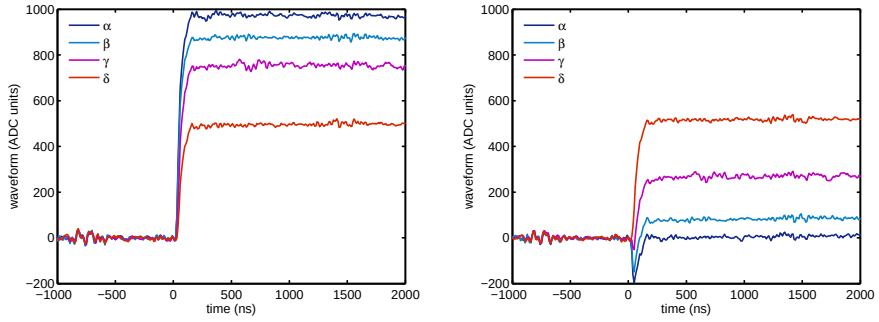

(a) (b)

Figure 3.40: *Raw waveform – baseline subtracted – of front-side strips n. 10 (a) and n. 11 (b) for the 1500 μm DSSSD with a 3 MeV proton impinging at the inter-strip gap – front injection – corresponding to the highlighted positions in the scatter plot of Fig. 3.38 (a). Position α corresponds to a particle fully impinging on front-side strip n. 10, position delta to a particle impinging in the inter-strip gap mid-point and β and γ to two intermediate positions.*

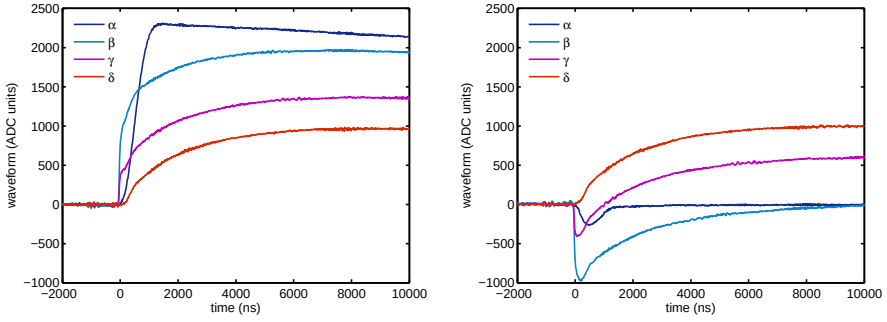

(a) (b)

Figure 3.41: *Raw waveform – baseline subtracted – of back strips n. 13 (a) and n. 14 (b) for the 1500 μm DSSSD with a 3 MeV proton impinging at the inter-strip gap – back injection – corresponding to the highlighted positions in the scatter plot of Fig. 3.39 (c). Position α corresponds to a particle fully impinging on back-side strips n. 13, position delta to a particle impinging in the inter-strip gap mid-point and β and γ to two intermediate positions.*

racy. In addition, we performed a careful qualification of the 2D response matrix of the DSSSDs in terms of amplitude and position exploiting the pulsed monochromatic ion beam available at the DEFEL line of the LaBeC Accelerator – INFN Firenze. In this way it has been possible to obtain a

precise and accurate energy calibration of each individual strip and of the corresponding amplifier over a wide energy range. In addition, thanks to the spatial definition of the beam and the availability of different pairs ion-energy (1 MeV, 3MeV, 5 MeV protons and 7.5 MeV Li), we evaluated the impact of the inter-strip injection on the signals shape showing a selection of the results. In particular we investigated the appearance of bipolar and opposite polarity signals in relation to the injection position and the ion penetration depth.

CHAPTER 4

3D Simulation Code for Charge Transport and Signal Formation in 2D Semiconductor Detectors Suitable for High Charge Injection Levels and High Electrode Segmentation

4.1 Introduction

We developed a 3D simulation code for electron-hole transport and signal formation in fully-depleted semiconductor detectors with 2D – linear or cylindrical geometry, as these are the most common topologies in nuclear physics applications – to the purpose of achieving a superior understanding of the signals formation process at a physical level which can be exploited both to correctly interpret acquired data and to give suggestions for the optimization of detection systems and signals processing techniques. Considering the importance of the mobile carrier contribution at the high charge injection levels foreseen in nuclear physics experiments the key point of our code is that we accounted for the full electron-hole cloud dynamics,

NOTE: The content of this chapter is partly based on the papers [30] and [49] coauthored by myself.

including therefore the mutual electrostatic interaction between the carriers and thermal diffusion. We adopted a microscopic approach, *i.e.* we compute the trajectory and the induced signal for every single charge carrier at each time step of the simulation. It is important to stress the fact that we kept into account the 3D nature of carrier-carrier electrostatic interaction and carrier dynamics which can not be simplified despite the 2D detector geometry. The induced current and charge signals at any arbitrary electrode are computed together with the carriers trajectories by superposing the contributions of individual carriers without additional computational effort. The chapter is organized as follows. In Section 4.2 we review the physical model and the simulation method; in Section 4.3 we show selected results of a thorough set of simulations conduced to qualify the code while in Section 4.4 we show the comparison of some simulation results with an analytical approximated model found in literature. In Section 4.5 we evaluate the effectiveness of two computation speed enhancement techniques – *charge clustering* and *adaptive carrier position update*. Finally, in Section 4.6 we present a set of simulations that reproduce the experimental conditions of the FARCOS DSSSD under ion beam at the INFN LaBeC (Sesto Fiorentino, Italy) reported in Section 3.3 (pag. 60) – *i.e.* protons and ^{7}Li ion impinging on the DSSSD with energy ranging from 1 to 7.5 MeV in different detector regions – with a special focus on the dependence of the induced signals upon the point of incidence in the inter-strip region.

4.2 Physical Model and Simulation Method

The simulation domain is depicted in Fig. 4.1 for a detector with a 2D linear geometry. The simulation volume is assumed indefinite along the z direction, while its *x-y* cross-section is defined by the Dirichlet or Neumann boundary conditions on the detector. The electron-hole cloud, on the contrary, maintains its intrinsic 3D nature, necessary for the correct computation of the mutual electrostatic interaction (the Coulomb force is a *radial* force).

The total electric field distribution in the simulation domain is obtained as the superposition of the 2D static field ($\vec{E}_{static}$) present on the detector volume due to the applied bias with the time-dependent 3D electric field contribution due to the *n* mobile carriers ($\vec{E}_{mobile}$):

$$\vec{E}_{tot}(\vec{r},t) = \vec{E}_{static}(\vec{r}) + \vec{E}_{mobile}\left(\vec{r},\vec{r}_i(t)\right) \quad i = 1,...,n \qquad (4.1)$$

The static field is computed by means of a dedicated 2D Poisson solver that takes into account the given Dirichlet or Neumann boundary conditions

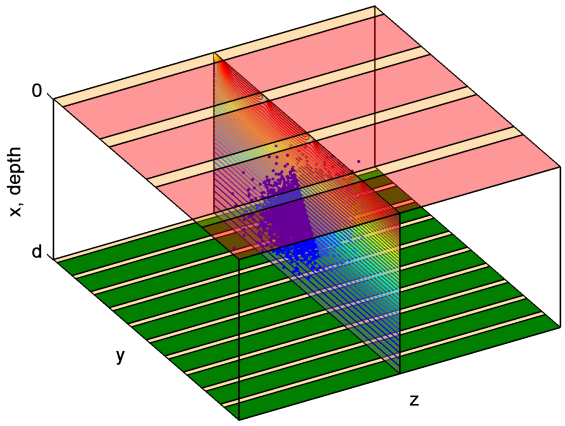

Figure 4.1: *Qualitative representation of the simulation volume for a 2D detector in linear geometry (in this case a double sided strip detector). The contour lines of the potential distribution in the central x-y cross-section show the static field due to the detector structure (stated in the boundary conditions and doping profile). The mobile carriers preserve their full 3D distribution and contribute with a 3D time-dependent field.*

of the *x*-*y* cross-section as well as the fixed charges of the fully depleted bulk. The time-dependent field due to the mobile carriers is computed by summing the exact Coulomb term of every single carrier without any approximation. In order to assure homogeneous Dirichlet conditions on both the surfaces of the detector at $x = 0$ and $x = d$ a truncated series of image charges of each individual carrier is added by means of an algorithm that controls the truncation error. A graphic representation of the series of image charges is depicted in Fig. 4.2. The impact of image charges on the boundary conditions on the remaining two orthogonal surfaces is typically much smaller also because the volume can be extended to the whole detector volume and it has been neglected.

At each simulation time step Δt, the 3D displacement of each mobile carrier is computed as the vector sum of the deterministic displacement Δr_1, obtained by the integration of the drift equation, and a Δr_2 random displacement that models the thermal diffusion [50]. The drift equation is integrated in the time step Δt by the Dormand-Price embedded $5^{th}(4^{th})$ order Runge-Kutta algorithm with adaptive step-size [51] controlled by the desired absolute tolerance, always kept smaller than the diffusive mean displacement. The diffusive displacement is randomly extracted from a 3D Gaussian distribution with standard deviation $\sigma = \sqrt{2D\Delta t}$, *i.e.* the stan-

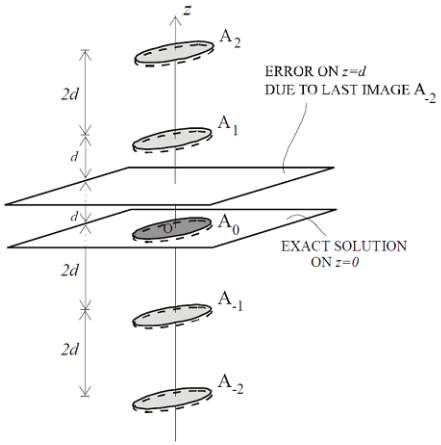

Figure 4.2: *Graphical representation of the series of image charges for a given charge distribution inside the detector volume. The series is truncated by an algorithm that controls the error at the boundaries of the simulation domain. [27]*

dard deviation of the thermal diffusion equation over Δt, being D the diffusion coefficient of the considered carrier, assumed constant during the time step. Since the carriers position is updated at the end of every time step, the dynamic field acting on a carrier during the step is computed considering the position of all the other carriers at the end of the previous time step, which is the last "known" position. For their importance, considerations about the mobility and diffusion models are deferred to subsection 4.2.1.

Induced charge and current signals on any desired electrode are computed at every time step by superposition of the individual carrier contributions according to Ramo's Theorem [52] without any significant additional computational effort. Fig. 4.3 gives a qualitative depiction of the physical problem, while equations of the charge and current induced on a specific electrode by a carrier are:

$$\begin{aligned} Q_{ind}(t) &= -q_c \cdot V_w(\vec{r}_c(t)) \\ I_{ind}(t) &= q_c \cdot \vec{v}_c(t) \cdot \vec{E}_w(\vec{r}_c(t)) \end{aligned} \tag{4.2}$$

where q_c, r_c and v_c are, respectively, the electric charge, position and velocity of the considered carrier at the time t; V_w and E_w are, respectively, the weighting potential and the weighting field of the considered electrode. Just to remind, the weighting potential is the potential computed in the simulation volume putting the considered electrode to 1 V and 0 V to all the others, and it gives a measure of the capacitive coupling between the carrier position and the electrode.

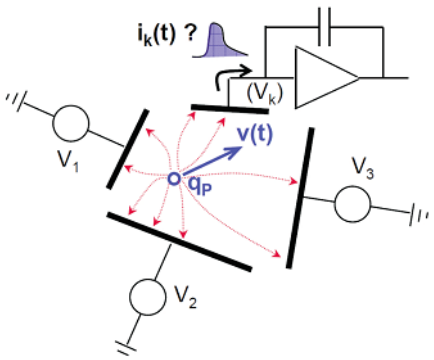

Figure 4.3: *Qualitative representation of the physical problem solved by Ramo's Theorem, that is to compute the charge and the current induced by a moving charge on a specific electrode of a system of electrodes.*

Position, velocity, electric field, mobility and diffusion, induced charges and currents of every single carrier at each time step are saved on binary files which can be used for further analyses and visualizations.

The code architecture has been designed to fully exploit the capability of modern multi-core machines where and, since the computational burden is concentrated in fully parallelizable subroutines, it can achieve a speed-up factor that goes pretty much linearly with respect to the number of used cores.

4.2.1 Mobility and Diffusion Models

Since our code is specifically targeted to high charge generation levels, we adopted a field-dependent model for the drift mobility coefficients, as in [53]:

$$\mu = \frac{\mu_0}{\left(1 + \left(\frac{\mu_0 E_{tot}}{v_{sat}}\right)^{\beta}\right)^{1/\beta}} \tag{4.3}$$

where μ identifies the overall mobility coefficient of electrons and holes, μ_0 is the low-field value, E_{tot} is the total electric field and β is a constant close to 1 – depending on the references – for both holes and electrons . The saturation velocity v_{sat}, according to [54], is expressed as:

$$v_{sat} = \frac{2.47 \cdot 10^7}{1 + 0.8 \exp\left(\frac{T(K)}{600}\right)} \quad (cm \cdot s^{-1}) \tag{4.4}$$

where T is the lattice temperature expressed in K. The dependence of the mobility coefficients and of other charge transport properties in Silicon on the electric field and on temperature has been carefully reviewed by [55], who substantially comes to the aforementioned parameterization, but gives also experimental evidences of anisotropic effects for both electrons and holes velocities in the crystallographic directions $\langle 100 \rangle$ and $\langle 111 \rangle$. It seems that the electron speed along $\langle 111 \rangle$ is greater than along $\langle 100 \rangle$ on equal field, while for hole is the opposite. Moreover, non-linear effects arise at low temperatures. Attempts to explain this behavior can be found in [56] for electrons and in [57] for holes, where anisotropy and non-linearity are ascribed to pure quantum-mechanic effects, *e.g.* valence and conduction valleys shape, inter and intra-valley scattering, repopulation mechanisms... Such behaviors can be correctly estimated only with appropriate Monte Carlo quantum-mechanic techniques (see [58] for an example of full-quantum approach), but since at common operating temperatures these effects are, after all, small, we rely on the empirical relations stated above with the only shrewdness of tuning all the parameters at best to match the physical condition of the simulated detector.

Concerning the diffusion coefficient D, Einstein's equation at lattice temperature has been maintained:

$$D = \mu(E_{tot}) V_{th} \tag{4.5}$$

where V_{th} is the thermal voltage at lattice temperature and $\mu(E_{tot})$ the field-dependent mobility coefficient Eq. 4.5 has demonstrated indeed to be in good agreement with the experimental data in literature up to high fields. General considerations about the diffusion coefficients dependence on crystallographic orientation and field in silicon can be found in [55], while for more detailed experimental reports, quantum-mechanic considerations and computational attempts refer to [59] for electrons and [60] for holes. From these works and others emerge the tendency to correct the Einstein's equation at high fields by introducing a mean carrier energy due to the fact that carriers are no more in thermal equilibrium with the lattice. Unfortunately difficulties immediately arise in the computation of electrons and holes mean energy at high fields in silicon due to the band structure complexity [61]. A naive extrapolation of the mean energies would indeed leads to non-physical results at high-field and this approach – at least for silicon – has been therefore discarded.

4.3 Code Validation

For the implementation of the code we chose the programming language FORTRAN 90/95 which showed faster performances with respect to the C language for our specific computational tasks. The code has been compiled with *gfortran ver. 4.4* and the parallel library *OpenMP ver. 3* directives have been extensively used in order to exploit the capability of modern multi-core machines in terms of parallel calculus. To carry out the simulations we used a server featuring 2 Xeon X5660 processors (2.80 GHz, 6C, cache 12 MB) with 48 GB DDR3 RAM.

In order to qualify the code we performed a set of simulations to compute the space-time evolution of an electrons cloud under different conditions and with varying number N of electrons. The initial cloud of N electrons was generated according to a 3D Gaussian distribution with 0.1 μm standard deviation. We studied the cases of pure thermal diffusion, pure Coulomb repulsion and both. The simulations were carried out either in an infinite detector volume (free expansion) or with a finite detector thickness d. In all cases, the material is silicon. We tested different values of the time step, ranging from 0.2 ns to 4 ns, while the total simulated time is always 1 μs. In the following subsections we discuss some of the most significant results that confirm the reliability of the code.

4.3.1 Cloud expansion in free space due to thermal diffusion only

We computed the standard deviation σ_x of the expanding electron cloud as function of time – for different values of the number of electrons N and of the time step Δt and we compared it with the theoretical standard deviation of thermal diffusion $\sqrt{2D_n t}$. The simulations has been carried out in the case of free expansion, *i. e.* with an infinite volume of silicon in absence of external field or fixed charges. The results for σ_x – all directions are equivalent, thanks to the spherical symmetry of the problem – are shown in Fig. 4.4 with N equal to 200, 2000 and 20000. In each figure, the curves with colors from blue to green represent increasing values of the time step Δt, while the red curve is the theoretical curve for the thermal diffusion. As the number of electrons increases, the statistical spread obviously reduces and the simulation curves tend to the theoretical one. The dependence on the time step Δt is not appreciable, as expected, due to the adaptive step-size used to solve the drift equation; moreover, carriers trajectories are independent from each other, since no mutual force is considered. In order to evaluate the statistical impact of the number of carriers we computed the L^2-norm of the deviations of the simulated values of σ_x with respect to the

theoretical ones over the total simulated time of 1 μs. Fig. 4.5 shows this L^2-norm of the deviations as function of the number of electrons N for different Δt values. As expected the average slope of the curves in the log-log plot follows approximately the $1/\sqrt{N}$ factor.

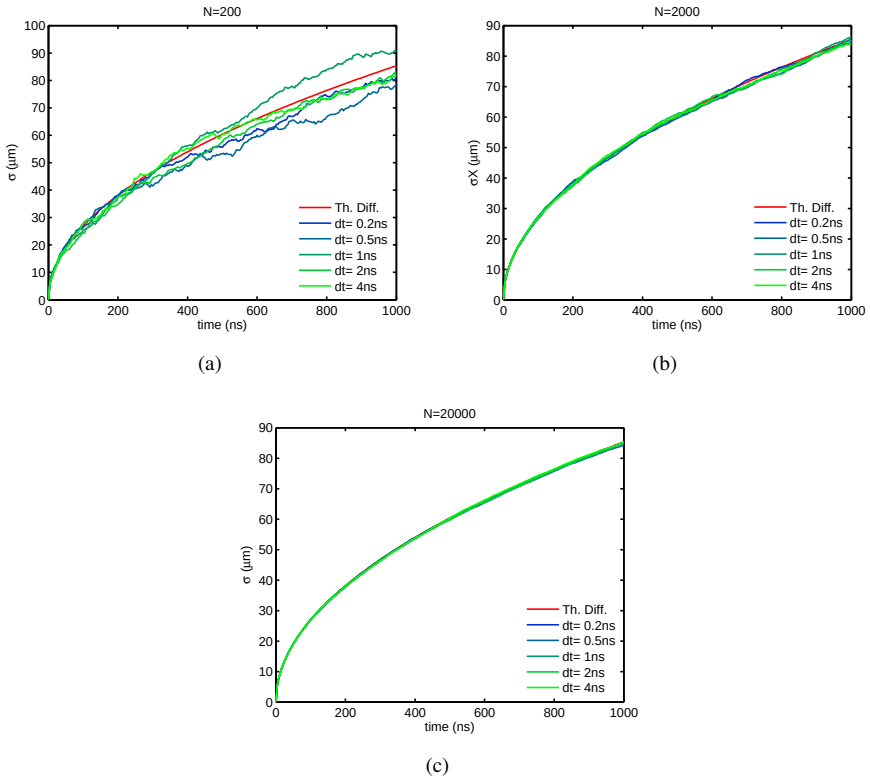

Figure 4.4: *Standard deviation of a cloud of N electrons expanding in free space due to pure thermal diffusion for different values of time step Δt. The red line stand for the theoretical curve $\sqrt{2D_n t}$. a) N=200, b) N=2000, c) N=20000.*

4.3.2 Cloud expansion with finite detector thickness due to Coulomb repulsion only

This set of simulations show the effect of the dynamic field of the mobile carriers (Coulomb repulsion) without thermal diffusion as the number of carriers N varies from 100 to 20000. For all simulations we used the time step Δt equal to 0.2 ns. In order to evaluate the impact of the detector thickness on the space-time evolution of the electron cloud, we carried out the simulations within an infinite volume (free expansion) as well as for

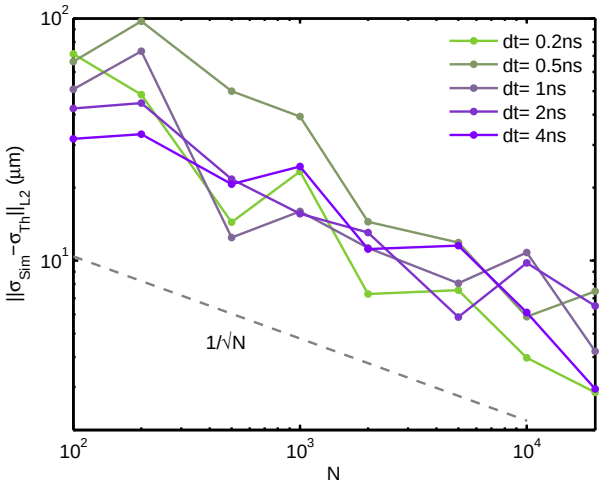

Figure 4.5: *L^2-norm of the standard deviations of the simulated values σ_x with respect to the theoretical ones in the total simulation time as a function of the number of electrons N, for different time steps Δt. The dashed line shows the $1/\sqrt{n}$ trend.*

two values of the detector thickness d.

The results are shown in Fig. 4.6 in the case of detector thickness d equal to 300 μm and 450 μm. We expect that, due to the finite volume thickness along the x direction, the spatial electron distribution does not maintain a spherical distribution, as the image charges will attract the electrons towards the surfaces $x = 0$ and $x = d$ which will stretch the cloud along x at the expense of the other two orthogonal directions. As expected, the standard deviation of the electron cloud along the depth σ_x (red line) lies above the corresponding values in the case of free expansion (green line), while the standard deviation in the orthogonal directions (σ_y equivalent to σ_z) lies below (black line). Coherently, the curve separation in greater in the case of d equal to 300 μm with respect to the 450 μm case.

4.4 Comparison with an Approximated Analytical Solution

Although the full analytical solution of the problem of an expanding electron cloud subject to thermal diffusion and Coulomb repulsion is not available [62], [63] derived an approximated analytical expression for the standard deviation of the electron cloud in free expansion that preserves the correct asymptotic behavior to the known analytical solutions in the limiting cases of pure thermal diffusion and pure Coulomb repulsion. According to [63] the approximated differential equation that governs the time evolu-

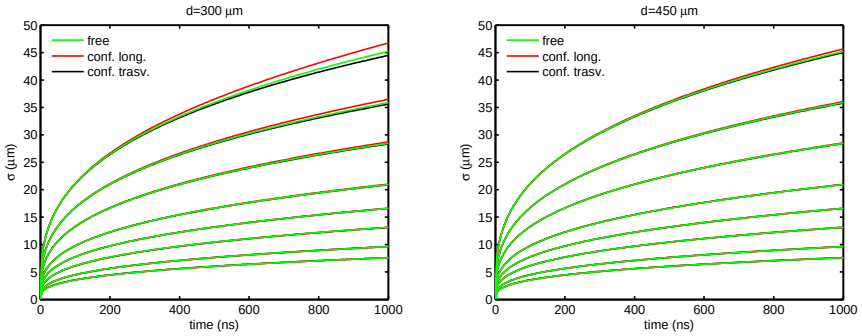

(a) (b)

Figure 4.6: *Standard deviation of a cloud of N electrons due to pure Coulomb repulsion for finite detector thickness (from the bottom to the top N =100, 200, 500, 1000, 2000, 5000, 10000, 20000). The red line is the standard deviation along the depth (longitudinal) while the black line is the standard deviation in the orthogonal direction (transversal) (a) $d = 300\mu m$ and (b) $d = 450\mu m$. For comparison the standard deviation in the case of free expanding ($d \to \infty$).*

tion of the standard deviation of the electron cloud distribution in presence of both thermal diffusion and Coulomb repulsion is:

$$\frac{\mathrm{d}\sigma^2(t)}{\mathrm{d}t} = 2D + \frac{Q_0 \mu K}{\sigma(t)} \tag{4.6}$$

where Q_0 stands for the total charge involved, μ is the mobility coefficient – which is taken to be a constant, D is the diffusion coefficient and K is a constant that summarize the effect of Coulomb repulsion and of the shape of the cloud. The integration of Eq. 4.6 leads to the expression:

$$2Dt = \sigma^2 - \sigma_0^2 - \frac{Q_0 \mu K}{D}(\sigma - \sigma_0) + \frac{1}{2}\left(\frac{Q_0 \mu K}{D}\right)^2 \ln\left(\frac{Q_0 \mu K + 2D\sigma}{Q_0 \mu K + 2D\sigma_0}\right) \tag{4.7}$$

In the case of free expansion due to Coulomb repulsion only, *i. e.* with $D = 0$, the integration of we Eq. 4.6 leads to the known exact solution [62]:

$$\sigma = \sqrt[3]{\sigma_0^3 + \frac{3}{2} Q_0 \mu K \cdot t} \tag{4.8}$$

To conduct a comparison with these analytical solutions we carried out a set of simulations of free expansion with $N = 100$, 200, 500, 1000, 5000,

10000, 20000 electrons. In order to probe higher charge values we carried out two additional simulations with N =20000 carriers, each carrier assumed to be a cluster of electrons leading to an equivalent total charge of $2 \cdot 10^5$ electrons (cluster charge $10q$) and of $2 \cdot 10^6$ electrons (cluster charge $100q$). The maximum time step is 0.2 ns. In the three high-charge simulations (N =20000) we improved the numerical accuracy by updating the carrier positions at every inner sub-interval of the adaptive step-size algorithm of the Runge-Kutta routine as described in Section 4.5.1. Fig. 4.7(a) shows the simulation results (symbols) in case of pure Coulomb repulsion and the fitting curves based on Eq. 4.8, while Fig. 4.7(b) shows the simulated points in case of both thermal diffusion and Coulomb repulsion together with the fitting curves based on 4.7. The agreement in both cases is very good (percentage error below 0.2% for Fig. 4.7(a), below 1% for Fig. 4.7(b)), except for low values of N (up to 1000), when thermal diffusion is present, due to poor statistics. The least-square fit of the simulated points, reported in Fig. 4.8, gives the value of the free parameter $Q_0\mu K$ for each curve. From the linear fit of $Q_0\mu K$ values vs Q_0 we then extracted the constant μK. In both cases (repulsion only, repulsion+diffusion) the results are consistent: $\mu K = 3.1 \cdot 10^{-3} \mu m^3/ns/N$, where N is the number of carriers.

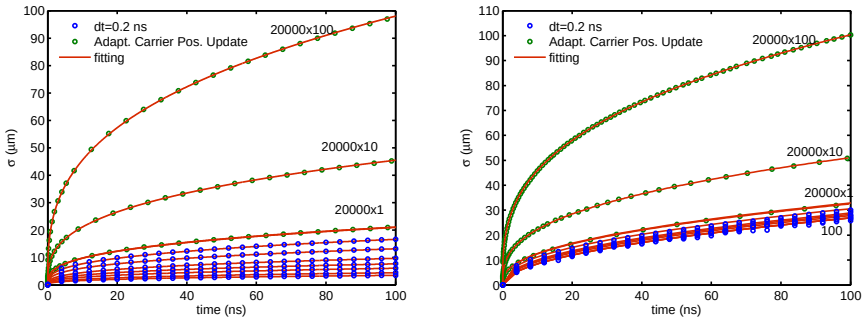

Figure 4.7: *Simulation of electron cloud (symbols). (a) Case of pure Coulomb repulsion, fitting curves based on 4.8. (b) Case of both thermal diffusion and Coulomb repulsion, fitting curves based on 4.7. The number of simulated electrons N varies from 100 to 20000 (from the bottom to the top of the figure) with two additional simulations of 20000 electrons where each carrier is conceived as a cluster of 10q and 100q respectively.*

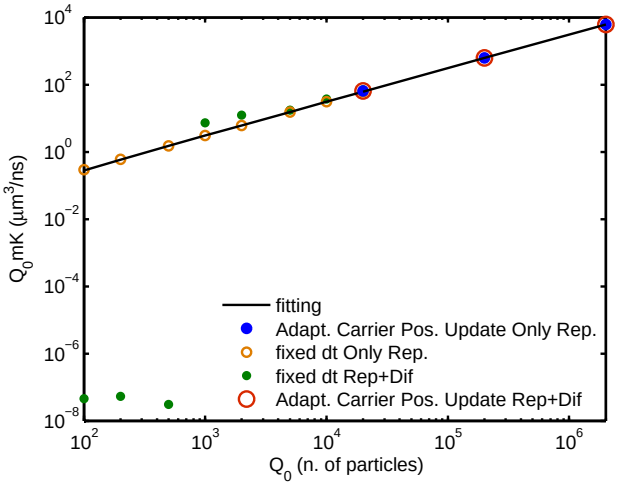

Figure 4.8: *Linear fitting of the extrapolated $Q_0 \mu K$ as a function of Q_0 for the different set of simulations. Simulations for low charge values and comprehensive of the thermal diffusion (green dots) have been discarded since the statistical spread gives unreliable results. The fitted value for μK is $3.1 \cdot 10^{-3} \mu m^3/ns/N$, where N is the number of electrons.*

4.5 Enhanced Numerical Methods

The computation of the dynamic field due to the mobile carriers is a CPU intensive operation, typically increasing with the square of the number of carriers. Indeed, our algorithm cycles over the total time span t_{max} with a time step Δt, and within it cycles over the total carriers N, computing for each of them the total electric field, including the Coulomb interaction due to all the remaining $N-1$ carriers by the superposition of each single contribution. Therefore we expect a linear dependence of the computational time on the number of time steps, while a quadratic dependence on N. Further, an increasing number of carriers puts to challenge also the numerical accuracy of the code. A great number of carriers means larger electrostatic mutual fields which are computed, within the Δt, considering the carriers position "frozen" at the end of the previous time step. Clearly, the accuracy of the dynamic field estimation relies strongly on the value of the time step Δt, especially when carriers are much close together (Coulomb field goes with $1/\Delta r^2$), a condition that typically happens at the the first time instants following the charge generation. Decreasing Δt does not seem the solution since the computational time would (linearly) increase.

Since our code is specifically targeted to high levels of charge injec-

tions, we elaborated and proved the effectiveness of two enhanced numerical techniques, namely the *charge clustering* and the *adaptive carrier position update*.

4.5.1 Charge clustering

This method consists of assigning to each carrier an electric charge larger than the elementary one – q. We call the ratio between this new charge and q *Macro Charge Factor*. The total simulated charge Q_{tot} can be then increased by a factor M, N remaining constant, since $Q_{tot} = N \cdot M$ with a negligible increase of the computational time. We probed the effectiveness of this simple but powerful method with a set of dedicated simulations. An electron cloud with total charge Q_{tot} =20000q is simulated as a set of clouds with varying number of electrons N and correspondingly M, such as $N \cdot M = Q_{tot}$ – N equals to 200, 400, 1000, 2000, 4000, 10000, 20000 and M equals to 100, 50, 20, 10, 5, 2, 1 q respectively. Then the cloud expands in free space due only to Coulomb repulsion – thermal diffusion is neglected since it does not depend on carriers charge – with t_{max} =1 μs and Δt =0.2 ns. The results are shown in Fig. 4.9 (a) in terms of the standard deviation σ of the clouds along one direction (all directions are equivalent due to the symmetry of the problem). As clearly visible from the percentage difference between the curves and the one with M =1q – which has been taken as reference – shown in Fig. 4.9 (b), the method is effective at least up to M =100q within the 1%. We expect it to hold even for larger values.

4.5.2 Adaptive carrier position update

This method consists of the dynamic adjustment of the value of the Runge-Kutta time step Δt at run-time in order to achieve an improved accuracy. Indeed, especially at the beginning of the simulation when the carriers are all packed together and the dynamic field exceeds the static field by orders of magnitude, it is crucial to update the carriers position as often as possible since their mutual interactions reflect in a interdependence of the trajectory paths. In this conditions, the time step is then shrunk down even to very small values (on the order of the ps). When on the contrary the carriers are spatially spread as a consequence of the cloud expansion and the dynamic field is negligible with respect to the static field, the algorithm increases the Δt since the trajectories are substantially independent each other and a too frequent position update would be useless. This allows a faster computation without any accuracy loss.

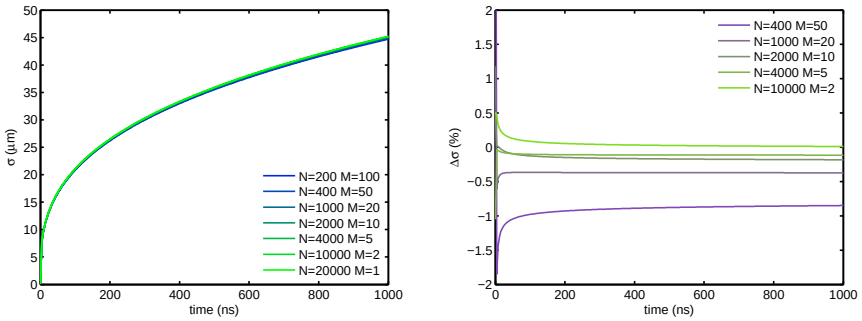

(a) (b)

Figure 4.9: *Standard deviation of clouds varying the number of electrons N and correspondingly the macro charge factor M to maintain constant the total charge $Q_{tot} = 20000q$(a). Difference in percentage of the same curves from the reference one ($M = 1q$) (b). The clouds are expanding in free space subject only to Coulomb repulsion. The value of the time step Δt is 0.2 ns.*

We determine the value of Δt according to the criterion of *maximum allowed displacement* and on a statistical basis. At each time step of the simulation, indeed, we compute that time as the interval a desired percentile of carriers would need to cover such allowed displacement. Maximum displacement values around 1 μm and a percentile of 1 seem to be a good compromise between accuracy and computational time for our practical cases. We tested the effectiveness of this technique running a set of simulations of an electron cloud expanding in free space due only to Coulomb repulsion, with 3D Gaussian initial distribution of σ_0 =0.1 μm, using fixed time step (0.1 ns) and adaptive carrier position update with a maximum allowed displacement of 10 nm, 100 nm, 1 μm, Macro Factor 1, 10, 100 q and a total time span of 10 ns. Results are reported in Fig. 4.10(a),(b),(c) for the standard deviation of the expanding cloud (all directions are equivalent), the average electric field acting on the carriers and the average speed of the carriers, respectively. The logarithmic scale enlighten the behavior at the very beginning of the charge explosion, showing how the simulation with fixed time step of 0.1 ns, which is already a relatively small value, looses a great deal of information with respect to the adaptive carrier position update method which, on the contrary, shrinks the time step down to the picoseconds scale to follow with greater accuracy the first instants of expansion. Looking at Fig. 4.10(a) we can identify several "regimes" of expansion: the standard deviation starts from its initial value σ_0, then it increases linearly with t due to velocity saturation and finally if goes with $t^{1/3}$

which is consistent with 4.8 where the mobility coefficient is assumed constant. The larger the Macro Factor, the longer the cloud would need to pass from the saturation velocity regime to the constant mobility regime. For the sake of clarity the theoretical curve of the pure thermal diffusion ($t^{1/2}$) is also shown, which would be the asymptotic value of any simulation which includes the thermal diffusion, according to 4.7. Fig. 4.10(b) shows the total electric fields averaged over all the carriers for each simulation. At the beginning of the time they reach extremely high values which justify all our concerns in terms of simulation accuracy and transport models, then they fall as t^{-2} when in saturation velocity regime and than as $t^{-2/3}$ when in constant mobility regime. These values can be qualitatively explained if we imagine σ as a kind of effective cloud radius, and the average field as the field on the surface of a sphere with that radius. In this way we establish the $1/\sigma^2$ relation we see in the graphs. Finally, Fig. 4.10(c) shows the speed by means of the average over all the carriers for each simulation. The initial plateau identifies the saturation velocity regime while the following decreasing trend correspond to the constant mobility regime.

The computational time needed to carry out the simulation with the ACPU method with maximum allowed displacement 1 μm is about the 70% in the case of M =100 and about the 25% in the case of M =1 of the computational time needed by the same simulation using the fixed time step 0.1 ns, since with the ACPU Δt is released after the critical first instants of expansion without spoiling the accuracy.

The effectiveness of the Adaptive Carrier Position Update method has been proven to go far beyond what is allowed with a fixed time step algorithm.

4.6 Simulations of the Double Sided Silicon Strip Detector of FARCOS

In the framework of the characterization of the Double Sided Silicon Strip Detectors of FARCOS we noticed some non-trivial and not yet fully understood effects regarding the induced signals on two neighbor strips when we inject ions into the inter-strip regions (see section 3.3, pag. 60). Due to the complexity of the charge transport mechanisms below this surface and the dependence on the particle type and energy, an intuitive understanding of the problem is rather difficult. In order to clarify this issue we ran a batch of significant and representative simulations presenting the qualitative correct interpretation and the quantitative validation by comparing the results with the experimental data shown in Subsection 3.3.5 (pag. 71).

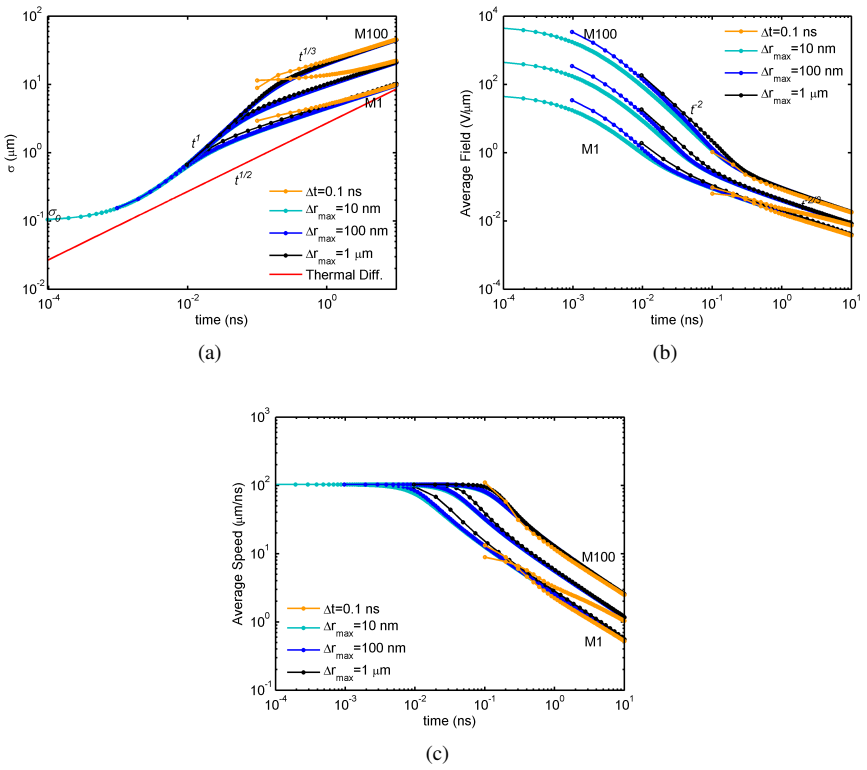

Figure 4.10: *Simulations of a cloud of 20000 electrons expanding in free space due only to Coulomb repulsion. Initial 3D Gaussian distribution with $\sigma_0 = 0.1\mu m$, Macro Factor M =1, 10 , 100 q, total time span 10 ns. Δt for the fixed time step case is 0.1 ns, while for the Adaptive Carrier Position Update the Maximum Allowed Displacement Δr_{max} is 10 nm, 100 nm and 1 μm respectively. (a) standard deviations along one direction (all directions are equivalent due to the symmetry of the problem), the theoretical thermal diffusion curve is also shown for comparison. Italic text identifies the several regimes of cloud expansion. (b) Total electric field averaged over all the electrons, same consideration for the italic text. (c) Velocity averaged over all the electrons.*

4.6.1 Simulation Setup

We assumed the injection of one proton of energy 1 MeV, 3 MeV and 5 MeV and of a ^{7}Li ion of energy 7.5 MeV on the $p-n$ junction side of the detector (*front injection*). The values of the total electron-hole pairs generated and the Macro Charge Factor used in our simulations for the different ions are reported in Table 4.1. The minimum time step for the Adaptive Carrier Position Update is 0.01 ns and the maximum is 0.5 ns. The Maximum Allowed Displacement is 2 μm, while the absolute tolerance in the

Runge-Kutta algorithm is 0.1 nm. The ionization profiles along the impinging direction have been obtained from SRIM2008 [43] and are shown in Fig. 4.11 for all the considered ions. The Bragg peak in silicon is at about 16 μm, 91 μm and 213 μm for 1, 3 and 5 MeV protons and 14 μm for ^{7}Li ion [42].

Table 4.1: *Values of the total electron-holes pairs generated and the Macro Charge Factor used in our simulations for the different impinging ions.*

Ion	e-h pairs	Macro Charge Factor (q)
1 MeV p	$2.778 \cdot 10^5$	27.78
3 MeV p	$8.333 \cdot 10^5$	83.33
5 MeV p	$1.388 \cdot 10^6$	138.89
7.5 MeV ^{7}Li	$2.083 \cdot 10^6$	208.33

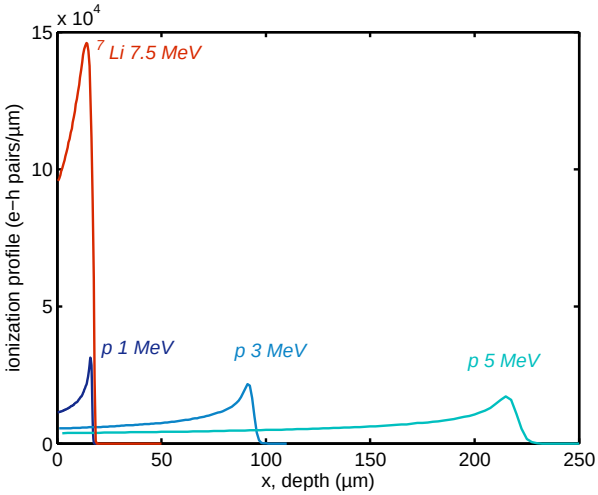

Figure 4.11: *Ionization profile for 1 MeV, 3 MeV and 5MeV protons and 7.5 MeV ^{7}Li ion in silicon, from SRIM2008 [43]. The Bragg peak in silicon is at about 16 μm, 91 μm, 213 μm and 14 μm respectively.*

Due to the high charge density of the ionization profiles especially in the 7.5 MeV ^{7}Li ion case, *plasma effects* are expected to become relevant. Plasma effects are the result of the creation of a high conductivity plasma along the particle trajectory which for some time – up to several ns – prevents the static electric field from separating holes and electrons. This "neutral" plasma is slowly eroded at the edges until the static electric field exceeds the internal electric field due to the Coulomb interactions between the carriers. The overall effect is a *delay* in the induced signals

that takes the name of *plasma erosion time*. Of course plasma erosion time increases as the charge density increases and the static electric field decreases [64] [65] [66].

We simulated two detectors thicknesses d =300 μm and d =1500 μm, the former biased at 25 V (depletion voltage of about 23 V) and the latter biased at 300 V (depletion voltage of about 270 V) to replicate exactly the experimental conditions. The simulation domain in centered on the 25 μm-wide inter-strip region of the junction side with a total span of 1 mm, allowing us to monitor signals on two neighbor p^+-strips, that we call STRIP 1 and STRIP 2. The back side is assumed uniform like being on the longitudinal section of a back strip. Fig. 4.12 showns, as an example, a zoomed view of the 2D potential surface in the nearby of the inter-strip area for the case of detector thickness 300 μm, biased at 25 V. In Fig. 4.13 (a) and (b) are instead reported the weighting potential surface and contour of STRIP 2 over the total detector area for the case d =300 μm, while in Fig. 4.14 (a) and (b) the same for the case d =1500 μm. The weighting potential of an electrode is computed by solving the Laplace equation in the simulation domain setting to 1 V the potential of the considered electrode and to 0 V all the others and it allows computing the amount of charge induced by a carrier at position $\vec{r}$ on that electrode by multiplying its charge times the value of the weighting potential at $\vec{r}$. The contour plots in Fig. 4.13 (b) and 4.14 (b) show clearly how the weighting potentials of STRIP 2 spread in the volume below the inter-strip gap and STRIP 1 up to a certain extent. This means that charges drifting in such region influence not only the charge induced on STRIP 1 but also on STRIP 2 – moreover in a non-monotonic way along the depth. We expect in addition that the signals shape depends strongly – for both the case d =300 μm and d =1500 μm – on the penetration depth along x due to the superficiality of the silicon dioxide potential perturbation, while a dependence on the $y-$direction due to the steepness of the weighting potential at the inter-strip region.

The values of the bulk doping, essentials to correctly simulate the static potentials, are extracted from the CV-measurements reported in Section 3.2 and are $\sim 2.36 \cdot 10^{11}$ cm^{-3} for the 300 μm DSSSD and $\sim 1.7 \cdot 10^{11}$ cm^{-3} for the 1500 μm DSSSD.

We simulated several significant positions of incidence for all the considered ions. Initial cloud charge distributions have been separately computed according to the ionization profiles shown in Fig. 4.11 along the depth while cylindrical distributions with radius 0.2 μm on the interaction surface have been assumed.

Fig. 4.15 (a) and (b) shows the positions of incidence, that we call A, B,

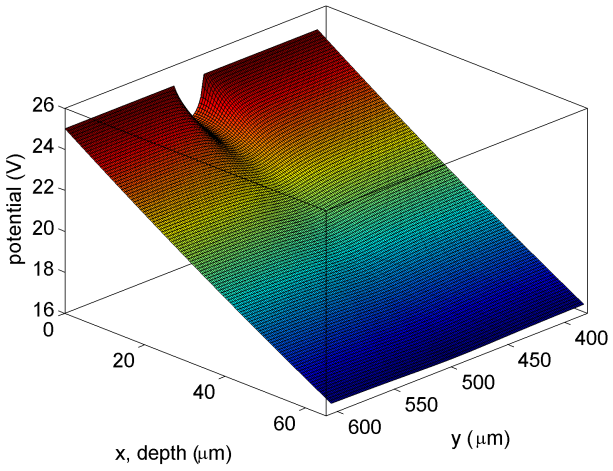

Figure 4.12: *Zoomed view of the 2D potential surface in the nearby of the inter-strip region for the case d=300 μm with detector bias 25 V.*

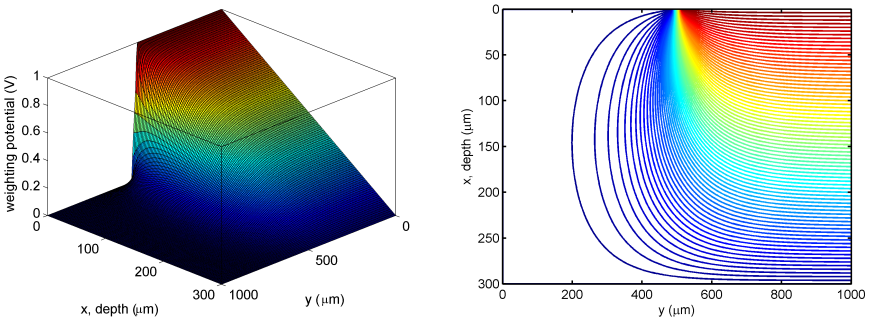

(a) (b)

Figure 4.13: *2D weighting potential surface (a) and contour plot (b) of STRIP 2 over the total simulation domain for the d =300 μm case.*

C and D together with the penetration depth of the ions (Bragg peak depth) with respect to the detector geometry , (b) being the zoomed version of (a) in order to see the less penetrating ions. The contour lines correspond to the static potential due to the boundary conditions. Position A serves as reference case since the condition of injection on one full strip is the "normal" condition. The considered strip is STRIP 1. Position B is right at the border between STRIP 1 and the inter-strip region, position C is at a one quarter of the distance between STRIP 1 and STRIP 2 and position D

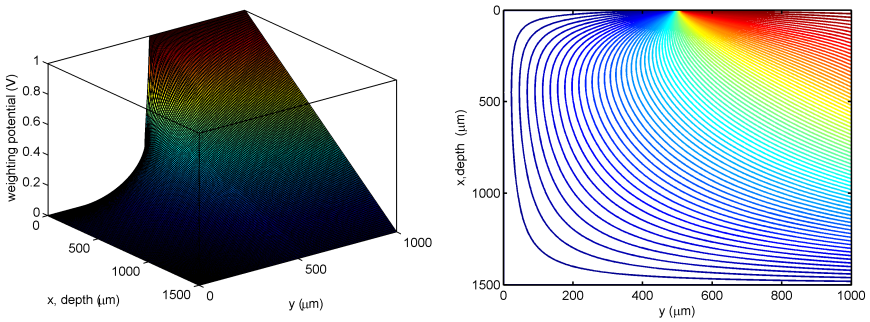

(a) (b)

Figure 4.14: *2D weighting potential surface (a) and contour plot (b) of STRIP 2 over the total simulation domain for the d =1500 μm case.*

at the center of the inter-strip region.

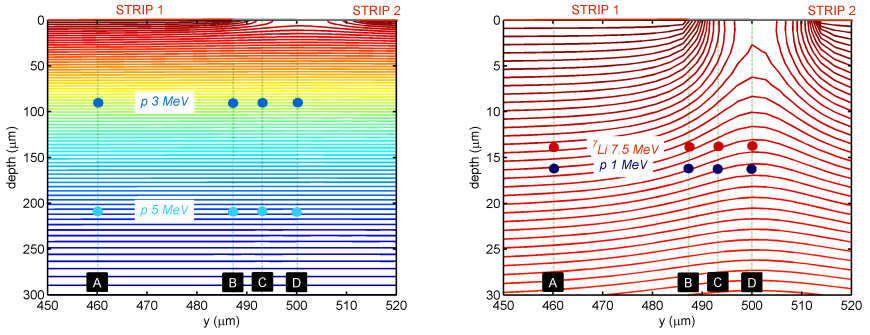

(a) (b)

Figure 4.15: *Sketch of the position of incidence simulated* A, B, C *and* D *together with the penetration depth of the considered ions (Bragg peak depth) with respect to the detector geometry. (b) is the zoomed version of (a) to better visualize the less penetrating ions. The contour lines correspond to the static potential due to the boundary condition – 25 V across the 300 μm DSSSD.*

4.6.2 Results of the Simulations

In the following paragraphs we report the results of the simulations in terms of the charge induced on STRIP 1 and STRIP 2 normalized to the elementary charge q. Being p^+-strips, the induced charge is negative when they

collect holes[1].

300 μm DSSSD

To give an idea of the charge cloud evolution within the detector volume we plotted a series of "snapshots" of the electrons and holes, taken at different times and for different ions – the one with the shorter penetration depth (7.5 MeV ^{7}Li) and the one with the longer penetration depth (5 MeV proton) – to highlight the effect of such difference. Fig. 4.16 (a) to (h) show on the left column the 2D projection of the electron-hole charge cloud for the 7.5 MeV ^{7}Li ion at t =5 ns, t =20 ns, t =30 ns and t =50 ns. On the right column the corresponding 3D version of the plot. Electrons are depicted in green, while holes in red. The underlying potential is the static potential due to the boundary conditions imposed on the detector. At the upper border of each figure there are STRIP 1 and STRIP 2. Fig. 4.17 (a) to (h) show the same for the 5 MeV proton.

Concerning the induced charges, Fig. 4.18 shows with continuous lines the induced charge on STRIP 1 for all the considered ions impinging on position A, *i.e.* full strip. The total of the charge is obviously collected by STRIP 1 and this serves as a reference signal. The dotted lines are the result of the same simulations but without taking into account the Coulomb interaction between the carriers with the purpose to underline its importance especially at high charge injection levels (7.5 MeV ^{7}Li ion rather than 1 MeV proton) when plasma effects become relevant. In the worst case (*i.e.* 7.5 MeV ^{7}Li ion), indeed, we notice that the full charge collection in presence of Coulomb interaction occurs about 20 ns later (plasma erosion time) with respect to the case without Coulomb interaction.

The asymptotic value of the induced charge reveals the *net* charge collected by the strip (since no charge loss occurred within the detector volume).

Fig. 4.19 (a) to (f) report the charge induced on STRIP 1 on the left column and STRIP 2 on the right column for all the considered ions impinging on position B, C and D on the first, second and third row, respectively. Considering STRIP 1, with the impinging position going from A to D we notice a progressive decrease of the induced charge for all the ions due to the fact that part of the holes are collected by STRIP 2. At position D, which is at the center of the inter-strip region, the induced charge correctly reach the half of its reference value. Also, we notice that at any position protons of higher energy feature longer collection time. The reason is that the deeper

[1] From another point of view, these signals can be interpreted as the charge preamplifier outputs that performs an ideal integration with a suitable proportionality factor.

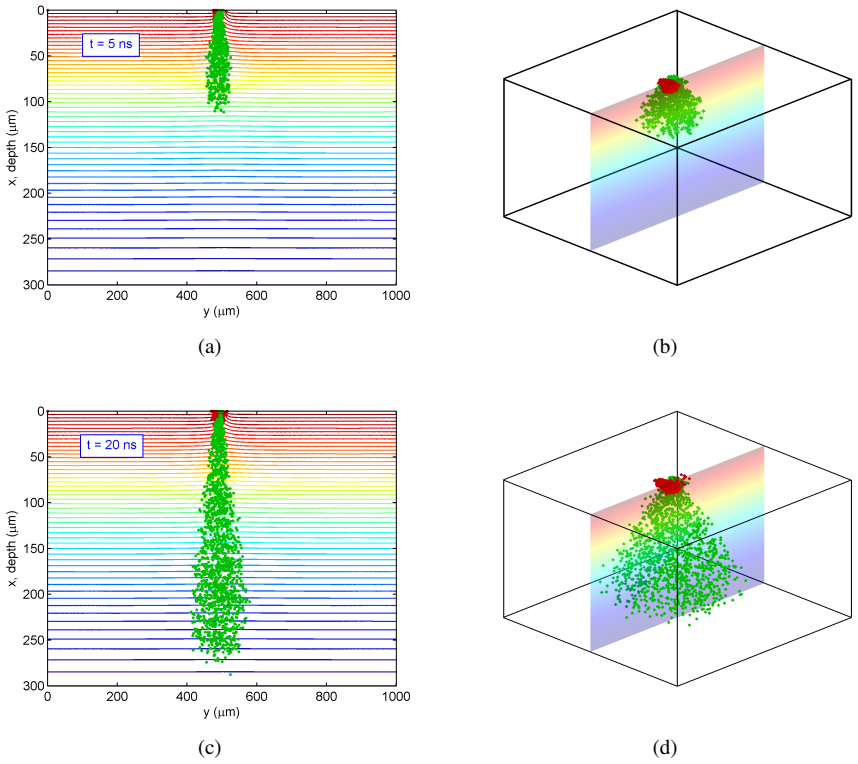

Figure 4.16

is the penetration, the longer (shorter) is the path of the holes (electrons) to their electrode and since holes are slower than electrons their contribution is the dominant one in terms of collection time. Also, at position D, the ^{7}Li ion shows a remarkable delay which is due to the combination of the high charge density and the proximity to the surface of the detector where the local electric field is much lower resulting in an increased plasma effect. Lastly, for position B and C we notice a slight increase of the signals slope at the beginning of the collection while a decrease of the slope for longer times for the less penetrating ions (1 MeV proton, 7.5 MeV ^{7}Li ion) with respect to the reference case A, without a significant difference in the total collection time. This is due to steepness of the weighting potential at those positions which results in a faster holes charge induction effects on STRIP 1 and a consequent increase of the slope at the beginning of the collection process while a decrease of the slope when their contribution is ended.

Considering STRIP 2, going from position D to B we notice that from

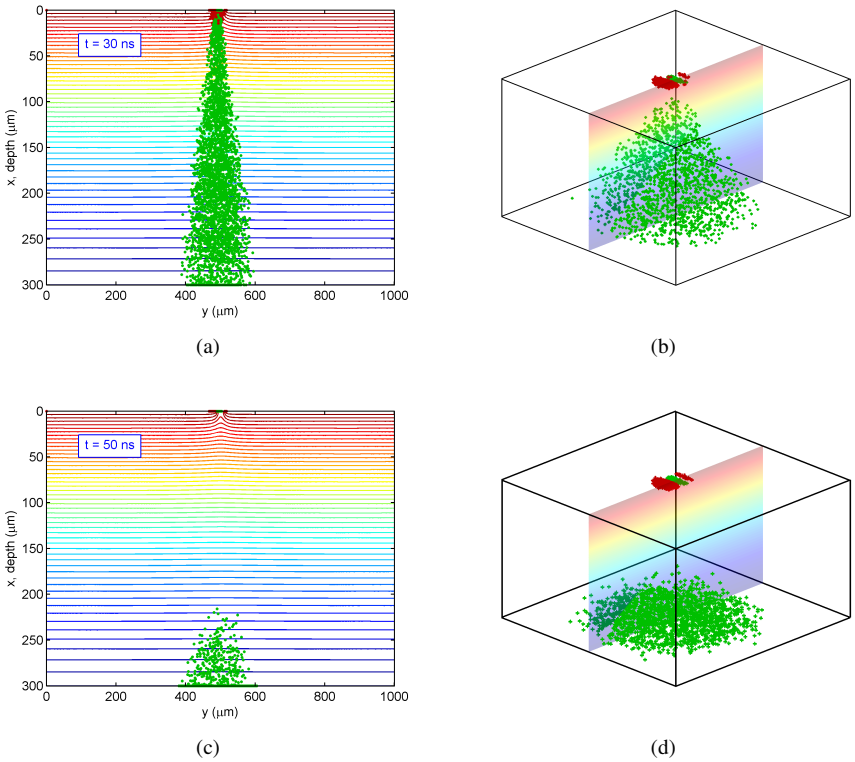

Figure 4.16: *2D projections (left column) and 3D (right column) snapshots of the electrons-holes charge cloud within the detector volume for the 7.5 MeV ^{7}Li ion impinging at position* B *of the 300 μm DSSSD and at different times – t =5 ns, t =20 ns, t =30 ns and t =50 ns. Electrons are green while holes are red. The underlying potential is the static potential due to the boundary conditions. STRIP 1 and STRIP 2 are at the upper border.*

a situation of substantial symmetry with respect to STRIP 1 we pass to a situation in which the most, if not the totality, of the charge is collected by STRIP 1. This is true in particular for the less penetrating ions – 7.5 MeV ^{7}Li ion and 1 MeV proton – since for 3 MeV and 5 MeV protons the penetration depth is such that the lateral spread resulting from the longer path covered by the holes always allows the collection of an even small fraction of the charge by STRIP 2. But the peculiarity of positions C and B is the appearance of bipolar or positive signals which are the consequence of pure charge induction of carriers which are not ultimately collected by STRIP 2[2]. In no cases signals with the opposite polarity can be ascribed to

[2]Remember that the asymptotic value of the induced charge corresponds to the *actual* collected charge.

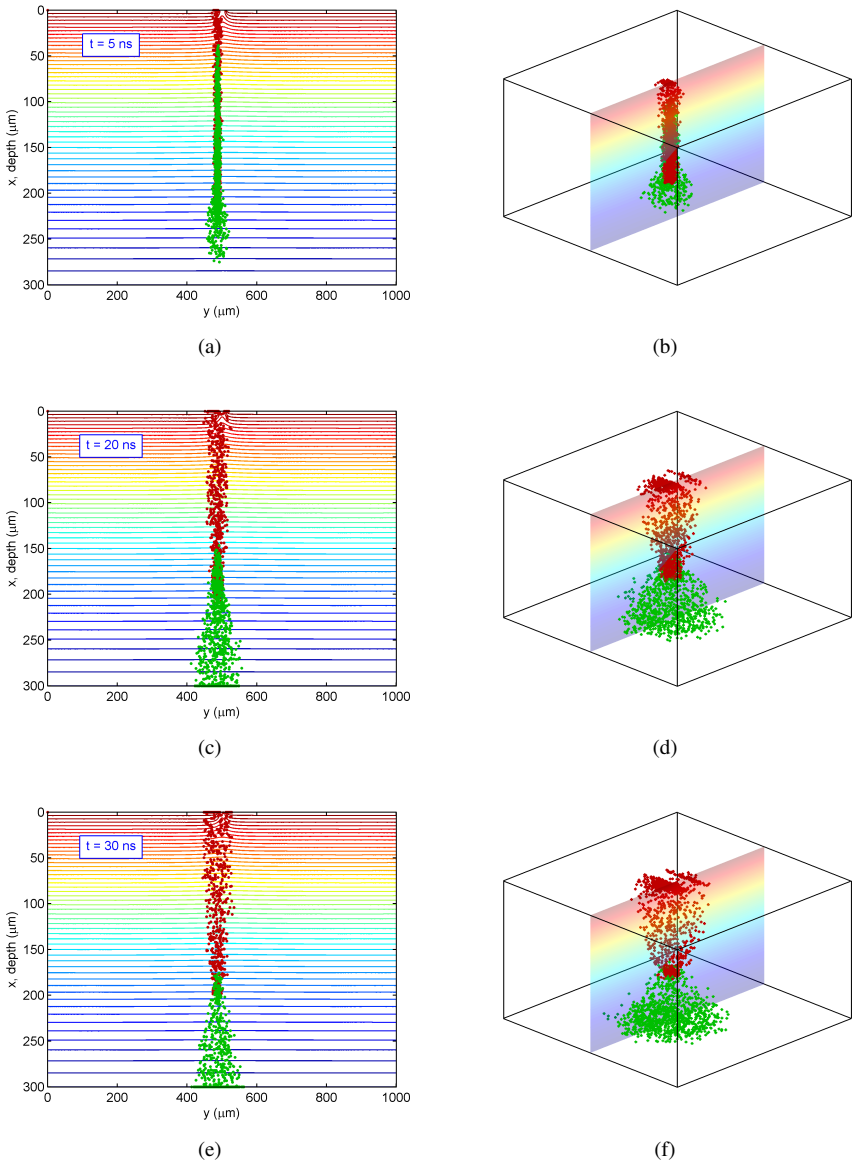

Figure 4.17

a p^+-strip collecting electrons. The shape of the induced bipolar or positive signals is due to the shape of the strips weighting field that in the proximity of the surface, underneath the inter-strip region, shown the steeper variations. That's why the short is the ion penetration depth, the larger are the induction effects. Looking at the value of the induced charge at the end of

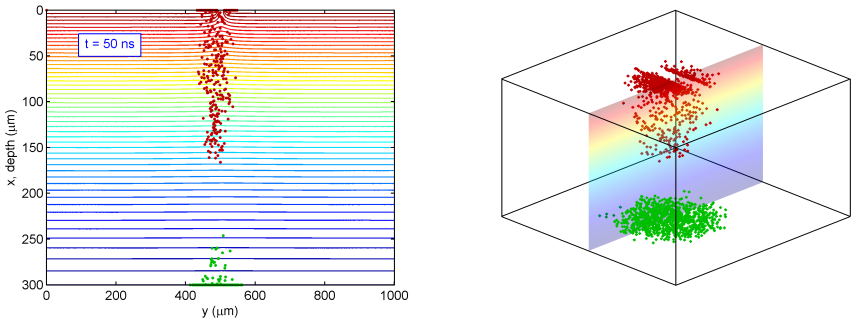

(a) (b)

Figure 4.17: *2D projections (left column) and 3D (right column) snapshots of the electrons-holes charge cloud within the detector volume for the 5 MeV ^{7}Li ion impinging at position* B *of the 300 μm DSSSD and at different times – t =5 ns, t =20 ns, t =30 ns and t =50 ns. Electrons are green while holes are red. The underlying potential is the static potential due to the boundary conditions. STRIP 1 and STRIP 2 are at the upper border.*

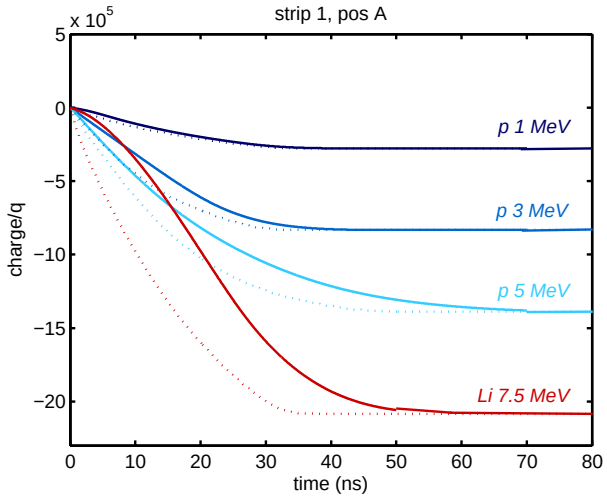

Figure 4.18: *Induced charge on STRIP 1 in case of position of incidence* A *(full strip) for all the considered ions and for the 300 μm case. Dotted lines differ from continuous lines for the omission of the Coulomb interaction computation in the simulations. The separation between the simulations with and without the Coulomb interaction computation increases due to plasma effects as the charge density increases (1 MeV proton to 7.5 MeV ^{7}Li ion).*

the transient, we can deduce that for bipolar signals we still have a partial charge collection, while for the positive ones we should expect a return to

zero. This is not the case for the 7.5 MeV ^{7}Li ion at position B because a small fraction of the electrons of the charge cloud "falls" into the potential well created below the inter-strip region and it is "lost" for the electrodes. This charge loss leads proportionally to the small offset visible for the 7.5 MeV ^{7}Li ion curve at the end of its transient. Lastly, it worths noticing that the depth of the potential well is deeply related to the boundary conditions imposed by the silicon dioxide layer.

In order to gain a better understanding on the mechanisms at the origin of the appearance of the bipolar and positive signals, it can be useful to visualize separately the contributions of electrons and holes to the total induced charge. Fig. 4.20 (a) and (b) show the induced charge of the 7.5 MeV ^{7}Li ion impinging on position B for STRIP 1 and STRIP 2 respectively. STRIP 1 always feels the holes coming closer (increasing weighting potential) and the electrons going further (decreasing weighting potential), so a negative net induced charge is summoned. On the contrary, STRIP 2 feels the holes moving away toward STRIP 1 (decreasing weighting potential) while the electrons coming closer for a little while and than correctly moving away (increasing and then decreasing weighting potential, see Fig. 4.13). This unbalance leads to the non-monotonic behavior of the net induced charge.

1500 μm DSSSD

Fig. 4.21 (a) to (h) report as an example four "snapshots" of the spatial distribution of the electron-hole cloud for the case of the 5 MeV proton impinging on position B taken at the times t =5 ns, t =10 ns, t =30 ns and t =70 ns.

Fig. 4.22 instead shows with continuous lines the induced charge on STRIP 1 for all the considered ions impinging on position A. Also in this case the total of the charge is collected by STRIP 1 and this serves as a reference signal. The dotted lines are the result of the same simulations but without taking into account the Coulomb interaction between the carriers. The smaller difference between the two kind of simulations here observed with respect to the 300 μm case for all the considered ions must be ascribed to the higher static electric field imposed by the biasing conditions which is strong enough to avoid significant plasma effects.

Fig. 4.23 (a) to (f) report the charge induced on STRIP 1 on the left column and STRIP 2 on the right column for all the considered ions impinging on position B, C and D on the first, second and third row, respectively. Considerations made for the 300 μm case holds also in this case, with few additional clarifications. Since the detector thickness is 1500 μm, now even the most penetrating ions under consideration (3 MeV and 5 MeV proton) can

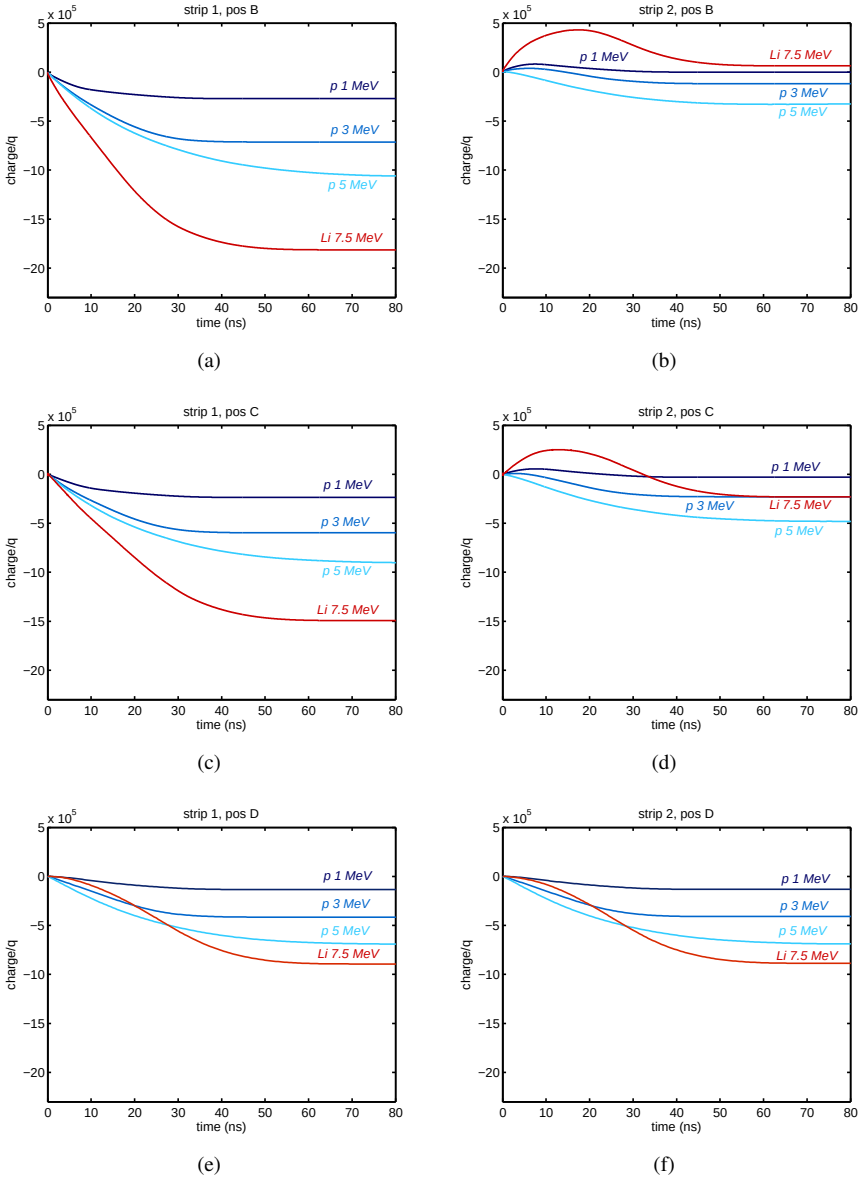

Figure 4.19: *Induced charge on STRIP 1 (left column) and STRIP 2 (right column) for all the considered ions and for the 300 μm DSSSD case, impinging on the positions* B *(border between STRIP 1 and the inter-strip region),* C *(a quarter of the distance between STRIP 1 and STRIP 2) and* D *(center of the inter-strip region).*

be considered absorbed relatively close to the surface. The strip weighting field, indeed, as clearly visible from the comparison of Fig. 4.13 (b) and

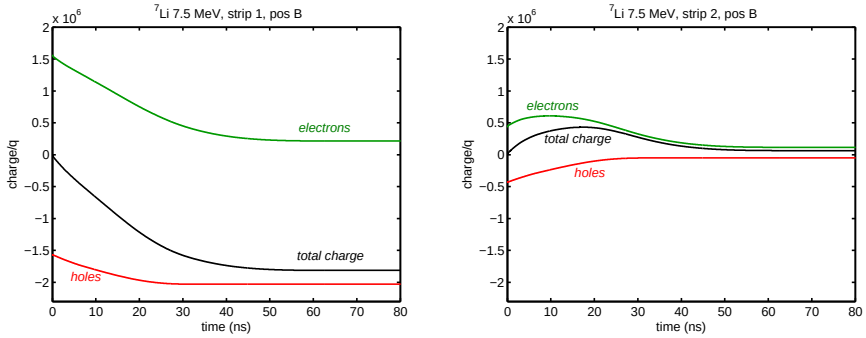

(a) (b)

Figure 4.20: *Induced charge on STRIP 1 (a) and on STRIP 2 (b) for the case of the 7.5 ^{7}Li ion impinging on position* B *in the 300 μm DSSSD. The total charge in separated in its basic holes and electrons contributions.*

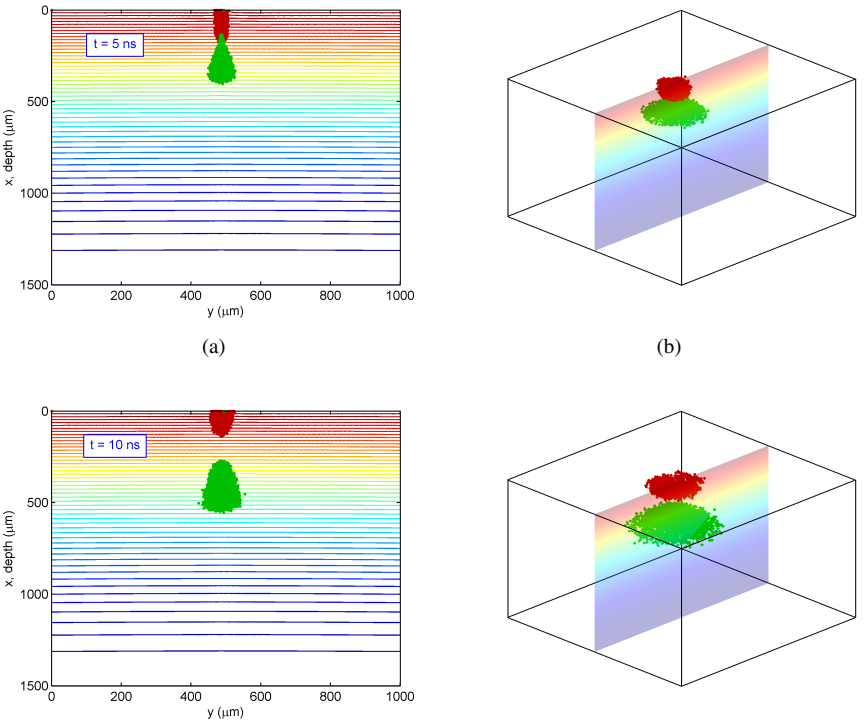

(a) (b)

(c) (d)

Figure 4.21

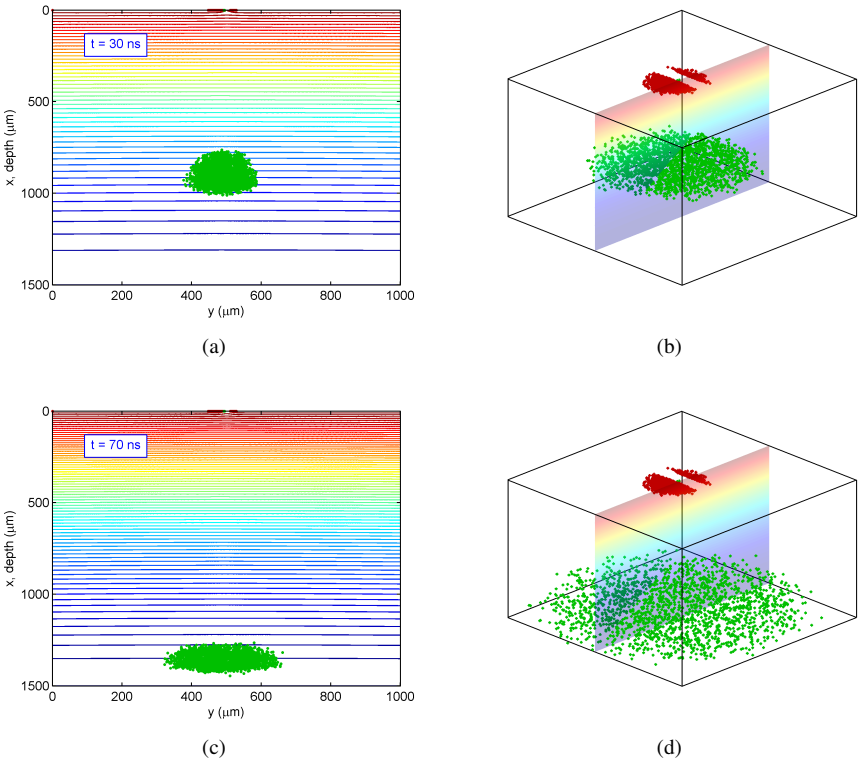

Figure 4.21: *2D projections (left column) and 3D (right column) snapshots of the electrons-holes charge cloud within the detector volume for the 5 MeV ^{7}Li ion impinging at position* B *of the 1500 μm DSSSD and at different times – t =5 ns, t =10 ns, t =30 ns and t =70 ns. Electrons are green while holes are red. The underlying potential is the static potential due to the boundary conditions. STRIP 1 and STRIP 2 are at the upper border.*

Fig. 4.14, is much more spatially spread and therefore induction effects are more pronounced and still effective even to a longer depth. Therefore, concerning the induced charge on STRIP 1 at impinging positions B and C, we notice that also for the 3 MeV and 5 MeV protons the signals slope at the beginning of the collection process is higher and for longer times is lower than the reference case A.

Concerning the induced charge on STRIP 2 at impinging positions B and C, the effect of the increased detector thickness is that bipolar and positive signals arise also for the 3 MeV and 5 MeV protons.

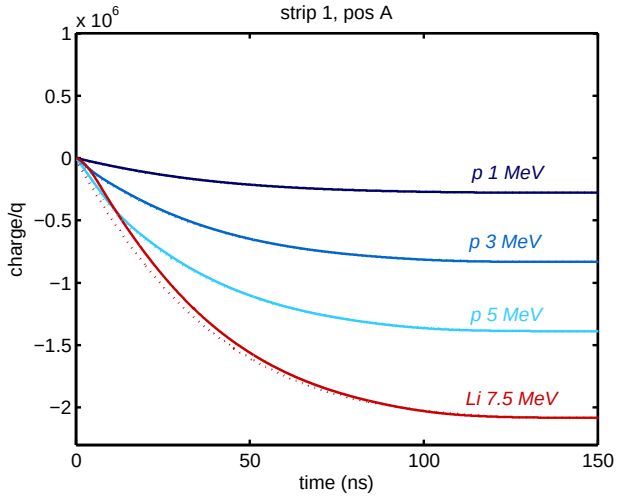

Figure 4.22: *Induced charge on STRIP 1 in case of position of incidence* A *(full strip) for all the considered ions and for the 1500 μm case. Dotted lines differ from continuous lines for the omission of the Coulomb interaction computation in the simulations. The separation between the two is extremely reduced in comparison with the 300 μm case since the static electric field due to the bias condition is now higher enough to avoid significant plasma effects.*

4.6.3 Comparison with Experimental Data

In order to assess the reliability of the simulations also from a quantitative point of view, we compared the simulation results with the experimental data presented in Subsection 3.3.5 (pag. 71). For the sake of clarity and without loosing any generality, in the following we present the comparison restricting the cases to the 3 MeV proton and to the 7.5 MeV ^{7}Li ion, since for our practical purposes they are representative of a "high" penetrating particle and of a "low" penetrating particle, respectively. Both the detector thicknesses are investigated. For all the considered cases, the comparison has been made between the digitized baseline subtracted raw waveforms at the output of the amplification chain pertaining to two neighbor strips of the front side and the induced charge signals resulting from the simulations convolved with the pulse response of the AAA amplifier, available in [34], and scaled by a suitable factor. We neglected the bandwidth limitation of the charge preamplifiers since it is large enough not to affect significantly the overall pulse response, actually limited by the AAA amplifier.

Fig. 4.25 (a) and (b) show the comparison between the simulated induced charges (continuous lines) and the digitized raw waveforms (dotted

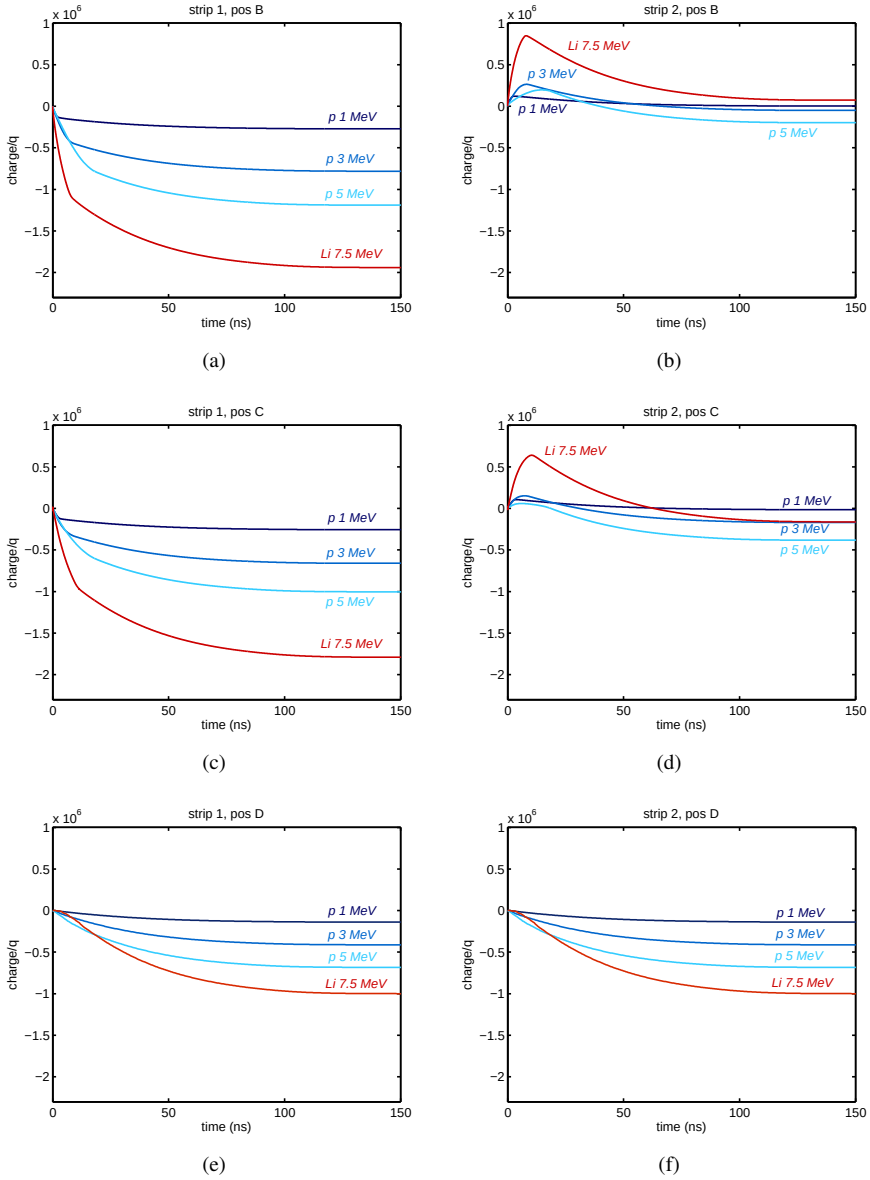

Figure 4.23: *Induced charge on STRIP 1 (left column) and STRIP 2 (right column) for all the considered ions and for the 1500 μm case, impinging on the positions* B *(border between STRIP 1 and the inter-strip region),* C *(a quarter of the distance between STRIP 1 and STRIP 2) and* D *(center of the inter-strip region).*

lines, each dot corresponding to a sample) in the case of a 3 MeV proton impinging on the front side inter-strip gap of the 300 μm DSSSD, for the two

neighbor strips STRIP 1 – corresponding to front strip n. 10 – and STRIP 2 – corresponding to front strip n. 11 – respectively. Signals represented within each graph pertain to the different simulated impinging positions A, B, C and D which correspond to the highlighted (estimated) locations α, β, γ and δ in the experimental *MAX+MIN* scatter plot of Fig. 4.24. The agreement between simulations and experimental data is clear at all impinging positions even if a sinusoidal disturbance sensibly spoils the measurements and prevent us from an accurate comparison.

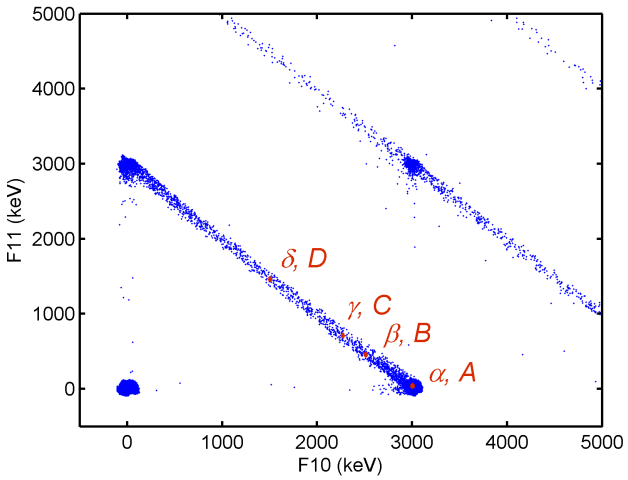

Figure 4.24: *Experimental MAX+MIN scatter plot for 3 MeV protons impinging on the 300 μm DSSSD between the front-side strips n. 10 and n. 11. The highlighted estimated locations α, β, γ and δ in the single-proton branch correspond to the simulated impinging positions* A, B, C *and* D.

Fig. 4.27 (a) and (b) show the comparison between the same entities for the 7.5 MeV ^{7}Li ion impinging on the front side inter-strip gap of the 300 μm DSSSD. The correspondence between the simulated impinging positions A, B, C and D and the experimental estimated locations α, β, γ and δ in the *MAX+MIN* scatter plot is shown in Fig. 4.26. Thanks to higher energy of the ^{7}Li ions with respect to the 3 MeV protons and to cleaner experimental conditions, the improved signal to noise ratio allows appreciating the excellent agreement between simulations and experimental data at all impinging positions. In particular, the great precision with which the transient edges – which retain all the information of the transport dynamics of electrons and holes – are reproduced confirms the reliability of the computational model and method despite the numerical difficulty posed by the significant presence of plasma effects. The small discrepancies in estimat-

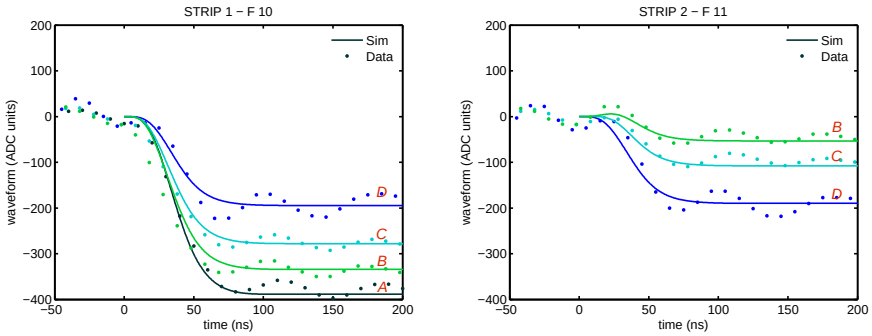

(a) (b)

Figure 4.25: *Comparison between the simulated induced charges (continuous lines) and the digitized raw waveforms (dotted lines, each dot corresponding to a sample) in the case of a 3 MeV proton impinging on the front side inter-strip region of the 300 μm DSSSD for STRIP 1-front strip n. 10 (a) and STRIP 2-front strip n. 11. Simulated results have been convolved with the pulse response of the AAA amplifier. Digitized waveforms have been baseline subtracted. The simulated impinging positions* A, B, C *and* D *correspond to the highlighted estimated locations α, β, γ and δ in the experimental scatter plot of Fig. 4.24.*

ing the values at the end of the integration phase for STRIP 2 at impinging positions B and C are linked to our lack of knowledge of the exact boundary conditions at the very edge of the strips, which depend both on the precise geometry of the transition between the p^+-implants and the insulating silicon dioxide and on the silicon dioxide electric properties which are likely modeled in a too naive way.

Fig. 4.29 (a) and (b) show the comparison between the same entities for the 3 MeV proton impinging on the front side inter-strip gap of the 1500 μm DSSSD. The correspondence between the simulated impinging positions A, B, C and D and the experimental estimated locations α, β, γ and δ in the *MAX+MIN* scatter plot is shown in Fig. 4.28. With respect to the 300 μm case, spurious disturbances are greatly reduced and the excellent agreement between simulations and measurements can be appreciated especially during the longer integration phase. The increased collection time is indeed due to the increased detector thickness that forces electrons to cover a longer path.

Fig. 4.31 (a) and (b) finally show the comparison between the same entities for the 7.5 MeV ^{7}Li ion impinging on the front side inter-strip gap of the 1500 μm DSSSD. The correspondence between the simulated impinging positions A, B, C and D and the experimental estimated locations α,

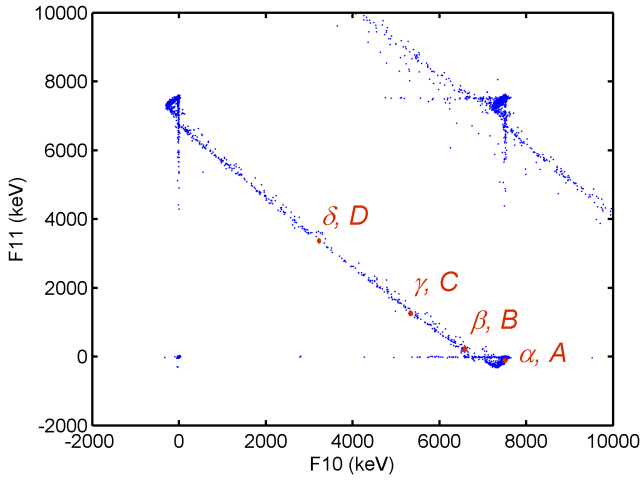

Figure 4.26: *Experimental MAX+MIN scatter plot for 7.5 MeV ^{7}Li ion impinging on the 300 μm DSSSD between the front-side strips n. 10 and n. 11. The highlighted estimated locations α, β, γ and δ in the single-ion branch correspond to the simulated impinging positions* A, B, C *and* D.

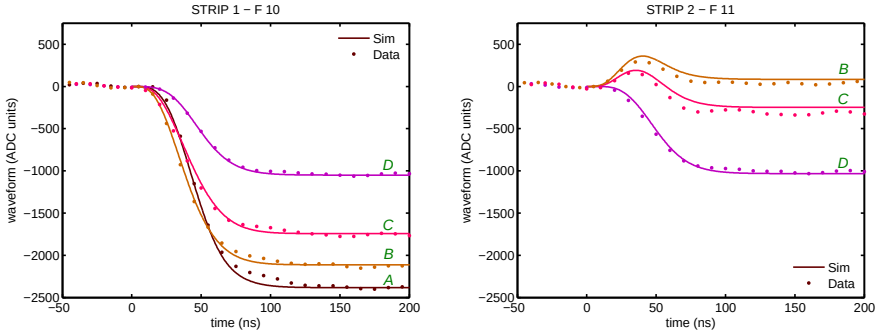

(a) (b)

Figure 4.27: *Comparison between the simulated induced charges (continuous lines) and the digitized raw waveforms (dotted lines, each dot corresponding to a sample) in the case of a 7.5 MeV ^{7}Li ion impinging on the front side inter-strip region of the 300 μm DSSSD for STRIP 1-front strip n. 10 (a) and STRIP 2-front strip n. 11. Simulated results have been convolved with the pulse response of the AAA amplifier. Digitized waveforms have been baseline subtracted. The simulated impinging positions* A, B, C *and* D *correspond to the highlighted estimated locations α, β, γ and δ in the experimental scatter plot of Fig. 4.26.*

β, γ and δ in the *MAX+MIN* scatter plot is shown in Fig. 4.30. Also in this case the agreement between simulations and measurements is excel-

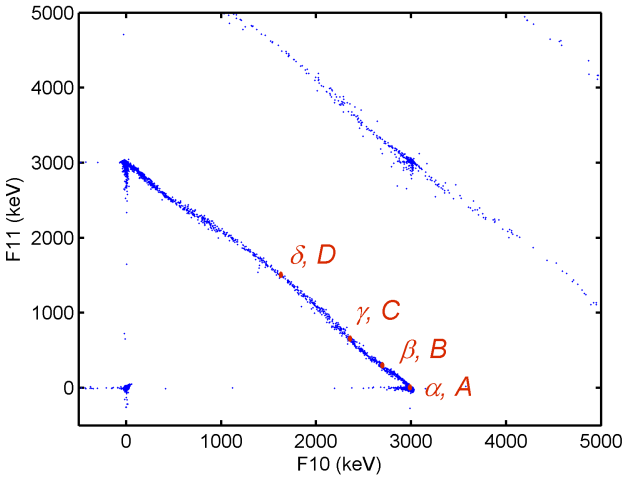

Figure 4.28: *Experimental MAX+MIN scatter plot for 3 MeV protons impinging on the 1500 μm DSSSD between the front-side strips n. 10 and n. 11. The highlighted estimated locations α, β, γ and δ in the single-proton branch correspond to the simulated impinging positions* A, B, C *and* D.

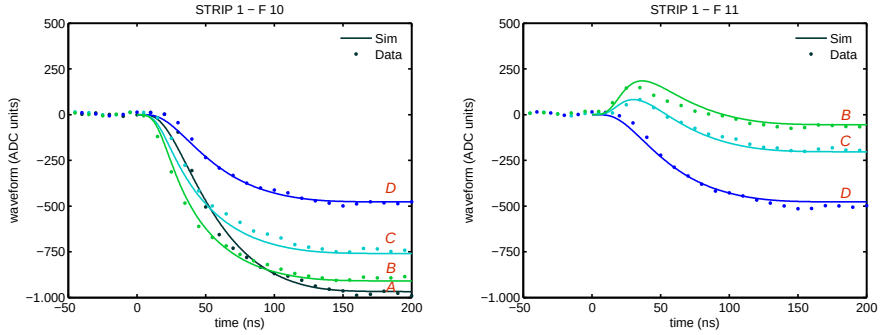

(a) (b)

Figure 4.29: *Comparison between the simulated induced charges (continuous lines) and the digitized raw waveforms (dotted lines, each dot corresponding to a sample) in the case of a 3 MeV proton impinging on the front side inter-strip region of the 1500 μm DSSSD for STRIP 1-front strip n. 10 (a) and STRIP 2-front strip n. 11. Simulated results have been convolved with the pulse response of the AAA amplifier. Digitized waveforms have been baseline subtracted. The simulated impinging positions* A, B, C *and* D *correspond to the highlighted estimated locations α, β, γ and δ in the experimental scatter plot of Fig. 4.28.*

lent. We ascribe the small discrepancies in the estimation of the values at the end of the integration phase for STRIP 2 at impinging positions B and

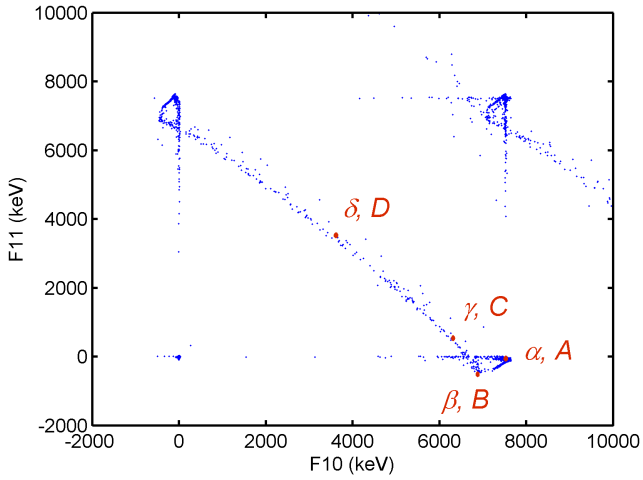

Figure 4.30: *Experimental MAX+MIN scatter plot for 7.5 MeV ^{7}Li ion impinging on the 1500 μm DSSSD between the front-side strips n. 10 and n. 11. The highlighted estimated locations α, β, γ and δ in the single-ion branch correspond to the simulated impinging positions* A, B, C *and* D.

C to the same consideration made for the 300 μm case.

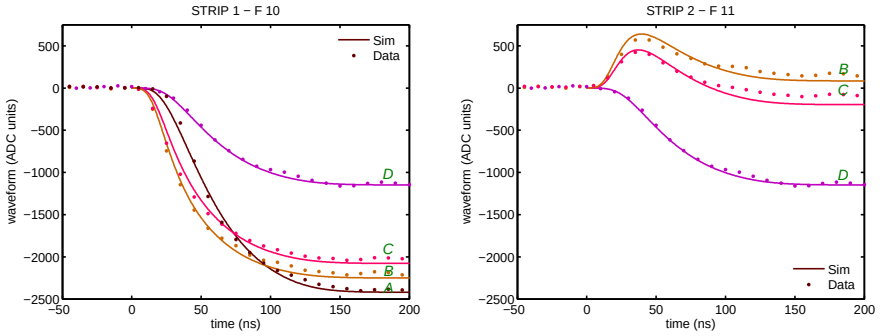

(a) (b)

Figure 4.31: *Comparison between the simulated induced charges (continuous lines) and the digitized raw waveforms (dotted lines, each dot corresponding to a sample) in the case of a 7.5 MeV ^{7}Li ion impinging on the front side inter-strip region of the 1500 μm DSSSD for STRIP 1-front strip n. 10 (a) and STRIP 2-front strip n. 11. Simulated results have been convolved with the pulse response of the AAA amplifier. Digitized waveforms have been baseline subtracted. The simulated impinging positions* A, B, C *and* D *correspond to the highlighted estimated locations α, β, γ and δ in the experimental scatter plot of Fig. 4.30.*

4.7 Conclusion

We developed a 3D simulation code for electron-hole transport and signal formation for fully-depleted semiconductor detectors with 2D geometry, aimed at accurately studying the response of segmented detectors to high density ionization tracks as in the case of FARCOS Double Sided Silicon Strip Detectors. Thermal diffusion and Coulomb interaction between the carriers have been included, preserving their full 3D nature. Carrier trajectories, induced currents and induced charges are computed by means of a microscopic approach, *i.e.* by superposing the contribution of every individual carrier. A set of simulations was carried out to test the code in basic conditions: the case of an expanding electrons cloud due to pure thermal diffusion or pure Coulomb repulsion, in an infinite volume or with finite detector thickness, for different time steps. We also reported the comparison with an analytical approximation in the case of an electron cloud in free expansion in presence of Coulomb repulsion and thermal diffusion. The effectiveness of a simple charge clustering technique and of the adaptive carrier position update (ACPU) algorithm for high charge levels have been evaluated by means of dedicated simulations of electrons clouds expanding in free space due to pure Coulomb repulsion. All results not only confirm the reliability of the code up to high charge levels, but also show the capability to access dynamic processes down to the ps time-scale without any increase of the computational time. Finally we computed the realistic case study of the space-time evolution of the electron-hole clouds resulting from a 1 MeV proton, 3 MeV proton, 5 MeV proton and a 7.5 MeV ^{7}Li ion impinging at different position in the inter-strip gap of the front side of the double sided silicon strip detectors of FARCOS. From the analysis of the induced charges on the two neighbor strips of the front side simulated we noticed non-negligible plasma effects at least for the detector with the lowest static electric field ($d = 300$ μm) and the appearance of bipolar and opposite polarity signals on one of the two strips when the ion is absorbed relatively close to the surface. The ultimate reason of such behavior has been found in the peculiar shape of the strips weighting potentials. Simulation results have also been compared with experimental data taken during the DSSSD response mapping campaign at INFN-LaBeC exposed in Section 3.3 (pag. 60) and the agreement between them is excellent.

CHAPTER 5

Extrapolation of CsI(Tl) Scintillation Parameters and Novel Particle Identification Techniques

5.1 Introduction

Caesium Iodide Thallium activated scintillators are the third and last detection layer of the FARCOS telescope and they are expected to absorb particles over a wide range of energy, mass and charge, due to their high stopping power. Exploiting the dependency of the scintillation decay on the ionization density of the absorbed particle, they are widely used for the identification of charged particles using pulse-shape discrimination techniques. It is well known indeed that the light output of the CsI(Tl) crystal can be modeled [69], [70] – at least in a given energy range – with a combination of two exponential functions with different time constants. Investigations on the dependence of the scintillation light on the particle type and energy have been carried out since the 1950s [71]. For *light charged particles* (LCPs), *i.e.* with Z$\leq$ 5, stopped in a CsI(Tl) scintillator, the charge comparison method – reported in [72] for Z=1 and Z=2 – allows isotopic

NOTE: The content of this chapter is partly based on the papers [67] and [68] coauthored by myself.

separation using the fast and the slow components of the CsI(Tl) signals.

In order to improve the commonly used identification techniques and to probe the merits of new ones, it would be beneficial to know the dependency of the scintillation time constants and of the intensities on the particle's ionization track over a wide energy range. A detailed study of the scintillation light pulse shape in CsI(Tl) at room temperature as a function of incoming photon energies in the 6-662 keV range is presented in [73]. However, the study has been performed in a dedicated laboratory setup by means of a delayed coincidence single photon counting method. This cannot be easily performed or could not even be possible in the case of heavy-ions interactions, produced in multi-fragmentation experiments where data have to be acquired during beam-time. References [74] and [75] investigate the response of CsI(Tl) scintillators – readout by PMTs – to light ions, intermediate mass fragments, and heavy ions over a large energy range using the INDRA array. In particular, they investigate the dependence of the luminescence and the quenching factor on the physics of the interaction at the microscopic level. However, for all the ions, they do not have access to the individual waveforms and derive the total light output from the fast and slow components, assuming a single exponential decay, without investigating the individual dependency of the two exponential functions on the particle charge, mass, and energy. Digital pulse shape acquisition [31] opens the possibility of transferring and storing the waveforms pertaining to each interaction in real-time beam experiments in order to perform further off-line analyses. A study of the CsI(Tl) scintillation characteristics in the case of heavy-ions interactions is presented in [76], although no account is taken of the dependence of the scintillation time constants and intensities on the particle energy. In our work, we directly investigate the dependence of the time constants and intensities of the CsI(Tl) scintillation light on the energy, charge, and mass of the impinging particle in the energy – deposited in the CsI(Tl) crystal – range 10-240 MeV for isotopes with Z$\leq$ 5 and also for ions with Z=6 with no isotopic dependence. The method relies on the direct fitting of digitized waveforms, and it is applied to a batch of waveforms measured with the CHIMERA multidetector at the INFN Laboratori Nazionali del Sud (Catania, Italy). Reference [77] presents a detailed discussion of the identification of light particles (up to Z=5) so far obtained with the CHIMERA CsI(Tl) scintillators using the *fast* and *slow* parameters computed with the *two-gate* method (see Section 1.4.1 pag. 15). The chapter is organized as follows. Section 5.2 illustrates the experimental setup and the model of the preamplifier output response to the light pulse coming from the CsI(Tl) scintillator. Section 5.3 deals with the

method used for the four-vector extraction and for the energy calibration while Section 5.4 investigates the dependence of the four-vector defining the scintillation light output on the particle charge, mass and energy. In Section 5.5 the conventional identification parameters are used as detection maps for particle identification and in Section 5.6 we probe the merits of novel Light Charged Particles identification techniques originated by applying the preceding analysis on a batch of CsI(Tl) signals coming from CHIMERA multidetector in the frame of the ASY-EOS experiment held at GSI (Darmstadt, Germany). It goes beyond the scope of this work to try to relate the identified dependences to the microscopic behavior of the particle interaction and energy release in the scintillator.

5.2 Experimental Setup and Modeling

The light output of the CsI(TI) crystal can be modeled [69], [70] – at least in a given energy range – with a combination of two exponential functions with different time constants:

$$L(t) = \frac{h_f}{\tau_f} e^{-t/\tau_f} + \frac{h_s}{\tau_s} e^{-t/\tau_s} \tag{5.1}$$

where $L(t)$ is the light pulse amplitude at time t, τ_f and τ_s are the decay time constants for the fast and slow components, respectively, and h_f and h_s are their intensities. Therefore, the light output can be fully defined by means of a four-vector (τ_f, τ_s, h_f, h_s). The ratio of the amplitudes of the two exponential pulses and the decay constants depends on the stopping power and therefore on the particle mass, charge, and energy.

In order to investigate the dependency of the four–vector on the particle mass, charge, and energy, we exploited the signals acquired in a experiment using the CHIMERA detector and beams delivered by the INFN-LNS Superconducting Cyclotron, Catania, Italy. Since the CHIMERA detector structure has been reviewed in Section 1.4.1 (pag. 15), we only add some informations about the digital data acquisition chain coupled to a small fraction of the detector units. The last subsection is devoted to the modeling of the output response of the preamplifier coupled to the photodiode detecting the light pulse given by 5.1.

5.2.1 The Digital Data Acquisition Chain of the CHIMERA Detector

Although the standard acquisition chain for CHIMERA is fully analogue, during several beam times the signals coming from a small fraction of the

detector units are split to feed also a dedicated digital acquisition chain. It has many similarities with the FARCOS digital DAQ described in Section 2.2.3 (pag. 35) and it works as follow.

The photodiode collects the scintillation light and produces a current output that feeds a large bandwidth high–dynamic range charge preamplifier [34]. The preamplifier output signal, whose shape retains the information of the original light output waveform, is first filtered by an anti-aliasing amplifier with adjustable bandwidth to fulfill the Nyquist requirement, then it is digitized by a 14 bit resolution ADC (*SIS9300*, Struck Innovative Systeme GmbH [78]) with selectable sampling frequency (100, 50, or 25 MS/s) to allow the proper time window choice. The *SIS9300* card is hosted on an *SIS3150* VME-board equipped with two ADSP-TS101S TigerSHARC digital signal processors (DSPs) and 64 MB SDRAM memory [79]. The on-board intelligence allows performing waveforms zero-suppression and on-line event parameter reconstruction [31]. The collection of the event parameters by means of digital pulse shape acquisition allowed us to obtain more precise results than in conventional acquisition with a fully analog readout chain. If desirable, the digitized waveforms – and not only the event parameters – are transferred to the host PC via the 1 Gb/s optical fiber and then stored, so that further off-line analyses are possible. The application of the digital pulse shape acquisition in several beam runs with different beam-target pairs made possible the assembly of a database of waveforms corresponding to the interaction of different ions in a wide energy range. This database is at the basis of the present work and represents a precious resource for the study and design of novel front-end electronics topologies and for the design and planning of novel experiments.

5.2.2 Model of the Preamplifier Output Signal

The current induced in the photodiode coupled to the scintillator shows a time dependence equal to that described by Eq. 5.1, assuming – as it is – a negligible collection time in the photodiode. This current signal is integrated by the charge preamplifier connected to the anode of the photodiode. The simplified schematics of the charge preamplifier is shown in Fig. 5.1 and the dynamic response is modeled as a two-pole low-pass filter. The pulse response can therefore be modeled as:

$$w(t) = -\frac{R_{feed}}{\tau_{feed} - \tau_a}\left(e^{-t/\tau_{feed}} - e^{-t/\tau_a}\right) \tag{5.2}$$

where τ_{feed} is the decay time constant of the feedback network, τ_a is the

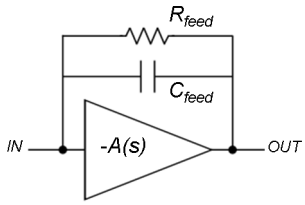

Figure 5.1: *Simplified schematics of the charge preamplifier.*

time constant of the closed loop pole introduced by the bandwidth limitation of the amplifier itself, and R_{feed} is the feedback resistance.

Neglecting the collection time in the photodiode, the preamplifier output signal is given by the convolution of the preamplifier pulse response, given by Eq. 5.2 with the induced current signal. The resulting waveform is the sum of two terms, one related to the fast component of the scintillation light and the other to the slow one:

$$V_{fit}(t) = V_{fast}(t) + V_{slow}(t) \tag{5.3}$$

where

$$\begin{aligned}
V_{fast}(t) &= -h_f R_{feed}\left(\frac{A}{\tau_f}e^{-t/\tau_f} + \frac{B}{\tau_{feed}}e^{-t/\tau_{feed}} + \frac{C}{\tau_a}e^{-t/\tau_a}\right) \\
V_{slow}(t) &= -h_s R_{feed}\left(\frac{D}{\tau_s}e^{-t/\tau_s} + \frac{E}{\tau_{feed}}e^{-t/\tau_{feed}} + \frac{F}{\tau_a}e^{-t/\tau_a}\right) \\
A &= \frac{-\tau_f^2}{\tau_a\tau_f - \tau_a\tau_{feed} + \tau_f\tau_{feed} - \tau_f^2} \\
B &= \frac{\tau_{feed}^2}{\tau_a\tau_f - \tau_a\tau_{feed} - \tau_f\tau_{feed} + \tau_{feed}^2} \\
C &= \frac{-\tau_a^2}{\tau_a\tau_f + \tau_a\tau_{feed} + \tau_f\tau_{feed} - \tau_a^2} \\
D &= \frac{-\tau_s^2}{\tau_a\tau_s - \tau_a\tau_{feed} + \tau_s\tau_{feed} - \tau_s^2} \\
E &= \frac{\tau_{feed}^2}{\tau_a\tau_s - \tau_a\tau_{feed} - \tau_s\tau_{feed} + \tau_{feed}^2} \\
F &= \frac{-\tau_a^2}{\tau_a\tau_s + \tau_a\tau_{feed} - \tau_s\tau_{feed} - \tau_a^2}
\end{aligned} \tag{5.4}$$

5.3 Four-Vector Extraction and Energy Calibration

The four-vector extraction has been applied to a batch of 50371 waveforms (2048 samples per waveform, sampling frequency 100 MS/s) acquired when a 21.5 MeV/u ^{20}Ne beam was impinging on a thin ^{12}C target. Data were collected by a telescope placed at polar angle θ=12.3° in the forward part of the multidetector.

5.3.1 Adopted Analysis Method for the Four–Vector Extraction

Fig. 5.2 shows the flowchart of the adopted analysis method. The first step is the selection of the waveforms pertaining to a specific isotope. We compute the conventional $\Delta E - E$ identification matrix, scatter-plotting the maximum of the waveform with respect to its baseline, both for the waveforms coming from the silicon detector and from the scintillator crystal, respectively, as shown in Fig. 5.3 (in MeV versus ADC units) for a selected range of signal amplitudes and energies for better visibility.

With the aid of a custom-developed graphical interface, we can select the branch of the scatter plot pertaining to a specific isotope. In Fig. 5.3, the dotted lines highlight the cluster related to ^{6}Li events. The corresponding CsI(Tl) waveforms are retrieved and stored separately. The procedure is repeated for all the identified isotopes.

Each CsI(Tl) waveform is baseline subtracted by fitting the samples occurring before the trigger time instant with a degree 1 polynomial function. This procedure allows a proper signal restoring, especially at typical low-rates when pile-up is not an issue.

The waveforms are then fitted, according to 5.3. The free parameters are the four-vector (τ_f, τ_s, h_f, h_s) and the delay time t_{del} (not included in 5.3 for the sake of simplicity), which is not well known *a priori*. The parameters kept constant are τ_{feed} =31 μs, τ_a=20 ns and R_{feed} =100 MΩ.

The fitting algorithm is a nonlinear least-square one based on the trust-region approach [80]. The basic idea underlying this method is to approximate the functional to be minimized with a simpler functional (normally the first two terms of the Taylor expansion), which reasonably reflects the behavior of the functional to be minimized in a neighborhood around the point. This neighborhood is the trust region that in the present case is restricted to a two-dimensional subspace [81].

In order to avoid numerical issues in the fitting algorithm, it is advisable to multiply the waveforms by a suitable factor. In the present work – taking into account the ranges of the parameters – the multiplying factor is 10^6. In addition, the fitting parameters are constrained over a wide range to fulfill

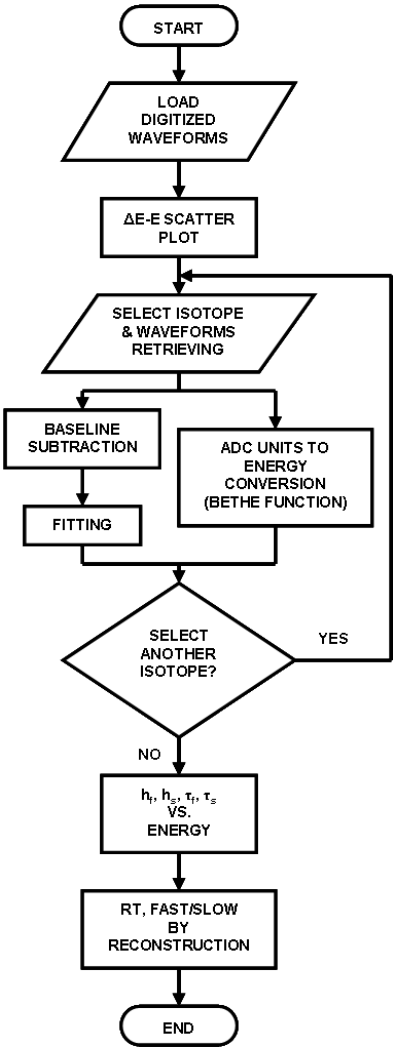

Figure 5.2: *Flowchart of the adopted analysis method for the determination of the CsI(Tl) scintillation time constants and intensities by direct fitting of the digitized waveforms.*

the requirement of the fast time constant being faster than the slow time constant. The applied constraints – on the unmodified parameters – are the following:

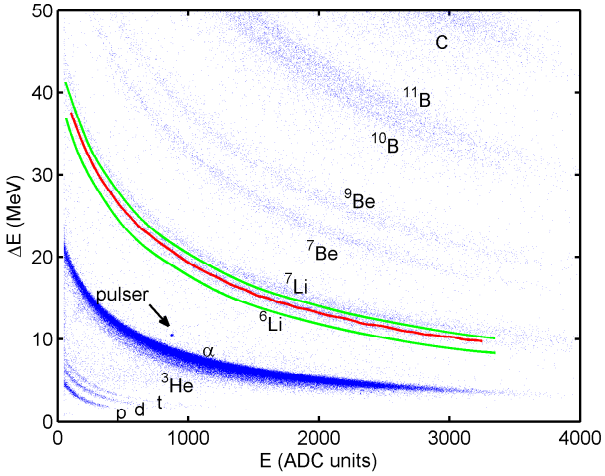

Figure 5.3: *$\Delta E - E$ identification matrix with the indication in green lines of the cluster relative to ^6Li events. The red line shows the spline interpolation for the same isotope, used in the energy calibration procedure (see Subsection 5.3.2).*

$$\begin{aligned} 10^{-10} < h_f < 10^2 \\ 10^{-12} < h_s < 10^2 \\ 50\,ns < \tau_f < 5\,\mu s \\ 500\,ns < \tau_s < 10\,\mu s \end{aligned} \tag{5.5}$$

The developed code relies on Matlab. The mutual independence of the analysis made on the waveforms allows exploiting parallel algorithms which significantly increase the computational speed. In our analysis, we used a cluster of two quad-core machines, each equipped with an *Intel* Core i5 CPU 750 operating at 2.67 GHz. The estimated computational time is about 48 ms to fit a single signal for each of the eight workers, plus the time needed to load the input file. Fig. 5.4 shows the waveform pertaining to a Li ion impinging on the scintillator with energy of 100 MeV together with the result of the fitting procedure. The contribution of the fast light output and of the slow light output computed with 5.3 using the results of the fitting are also shown. A final check allows rejecting the results of the fitting if the error between the normalized noisy original signal and the waveform reconstructed from the fitted parameters exceeds a given threshold. Table 5.1 lists the number of waveforms used for the fitting algorithm for every isotope, and the number and percentage of the discarded waveforms after fitting.

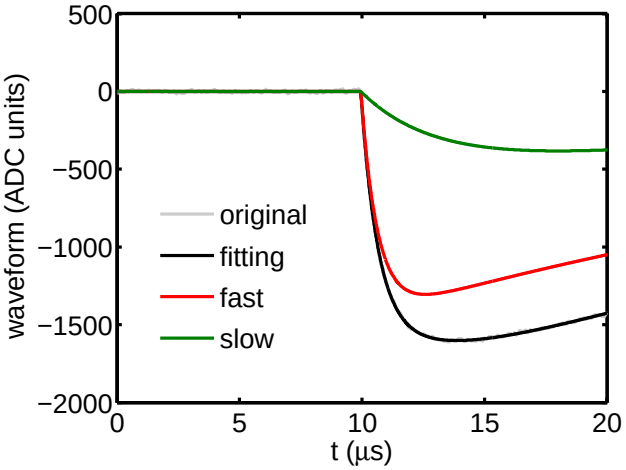

Figure 5.4: *Result of the fitting procedure in the case of a waveform pertaining to a ^6Li ion impinging on the scintillator with energy of 100 MeV. Only a portion of the digitized waveform is shown in figure for sake of visibility.*

Table 5.1: *Number of waveforms fitted per isotope and number and percentage of discarded waveforms after fitting.*

Isotope	Fitted waveforms	Discarded after fitting	% of discarded
p	6276	988	16
d	1977	401	20
t	664	130	20
^3He	7000	602	9
α	7000	437	6
^6Li	4163	260	6
^7Li	2791	388	14
^7Be	2147	180	8
^9Be	1970	155	8
^{10}B	4671	369	8
^{11}B	4712	380	8
C	7000	505	7

5.3.2 Energy Calibration

A further step is the energy calibration of the amplitude of the CsI(Tl) waveforms. Since the light production within the scintillator depends not only on the energy of the incident particle but also on its charge and mass [69], the calibration must be performed isotope by isotope.

The energy calibration for the silicon detector relies on the knowledge of the preamplifier gain. The consistency of the results is validated with

the punch-through energies calculated separately for the different ions and with the position of the cluster due to the elastic scattering of the incident beam. In this way, the $\Delta E - E$ matrix shown in Fig. 5.3 is plotted in MeV versus ADC units, and we select the branch that corresponds to a given ion (highlighted with dotted lines for the case of ^{6}Li ions). We re-bin the E axis (in ADC units) and compute the average ΔE value for each bin. The width of the bin is chosen as a compromise between the required accuracy and the available statistics. A spline interpolation of the (E, ΔE) pairs provides the relationship of the energy loss ΔE in the silicon detector (in MeV) with the energy E (in ADC units) deposited in the scintillator. The gray line in Fig. 5.3 shows the spline interpolation for the ^{6}Li isotope.

We choose a representative set of points onto the spline and compute the total kinetic energy of the particle, by integration of the Bethe formula [8] with an iterative algorithm known the (nominal) thickness of the Si detector. The calculation has been made under the assumption of a constant mean excitation potential inside the Bethe formula, according to the values of [82]. The energy of the ion impinging on the CsI(Tl) (*i.e.*, the energy released in the scintillator under the assumption of full absorption) is obtained by subtracting the energy deposited in the Si detector from the total kinetic energy obtained by the integration of the Bethe formula. Fig. 5.5(a) shows the CsI(Tl) output pulse height as a function of the energies computed according to the procedure described above. The fit of the calculated points with the nonlinear function [83]:

$$L(E) = \gamma E + \beta(e^{-\alpha E} - 1) \tag{5.6}$$

where α, β and γ are free fitting parameters that depend on the isotope atomic and mass numbers, provides the calibration curve CsI(Tl)-pulse height versus energy. The fitting curves are shown in Fig. 5.5(a) with solid lines. For the sake of visibility, Fig. 5.5(b) shows a zoom for ions with Z$\leq$ 2. According to [84], 5.6 seems to offer the most satisfactory results in the considered energy range. Table 5.2 reports the fitting parameters of 5.6 for all the identified isotopes.

5.4 Four-Vector Dependence on the Energy and on the Particle Type

Knowledge of the four-vector extracted with the fitting procedure allows reconstructing the light output pulse for each impinging ion. Fig. 5.6 shows the light output pulse produced by an α particle and a ^{6}Li ion impinging

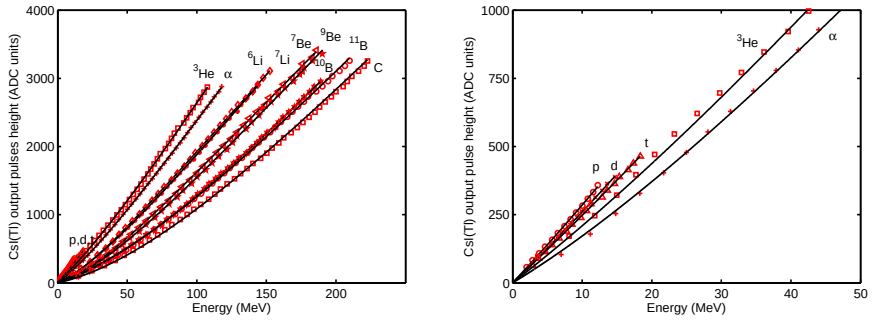

(a) (b)

Figure 5.5: *(a) Scintillator output pulse amplitude for the different isotopes as a function of the energies computed according to the procedure discussed in Section 5.3.2. The lines are the fits of the calculated points with the nonlinear function given by 5.6. (b) Same as (a) only for isotopes with Z$\leq$ 2 on a magnified scale.*

Table 5.2: *Fitting coefficients for the energy calibration*

Isotope	α $(ADCunits \cdot MeV^{-1})$	β $(ADCunits)$	γ (MeV^{-1})
p	$2.18 \cdot 10^{-2}$	576	39.8
d	$2.98 \cdot 10^{-2}$	348	34.9
t	$2.09 \cdot 10^{-2}$	364	31.6
^3He	$1.98 \cdot 10^{-2}$	586	31.4
α	$3.12 \cdot 10^{-2}$	386	27.5
^6Li	$4.21 \cdot 10^{-2}$	352	22.6
^7Li	$2.81 \cdot 10^{-2}$	496	23.4
^7Be	$3.08 \cdot 10^{-2}$	484	20.8
^9Be	$2.35 \cdot 10^{-2}$	638	21.2
^{10}B	$1.38 \cdot 10^{-2}$	1090	20.9
^{11}B	$1.12 \cdot 10^{-2}$	1280	21.2
C	$1.09 \cdot 10^{-2}$	1510	20.8

on the scintillator at an energy of 100 MeV. The difference of the time constants hidden in the waveforms is evident.

Fig. 5.7 shows the four-vector components (τ_f, τ_s, h_f, h_s) obtained from the fit of the waveforms pertaining to all the identified isotopes as a function of energy. For the sake of visibility for the time constants, we represent in the figures the average value of the distribution with continuous lines. The error bars indicate the $\pm\sigma$ confidentiality level of the distribution. The values of the fast time constant (τ_f) range from 500 ns to 1 μs at maximum. For a given energy of the incident particle, the fast time constant decreases with the increase of the atomic number, and for a given atomic number, de-

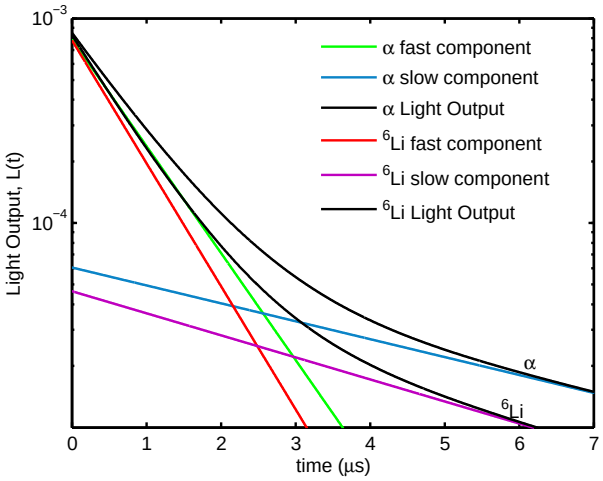

Figure 5.6: *Light Output $L(t)$ corresponding to an α particle and a ^{6}Li ion impinging on the scintillator at energy of 100 MeV, computed exploiting the result of the fitting procedure described in 5.3.1.*

creases with the increase of the mass number. For a given isotope, the sensitivity to the particle energy of the fast time constant smoothly decreases as energy increases. The fast time constants for Z>4 collapse into a single cluster and also the dependence on the particle energy becomes even less evident as the atomic number increases. A similar behavior is observed for the slow time constant (τ_s) ranging from 1 μs to 6 μs at maximum; however, the separation of the clusters pertaining to different isotopes is less evident. The intensities of the fast and slow components show a marked dependence both on the energy and on the particle type (charge and mass). Good separation is achieved even for heavier ions (at least up to Z=6) and isotopic dependence appears up to Z=5. The intensities of the fast and slow components increase more than linearly with energy and the nonlinear dependence becomes more pronounced as the atomic number increases. The behavior of the intensity of the fast component for Z=1 is remarkable, which shows no isotopic dependence as a function of the energy and is nearly overlapped to the cluster of the intensities of the fast component of ^{3}He at low energies.

It is relevant to note that if we scatter plot the intensities of the slow component multiplied by the atomic number of the considered particle (as shown in Fig. 5.8(b)) all the curves coalesce in a single curve, thus demonstrating the inverse proportionality of h_s with the particle charge. The dependence of h_f with the particle charge is less evident. The scatter plot of the intensities of the fast component multiplied by the square root of the

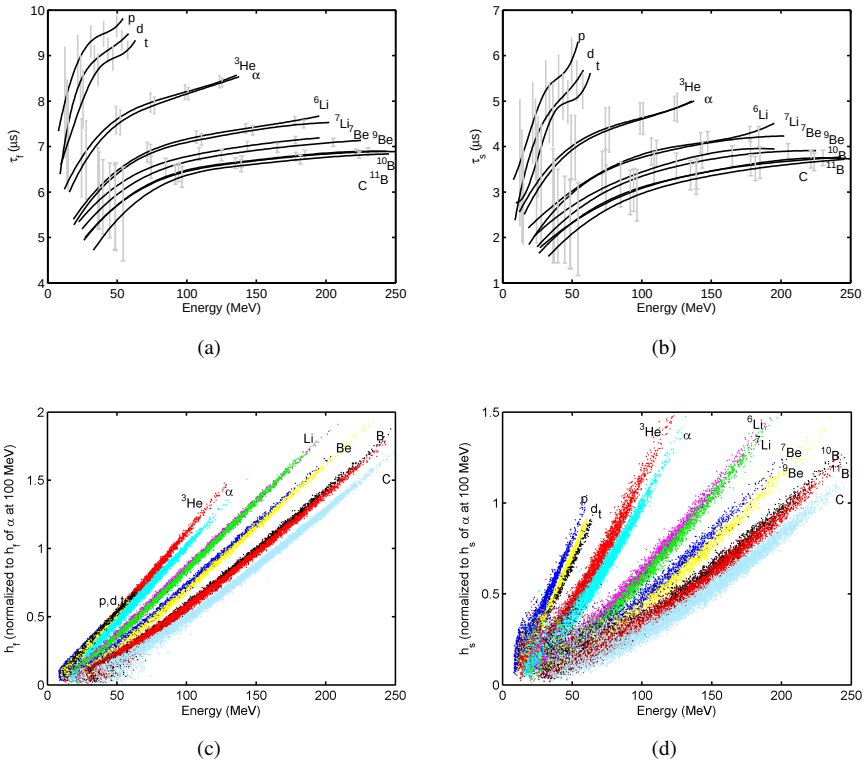

Figure 5.7: *Four-vector components (τ_f, τ_s, h_f, h_s) obtained from the fit of the waveforms pertaining to all the identified isotopes as a function of energy. (a) Fast component time constant τ_f. The continuous lines indicate the average value of the distribution. The error bars indicate the $\pm\sigma$ confidentiality level of the distribution. (b) Slow component time constant τ_s. The continuous lines indicate the average value of the distribution. The error bars indicate the $\pm\sigma$ confidentiality level of the distribution. (c) Fast component intensity h_f normalized to the fast component intensity of an α particle impinging with an energy of 100 MeV. (d) Slow component intensity h_s normalized to the slow component intensity of an α particle impinging with an energy of 100 MeV.*

atomic number of the considered particle (as shown in Fig. 5.8(a)) shows a single broad band, thus indicating a dependence of h_f with the inverse of the square root of the particle charge.

In order to gain a better insight in the intensity balance between the fast and slow component in CsI(Tl) and on their dependence on the particle energy, mass, and charge, we plotted in Fig. 5.9 the relative intensity of the fast and slow components with respect to the total light output intensity (sum of the two intensities) as a function of the particle energy per nucleon

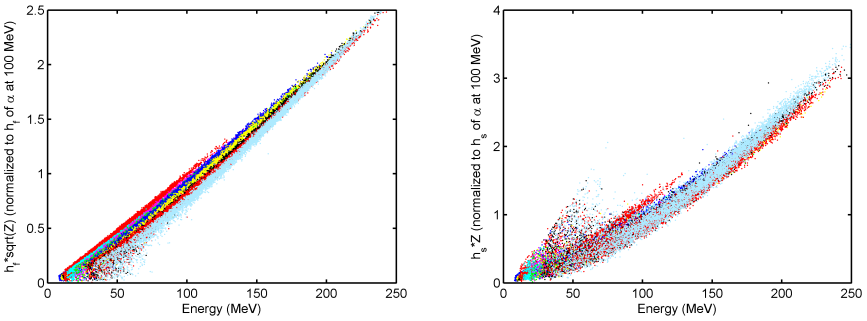

(a) (b)

Figure 5.8: *(a) Fast component intensity h_f (normalized to the fast component intensity of an α particle impinging with an energy of 100 MeV) multiplied by the square root of the atomic number as a function of energy. (b) Slow component intensity h_s (normalized to the slow component intensity of an α particle impinging with an energy of 100 MeV) multiplied by the atomic number as a function of energy.*

(*i.e.*, particle energy normalized to the mass number). The represented values are the averages obtained on the whole data set. As it is readily seen from the figure, there is no isotopic dependence both for the fast and the slow relative intensities as a function of the energy per nucleon. The separation of the branches of ^{3}He and α particles is an artifact that arises from the presence of waveforms pertaining to the tail of the high-statistics α particle cluster that hides in the ^{3}He cluster in the $\Delta E - E$ scatter plot that are wrongly attributed to ^{3}He. To these events, we attribute a wrong energy per nucleon, thus altering the statistics and the extraction of the average intensities of the fast and slow components. From Fig. 5.9, we can conclude that the dependence of the relative intensities is on the velocity of the impinging particle and not on its energy and mass independently. In addition, at a given energy per nucleon, the relative intensity of the fast (slow) component increases (decreases) with the increase in the atomic number.

Fig. 5.10 shows the behavior of the relative intensity of the fast and slow components as a function of the atomic number for two different values of the particle energy per nucleon. The two values (10 MeV/u and 20 MeV/u) have been chosen to have sufficient statistics for all the identified isotopes. The relative intensity of the fast (slow) component tends to increase (decrease) at increasing charge levels. It is relevant to notice that for charge levels above Z=3, the relative intensities tends to saturate to a value independent of Z. In addition, the difference in the relative intensity for the two values of energy per nucleon tends to decrease as the charge level increases.

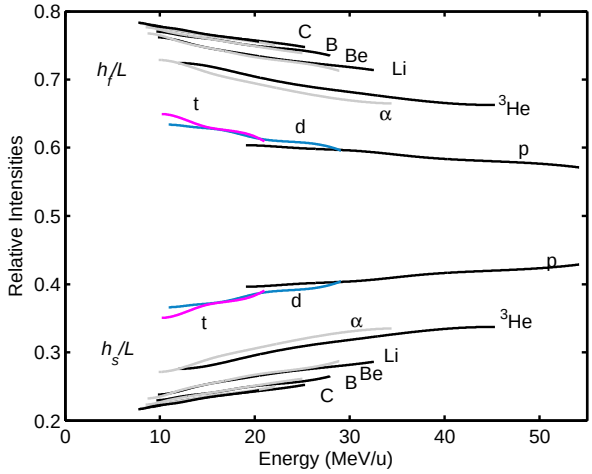

Figure 5.9: *Relative intensities of the fast and slow component with respect to the total light output intensity (sum of the two intensities) as a function of the particle energy per nucleon (in MeV/u) for the different particles. For each atomic number Z> 1, the lighter isotope is indicated with a black line and the heavier one with a gray line.*

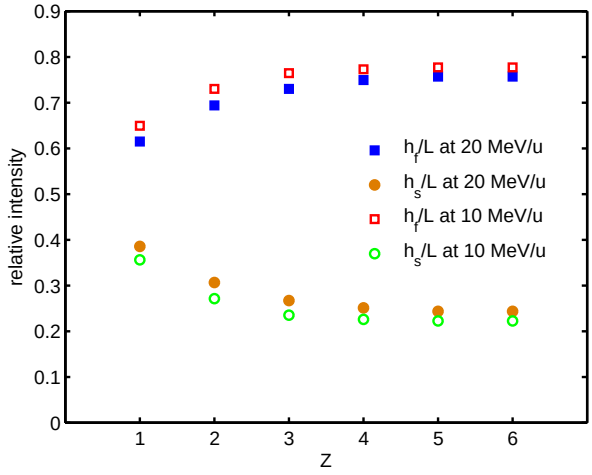

Figure 5.10: *Relative intensities of the fast and slow component with respect to the total light output intensity (sum of the two intensities) as a function of the particle charge for two values of the energy per nucleon (10 MeV/u, 20 MeV/u).*

We also found that, for a given isotope, the ratio of the intensities of the fast and slow components slowly decreases as energy increases. Due to the (direct) dependence of the stopping power on the impinging particle charge

and the (inverse) dependence on the particle velocity [8] – that, at a given energy, translates in a (direct) dependence on the impinging particle mass – it turns out that, at a given particle energy, the fast component of the light output dominates for large values of the stopping power.

5.5 Reconstruction of Conventional 2D Detection Maps

The joint knowledge of the four-vector defining the light output for each particle and of the particle energy allows the reconstruction of different detection maps for particle identification, in addition to the well known *fast/slow* scatter plot [70]. The conventional *fast* and *slow* components, respectively, computed as the value of the preamplifier output (reconstructed with the parameters obtained by the waveform fitting) at T=600 ns and the difference of the values of the reconstructed preamplifier output at $T_{s,1}$ =900 ns and $T_{s,2}$ =6 μs are scatter plotted in Figs. 5.11 (a) and (b) as a function of the particle energy. Owing to the behavior of the intensity of the fast component as a function of energy, also in the detection map of the fast component against the energy, the clusters of protons, deuterons, and tritons coalesce in a single broadband that is nearly overlapped to the ones of ^{3}He and α. From an experimental point of view, this fact allows calibrating the fast component for protons and extending the obtained calibration also to deuterons and tritons. In addition, both in the detection map of the fast component and of the slow component, the band assigned to ^{3}He splits into two bands. The less sloping branch refers to the α particle events that in the $\Delta E - E$ scatter plot are located in the tail of the α particles cluster that overlaps with the one of ^{3}He and therefore wrongly attributed to the batch of waveforms of ^{3}He and calibrated with the calibration curve of ^{3}He instead of α particles. The difference in the pairs of intensity and time constant of the fast and slow components for ^{3}He and for α particles highlights the wrong attribution and causes the splitting shown most clearly in Fig. 5.11(b).

The identification capability of the detection map of the slow component against energy is much better than the one of the fast component, and isotopic separation is possible for Z up to 5 and with very low energy threshold. Fig. 5.12 shows the 10%–90% rise time of the reconstructed preamplifier output pulses as a function of the particle energy. This is an additional identification plot that takes advantage of the dependence on the particle type mainly of the fast time constant and allows very good isotopic separation for low Z elements. The cause of the ^{3}He splitting is the same discussed above.

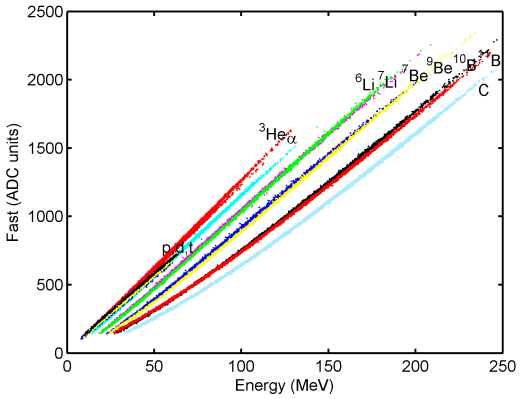

(a)

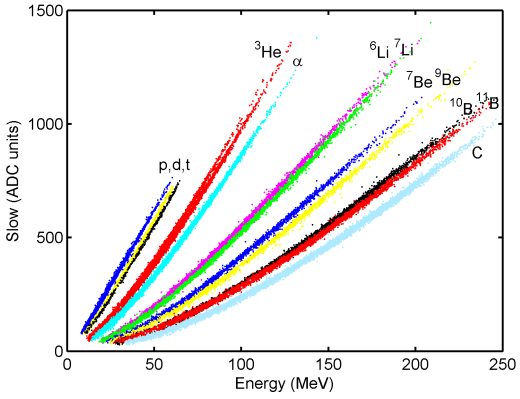

(b)

Figure 5.11: *(a) Fast component, computed as the value of the reconstructed preamplifier output at $T = 600$ ns, as a function of the particle energy for the different particles. (b) Slow component, computed as the difference of the values of the reconstructed preamplifier output at $T_{s,1} = 900$ ns and $T_{s,2} = 6$ μs, as a function of the particle energy for the different particles.*

5.6 Search for Novel 2D Detection Maps

The search for different identification plots for particle identification – especially at relativistic energies – prompted us to investigate the dependence of the pulse rise-time on the pulse amplitude and its relationship with the fast and slow components. The choice of the pulse rise-time as possible event parameter is suggested by the Pausch technique [85] performed for particles stopping in the silicon layer, since the decay constant associated with

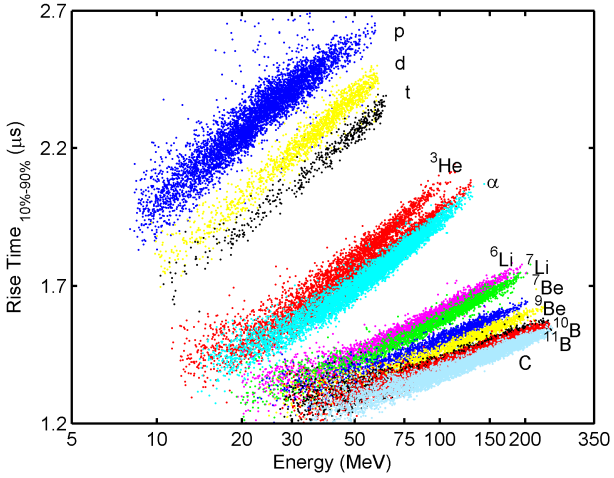

Figure 5.12: *Reconstructed preamplifier output pulse 10% - 90% rise-time as a function of the particle energy for the different particles.*

the fast component depends [86] on the ionization density for ion charges of Z$\leq$ 4, $\tau_f \sim (dE/dx)^{-1} = f(E, Z, A)$.

5.6.1 Approximated Analytical Model for Fast/Slow and Rise–Time Correlation

Due to the transcendental dependence of the preamplifier output on time shown in 5.1, it is not possible to find a closed expression for the pulse rise time as a function of the light output. However, some approximations are possible that highlight the relationship between the pulse rise time, the fast and slow components and the pulse height.

If we consider only the fast light output in 5.1 and compute it for the two time values defining the pulse rise time, the rise time RT_{fast} is given by:

$$RT_{fast} = \tau_f \log\left(\frac{1-a}{1-b}\right) \tag{5.7}$$

where a and b are the two fractions of the pulse amplitude considered for the rise time computation. Taking into account the dependence of the fast time constant on the energy and on the fragment charge and mass, we computed the RT_{fast}. As illustrated in Fig. 5.13, in the case of the 30% 70% rise time (*i.e.* $a = 0.3$ and $b = 0.7$), for protons and ^{6}Li ions, the difference between the rise time and the so-called RT_{fast} is not negligible

but the two rise times can be assumed to be proportional with a coefficient nearly constant over a wide energy range.

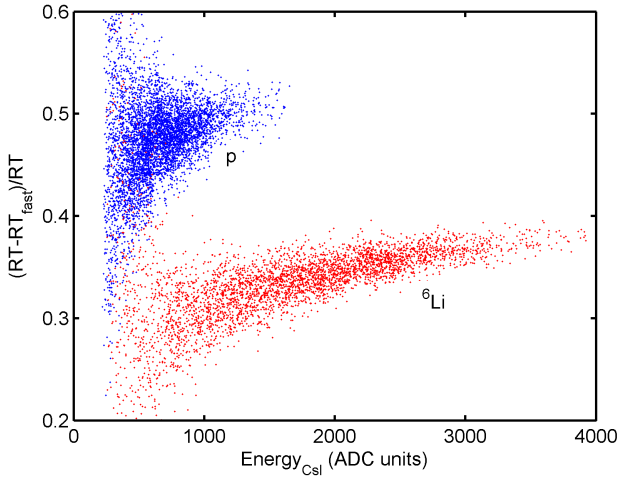

Figure 5.13: *Relative variation of the pulse rise time and of the rise time computed taking into account only the fast light output RT_{fast} as a function of the pulse amplitude for protons and ^{6}Li ions.*

In addition we can compute the fast and slow components as due respectively only to the fast light output $Fast_{fast}$ and to the slow light output $Slow_{slow}$:

$$\begin{aligned} Fast_{fast} &= h_f \left(1 - e^{-T/\tau_f}\right) \\ Slow_{slow} &= h_s \left(e^{-T_{s,1}/\tau_s} - e^{-T_{s,2}/\tau_s}\right) \end{aligned} \tag{5.8}$$

where T is the upper limit of the fast gate (600 ns in the present case, the lower limit is 0 ns) and $T_{s,1}$ (900 ns) and $T_s, 2$ (6 μs) are the lower and the upper limits, respectively, for the slow gate. Taking into account the true dependence of h_f on the energy and on the fragment charge and mass, we verified that the difference between the $Fast_{fast}$ and the fast component is below 10% for all the considered energies and for Z up to 3 and, in addition, $Fast_{fast}$ is proportional to the fast component. Moreover the $Slow_{slow}$, computed taking into account the true dependence of h_s on the energy and on the fragment charge and mass, is proportional to the slow component as shown in Fig. 5.14.

From Eq. 5.7 we can express the fast time constant as a function of the rise time RT_{fast} and therefore express the fast component (due to only the fast light output) as:

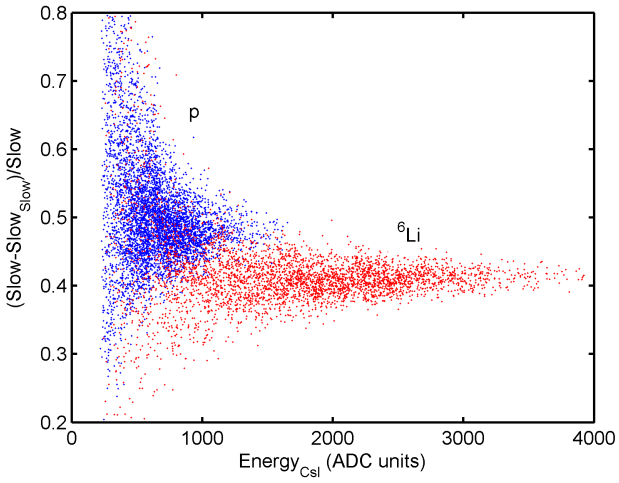

Figure 5.14: *Relative variation of the slow component and of the $Slow_{slow}$ as a function of the pulse amplitude for protons and ^{6}Li ions.*

$$Fast_{fast} = h_f \left(1 - e^{-\alpha/RT_{fast}}\right) \tag{5.9}$$

where $\alpha = T \log\left[\frac{1-a}{1-b}\right]$.
The combination of 5.8 and 5.9 leads to:

$$\frac{Slow}{Fast} \propto \frac{Slow_{slow}}{Fast_{fast}} = \frac{h_s}{h_f} \frac{e^{-T_{s,1}/\tau_s} - e^{-T_{s,2}/\tau_s}}{1 - e^{-\alpha/RT_{fast}}} \tag{5.10}$$

Due to the low dependence of the slow time constant on the energy and on the fragment mass and charge, the numerator in 5.10 can be assumed nearly constant, in addition the ratio of the slow and fast light output intensities h_s/h_f shows only a moderate dependence on energy and the pulse rise time and what we called RT_{fast} are proportional. Moreover α is normally below 0.4. Therefore the ratio of the slow and the fast components shows a nearly direct dependence on the pulse rise time since the denominator can be considered inversely proportional to the pulse rise time. This is also evident from Fig. 5.15 that shows the scatter plot of the $Slow_{slow}/Fast_{fast}$ against the pulse rise time.

As a consequence we wanted to probe the pulse rise-time and the ratio of the Slow and Fast components against the pulse height as identification plots.

The hint to scatter plot the pulse amplitude against the ratio of the fast and slow components derives from the marked dependence of the fast and

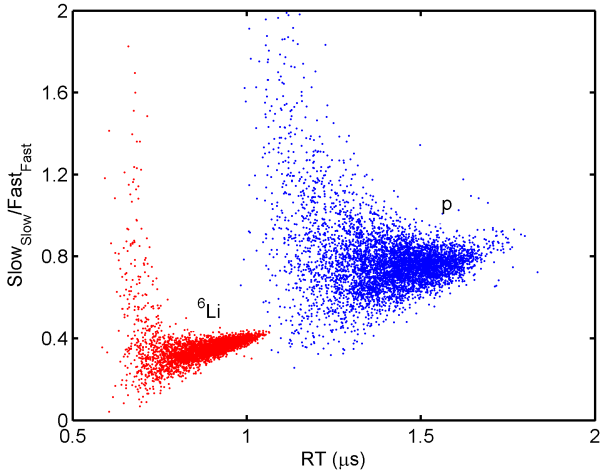

Figure 5.15: *Scatter plot of the $Slow_{slow}/Fast_{fast}$ against the pulse rise time for protons and ^6Li ions.*

slow components on the pulse amplitude – even more evident on the energy (see Fig. 5.5). The better identification capability could rely on the introduction of a third variable, *i.e.* the pulse amplitude, that is hidden in the conventional fast/slow scatter plot. In addition, a better identification capability does not necessarily imply that the resolution on the branches of the scatter plot is improved but that the branches separation is increased. Since the dependence of the relative intensities of the fast and slow components (with regards to the total light output intensity) is on the velocity of the impinging particle, the relative intensity of the slow (fast) component increases (decreases) with the energy per nucleon, in addition the slow (fast) component decrease (increase) with the particle charge. Due to the aforementioned dependencies, the computation of the ratio of the slow and the fast components enhances the separation of the branches pertaining to the different isotopes.

As shown in Fig. 5.16 the pulse rise time shows a full correlation with the ratio of the Slow and Fast components. For the data at relativistic energies the approximations considered to derive the explicit dependence of the Slow/Fast ratio on the pulse Rise-Time begin to fail, however the Slow/Fast ratio shows a linear dependence on the Rise-Time for ^{6}Li and for particles up to E_α ∼500 MeV as shown in Fig. 5.17, while for higher α energies and for protons we observe a clear deviation from linearity. These considerations suggest the possibility to scatter plot the pulse rise time with respect

to the pulse energy (*i.e.* amplitude) as an alternative identification plot. In any case we expect a similarity of the (*Energy*$_{CsI}$*–RT*) and (*Energy*$_{CsI}$*–Slow/Fast*) scatter plots.

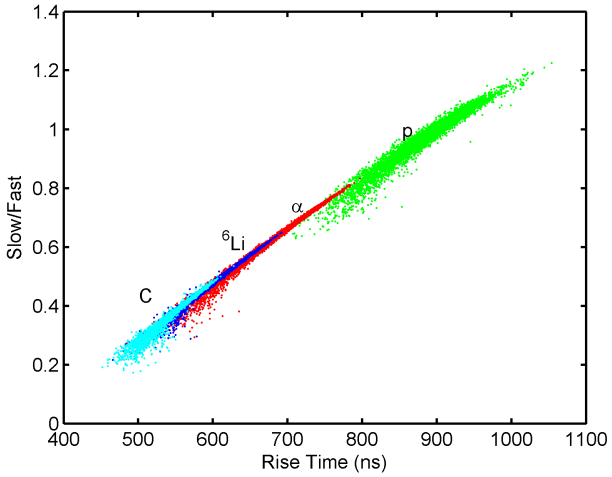

Figure 5.16: *(Slow/Fast, RT) scatter plot for $^{20}Ne+^{12}C$ at 21.5 MeV/u. The rise-time is computed as 30% - 70%.*

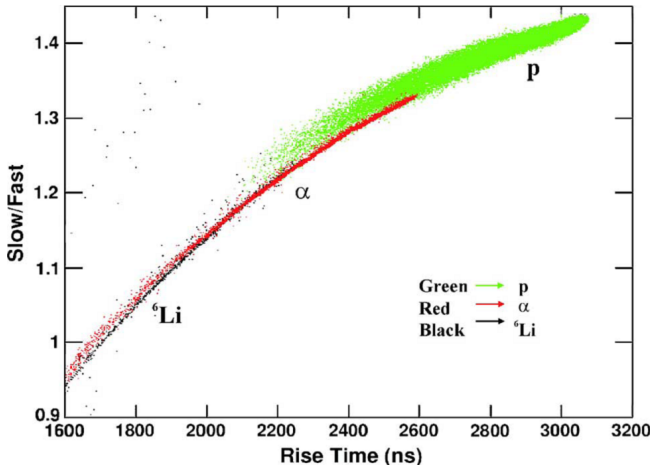

Figure 5.17: *(Slow/Fast, RT) scatter plot for $^{96}Zr+^{96}Zr$ at 400 MeV/u. The rise-time is computed as 30% - 70%.*

5.6.2 Merits of New Detection Maps at GSI Energies

We probed the merits of the new detection maps, namely the *Energy$_{CsI}$–Slow/Fast* and the *Energy$_{CsI}$–Rise Time* scatter plots, on a batch of waveforms acquired by a CHIMERA telescope in the frame of the ASY-EOS experiment held at GSI in Darmstadt (D) in May 2011 [87]. The purpose of the experiment was the measurement of direct and elliptic flows of neutrons, protons and light complex particles in reaction of isospin asymmetric neutron rich systems, as: ^{197}Au+^{197}Au, ^{96}Ru+^{96}Ru and ^{96}Zr+^{96}Zr at 400 MeV/u. The results will help to study the asymmetry term of the Equation of State of the Nuclear Matter (EOS) [88] and provide quantitative information on the density dependence of the symmetry energy at densities larger than required for saturation. For the experiment, only four wheels (*i.e.* eight detector rings) of CHIMERA were moved to GSI. They were used to determine the impact parameters and reconstruct the reaction plane, assuring a 2π azimuthal coverage around the beam for light charged particle measurement. The batch of waveforms we are referring to comes from the telescope R5-20 located at $\theta = 12.25°$ and $\phi = 180°$. The preamplifier waveforms, sampled at 50 MS/s (20 ns time interval), are baseline subtracted and filtered with a 87 taps FIR filter, as described in detail in [76]. The event parameters have been extracted from the digitized waveforms as described in Section 5.5.

Fig. 5.18, 5.19(a) and (b) show the conventional *Fast–Slow*, the *Energy$_{CsI}$–Slow/Fast* and *Energy$_{CsI}$–Rise Time* – energy expressed in ADC units – scatter plots respectively, in the case ^{96}Zr+^{96}Zr at 400 MeV/u. The power of the *E$_{CsI}$–RT* and *E$_{CsI}$–S/F*) representations is evident. In fact, the separation between protons and fast protons is very sharp, and the isotopic separation among Z=1, 2, 3, 4 products is evident for all energies, even towards low particle energy. Moreover the punch-through points for all the products are clearly identified. The fast protons have enough energy to punch through the CsI(Tl) crystal. The identification of this proton cluster is crucial in experiments at very high beam energies. Z=1 and Z=2 isotopes emitted in the quasi-projectile fragmentation can provide important experimental information on the EOS of the nuclear matter since their identification could contribute to the knowledge of the asymmetry term of the EOS [89]. The punch-through cusp appears since the energy of the detected isotopes exceed those corresponding to their energy range in 12 cm thick CsI(Tl) crystals. The gathering of the events pertaining to punching-through particles therefore creates a cusp in the corresponding cluster in the scatter plots. As their energies increase, the corresponding isotope lines

display a back-bending behavior, due to the decreased energy lost in the CsI(Tl) by the crossing isotopes. In the scatter plots of Fig. 5.19(a) and (b) the punch-through energy points and the back-bending behavior are more prominent than in the conventional *Fast–Slow* scatter plot of Fig. 5.18.

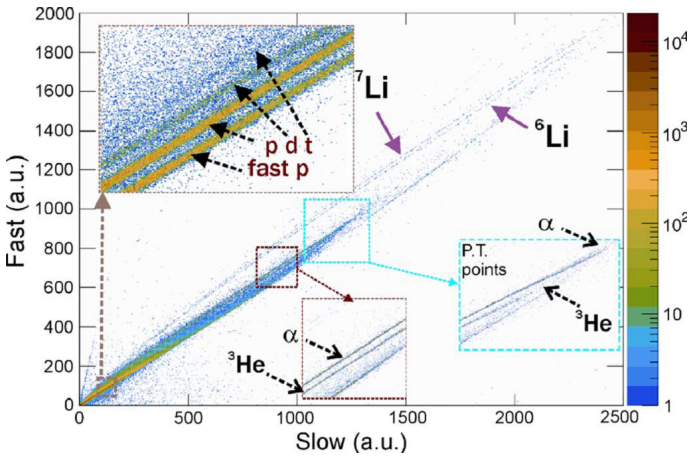

Figure 5.18: *Fast–Slow scatter plot for ^{96}Zr+^{96}Zr at 400 MeV/u. The punch-through points (P.T.) for ^{3}He and α are shown in the inset.*

In order to compare the LCP separation power of the three different representations of the collected data – E_{CsI}*–Slow/Fast*, E_{CsI}*–RT* and *Fast–Slow* – we computed the *Figure of Merit* (FoM) [90] for various energy bins of Z=1 (p, d), Z=2 (^{3}He,α) and Z=3 (^{6}Li, ^{7}Li) isotopes. Each energy bin contains events whose pulse height falls within a given range. The FoM is defined as the separation between two peaks, *i.e.* the distance between their centroids, divided by the sum of their Full Widths at Half Maximum (FWHM). The FoM is certainly one the simplest algorithm to be used for classifying particle identification because it uses only the first two moments of the distributions. Larger values of the FoM signify better identification. A value of the FoM of 0.75 corresponds to well separated identical (equal intensity and FWHM) Gaussians, with a peak-to-valley ratio of 2.0 [90].

In order to compute the FoM in the chosen scatter plot, we proceed as follows. At first, we consider each isotope cluster separately. The line of maximum density of the cluster is then approximated with a polygonal line, as shown in Fig. 5.20(a).We have two of these lines for each FoM to be computed. We call (x_E,y_E) the coordinate of an event in the scatter plot (whatever they actually are, *i.e.* E_{CsI}*–Slow/Fast*, E_{CsI}*–RT* and *Fast–Slow*. The two intersections of the horizontal line given by $y = y_E$ with the polygonals identify two points on the scatter plot, whose coordinates are

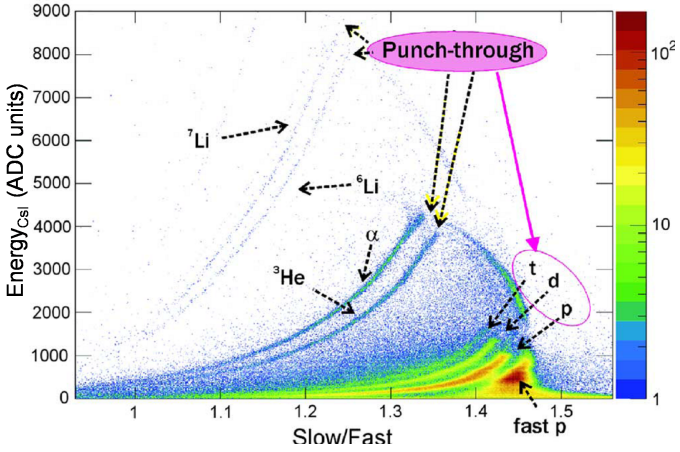

(a)

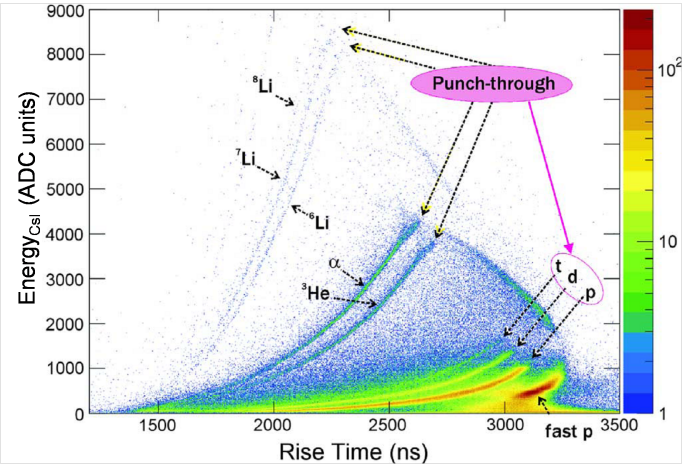

(b)

Figure 5.19: *(a) E_{CsI}–S/F and (b) E_{CsI}–RT scatter plots for ^{96}Zr+^{96}Zr at 400 MeV/u.*

given by (x_0,y_E) and (x_1,y_E). Along this line, we compute the parameter $p_E = x_E - x_0/(x_1 - x_0)$ – henceforth called parametric coordinate – which is the affine transformation constrained by the requirement that events lying on the polygonal of the first cluster have $p_E = 0$ and events lying on the polygonal of the second cluster have $p_E = 1$, as shown in Fig. 5.20(b). By using the parametric coordinate, we obtain the histogram (5.20(c)). In order to compute the FoM, the histograms are fitted with a sum of two arbitrary Gaussians representing the two peaks plus a linear background. Table 5.3 shows the values of the computed FoMs for different pairs of

isotopes for all the three used identification plots and various bins for 87 taps filters. It is possible to note that only in 12.5% of the bins the usual *Fast–Slow* representation gives the best FoM.

The E_{CsI}*–Slow/Fast* representation has the best FoM in 25% of the bins, while the E_{CsI}*–RT* representation features best results in 62.5% of the bins. A typical FoM statistical error is estimated to be ~ 0.10 in the worst case. We also checked the use of a narrower filter (27 taps). In this case the obtained FoM results are a little bit worse ($\sim 0.10\%$) than in the case of 87 tap filter for the E_{CsI}*–RT* scatter plot, as expected due to the impact of the series noise of the frontend electronics. For the other two representations E_{CsI}*–Slow/Fast* and *Fast–Slow* the results are markedly worse for Z=2 ($\sim$40%) and Z=3 ($\sim$30%) isotopes. For protons and deuterons with a 27 tap filter the identification is not at all possible, since at lower energies the impact of the electronic noise is even more relevant and a 27 tap filter does not provide adequate filtering for the series noise.

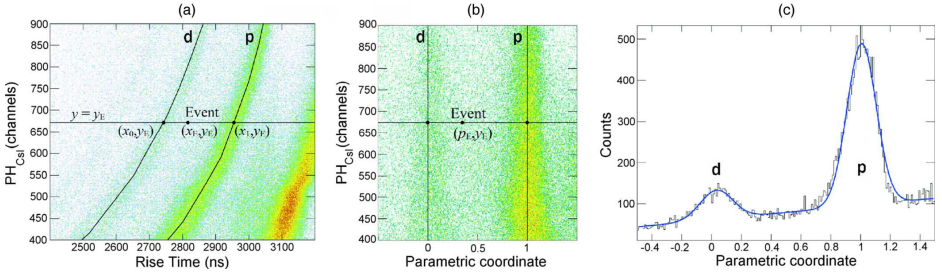

Figure 5.20: *The transformation used for computing the FoMs, exemplified with the pair p, d in the E_{CsI}–RT scatter plot. In (a), the polygonals used to compute the parametric coordinate p_E for each event are shown; in (b) the representation in the transformed coordinate system (Energy$_{CsI}$, p_E); in (c) the projection of the selected pulse height interval in the transformed coordinate system; the histogram is fitted with two Gaussian and a linear background.*

5.7 Conclusion

In the framework of the FARCOS CsI(Tl) scintillator characterization, we investigated the dependence of the time constants and intensities of the CsI(Tl) scintillation light on the energy, charge, and mass of the impinging particles by direct fitting of the digitized waveforms digitally acquired at the output of the scintillator. The data set used in the present work is a batch of waveforms measured with the CHIMERA multidetector. The four-vector defining the light output (τ_f, τ_s, h_f, h_s) has been obtained in

Table 5.3: *FoM values for different LCP pairs and representations.*

Ions	Energy$_{CsI}$ (ADC units)		FoM (87 taps)		
	min	max	*E_{CsI}–S/F*	*E_{CsI}–RT*	*F–S*
p, d	300	400	1.24	1.17	1.32
	400	500	0.90	1.48	0.84
	500	600	1.41	1.83	0.87
	600	700	1.31	2.00	1.30
	700	800	1.30	2.15	1.37
	800	900	1.33	2.37	1.38
^{3}He, α	1000	1500	2.56	2.46	2.49
	1500	2000	3.33	4.04	3.49
	2000	2500	3.70	4.02	3.30
	2500	3000	3.61	4.51	3.62
	3000	3500	3.46	4.07	3.58
^{6}Li, ^{7}Li	2000	3000	2.15	1.41	1.89
	3000	4000	3.05	2.08	2.62
	4000	5000	2.78	2.74	2.82
	5000	6000	3.57	3.81	3.28
	6000	7000	3.84	2.80	2.89

the energy – deposited in the CsI(Tl) crystal – range 10 240 MeV for isotopes with Z$\leq$5 and also for ions with Z=6 – with no isotopic dependence – by analyzing the waveforms acquired when a 21.5 MeV/u ^{20}Ne beam was bombarding a ^{12}C target. The values of the fast time constant (τ_f) range from 500 ns to 1 μs at maximum with isotopic separation for Z up to 3. The values of the slow time constant (τ_s) range from 1 to 6 μs at maximum, and the separation of the clusters pertaining to different isotopes is less evident. The intensity of the slow component (h_s) turns out to be inversely proportional to the particle charge, while no particular evidence of the dependence of h_f with the particle charge can be gained. Moreover, the relative intensities depends on the velocity of the impinging particle and not on its energy and mass independently. In addition we reported the results of the investigation of novel identification plots (*Energy$_{CsI}$–Slow/Fast* and *Energy$_{CsI}$–Rise-Time*) that arise from the analysis of the conventional identification parameters (*Slow*, *Fast*, *Rise-Time*). We probed the Figure of Merit of the new identification plots at the relativistic energies reached at GSI and they give better results than the conventional *Fast-Slow* plot in almost the 90% of the cases.

CHAPTER 6

First On-Beam Test of a FARCOS telescope

6.1 Introduction

Four FARCOS clusters were tested on-beam for the first time during a measurement run in July 2012 at Laboratori Nazionali del Sud (*INFN*, Catania). In this brief chapter we describe the experimental conditions in Section 6.2, and review some preliminary results obtained with our digital DAQ system for the telescope T3 in Section 6.3.

6.2 Experimental Conditions

The accelerated beams were 62 MeV/u protons and α-particles and 20 MeV/u ^{20}Ne ions. Different targets (thin Au, thick Au, Al_2O_3, Pb+C, Al, CD_2) were selected with the aim to study known reactions (such as (p,d), (p,t), (d,t)) as well as elastic collisions to provide a large variety of particles scattered at different angles and energies with the main goal of probing the uniformity of the light yield of the CsI(TI) scintillators. The detectors were placed at polar angle θ=6°. Fig. 6.1 shows the setup in the CHIMERA experimental chamber. In the experimental chamber there was also a mixed

NOTE: The content of this chapter is partly based on the paper [6] coauthored by myself.

nuclide α-source for calibration purposes.

Our digital DAQ system, described in detail in Section 2.2.3 (pag. 35), acquired the waveforms pertaining to the FARCOS telescope T3 – the upper-right one in Fig. 6.1 – which was composed by a 300 μm Double Sided Silicon Strip Detector and three CsI(Tl) scintillator crystals. Unfortunately, during the mounting, the bonding wires of strips n. 15, 16, 17 and 32 of the front side were damaged but we were not aware of it and it was not possible to repair them since before closing the vacuum chamber only tests with the pulser were performed. They were therefore left floating.

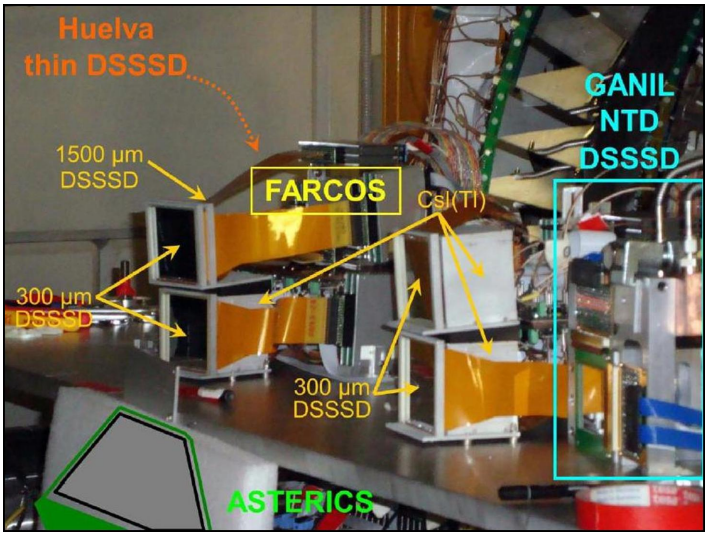

Figure 6.1: *Photo of the experimental setup at Laboratori Nazionali del Sud in Catania during the on-beam test carried out in July 2012. Other detectors were profiting of the accelerated beams. An NTD silicon microstrip detector developed at GANIL, two thin microstrip detectors developed by University of Huelva and the Asterics detector of Rochester University.*

6.3 Preliminary Results

In this section we reports some of the preliminary results obtained being the data analysis still on-going.

In all the reported cases, the digitized waveforms delivered by the DAQ have been digitally baseline subtracted and filtered with a triangular filter of 201 taps kernel, since we found that this is the better width for a filter of such shape for the extraction of the maximum amplitude.

6.3.1 DSSSD Energy Calibration

The energy calibration is made independently for all the strips of the front side and of the back side of the 300 μm DSSSD exploiting the mixed nuclide α-source. The energy calibration is essential since it allows an homogeneous comparison or sum of events occurred at different strips in order to perform analysis such as $\Delta E - E$. The ^{239}Pu, ^{241}Am and ^{244}Cm radionuclide of the mixed nuclide α-source gives three main peaks at 5156.6 keV, 5485.6 keV and 5804.8 keV. The list of the most intense α-particles peaks of the different radionuclides is reported in Table 6.1.

Table 6.1: *Energies and intensities of the most intense α-particles emitted by the different radionuclides [91].*

Radinuclide	α particle energy (keV)	Intensity (%)
^{239}Pu	5105	11.5
	5143	15.1
	5156.6	73.4
^{241}Am	5388	1.4
	5443	12.8
	5485.6	85.2
^{244}Cm	5763	23.3
	5804.8	76.7

An example of spectrum taken with the DSSSD is shown in Fig. 6.2 for strip n. 12 of the front side. All the waveforms are obtained with the AAA gain 8x. From the calibrations we extract the energy resolution for each strip of both the front and the back side (obviously except the non-bonded ones). Fig. 6.3 (a) and (b) show the energy resolution expressed in keV FWHM for the ^{239}Pu peaks for the front and back side, respectively. The mean energy resolution is 27.1 keV FWHM with a dispersion of σ =3.1 keV for the front side and 44.7 FWHM keV with a dispersion of σ =16.5 keV for the back side. As already commented we expect the resolution being worse in the case of the back side strips due to the contribution of the parallel noise coming from the inter-strip resistance.

6.3.2 $\Delta E - E$ Scatter Plots and CsI Energy Spectra

By analyzing the waveforms collected with the digital DAQ we compute the conventional $\Delta E - E$ identification matrix, scatter-plotting the maximum of the waveform with respect to its baseline, both for the waveforms coming from the strips of the 300 μm-thick DSSSD pertaining to telescope T3 and from the corresponding CsI(Tl) scintillator crystal. In the following scatter plots, E and ΔE are expressed in ADC units. The former refers to CsI(Tl)

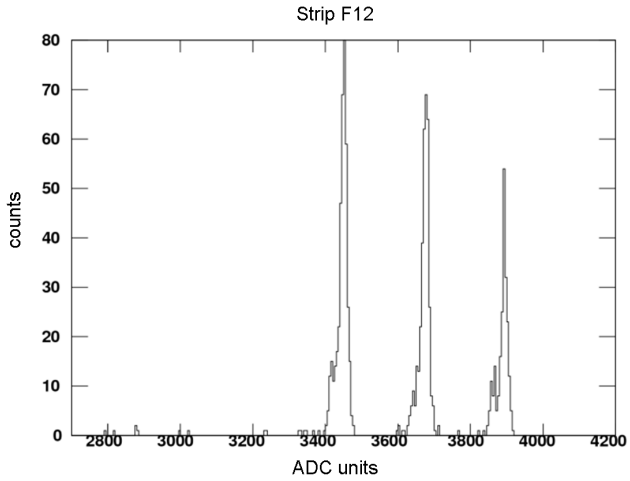

Figure 6.2: *Example of α-spectrum obtained for strip n. 12 of the front side of the 300 μm DSSSD of telescope T3. Waveforms have been previously digitally filtered with a triangular filter 201 taps kernel. The three main peaks are, respectively, at 5156.6 keV (^{239}Pu), at 5485.6 keV (^{241}Am) and at 5804.8 keV (^{244}Cm).*

crystals n. 3 of telescope T3 obtained without any rejection of the events split between CsI(Tl) crystals n. 3 and n. 2, while the latter refers – thanks to the calibration procedure – to the sum of the events pertaining to the strips of the front or back side just in front of the CsI(Tl) crystal, thus covering a quarter of the total active area of the telescope.

Let's consider the reaction 62 MeV/u α on Pb+C (with AAA gain 4x). Fig. 6.4 shows the spatial distribution of events on telescope T3. From the bottom-right corner to the upper-left corner of the figure we see a decreasing events count which reflects the statistics of the incoming byproducts. Events that fall in the strips left floating – the three central ones and the last one of the front side – are partially collected by the neighbor strips resulting in an artificial increase of their counts. The poor count of the first strip is on the contrary probably due to the shadow zone of some shielding.

The $\Delta E - E$ scatter plots are shown in Fig. 6.5 where in (a) the ΔE refers to the front strips and in (b) to the back strips. The isotopic separation for p, d, and t and for ^{3}He and ^{4}He is very good in both cases and the elastic scattering peaks are well visible. The unwanted horizontal lines from 0 to the elastic peaks are for the most part caused by particles that hit the CsI(Tl) crystal only partially, and for a minor part by events that have been triggered improperly leading to an erroneous parameters extraction from the digitized waveform. The continuation of the lines toward higher energies is due to pile-up effects in CsI(Tl) waveforms. In principle it is possible to filter such

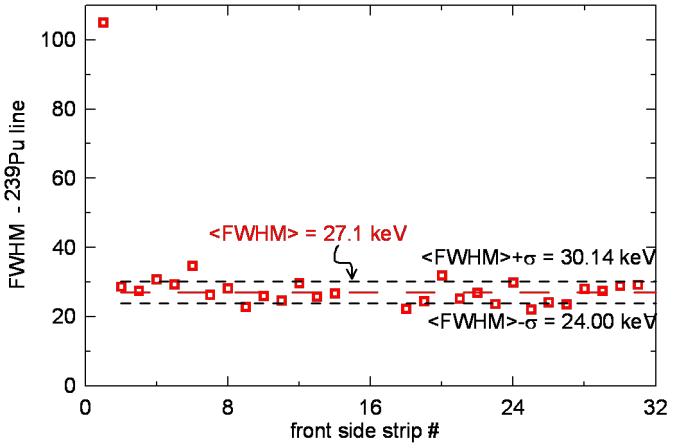

(a)

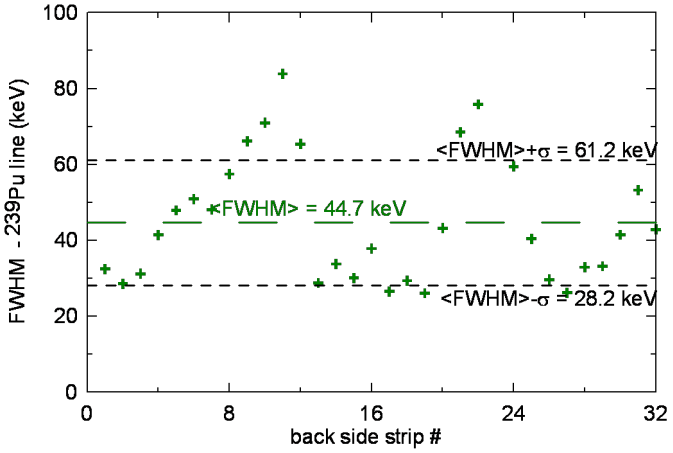

(b)

Figure 6.3: *Energy resolution at the ^{239}Pu line expressed in keV FWHM for the strips of the front side (a) and of the back side (b).*

kind of events and "clean" the scatter plots. Channelling effects, though not dominant, can also be present. The vertical lines above the elastic scattering peak are on the contrary caused by multiple events in the DSSSD which when added give an abnormally high energy.

Thanks to the elastic scattering peak of the 62 MeV/u α beam, we have been able to assess the energy resolution power of the CsI(Tl) scintillators. Fig. 6.7 (a) shows the energy spectrum in the proximity of the elastic scattering peak for CsI(Tl) crystal n. 2 of telescope T3. The energy resolution extracted by Gaussian-fitting the main peak is 0.86% FWHM of the peak

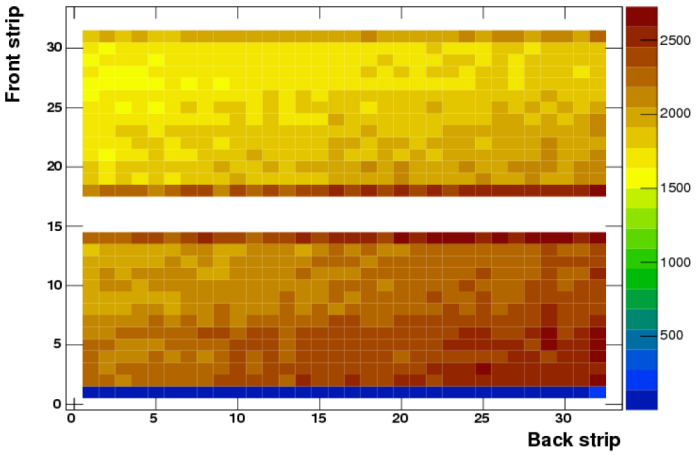

Figure 6.4: *Spatial distribution of events on T3 telescope for the reaction 62 MeV/u α on Pb+C.*

centroid. The pixelation of the DSSSD allowed us to correct in the data analysis phase for the spatial light yield non-uniformity. Indeed, the number of the front strip and of the back strip of the DSSSD that fire at every event gives the $x - y$ position of the impinging particle, while the elastic scattering peak in the CsI(Tl) is used as energy reference. The results are the 2D correction maps shown in Fig. 6.6 which can be exploited in principle in every acquisition. In this case each pixel correspond to a cluster of 2×2 DSSSD strips due to the poor statistics. Fig. 6.6 (a) refers to CsI(Tl) crystal n. 2 of telescope T3 while Fig. 6.6 (b) refers to crystal n. 3 of the same telescope. The figure shows the differential light yield with respect to the average light yield, expressed in percentage, computed as:

$$\Delta Yield_{i,j}(\%) = \frac{Yield_{i,j} - \langle Yield \rangle}{\langle Yield \rangle} \times 100 \tag{6.1}$$

where i and j identify the front and the back strips that determine the pixel.

Fig. 6.7 (b) shows the corrected CsI(Tl) energy spectrum in the proximity of the elastic scattering peak for crystal n. 2. The resolution of the main peak is improved to 0.65% FWHM of the peak centroid. Both in the non-corrected and even more in the corrected spectrum a small but clear satellite peak emerges at energies just above the supposed elastic scattering peak. Its origin it is not an instrumentation artifact but it seems rather due to the compound nature of the target where Pb and C atoms scatter in a slightly different way the incoming beam.

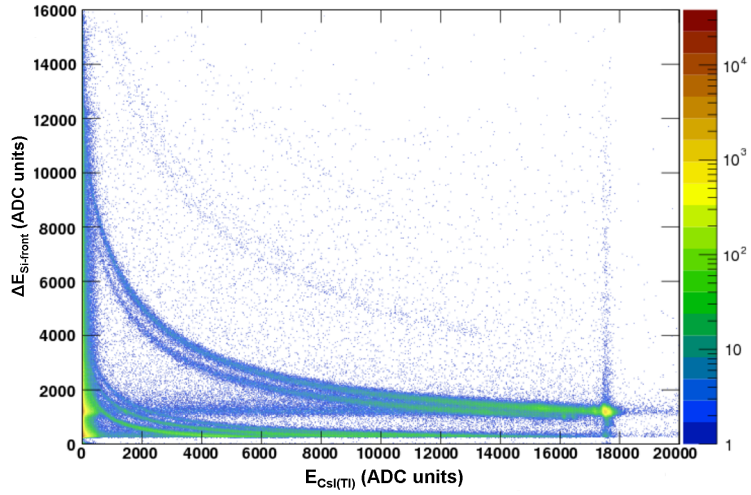

(a)

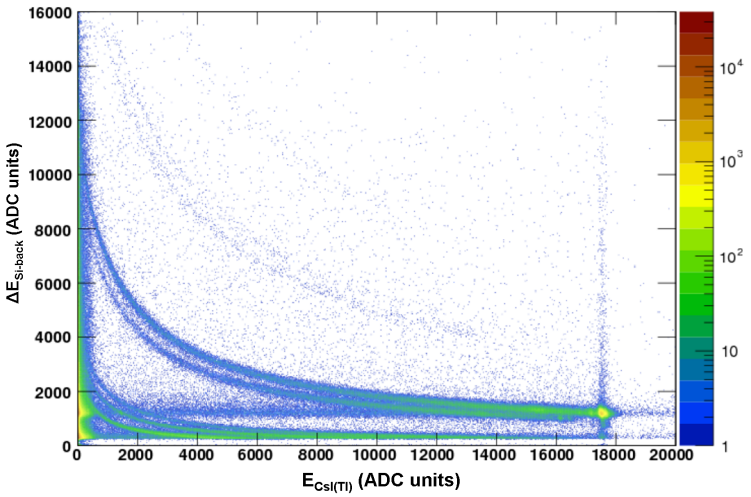

(b)

Figure 6.5: *$\Delta E - E$ scatter plots for the reaction 62 MeV/u α on Pb+C, using the CsI(Tl) crystal n. 3 of telescope T3 for the E and the sum of the signals of the front strips (a) or the back strips (b) just in front of the scintillator as ΔE.*

Applying the CsI(Tl) correction map to the $\Delta E - E$ scatter plot of Fig. 6.5 (a), we obtain the one shown in Fig. 6.8, where a slightly increased isotopic separation is obtained.

The 62 MeV/u α beam was also used on an thick Au target (with AAA gain 8x). Fig. 6.9 shows the spatial distribution of events on telescope T3.

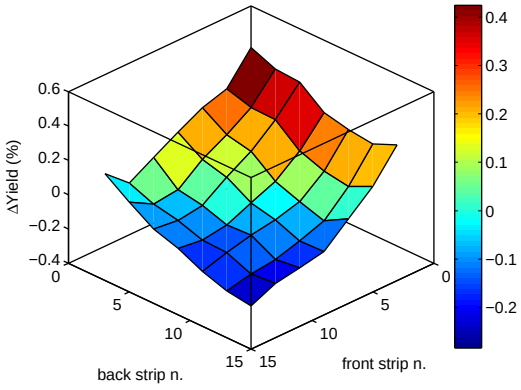

(a)

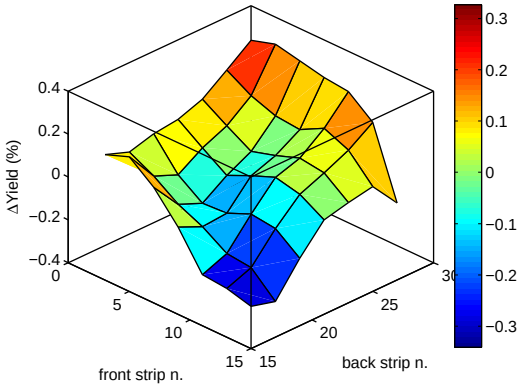

(b)

Figure 6.6: *2D correction map for the CsI(Tl) crystal n. 2 (a) and n. 3 (b) of telescope T3. The surfaces represent the differential light yield with respect to the average light yield, expressed in percentage. Each pixel of these maps correspond to a cluster of 2×2 DSSSD strips due to the poor statistics.*

The $\Delta E - E$ scatter plot using the front side strips of the DSSSD and the corrected values of the energy of the CsI(Tl) is shown in Fig. 6.10. The isotopic separation for p, d, and t and for ^{3}He and ^{4}He is very good also in this case. Considerations made for the 62 MeV/u α on Pb+C case, regarding the strait horizontal and vertical lines, still holds.

The presence of a small intensity satellite peak with energy slightly greater than the supposed elastic scattering peak, can be explained in this case with a possible non-uniformity of the target thickness, which causes the elastically scattered α-particles to experience different energy losses

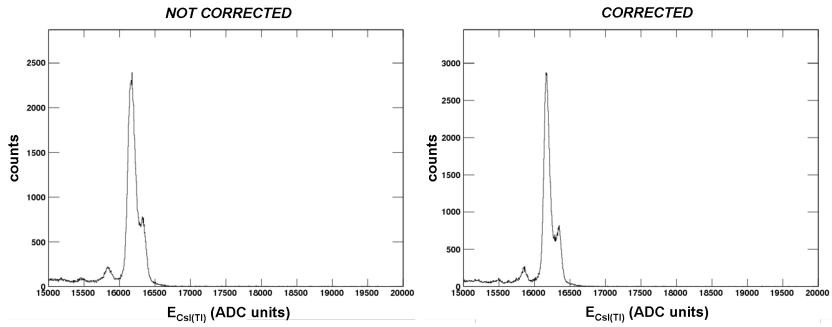

(a) (b)

Figure 6.7: *(a) Energy spectrum of the CsI(Tl) crystal n. 2 of telescope T3 in the range of the elastic scattering peak of the 62 MeV/u α beam impinging on the Pb+C target. (b) Energy spectrum of the same acquisition corrected for the CsI(Tl) spatial light yield non-uniformity exploiting the DSSSD pixelation.*

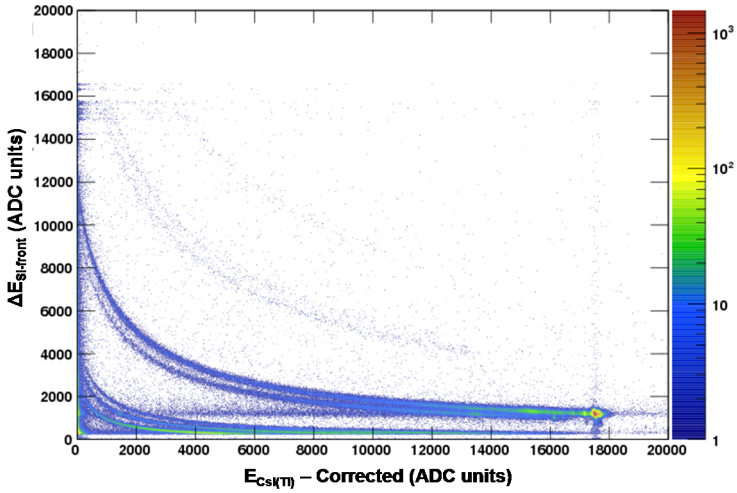

Figure 6.8: *$\Delta E - E$ scatter plots corrected for the CsI(Tl) light yield non-uniformity for the reaction 62 MeV/u α on Pb+C, using the CsI(Tl) crystal n. 3 of telescope T3 for the E and the sum of the signals of the front strips just in front of the scintillator as ΔE.*

within the target before to reach the detector.

Lastly, Fig. 6.11 shows the spatial distribution of events on telescope T3 for the reaction 20 MeV/u ^{20}Ne on Deuterated Polyethylene (CD_2) (with AAA gain 1x).

$\Delta E - E$ scatter plots using the front strips and the back strips are shown in Fig. 6.12 (a) and (b) respectively. A batch of unwanted horizontal lines

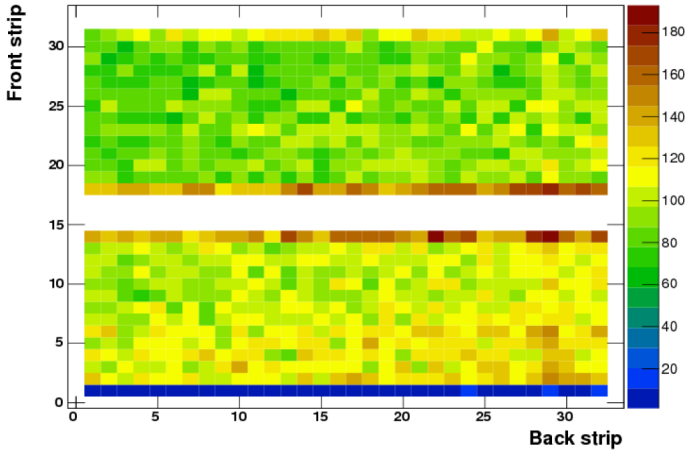

Figure 6.9: *Spatial distribution of events on T3 telescope for the reaction 62 MeV/u α on Au.*

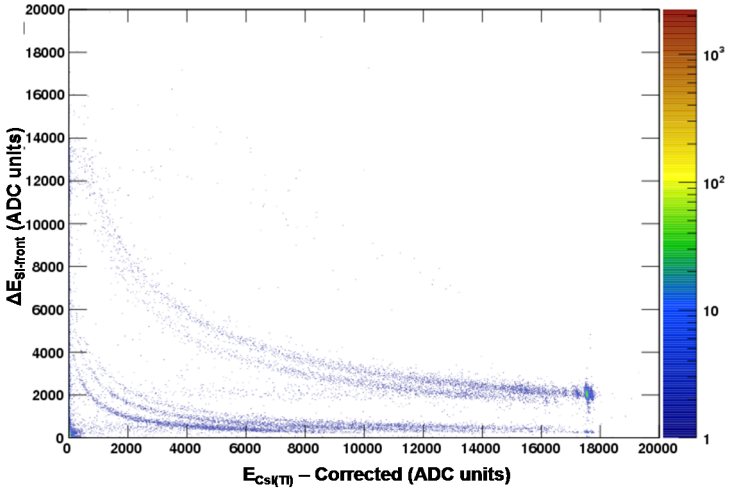

Figure 6.10: *$\Delta E - E$ scatter plot corrected for the CsI(Tl) light yield non-uniformity for the reaction 62 MeV/u α on Au, using the CsI(Tl) crystal n. 3 of telescope T3 for the E and the sum of the signals of the front strips just in front of the scintillator as ΔE.*

arise in the upper part of the figures for the saturation of the DSSSD read-out channels which occurs at different levels since their gains and offsets do not perfectly match.

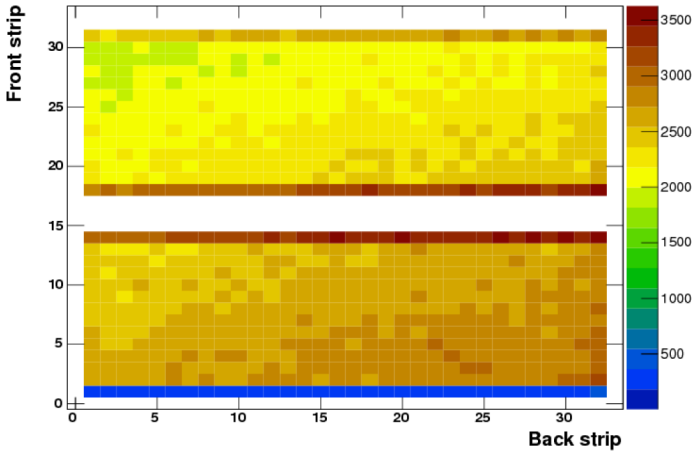

Figure 6.11: *Spatial distribution of events on T3 telescope for the reaction 20 MeV/u ^{20}Ne on CD_2 (Deuterated Polyethylene).*

6.4 Conclusion

We presented some preliminary results from the first on-beam test for FARCOS held at the Laboratori Nazionali del Sud (*INFN*, Catania) in July 2012. Exploiting our digital DAQ we have been able to record and store all the waveforms pertaining to telescope T3 and to process them off line. A mixed nuclide α-source provided the calibration for the DSSSD, allowing also the estimation of the energy resolution for each individual strip. $\Delta E - E$ identification matrix are presented for the reaction 62 MeV/u α on Pb+C, 62 MeV/u α on Au and 20 MeV/u ^{20}Ne on CD_2 using as ΔE stage either the front-side strips or the back-side strips for comparison purposes. Thanks to the pixelation of the DSSSD and the elastic scattering peak of the 62 MeV/u α on Pb+C it has been possible to evaluate the 2D light yield non-uniformity of the CsI(Tl) crystals and to provide an effective correction map.

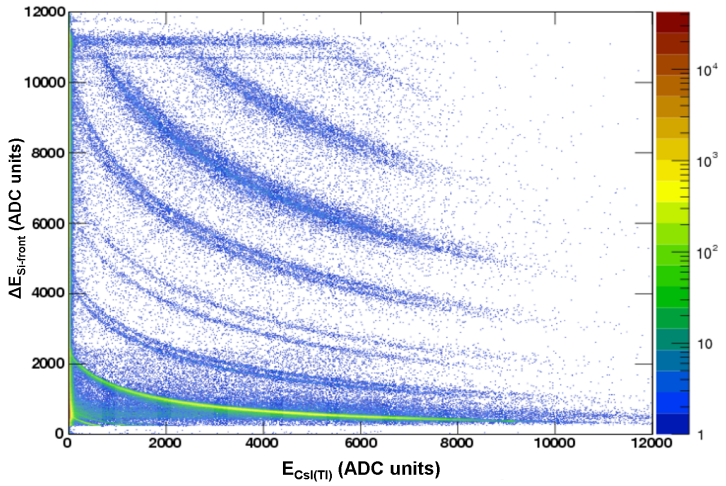

(a)

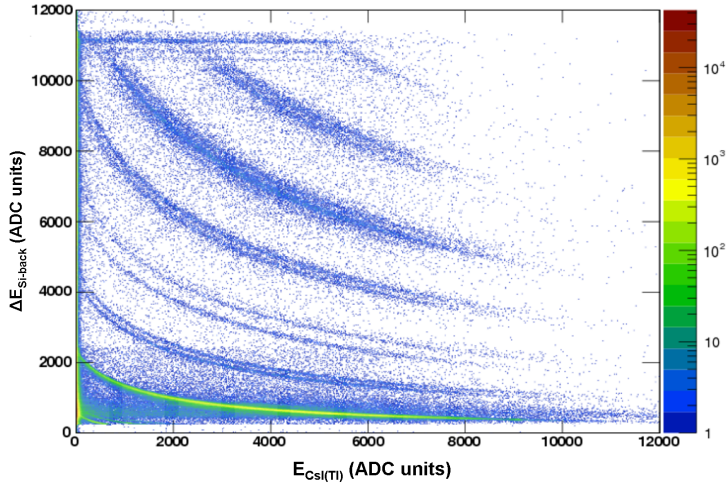

(b)

Figure 6.12: *$\Delta E - E$ scatter plots for the reaction 20 MeV/u ^{20}Ne on CD_2 (Deuterated Polyethylene), using the CsI(Tl) crystal n. 3 of telescope T3 for the E and the sum of the signals of the front strips (a) or the back strips (b) just in front of the scintillator as ΔE.*

CHAPTER 7

Conclusion

FARCOS (Femtoscope ARay for COrrelation ans Spectroscopy) is a novel modular and versatile detection system for particle correlation and spectroscopy of Light Charged Particles and Intermediate Mass Fragments in multi-fragmentation heavy-ion collision nuclear physics experiments with stable and unstable beams. It features high angular and energy resolution and an ambitious goal would be to achieve a full particle identification exploiting, together with the standard identification techniques, Pulse Shape Analysis techniques. In this respect, the possibility to use our digital DAQ system for the direct waveforms digitization would be beneficial. Each FARCOS telescope is composed by Double Sided Silicon Strip Detectors and thick CsI(Tl) scintillators.

In order to optimize the DSSSD performances, we carried out a detailed characterization of the detectors fundamental physical parameters such as leakage currents, capacitances and related entities as a function of the applied bias and of the frequency. In particular, we investigated the two main contribution to the strip capacitance, namely the bulk capacitance – the capacitance of one strip toward the whole other side – and the inter-strip capacitance – the capacitance between two adjacent strips of the same de-

tector side. We evaluated also the impact of the LCR-meter accuracy on the measurements. In addition, at the INFN-LaBeC facility (Firenze) we were able to finely map the detector response in amplitude and position exploiting the monochromatic pulsed ion beam available at DEFEL beamline and the digital DAQ system. In this way we obtained a precise energy calibration of each individual strip and of the associated amplifier over a wide energy range. In addition, thanks to the spatial definition of the beam together with the availability of different pairs ion-energy (1 MeV, 3MeV, 5 MeV protons and 7.5 MeV Li), we probed the impact of the inter-strip injection on the induced waveforms shape, relating the appearance of bipolar and opposite polarity signals – that can greatly spoil the overall performances – to the impact position and penetration depth of the ions. We foresee additional beamtimes in order to test and characterize the second version of the front-end electronics modules which have been specifically designed to increase the system stability.

In order to obtain a deeper understanding of the signals formation processes in silicon detectors and in particular in the DSSSDs, we developed a novel simulation tool for the 3D electron-hole transport computation and signals formation in semiconductor detectors having 2D geometry. We carefully took into account the thermal diffusion and especially the Coulomb mutual interaction between the carriers in the charge cloud in order to properly simulate the high charge injection levels expected for FARCOS. To this purpose we developed several custom numerical techniques, such as *charge clustering* and *adaptive carrier position update* the effectiveness of which has been tested and evaluated. We presented a set of simulations of the DSSSD aimed to the study of the impact of the inter-strip injection on the waveforms shape reproducing the experimental conditions as at LaBeC. The results are in excellent agreement with the experimental data and are clarifying since they allow the disentanglement of the electrons and holes contributions to the overall signals and the possibility to relate the signals shape to the carriers drift paths and the electrodes weighting potentials. Forthcoming improvements of the simulation tool would be the extension of the detector geometry to the full 3D and the possibility to include charge-trapping effects.

CsI(Tl) scintillation light dependence on the energy, charge and mass of the impinging particle is at the basis of the particle identification techniques. To gain a better insight on this we investigated the dependence of the scintillation light time constants and intensities on the energy, charge and mass of the impinging particle by direct fitting of the digitized waveforms acquired at the output of the scintillators. We showed the results

obtained from a batch of waveforms acquired with the CHIMERA detector pertaining to isotopes with Z$\leq$5 and to ions with Z=6 in the energy range 10-240 MeV. From the analysis of the dependence of the standard parameters (*fast*, *slow* and *rise-time*) on the particle parameters, we probed the figures of merit of novel identification plots (*energy–Rise-Time* and *energy-slow/fast*) with the conclusion that they lead to improved performances at least at relativistic energies.

Four FARCOS telescopes were tested on-beam for the first time in July 2012 at the INFN-LNS (Catania) with the purpose to test the overall system functionality and to probe the light yield uniformity of the CsI(Tl) crystals. We exploited our digital DAQ system on telescope T3 (composed by a 300 μm DSSSD and 3 CsI(Tl) crystals) allowing us to perform off-line analyses. Using a mixed-nuclide α-source we were able to calibrate the DSSSD allowing also the estimation of the energy resolution for each individual strip with excellent results. We presented the classical $\Delta E - E$ identification plots for the reactions 62 MeV/u α on Pb, 62 MeV/u α on Au and 20 MeV/u ^{20}Ne on CD_2 and the isotopic separation up to ^{4}He is very good. In addition, thanks to the DSSSD pixelation it has been possible to evaluate the 2D light yield non-uniformity of the CsI(Tl) crystals n. 2 and n. 3 which are below 0.5%. The obtained correction maps provide an effective correction tool and they could be exploited also in future acquisitions.

APPENDIX $\mathcal{A}$

Technical Drawings and PCBs Layout

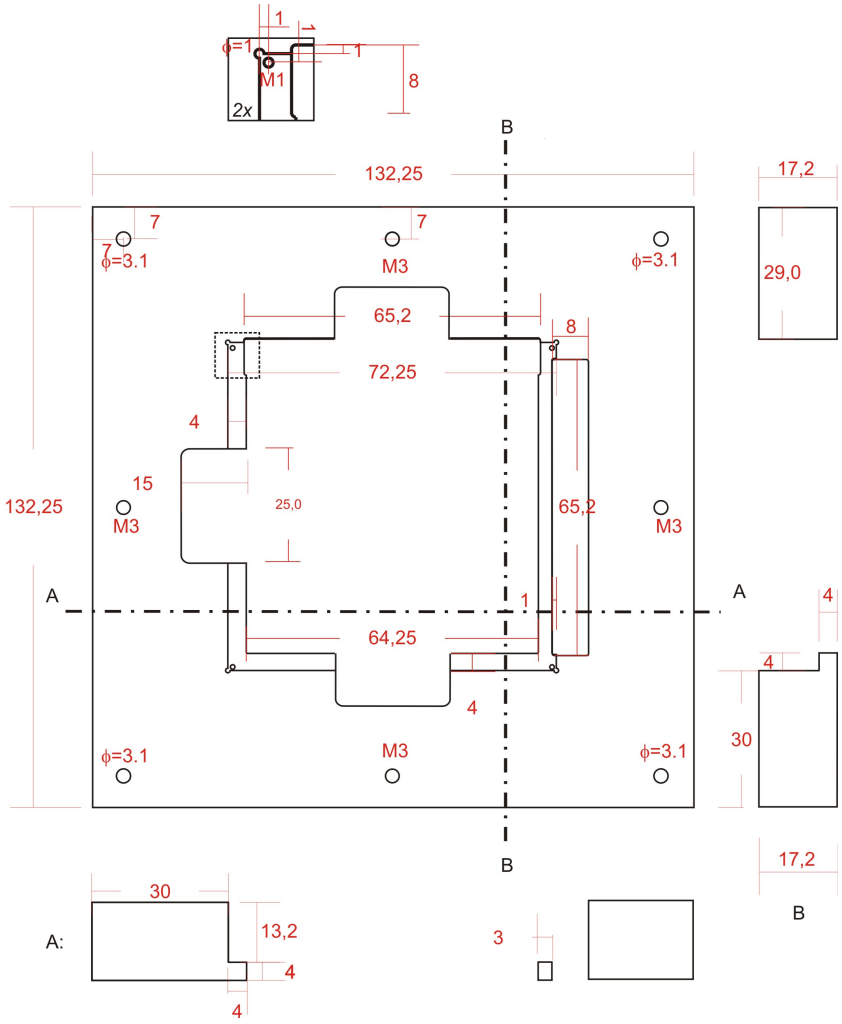

Figure A.1: *Drawing of the DSSSD aluminum holder.*

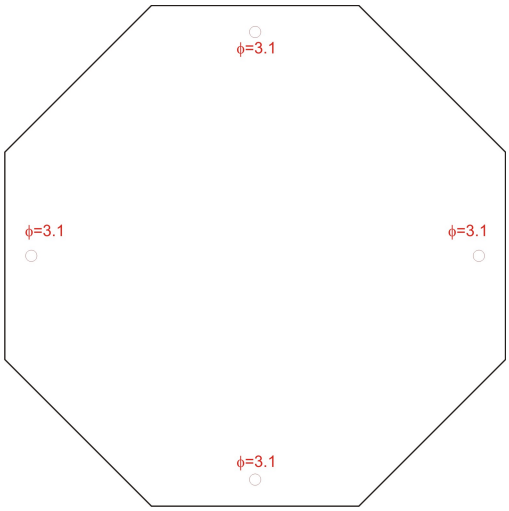

Figure A.2: *Drawing of the DSSSD holder top cover.*

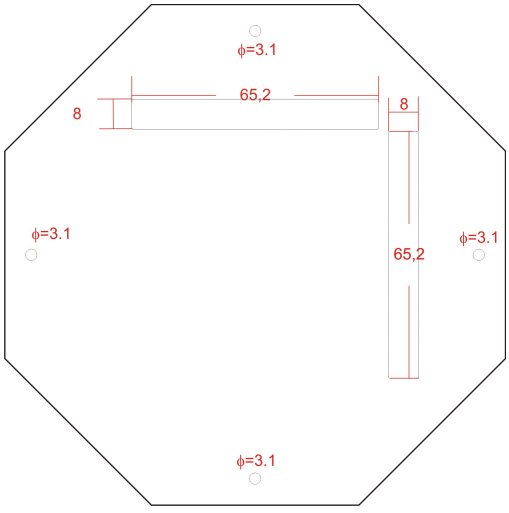

Figure A.3: *Drawing of the DSSSD holder bottom cover.*

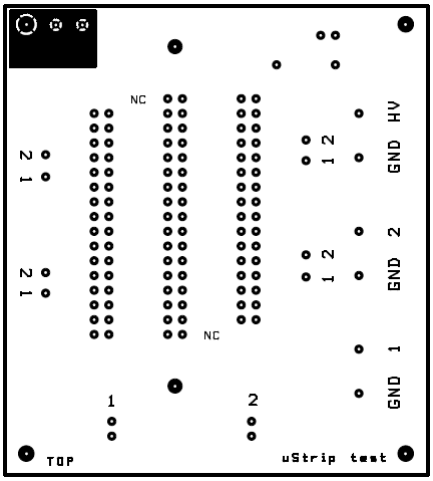

Figure A.4: *Layout of the top layer of a deviation PCB board.*

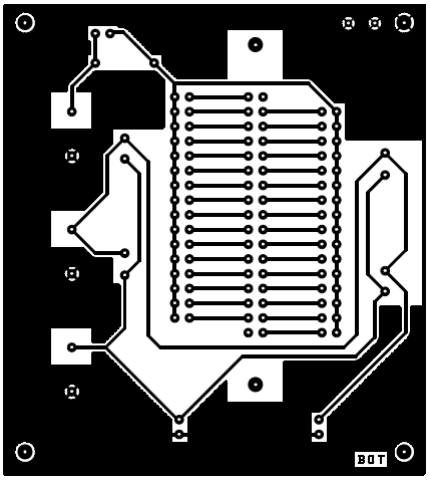

Figure A.5: *Layout of the bottom layer of a deviation PCB board.*

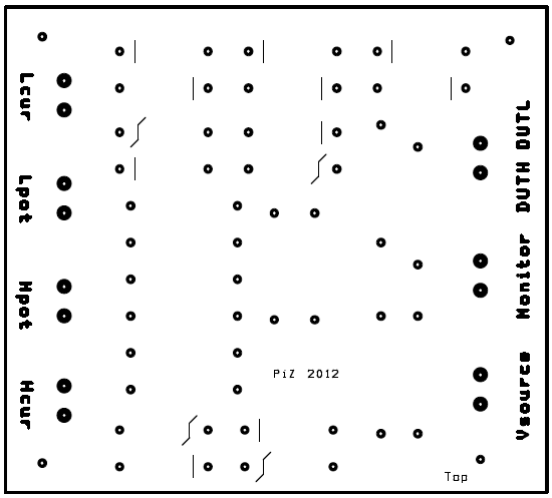

Figure A.6: *Layout of the top layer of the CV measurement probe pcb board.*

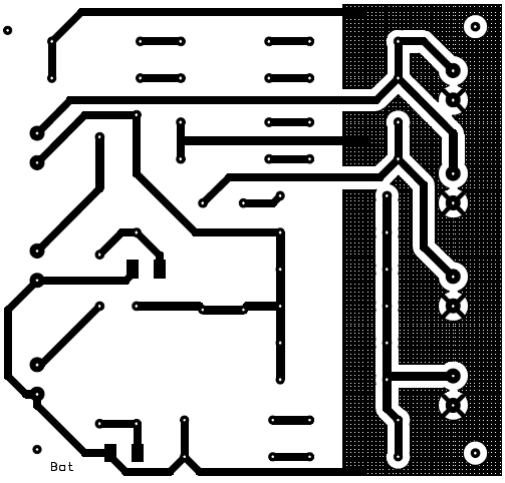

Figure A.7: *Layout of the bottom layer of the CV measurement probe pcb board.*

Acknowledgment

I WISH to thank first of all Chiara Guazzoni and Andrea Castoldi, masters and friends, without whom the present work would not exist as well as my personal and professional growth in these last three years.

How not to mention then the lab-mates and friends who bore with me all the these efforts – Giuseppe Vito Montemurro aka Beppe, the always-complaining Davide Mezza and the young Tommaso Parsani...

Special thanks also to Filippo Riccio for his unrivaled ability with computers, Ciro Boiano for his philosophical approach to the discipline, Luca Carraresi for his helpfulness at LaBeC laboratories, Gary Royle for his hospitality at UCL and Giuseppe Cardella for the careful review of this work.

Thanks to my family that always supported me in all my decisions and always suggested me for the best.

Last and most important, thanks to Daniela, the woman I met by chance or fate just before the beginning of my PhD and that is now my wife, for always reminding me the truly important things in life.

List of Figures

1.1 Artistic representation of the time evolution of an heavy-ion collision with highlighted the different reaction phases. To give an idea of the time scale of the process, the freeze-out phase (fragment ejection) occurs some 10^{-22} s after the beginning of the collision. 3

1.2 Example of (a) proton-proton correlation function for the reaction ^{14}N+^{197}Au at 75 MeV per nucleon. Each curve derive from a different total momentum gating. The dashed lines are computed assuming Gaussian-shaped source function. (b) corresponding source functions computed with the imaging techniques [2]. 5

1.3 Qualitative example of Bragg curves, being the solid one for a single particle while the dotted one for an average over a bunch of identical particles. [7]. 8

1.4 Range-Energy curve computed for different light charged particles in Silicon. [7]. 9

1.5 Example of ΔE-E plots taken with the CHIMERA detector for the reaction ^{20}Ne+^{12}C at 21.5 MeV/u and at a polar angle $\theta = 12.3^{\circ}$ and for two different zooming factors. (a) shows the charge identification power for heavy fragments while (b) shows the charge and mass resolution power for light charged particles. 10

1.6 Schematic diagram of the common gate method applied to a waveform coming from the shaping of a photodiode signal associated to the CsI(Tl) crystal [9]. 11
1.7 Example of *Fast-Slow* identification matrix taken with the CHIMERA detector for the reaction ^{124}Sn+^{64}Ni at 35 MeV/u and at a polar angle $\theta = 21.5^{\circ}$ [9]. 11
1.8 Example of ToF identification matrix taken with the CHIMERA detector for the reaction ^{124}Sn+^{64}Ni at 35 MeV/u and at a polar angle $\theta = 10^{\circ}$ [9]. The region labeled with **A** refers to particles stopping in the detector for which Eq. 1.6 holds, while the region labeled with **B** refers to particles punching through the first detector. 13
1.9 Example of energy–rise-time identification matrix in conjunction with the $\Delta E - E$ plot obtained for particles punching through the silicon detector taken with the CHIMERA detector for the reaction ^{20}Ne+^{12}C at 21 MeV/u and at a polar angle $\theta = 5.8^{\circ}$ and detector mounted in front injection [13]. 14
1.10 Example of energy–rise-time identification matrix in conjunction with the $\Delta E - E$ plot obtained for particles punching through the silicon detector taken with the CHIMERA detector for the reaction ^{20}Ne+^{12}C at 21 MeV/u and at a polar angle $\theta = 5.8^{\circ}$ and detector mounted in back injection [13]. 15
1.11 Overview of the whole CHIMERA detection array [15]. . . 16
1.12 Schematic drawing of the MUST2 6-telescopes array [21]. . 19
1.13 Exploded view of a MUST2 telescope [21]. 20
1.14 Basic schematic of one channel of the MATE ASIC [22]. . . 21
1.15 Technical drawing of a single HiRA telescope color-coded (see text for the complete description) [23]. 24
1.16 Photograph of 16 HiRA telescopes configured for transfer reaction experiment [26]. 24
1.17 Diagram of one channel of the HiRA ASIC [26]. 26

2.1 Exploded view of the FARCOS telescope. 30
2.2 Views from different angles of a full FARCOS telescope. The four gray blocks are the CsI(Tl) scintillator with the reading photodiode on the rear of each of them. The two yellow-framed parts are the DSSSD, the thin one before the thick one. 31
2.3 Technical drawing of a Double Sided Silicon Strip Detector together with its Kapton cables [33]. 32

2.4 Examples of possible configurations for FARCOS array used (a) for studies of fragments decay produced by projectile excitation and breakup and (b) for studies of two-particles correlations in heavy ion collision where a complete wall is mandatory [4]. 33
2.5 Semplified schematic of one channel of the custom CPAs. . 34
2.6 Semplified schematic of one channel of the custom CPAs. . 34
2.7 Illustration of the Digital DAQ. 36
2.8 Block diagram of the control software with the indication of the data and control parameters flow between different software components. 37
2.9 Energy resolutions, expressed in terms of FWHM, in the case of (a) 300 μm thick and (b) 1500 μm thick DSSSDs, respectively as a function of the first transistor drain current and of the strip width for a fixed peaking time of 200 ns. The dash-dotted lines represent the curves of constant power dissipation, while the gray shadowed area below 1 mA shows the limitation imposed by the BF862 minimum drain current. The vertical gray dotted line acts as guideline for the resolution achievable with the proposed BB7 DSSSD. . . . 40

3.1 Close up of the DSSSD mounted inside the vacuum chamber and the custom made deviation PCB boards for the CV measurements. 43
3.2 Sketch of the setup configuration for bulk capacitance measurements. 45
3.3 Sketch of the setup configuration for the inter-strip capacitance measurements. 45
3.4 Photograph of the whole experimental setup for the CV measurements. 46
3.5 Current versus voltage characteristics for the 300 μm-thick detector (a) and the 1500 μm-thick detector (b). Red curves refer to measurements performed in air. Blue curves, on the contrary, refers to the total-but strip n. 11 current measured in vacuum along with the CV measurements with the preliminary setup. The light blue curve in (a) corresponds the total but strip n. 01 current measured with the same setup of the blue ones. 48

3.6 (a) Capacitance versus voltage measurements for the bulk capacitance of front strip n. 10 of the 300 μm DSSSD, for different values of the voltage test signal frequency. (b) Dissipation Factor versus the bias voltage for all the considered frequencies. 49

3.7 (a) Capacitance versus voltage measurements for the bulk capacitance of back strip n. 13 of the 300 μm DSSSD, for different values of the voltage test signal frequency. (b) Dissipation factor versus the bias voltage for all the considered frequencies. 49

3.8 Measurement accuracy due to the LCR-meter for the Capacitance (a) and the Dissipation Factor (b). Each color-maps represent the accuracy of the measurement expressed in the percentage of the measured capacitance or in absolute value for D, function of the frequency and the capacitance value itself. The superposed lines correspond to the measured capacitance for the case of front strip n. 10, 300 μm thick detector, each line being made at constant frequency and for a voltage sweep. 50

3.9 (a) Capacitance versus voltage measurements for the bulk capacitance of front strip n. 10 of the 1500 μm DSSSD, for different values of the voltage test signal frequency. (b) Dissipation factor versus the bias voltage for all the considered frequencies. 51

3.10 (a) Capacitance versus voltage measurements for the bulk capacitance of the strip n. 13 of the back side of the 1500 μm DSSSD, for different values of the voltage test signal frequency. (b) Dissipation factor versus the bias voltage for all the considered frequencies. 51

3.11 Measurement accuracy due to the LCR-meter for the capacitance (a) and the dissipation factor (b). Each color-maps represent the accuracy of the measurement expressed in the percentage of the measured capacitance or in absolute value for D, function of the frequency and the capacitance value itself. The superposed lines correspond to the measured capacitance for the case of front strip n. 10, 1500 μm thick detector, each line being made at constant frequency and for a voltage sweep. 52

3.12 Bulk capacitance–voltage measurement for n. 01 (a) and back strip n. 01 (b) in the case of 300 μm-thick detector. On the front side case the contribution of the floating guard rings increase the dependence on the frequency and increases the value of the measured capacitance. 53
3.13 Bulk capacitance–voltage measurement for front strip n. 01 (a) and back strip n. 01 (b) in the case of 1500 μm-thick detector. Border effects are less evident than the case of 300 μm-thick detector since the increased detector thickness reduces the relative impact of the strip-guard ring interaction. . 53
3.14 Inter-strip capacitance-voltage measurement between strip n. 10 and n. 11 of the front side for the 300 μm case (a) and corresponding dissipation factor (b). 54
3.15 Inter-strip capacitance-voltage measurement between strip n. 10 and n. 11 of the front side for the 300 μm case plotted as a surface to better grasp the frequency dependence. 54
3.16 Inter-strip capacitance-voltage measurement between strip n. 13 and n. 14 of the back side for the 300 μm-thick case for all the considered frequencies. 55
3.17 Polar plot of the complex total impedance measured by the LCR-meter between the strip n. 13 and n. 14 of the back side of the 300 μm-thick detector. The modulus of the impedance is in logarithmic scale. Each line pertains to a specific frequency and correspond to a voltage sweep with voltage. . . 56
3.18 Inter-strip parallel resistance versus voltage between strip n. 13 and n. 14 of the back side for the 300 μm-thick case for all the considered frequencies. 56
3.19 Measurement accuracy due to the LCR-meter for capacitance (a) and the dissipation factor (b). Each color-maps represent the accuracy of the measurement expressed as the percentage of the measured capacitance or in absolute value for D, function of the frequency and the capacitance value itself. The superposed lines correspond to the measured inter-strip capacitance for the case of front strip n. 10 versus n. 11, 300 μm thick detector, each line being made at constant frequency and for a voltage sweep. 57
3.20 Inter-strip capacitance–voltage measurement between strip n. 10 and n. 11 of the front side for the 1500 μm case (a) and corresponding dissipation factor (b). 58

3.21 Inter-strip capacitance-voltage measurement between strip n. 13 and n. 14 of the back side for the 1500 μm case. . . . 58
3.22 Polar plot of the complex total impedance measured by the LCR-meter between the strip n. 13 and n. 14 of the back side of the 1500 μm-thick detector. The modulus of the impedance is in logarithmic scale. Each line pertains to a specific frequency and correspond to a voltage sweep with voltage. 59
3.23 Inter-strip parallel resistance versus voltage between strip n. 13 and n. 14 of the back side for the 1500 μm-thick case for all the considered frequencies. 59
3.24 Measurement accuracy due to the LCR-meter for the capacitance (a) and the dissipation factor (b). Each color-maps represent the accuracy of the measurement expressed as the percentage of the measured capacitance or in absolute value for D, function of the frequency and the capacitance value itself. The superposed lines correspond to the measured inter-strip capacitance for the case of front strip n. 10 versus n. 11, 1500 μm thick detector, each line being made at constant frequency and for a voltage sweep. 60
3.25 Aerial view of the experimental area inside the LaBeC facility at Sesto Fiorentino (FI), Italy. In the foreground stands out the 3 MV Tandetron accelerator. 62
3.26 Schematic drawing of the DEFEL line with all of its components highlighted, including the predeflector and deflector drivers [44]. 63
3.27 Predeflector-deflector synchronization signals for the creation of bunches of protons from a continuous beam [40]. 64
3.28 Scheme of principle of the experimental setup at the DEFEl beamline. The host PC is located outside the radiation controlled area. 64
3.29 Photograph of the DSSSD mounted on the mechanical frame and housed in the vacuum chamber. 65
3.30 Photograph of the digital DAQ system equipment and of the power supplies just outside the vacuum chamber. 66
3.31 Ionization profile for 1 MeV, 3 MeV and 5MeV protons and 7.5 MeV ^{7}Li ion in silicon, from SRIM2008 [43]. The Bragg peak in silicon is at about 16 μm, 91 μm, 213 μm and 14 μm respectively. 67

3.32 Energy spectrum collected in the case of 3 MeV proton interaction on one strip of the front side (a) and one strip of the ohmic side (b). Since the number of ions per bunch reflects their original distribution in the beam, the spectra envelope is roughly a Poissonian. The insets show a detail of the single 3 MeV proton peak together with its Gaussian fitting that allows the estimation of the peak centroid and FWHM. . . . 68

3.33 Energy calibration for the front-side strip n. 12 considering the peaks of the 3 MeV protons plus the 7.5 MeV Li ion, acquired in the same configuration (back injection, AAA gain 2x) and with energy corrected as described in the text. The sensitivity resulting from the least-square linear fitting is 39.851 mV/MeV (7.502 keV/LSB). 69

3.34 Integral non-linearity for the case of Fig. 3.33. The overall INL r.m.s. value is 0.45 LSB (3.35 keV). 70

3.35 Energy resolution expressed in FWHM of the single 3 MeV proton peak for one strip of the front side and two of the ohmic side, representative of the behavior of all the others, as measured with 3 MeV proton on the 300 μm DSSSD as a function of the digital triangular filter half-width. 71

3.36 3 MeV protons impinging on the inter-strip region of the 300 μm DSSSD between front-side strips n. 10 and n. 11 – front injection (a) and (b), between back-side strips n. 12 and n. 13 – back injection (c) and (d). On the left column the scatter plots of the $MAX+MIN$ of the two neighbor strips, on the right column the plot of the sorted events parameters pertaining to the one proton subset. 73

3.37 7.5 MeV Li ions impinging on the inter-strip region of the 300 μm DSSSD between front-side strips n. 10 and n. 11 – front injection (a) and (b), between back-side strips n. 12 and n. 13 – back injection (c) and (d). On the left column the scatter plots of the $MAX+MIN$ of the two neighbor strips, on the right column the plot of the sorted events parameters pertaining to the one Li ion subset. 75

3.38 3 MeV protons impinging on the inter-strip region of the 1500 μm DSSSD between front-side strip n. 10 and n. 11 – front injection (a) and (b), between back-side strips n. 13 and n. 14 – back injection (c) and (d). On the left column the scatter plots of the $MAX+MIN$ of the two neighbor strips, on the right column the plot of the sorted events parameters pertaining to the one proton subset. 76

3.39 7.5 MeV Li ion impinging on the inter-strip region of the 1500 μm DSSSD between front-side strips n. 10 and n. 11 – front injection (a) and (b), between back-side strips n. 13 and n. 14 – back injection (c) and (d). On the left column the scatter plots of the $MAX+MIN$ of the two neighbor strips, on the right column the plot of the sorted events parameters pertaining to the one Li ion subset. 77

3.40 Raw waveform – baseline subtracted – of front-side strips n. 10 (a) and n. 11 (b) for the 1500 μm DSSSD with a 3 MeV proton impinging at the inter-strip gap – front injection – corresponding to the highlighted positions in the scatter plot of Fig. 3.38 (a). Position α corresponds to a particle fully impinging on front-side strip n. 10, position $delta$ to a particle impinging in the inter-strip gap mid-point and β and γ to two intermediate positions. 78

3.41 Raw waveform – baseline subtracted – of back strips n. 13 (a) and n. 14 (b) for the 1500 μm DSSSD with a 3 MeV proton impinging at the inter-strip gap – back injection – corresponding to the highlighted positions in the scatter plot of Fig. 3.39 (c). Position α corresponds to a particle fully impinging on back-side strips n. 13, position $delta$ to a particle impinging in the inter-strip gap mid-point and β and γ to two intermediate positions. 78

4.1 Qualitative representation of the simulation volume for a 2D detector in linear geometry (in this case a double sided strip detector). The contour lines of the potential distribution in the central *x*-*y* cross-section show the static field due to the detector structure (stated in the boundary conditions and doping profile). The mobile carriers preserve their full 3D distribution and contribute with a 3D time-dependent field. . 83

4.2 Graphical representation of the series of image charges for a given charge distribution inside the detector volume. The series is truncated by an algorithm that controls the error at the boundaries of the simulation domain. [27] 84

4.3 Qualitative representation of the physical problem solved by Ramo's Theorem, that is to compute the charge and the current induced by a moving charge on a specific electrode of a system of electrodes. 85

4.4 Standard deviation of a cloud of N electrons expanding in free space due to pure thermal diffusion for different values of time step Δt. The red line stand for the theoretical curve $\sqrt{2D_n t}$. a) N=200, b) N=2000, c) N=20000. 88

4.5 L^2-norm of the standard deviations of the simulated values σ_x with respect to the theoretical ones in the total simulation time as a function of the number of electrons N, for different time steps Δt. The dashed line shows the $1/\sqrt{n}$ trend. . . . 89

4.6 Standard deviation of a cloud of N electrons due to pure Coulomb repulsion for finite detector thickness (from the bottom to the top N =100, 200, 500, 1000, 2000, 5000, 10000, 20000). The red line is the standard deviation along the depth (longitudinal) while the black line is the standard deviation in the orthogonal direction (transversal) (a) $d = 300\mu m$ and (b) $d = 450\mu m$. For comparison the standard deviation in the case of free expanding ($d \to \infty$). 90

4.7 Simulation of electron cloud (symbols). (a) Case of pure Coulomb repulsion, fitting curves based on 4.8. (b) Case of both thermal diffusion and Coulomb repulsion, fitting curves based on 4.7. The number of simulated electrons N varies from 100 to 20000 (from the bottom to the top of the figure) with two additional simulations of 20000 electrons where each carrier is conceived as a cluster of $10q$ and $100q$ respectively. 91

4.8 Linear fitting of the extrapolated $Q_0\mu K$ as a function of Q_0 for the different set of simulations. Simulations for low charge values and comprehensive of the thermal diffusion (green dots) have been discarded since the statistical spread gives unreliable results. The fitted value for μK is $3.1 \cdot 10^{-3}\mu m^3/ns/N$, where N is the number of electrons. . . . 92

4.9 Standard deviation of clouds varying the number of electrons N and correspondingly the macro charge factor M to maintain constant the total charge $Q_{tot} = 20000q$(a). Difference in percentage of the same curves from the reference one (M =1q) (b). The clouds are expanding in free space subject only to Coulomb repulsion. The value of the time step Δt is 0.2 ns. 94
4.10 Simulations of a cloud of 20000 electrons expanding in free space due only to Coulomb repulsion. Initial 3D Gaussian distribution with $\sigma_0 = 0.1\mu m$, Macro Factor M =1, 10 , 100 q, total time span 10 ns. Δt for the fixed time step case is 0.1 ns, while for the Adaptive Carrier Position Update the Maximum Allowed Displacement Δr_{max} is 10 nm, 100 nm and 1 μm respectively. (a) standard deviations along one direction (all directions are equivalent due to the symmetry of the problem), the theoretical thermal diffusion curve is also shown for comparison. Italic text identifies the several regimes of cloud expansion. (b) Total electric field averaged over all the electrons, same consideration for the italic text. (c) Velocity averaged over all the electrons. 96
4.11 Ionization profile for 1 MeV, 3 MeV and 5MeV protons and 7.5 MeV ^{7}Li ion in silicon, from SRIM2008 [43]. The Bragg peak in silicon is at about 16 μm, 91 μm, 213 μm and 14 μm respectively. 97
4.12 Zoomed view of the 2D potential surface in the nearby of the inter-strip region for the case d=300 μm with detector bias 25 V. 99
4.13 2D weighting potential surface (a) and contour plot (b) of STRIP 2 over the total simulation domain for the d =300 μm case. 99
4.14 2D weighting potential surface (a) and contour plot (b) of STRIP 2 over the total simulation domain for the d =1500 μm case. 100
4.15 Sketch of the position of incidence simulated A, B, C and D together with the penetration depth of the considered ions (Bragg peak depth) with respect to the detector geometry. (b) is the zoomed version of (a) to better visualize the less penetrating ions. The contour lines correspond to the static potential due to the boundary condition – 25 V across the 300 μm DSSSD. 100

4.16 102

4.16 2D projections (left column) and 3D (right column) snapshots of the electrons-holes charge cloud within the detector volume for the 7.5 MeV ^{7}Li ion impinging at position B of the 300 μm DSSSD and at different times – t =5 ns, t =20 ns, t =30 ns and t =50 ns. Electrons are green while holes are red. The underlying potential is the static potential due to the boundary conditions. STRIP 1 and STRIP 2 are at the upper border. 103

4.17 104

4.17 2D projections (left column) and 3D (right column) snapshots of the electrons-holes charge cloud within the detector volume for the 5 MeV ^{7}Li ion impinging at position B of the 300 μm DSSSD and at different times – t =5 ns, t =20 ns, t =30 ns and t =50 ns. Electrons are green while holes are red. The underlying potential is the static potential due to the boundary conditions. STRIP 1 and STRIP 2 are at the upper border. 105

4.18 Induced charge on STRIP 1 in case of position of incidence A (full strip) for all the considered ions and for the 300 μm case. Dotted lines differ from continuous lines for the omission of the Coulomb interaction computation in the simulations. The separation between the simulations with and without the Coulomb interaction computation increases due to plasma effects as the charge density increases (1 MeV proton to 7.5 MeV ^{7}Li ion). 105

4.19 Induced charge on STRIP 1 (left column) and STRIP 2 (right column) for all the considered ions and for the 300 μm DSSSD case, impinging on the positions B (border between STRIP 1 and the inter-strip region), C (a quarter of the distance between STRIP 1 and STRIP 2) and D (center of the inter-strip region). 107

4.20 Induced charge on STRIP 1 (a) and on STRIP 2 (b) for the case of the 7.5 ^{7}Li ion impinging on position B in the 300 μm DSSSD. The total charge in separated in its basic holes and electrons contributions. 108

4.21 108

4.21 2D projections (left column) and 3D (right column) snapshots of the electrons-holes charge cloud within the detector volume for the 5 MeV ^{7}Li ion impinging at position B of the 1500 μm DSSSD and at different times – t =5 ns, t =10 ns, t =30 ns and t =70 ns. Electrons are green while holes are red. The underlying potential is the static potential due to the boundary conditions. STRIP 1 and STRIP 2 are at the upper border. 109

4.22 Induced charge on STRIP 1 in case of position of incidence A (full strip) for all the considered ions and for the 1500 μm case. Dotted lines differ from continuous lines for the omission of the Coulomb interaction computation in the simulations. The separation between the two is extremely reduced in comparison with the 300 μm case since the static electric field due to the bias condition is now higher enough to avoid significant plasma effects. 110

4.23 Induced charge on STRIP 1 (left column) and STRIP 2 (right column) for all the considered ions and for the 1500 μm case, impinging on the positions B (border between STRIP 1 and the inter-strip region), C (a quarter of the distance between STRIP 1 and STRIP 2) and D (center of the inter-strip region). 111

4.24 Experimental *MAX+MIN* scatter plot for 3 MeV protons impinging on the 300 μm DSSSD between the front-side strips n. 10 and n. 11. The highlighted estimated locations α, β, γ and δ in the single-proton branch correspond to the simulated impinging positions A, B, C and D. 112

4.25 Comparison between the simulated induced charges (continuous lines) and the digitized raw waveforms (dotted lines, each dot corresponding to a sample) in the case of a 3 MeV proton impinging on the front side inter-strip region of the 300 μm DSSSD for STRIP 1-front strip n. 10 (a) and STRIP 2-front strip n. 11. Simulated results have been convolved with the pulse response of the AAA amplifier. Digitized waveforms have been baseline subtracted. The simulated impinging positions A, B, C and D correspond to the highlighted estimated locations α, β, γ and δ in the experimental scatter plot of Fig. 4.24. 113

4.26 Experimental *MAX+MIN* scatter plot for 7.5 MeV ^{7}Li ion impinging on the 300 μm DSSSD between the front-side strips n. 10 and n. 11. The highlighted estimated locations α, β, γ and δ in the single-ion branch correspond to the simulated impinging positions A, B, C and D. 114

4.27 Comparison between the simulated induced charges (continuous lines) and the digitized raw waveforms (dotted lines, each dot corresponding to a sample) in the case of a 7.5 MeV ^{7}Li ion impinging on the front side inter-strip region of the 300 μm DSSSD for STRIP 1-front strip n. 10 (a) and STRIP 2-front strip n. 11. Simulated results have been convolved with the pulse response of the AAA amplifier. Digitized waveforms have been baseline subtracted. The simulated impinging positions A, B, C and D correspond to the highlighted estimated locations α, β, γ and δ in the experimental scatter plot of Fig. 4.26. 114

4.28 Experimental *MAX+MIN* scatter plot for 3 MeV protons impinging on the 1500 μm DSSSD between the front-side strips n. 10 and n. 11. The highlighted estimated locations α, β, γ and δ in the single-proton branch correspond to the simulated impinging positions A, B, C and D. 115

4.29 Comparison between the simulated induced charges (continuous lines) and the digitized raw waveforms (dotted lines, each dot corresponding to a sample) in the case of a 3 MeV proton impinging on the front side inter-strip region of the 1500 μm DSSSD for STRIP 1-front strip n. 10 (a) and STRIP 2-front strip n. 11. Simulated results have been convolved with the pulse response of the AAA amplifier. Digitized waveforms have been baseline subtracted. The simulated impinging positions A, B, C and D correspond to the highlighted estimated locations α, β, γ and δ in the experimental scatter plot of Fig. 4.28. 115

4.30 Experimental *MAX+MIN* scatter plot for 7.5 MeV ^{7}Li ion impinging on the 1500 μm DSSSD between the front-side strips n. 10 and n. 11. The highlighted estimated locations α, β, γ and δ in the single-ion branch correspond to the simulated impinging positions A, B, C and D. 116

4.31 Comparison between the simulated induced charges (continuous lines) and the digitized raw waveforms (dotted lines, each dot corresponding to a sample) in the case of a 7.5 MeV ^{7}Li ion impinging on the front side inter-strip region of the 1500 μm DSSSD for STRIP 1-front strip n. 10 (a) and STRIP 2-front strip n. 11. Simulated results have been convolved with the pulse response of the AAA amplifier. Digitized waveforms have been baseline subtracted. The simulated impinging positions A, B, C and D correspond to the highlighted estimated locations α, β, γ and δ in the experimental scatter plot of Fig. 4.30. 116

5.1 Simplified schematics of the charge preamplifier. 123

5.2 Flowchart of the adopted analysis method for the determination of the CsI(Tl) scintillation time constants and intensities by direct fitting of the digitized waveforms. 125

5.3 $\Delta E - E$ identification matrix with the indication in green lines of the cluster relative to ^6Li events. The red line shows the spline interpolation for the same isotope, used in the energy calibration procedure (see Subsection 5.3.2). 126

5.4 Result of the fitting procedure in the case of a waveform pertaining to a ^{6}Li ion impinging on the scintillator with energy of 100 MeV. Only a portion of the digitized waveform is shown in figure for sake of visibility. 127

5.5 (a) Scintillator output pulse amplitude for the different isotopes as a function of the energies computed according to the procedure discussed in Section 5.3.2. The lines are the fits of the calculated points with the nonlinear function given by 5.6. (b) Same as (a) only for isotopes with Z$\leq$ 2 on a magnified scale. 129

5.6 Light Output $L(t)$ corresponding to an α particle and a ^{6}Li ion impinging on the scintillator at energy of 100 MeV, computed exploiting the result of the fitting procedure described in 5.3.1. 130

5.7 Four-vector components (τ_f, τ_s, h_f, h_s) obtained from the fit of the waveforms pertaining to all the identified isotopes as a function of energy. (a) Fast component time constant τ_f. The continuous lines indicate the average value of the distribution. The error bars indicate the $\pm\sigma$ confidentiality level of the distribution. (b) Slow component time constant τ_s. The continuous lines indicate the average value of the distribution. The error bars indicate the $\pm\sigma$ confidentiality level of the distribution. (c) Fast component intensity h_f normalized to the fast component intensity of an α particle impinging with an energy of 100 MeV. (d) Slow component intensity h_s normalized to the slow component intensity of an α particle impinging with an energy of 100 MeV. 131

5.8 (a) Fast component intensity h_f (normalized to the fast component intensity of an α particle impinging with an energy of 100 MeV) multiplied by the square root of the atomic number as a function of energy. (b) Slow component intensity h_s (normalized to the slow component intensity of an α particle impinging with an energy of 100 MeV) multiplied by the atomic number as a function of energy. 132

5.9 Relative intensities of the fast and slow component with respect to the total light output intensity (sum of the two intensities) as a function of the particle energy per nucleon (in MeV/u) for the different particles. For each atomic number Z$>$ 1, the lighter isotope is indicated with a black line and the heavier one with a gray line. 133

5.10 Relative intensities of the fast and slow component with respect to the total light output intensity (sum of the two intensities) as a function of the particle charge for two values of the energy per nucleon (10 MeV/u, 20 MeV/u). 133

5.11 (a) Fast component, computed as the value of the reconstructed preamplifier output at $T = 600$ ns, as a function of the particle energy for the different particles. (b) Slow component, computed as the difference of the values of the reconstructed preamplifier output at $T_{s,1} = 900$ ns and $T_{s,2} = 6$ μs, as a function of the particle energy for the different particles. 135

5.12 Reconstructed preamplifier output pulse 10% - 90% risetime as a function of the particle energy for the different particles. 136

5.13 Relative variation of the pulse rise time and of the rise time computed taking into account only the fast light output RT_{fast} as a function of the pulse amplitude for protons and ^{6}Li ions. 137
5.14 Relative variation of the slow component and of the $Slow_{slow}$ as a function of the pulse amplitude for protons and ^{6}Li ions. 138
5.15 Scatter plot of the $Slow_{slow}/Fast_{fast}$ against the pulse rise time for protons and ^{6}Li ions. 139
5.16 (Slow/Fast, RT) scatter plot for ^{20}Ne+^{12}C at 21.5 MeV/u. The rise-time is computed as 30% - 70%. 140
5.17 (Slow/Fast, RT) scatter plot for ^{96}Zr+^{96}Zr at 400 MeV/u. The rise-time is computed as 30% - 70%. 140
5.18 Fast–Slow scatter plot for ^{96}Zr+^{96}Zr at 400 MeV/u. The punch-through points (P.T.) for ^{3}He and α are shown in the inset. 142
5.19 (a) E_{CsI}–S/F and (b) E_{CsI}–RT scatter plots for ^{96}Zr+^{96}Zr at 400 MeV/u. 143
5.20 The transformation used for computing the FoMs, exemplified with the pair p, d in the E_{CsI}–*RT* scatter plot. In (a), the polygonals used to compute the parametric coordinate p_E for each event are shown; in (b) the representation in the transformed coordinate system (Energy$_{CsI}$, p_E); in (c) the projection of the selected pulse height interval in the transformed coordinate system; the histogram is fitted with two Gaussian and a linear background. 144

6.1 Photo of the experimental setup at Laboratori Nazionali del Sud in Catania during the on-beam test carried out in July 2012. Other detectors were profiting of the accelerated beams. An NTD silicon microstrip detector developed at GANIL, two thin microstrip detectors developed by University of Huelva and the Asterics detector of Rochester University. 148
6.2 Example of α-spectrum obtained for strip n. 12 of the front side of the 300 μm DSSSD of telescope T3. Waveforms have been previously digitally filtered with a triangular filter 201 taps kernel. The three main peaks are, respectively, at 5156.6 keV (^{239}Pu), at 5485.6 keV (^{241}Am) and at 5804.8 keV (^{244}Cm). 150
6.3 Energy resolution at the ^{239}Pu line expressed in keV FWHM for the strips of the front side (a) and of the back side (b). . . 151

6.4 Spatial distribution of events on T3 telescope for the reaction 62 MeV/u α on Pb+C. 152
6.5 $\Delta E - E$ scatter plots for the reaction 62 MeV/u α on Pb+C, using the CsI(Tl) crystal n. 3 of telescope T3 for the E and the sum of the signals of the front strips (a) or the back strips (b) just in front of the scintillator as ΔE. 153
6.6 2D correction map for the CsI(Tl) crystal n. 2 (a) and n. 3 (b) of telescope T3. The surfaces represent the differential light yield with respect to the average light yield, expressed in percentage. Each pixel of these maps correspond to a cluster of 2×2 DSSSD strips due to the poor statistics. . . . 154
6.7 (a) Energy spectrum of the CsI(Tl) crystal n. 2 of telescope T3 in the range of the elastic scattering peak of the 62 MeV/u α beam impinging on the Pb+C target. (b) Energy spectrum of the same acquisition corrected for the CsI(Tl) spatial light yield non-uniformity exploiting the DSSSD pixelation. . . . 155
6.8 $\Delta E - E$ scatter plots corrected for the CsI(Tl) light yield non-uniformity for the reaction 62 MeV/u α on Pb+C, using the CsI(Tl) crystal n. 3 of telescope T3 for the E and the sum of the signals of the front strips just in front of the scintillator as ΔE. 155
6.9 Spatial distribution of events on T3 telescope for the reaction 62 MeV/u α on Au. 156
6.10 $\Delta E - E$ scatter plot corrected for the CsI(Tl) light yield non-uniformity for the reaction 62 MeV/u α on Au, using the CsI(Tl) crystal n. 3 of telescope T3 for the E and the sum of the signals of the front strips just in front of the scintillator as ΔE. 156
6.11 Spatial distribution of events on T3 telescope for the reaction 20 MeV/u ^{20}Ne on CD_2 (Deuterated Polyethylene). 157
6.12 $\Delta E - E$ scatter plots for the reaction 20 MeV/u ^{20}Ne on CD_2 (Deuterated Polyethylene), using the CsI(Tl) crystal n. 3 of telescope T3 for the E and the sum of the signals of the front strips (a) or the back strips (b) just in front of the scintillator as ΔE. 158

A.1 Drawing of the DSSSD aluminum holder. 164
A.2 Drawing of the DSSSD holder top cover. 165
A.3 Drawing of the DSSSD holder bottom cover. 165
A.4 Layout of the top layer of a deviation PCB board. 166

A.5 Layout of the bottom layer of a deviation PCB board. 166
A.6 Layout of the top layer of the CV measurement probe pcb board. 167
A.7 Layout of the bottom layer of the CV measurement probe pcb board. 167

List of Tables

1.1 Identification for light particles with Z$\leq$ 3 [15] 18
1.2 Identification for fragments with Z$>$ 3 [15] 18

4.1 Values of the total electron-holes pairs generated and the Macro Charge Factor used in our simulations for the different impinging ions. 97

5.1 Number of waveforms fitted per isotope and number and percentage of discarded waveforms after fitting. 127
5.2 Fitting coefficients for the energy calibration 129
5.3 FoM values for different LCP pairs and representations. . . . 145

6.1 Energies and intensities of the most intense α-particles emitted by the different radionuclides [91]. 149

Bibliography

[1] S. Shlomo, "Equation of State of Symmetric And Asymmetric Nuclear Matter At Various Densities And Temperatures," *Journal of Physics: Conference Series*, vol. 337, no. 012014, pp. 1–4, 2012.

[2] G. Verde, A. Chibihi, R. Ghetti, R. Helgesson, "Correlations and Characterization of Emitting sources," *Eur. Phys. J. A*, vol. 30, pp. 81–108, 2006.

[3] A. Pagano *et al.*, "Fragmentation studies with the CHIMERA detector at LNS in Catania: Recent progress," *Nucl. Phys. A*, vol. 734, pp. 504–511, 2004.

[4] G. Verde, *et al.*, "The Farcos project: Femtoscope Array for Correlations and Femtoscopy," *Journal of Physics: Conference Series*, vol. 420, no. 012158, pp. 1–8, 2013.

[5] G. Verde, "Particle-Particle Correlations: Femtoscopy and Tools for Spectroscopy," *EPJ Web of Conference*, vol. 31, no. 00033, pp. 1–12, 2012.

[6] L. Acosta, F. Amorini, A. Anzalone, L. Auditore, C. Boiano, G. Cardella, A. Castoldi, A. Chbihi, E. De Filippo, L. Francalanza, E. Geraci, S. Giani, C. Guazzoni, E. La Guidara, G. Lanzalone, I. Lombardo, S. Lo Nigro, D. Loria, C. Maiolino, I. Martel, T. Minniti, A. Pagano, E. V. Pagano, M. Papa, T. Parsani, S. Pirrone, G. Politi, F. Porto, F. Riccio, F. Rizzo, P. Russotto, A. M. Sanchez-Benitez, J. A. Duenas, R. Berjillos, S. Santoro, A. Trifirò, M. Trimachi, G. Verde, M. Vigilante, and P. Zambon, "FARCOS: a versatile and modular Femtoscopy Array for Correlations and Spectroscopy," *2012 IEEE Nuclear Science Symposium and Medical Imaging Conference Record*, no. N20-6, pp. 1547–1553, 2012.

[7] G. F. Knoll, *Radiation Detection and Measurement – Third Edition*. John Wiley Sons, Inc., 2000.

[8] H. Bethe and J. Ashkin, *Experimental Nuclear Physics*. E. Segrè, Ed. New York: Wiley, 1953.

[9] P. Russotto, *Dynamic Emission of Heavy Fragments in the* $^{112,124}Sn+^{58,64}Ni$ *Reaction at 35 AMeV as Seen with CHIMERA*. PhD Thesis, 2006.

[10] Pausch *et al.*, "Particle identification in a wide dynamic range based on pulse-shape analysis with solid state detectors," *Nucl. Instrum. Meth. Phys. Res. A*, vol. 349, pp. 281–284, 1994.

[11] G. Pausch *et al.*, "Identification of light charged particles and heavy ions in silicon detectors by means of pulse-shape discrimination," *IEEE Trans. Nucl. Sci.*, vol. 43, no. 3, pp. 1097–1101, 1996.

[12] M. Mutterer *et al.*, "Breakthrough in pulse-shape based particle identification with silicon detectors," *IEEE Trans. Nucl. Sci.*, vol. 47, pp. 756–759, 2000.

[13] M. Alderighi *et al.*, "Charge Identification in Large Area Planar Silicon Detectors, Using Digital Pulse Shape Acquisition," *IEEE Trans. Nucl. Sci.*, vol. 53, no. 1, pp. 279–285, 2006.

[14] A. Castoldi, C. Guazzoni, "Impact of detector parameters on light charged particle and intermediate mass fragments identification through pulse-shape analysis," *Nucl. Instrum. Meth. Phys. Res. A*, vol. 624, pp. 317–320, 2010.

[15] available online at `https://192.84.151.50/joomla/index.php?option=com_content&view=frontpage&Itemid=1`.

[16] S. Aiello *et al.*, "The enhanced data acquisition system for the 4π detector CHIMERA," *IEEE Trans. Nucl. Sci.*, vol. 47, pp. 114–118, 2000.

[17] Struck Innovative System GmbH, Hamburg, Germany, *SIS3300/SIS3301 65/80/100 MHz VME FADCs - User Manual*, 2004.

[18] Y. Blumenfeld *et al.*, "MUST: A silicon strip detector array for radioactive beam experiments," *Nucl. Instrum. Meth. Phys. Res. A*, vol. 421, pp. 471–491, 1999.

[19] E. Pollacco *et al.*, "MUST2: A new generation array for direct reaction studies," *Eur. Phys. J. A*, vol. 25, no. s01, pp. 287–288, 2005.

[20] E. Pollacco *et al.*, "MUST II: Large solid angle light charged particle telescope for inverse kinematics studies with radioactive beams.," *AIP Conference Proceedings, Application of Accelerators in Research and Industry*, vol. 680, pp. 313–316, 2003.

[21] available online at `http://pro.ganil-spiral2.eu/laboratory/detectors/charged-particles/must2/`.

[22] P. Baron *et al.*, "MATE, a single front-end ASIC for silicon strip, Si(Li) and CsI detectors.," *IEEE 2003 Nuclear Science Symposium Conference Records*, vol. 1, pp. 386–390, 2003.

[23] M.S. Wallace *et al.*, "The high resolution array (HiRA) for rare isotope beam experiments," *Nucl. Instrum. Meth. Phys. Res. A*, vol. 583, pp. 302–312, 2007.

[24] B. Davin *et al.*, "LASSA: a large area silicon strip array for isotopic identification of charged particles," *Nucl. Instrum. Meth. Phys. Res. A*, vol. 473, pp. 302–318, 2001.

[25] available online at `http://www.micronsemiconductor.co.uk/pdf/bb.pdf`.

[26] available online at `http://www.nscl.msu.edu/science/nuggets/wavefunctions`.

[27] A. Castoldi and C. Guazzoni, "Induced current signals in planar pn diodes for Light Charged Products identification," *2006 IEEE Nuclear Science Symposium Conference Record*, no. N14-143, pp. 464–468, 2006.

[28] M. Alderighi *et al.*, "CHIMERA Data Acquisition Via Digital Sampling Technique," *IEEE Trans. Nucl. Sci.*, vol. 51, no. 4, pp. 1475–1481, 2004.

[29] D. Vasileska, S. M. Goodnick, "Computational Electronics," *Material Science and Engineering R*, vol. 38, pp. 181–236, 2002.

[30] A. Castoldi, C. Guazzoni, P. Zambon, "A 3-D Simulation Code of Electron-Hole Transport and Signal Formation with Coulomb Repulsion and Thermal Diffusion in 2-D Semiconductor Detectors," *2012 IEEE Nuclear Science Symposium and Medical Imaging Conference Record (NSS/MIC)*, no. N14-67, pp. 961–967, 2012.

[31] F. Amorini *et al.*, "On-board digital signal processing for 4π-Detector large-area telescopes," *IEEE Trans. Nucl. Sci.*, vol. 54, no. 1, pp. 208–213, 2007.

[32] J. Pouthas *et al.*, "INDRA, a 4π charged product detection array at GANIL," *Nucl. Instrum. Meth. Phys. Res. A*, vol. 357, pp. 418–442, 1995.

[33] available online at `http://www.micronsemiconductor.co.uk/index.asp`.

[34] C. Boiano, C. Guazzoni, P. Guazzoni, L. Zetta, A. Pagano, "A 16-Channel Programmable Antialiasing Amplifier," *2010 IEEE Nuclear Science Symposium Conference Records*, pp. 1389–1391, 2010.

[35] Struck Innovative System GmbH, Hamburg, Germany, *SIS3302 100 MHz l6-bit VME Digitizer - User Manual*, 2009.

[36] Struck Innovative System GmbH, Hamburg, Germany, *SIS1100/3100 - User Manual*, 2008.

[37] R. Brun and F. Rademakers, "ROOT - An object oriented data analysis framework," *Nucl. Instrum. Meth. Phys. Res. A*, vol. 389, pp. 81–86, 1997.

[38] L. Acosta, F. Amorini, A. Anzalone, L. Auditore, C. Boiano, G. Cardella, L. Carraresi, A. Castoldi, A. Chbihi, E. De Filippo, L. Francalanza, E. Geraci, S. Giani, C. Guazzoni, E. La Guidara, G. Lanzalone, I. Lombardo, S. Lo Nigro, D. Loria, C. Maiolino, I. Martel, T. Minniti, G. V. Montemurro, A. Pagano, E. V. Pagano, M. Papa, T. Parsani, S. Pirrone, G. Politi, F. Porto, F. Riccio, F. Rizzo, P. Russotto, A. M. Sanchez-Benitez, J. A. Duenas, R. Berjillos, S. Santoro, F. Taccetti, A. Trifirò, M. Trimachi, G. Verde, M. Vigilante, and P. Zambon, "Mapping the Amplitude and Position Response of Double Sided Silicon Strip Detectors with Monochromatic Single Protons," *2012 IEEE Nuclear Science Symposium and Medical Imaging Conference Record (NSS/MIC)*, no. N14-217, pp. 1358–1364, 2012.

[39] A. Castoldi, C. Guazzoni, T. Parsani, F. Riccio, P. Zambon, C. Boiano, L. Carraresi, F. Taccetti, L. Acosta, G. Cardella, T. Minniti, G. Verde, L. Quattrocchi, A. Trifirò, "Experimental Investigation of the Impact of Inter-Strip Incidence on the Signal Shape in Double Sided Silicon Strip Detectors for Particle Identification," *2013 IEEE Nuclear Science Symposium and Medical Imaging Conference Record (NSS/MIC)*, no. N26-4, 2013.

[40] F. A. Mirto, and L. Carraresi, "The pulsed beam facility at the Tandetron accelerator in Florence," *Nucl. Instrum. Meth. Phys. Res. B*, vol. 266, pp. 2113–2116, 2008.

[41] P. A. Mandò, "INFN-LABEC, Nuclear Techniques for Cultural Heritage and Environmental Applications," *Nuclear Physics News*, vol. 19, pp. 5–12, 2009.

[42] Available online at `physics.nist.gov/PhysRefDataiStar/TextiPSTAR.html`.

[43] SRIM, The Stopping and Range of Ions in Matter, available online at `http://www.srim.org`

[44] L. Giuntini *et al.*, "The pulsed beam facility at LABEC: status and perspectives," *INPC 2013*.

[45] V. Eremin, J. Bohm, S. Roe, G. Ruggero, P. Weilhammer, "The charge collection in single side silicon microstrip detectors," *Nucl. Instrum. Meth. Phys. Res. A*, vol. 500, pp. 121–132, 2003.

[46] S. Takeda *et al.*, "Development of double-sided silicon strip detectors (DSSD) for a Compton telescope," *Nucl. Instrum. Meth. Phys. Res. A*, vol. 579, pp. 859–865, 2007.

[47] D. Torresi *et al.*, "Influence of the interstrip gap on the response and the efficiency of Double Sided Silicon Strip Detectors," *Nucl. Instrum. Meth. Phys. Res. A*, vol. 713, pp. 11–18, 2013.

[48] J. Yorkstone, A. C. Shotter, D. B. Syme and G. Huxtable, "Interstrip surface effects in oxide passivated ion-implanted silicon strip detectors," *Nucl. Instrum. Meth. Phys. Res. A*, vol. 262, pp. 353–358, 1987.

[49] A. Castoldi, P. Zambon, "Simulation of the 3-D Coulomb Explosion of the Electron-Hole Distribution at High Injection Levels in 2-D Semiconductor Detectors," *2013 IEEE Nuclear Science Symposium and Medical Imaging Conference Record (NSS/MIC)*, no. N46-6, 2013.

[50] A. Castoldi, E. Gatti, "Fast tools for 3-D design problems in semiconductor detectors," *Nucl. Instrum. Meth. Phys. Res. A*, vol. 377, pp. 381–386, 1996.

[51] W. H. Press, S. A. Teukolsky, W. T. Vetterling, B. P. Flannery, *Numerical Recipes - Third Edition*. Cambridge University Press, 2007.

[52] S. Ramo, "Currents Induced by Electron Motion," *Proceedings of the I.R.E.*, vol. 27, no. 9, pp. 584–585, 1939.

[53] D. M. Caughey, R. E. Thomas, "Carrier Mobilities in Silicon Empirically Related to Doping and Field," *Proceeding IEEE*, no. 55, pp. 2192–2193, 1967.

[54] S. A. Schwarz, S. E. Russe, "Semi-Empirical Equations for Electron Velocity in Silicon: Part II - MOS Inversion Layer," *IEEE Trans. Electron Devices*, vol. 30, no. 12, pp. 1634–1639, 1983.

[55] C. Jacoboni, C. Canali, G. Ottaviani and A. Alberigi Quaranta, "A Review of Some Charge Transport Properties of Silicon," *Solid-State Electronics*, vol. 20, pp. 77–89, 1977.

[56] C. Canali, C. Jacoboni, F. Nava, G. Ottaviani and A. Alberigi-Quaranta, "Electron drift velocity in silicon," *Physical Review B*, vol. 12, no. 1, pp. 2265–2284, 1975.

[57] G. Ottaviani, L. Reggiani, C. Canali, F. Nava and A. Alberigi-Quaranta, "Hole drift velocity in silicon," *Physical Review B*, vol. 12, no. 8, pp. 3318–3329, 1975.

[58] T. Kunikiyo, M. Takenaka, Y. Kamakura, M. Yamaji, H. Mizuno *et al.*, "A Monte Carlo simulation of anisotropic electron transport in silicon including full band structure and anisotropic impact ionization model," *J. Appl. Phys.*, vol. 75, p. 297, 1994.

[59] R. Brunetti, C. Jacoboni, F. Nava and L. Reggiani, G. Bosman and R. J. J. Zijlstra, "Diffusion coefficient of electron in silicon," *J. Appl. Phys.*, vol. 52, no. 11, pp. 6713–6722, 1981.

[60] L. Reggiani, R. Brunetti and E. Normantas, "Diffusion coefficient of holes in silicon by Monte Carlo simulation," *J. Appl. Phys*, vol. 59, pp. 1212–1215, 1986.

[61] P. S. Cheung and C. J. Hearn, "The diffusion of electrons in semiconductors in high electric fields," *J. Phys. C: Solid State Phys.*, vol. 5, pp. 1563–1572, 1972.

[62] E. Gatti, A. Longoni, P. Rehak and M. Sampietro, "Dynamics of electrons in drift detectors," *Nucl. Instrum. Meth. Phys. Res. A*, vol. 253, pp. 393–399, 1987.

[63] V. L. Rykov, R. Bellwied, A. French, J. R. Hall, C. Pruneau, W. K. Wilson, "SDD Signal Parametrization," *STAR Note*, vol. 170, 1994.

[64] P. A. Tove and W. Seibt, "Plasma Effects in Semiconductor Detectors," *Nucl. Instrum. Meth.*, vol. 51, no. 2, pp. 261–269, 1967.

[65] W. Seibt, K. E. Sundstrom and P. A. Tove, "Charge Collection in Silicon Detector for Strongly Ionizing Particles," *Nucl. Instrum. Meth.*, vol. 113, pp. 317–324, 1973.

[66] E. C. Finch, A. A. Cafolla and M. Asghar, "The Plasma Decay Time in Semiconductor Detectors for Energetic Heavy Ions," *Nucl. Instrum. Meth.*, vol. 198, pp. 547–556, 1982.

[67] F. Amorini, C. Boiano, G. Cardella, A. Castoldi, E. De Filippo, E. Geraci, L. Grassi, C. Guazzoni, P. Guazzoni, E. La Guidara, I. Lombardo, A. Pagano, S. Pirrone, G. Politi, F. Porto, F. Riccio, F. Rizzo, P. Russotto, G. Verde, P. Zambon and L. Zetta, "Investigation of the Dependence of CsI(Tl) Scintillation Time Constants and Intensities on Particles Energy, Charge and Mass Through Direct Fitting of Digitized Waveforms," *IEEE Trans. Nucl. Sci.*, vol. 59, no. 4, pp. 1772–1780, 2012.

[68] L. Acosta, F. Amorini, R. Bassini, C. Boiano, G. Cardella, E. De Filippo, L. Grassi, C. Guazzoni, P. Guazzoni, M. Kiš, E. La Guidara, Y. Leifels, I. Lombardo, T. Minniti, A. Pagano, M. Papa, S. Pirrone, G. Politi, F. Porto, F. Riccio, F. Rizzo, P. Russotto, S. Santoro, W. Trautmann, A. Trifirò, G. Verde, P. Zambon and L. Zetta, "Probing the Merits of Different Event Parameters for the Identification of Light Charged Particles in CHIMERA CsI(Tl) Detectors With Digital Pulse Shape Analysis," *IEEE Trans. Nucl. Sci.*, vol. 60, no. 1, pp. 284–292, 2013.

[69] F. Benrachi *et al.*, "Investigation of the performance of CsI(Tl) for charged particle identification by pulse-shape analysis," *Nucl. Instrum. Meth. Phys. Res. A*, vol. 281, pp. 137–142, 1989.

[70] J. Alarja *et al.*, "Charged particles identification with a CsI(Tl) scintillator," *Nucl. Instrum. Meth. Phys. Res. A*, vol. 242, pp. 352–354, 1986.

[71] J. B. Birks, *The Theory and Practice of Scintillation Counting*. New York: Pergamon Press, 1964.

[72] D. Guinet *et al.*, "Using the combination of CsI(Tl) and photodiode for identification and energy measurement of light particles," *Nucl. Instrum. Meth. Phys. Res. A*, vol. 278, pp. 614–616, 1989.

[73] A. Syntfeld-Każuch, M. Moszyński, L. Świderski, W. Klamra, and A. Nassalski, "Light pulse shape dependence on γ-ray energy in CsI(Tl)," *IEEE Trans. Nucl. Sci.*, vol. 55, no. 3, pp. 1246–1250, 2008.

[74] M. Pârlog, "Response of CsI(Tl) scintillators over a large range in energy and atomic number of ions. Part I: Recombination and δ-electrons," *Nucl. Instrum. Meth. Phys. Res. A*, vol. 482, pp. 674–692, 2002.

[75] M. Pârlog, "Response of CsI(Tl) scintillators over a large range in energy and atomic number of ions. Part II: Calibration and identification in the INDRA array," *Nucl. Instrum. Meth. Phys. Res. A*, vol. 482, pp. 693–706, 2002.

[76] P. Guazzoni, F. Previdi, S. Russo, M. Sassi, S. M. Savaresi, and L. Zetta, "Pulse shape analysis using subspace identification method and particle identification using neural network in CsI(Tl) scintillators," *2005 IEEE Nuclear Science Symposium Conference Record*, pp. 1341–1345, 2005.

[77] M. Alderighi *et al.*, "Particle identification method in the CsI(Tl) scintillator used for the CHIMERA 4π detector," *Nucl. Instrum. Meth. Phys. Res. A*, vol. 489, pp. 257–265, 2002.

[78] Struck Innovative System GmbH, Hamburg, Germany, *SIS9300 ADC CMC - User Manual*.

[79] Struck Innovative System GmbH, Hamburg, Germany, *SIS3150 ADC CMC Carrier - User Manual*.

[80] J. J. Moré and D. C. Sorensen, "Computing a trust region step," *SIAM J. Sci. Stat. Comput.*, vol. 4, no. 3, pp. 553–572, 1983.

[81] R. H. Byrd, R. B. Schnabel, and G. A. Shultz, "Approximate solution of the trust region problem by minimization over two-dimensional subspaces," *Math. Programm.*, vol. 40, pp. 247–263, 1988.

[82] J. F. Ziegler, "The stopping of light ions in elemental matter," *J. Appl. Phys/Rev. Appl. Phys.*, vol. 85, pp. 1249–1272, 1999.

[83] E. Valtonen, J. Peltonen, and J. J. Torsti, "Response of BGO and CsI(Tl) scintillators to heavy ions," *Nucl. Instrum. Meth. Phys. Res. A*, vol. 286, p. 169, 1990.

[84] N. Colonna *et al.*, "Calibration of the response function of CsI(Tl) scintillators to intermediate-energy heavy ions," *Nucl. Instrum. Meth. Phys. Res. A*, vol. 321, pp. 529–534, 1992.

[85] G. Pausch, W. Bohne, and D. Hilscher, "Particle identification in solid state detectors by means of pulse-shape analysis-results of computer simulations," *Nucl. Instrum. Meth. Phys. Res. A*, vol. 337, pp. 573–587, 1994.

[86] T. Masuda *et al.*, "The fluorescent decay of CsI(Tl) scintillator for charged particles of different ionization density," *Nucl. Instrum. Meth. Phys. Res. A*, vol. 322, pp. 135–136, 1992.

[87] C. Lemmon *et al.*, "Proposal for SIS Experiment S394 2009," *Unpublished.* available online at `http://www.ct.infn.it/asyeos2010R`.

[88] W. Trautmann *et al.*, "Differential neutron-proton squeeze-out," *Prog. Part. Nucl. Phys.*, vol. 62, pp. 425–426, 2009.

[89] M. B. Tsang *et al.*, "Constraints on the Density Dependence of the Symmetry energy," *Phys. Rev. Lett.*, vol. 102, p. 122701 (4 pages), 2009.

[90] R. A. Winyard *et al.*, "Pulse shape discrimination in inorganic and organic scintillators," *Nucl. Instrum. Meth.*, vol. 95, pp. 141–153, 1971.

[91] Isotrak, *Alpha Spectrometer Sources*. available online at `http://www.hightechsource.co.uk`.